FIBER REINFORCED POLYPROPYLENE NANOCOMPOSITES

THÈSE N^{O} 3851 (2007)

PRÉSENTÉE LE 17 AOÛT 2007

À LA FACULTÉ DES SCIENCES ET TECHNIQUES DE L'INGÉNIEUR

Laboratoire de technologie des composites et polymères

SECTION DE SCIENCE ET GÉNIE DES MATÉRIAUX

ÉCOLE POLYTECHNIQUE FÉDÉRALE DE LAUSANNE

POUR L'OBTENTION DU GRADE DE DOCTEUR ÈS SCIENCES

PAR

Chrystèle HOUPHOUET-BOIGNY

ingénieur en science des matériaux diplômée EPF
et de nationalité française

acceptée sur proposition du jury:

Prof. A. Mortensen, président du jury
Prof. J.-A. E. Månson, Dr C. J. G. Plummer, directeurs de thèse
M. K.-L. Brentrup, rapporteur
Dr T. Meyer, rapporteur
Prof. I. Verpoest, rapporteur

ÉCOLE POLYTECHNIQUE
FÉDÉRALE DE LAUSANNE

Lausanne, EPFL
2007

« C’est une grande folie que de vouloir être sage tout seul »
La Rochefoucauld, 1664

ACKNOWLEDGEMENTS

First, I would like to thank Professor Jan-Anders E. Månson, director of my thesis and head of the Laboratory of Composite and Polymer Technology (LTC), for allowing me to conduct this work in his laboratory under excellent working conditions, for opening up opportunities and for being concerned at a human level as well.

My warm thanks go to Dr. Christopher Plummer, director and supervisor of my thesis, for his challenging scientific guidance and advice, as well as for his patience in reading and providing corrections to my work in general and to this document in particular.

I am obliged to Dr. Martyn Wakeman, Dr. Pierre-Etienne Bourban and Dr. Pierre Dumont for valuable scientific discussions and advice, and in particular to Dr. Véronique Michaud in initiating me to the fundamentals and use of the impregnation model she developed. I also would like to thank Dr. Laurence Mathieu for her help in many aspects of my work.

Professor László Forró, head of the Institut of Condensed Matter (IPMC), Dr. Csilla Miko and Dr. Arnaud Magrez are thanked for providing me with carbon nantotubes and sharing their facilities. Dr. Pascal Hubert and Behnam Ashrafi are also thanked for interesting discussions and calculation of nanocomposite mechanical properties. I am grateful to Dr. Kurt Schenk for his interest and availability in introducing me to X-ray measurements on fibers. I would like to thank the CIME for the access to its facilities and in particular Danièle Laub and Guido Milanesi.

I also thank all the students who have contributed to this work through semester projects or bachelor theses: Helen Griffiths, Michèle Bernet, Pierre-David André, Julien Brelle, Christian Buechel, Tina Ventura, Marc Corthay, Didier Hayem and Sandra Galmarini.

For all technical support and design ideas, Fabio Demarco, Marcel Kohler and Sebastien Lavanchy are warmly thanked. I am grateful to all technicians of IMX workshop for their expertise and rapidity.

Special thanks are due to Antoinette Marciano, Christine Vuichoud, Maria Delaloye and Chiara Domini for their help with administrative issues.

I would like to thank personally all LTC members for the good times we spent together and in particular my office mates, Antonio, Lars, Valerie and Christian who helped me to keep “the mind of the beginner” spirit.

Finally, I would like to thank my family and friends…

ABSTRACT

The aim of this thesis is to assess the feasibility of integrating nanoparticles into glass fiber (GF) reinforced isotactic polypropylene (iPP) composites via existing thermoplastic processing routes, and to investigate whether this results in significant improvements in the mechanical properties of the final composites. A longer term aim will be to extend the approach to the preparation of hybrid composites with added non-structural functionality. However, the nanoparticles that have provided the focus for the present project, montmorillonite layered silicates (MMT) and nanocarbons, were chosen for their potential as structural reinforcing elements. A melt-spinning grade and a film grade of iPP were used to prepare iPP-based nanocomposite precursors in the form of melt-spun fibers and extrusion-calendered films respectively. Long glass fiber (LGF) and glass mat thermoplastic (GMT) composites were then compression-molded from co-woven, co-wound and intercalated semi-finished products. The processing behavior and structural performance of the resulting composites are discussed in terms of the matrix morphology and its influence on the matrix rheological and mechanical properties, and interactions between the matrix and the reinforcing fibers.

The nanocomposites were prepared by either (i) combined solvent and melt-mixing or (ii) direct melt-mixing. Combined solvent and melt-mixing was more suitable for dispersing carbon nanofibers (CNF), which tended to agglomerate. With iPP/MMT, both routes gave a mixed intercalated-exfoliated morphology with an MMT interlayer spacing up to 57 % greater than in the as-received MMT. However, direct melt-mixing was considered to be better suited to industrial requirements, and also more convenient for laboratory scale preparation. Melt-compounded iPP/MMT injection moldings showed a monotonic increase in stiffness with increasing MMT content, a 40 % increase in tensile modulus being measured at 13.5 wt% MMT, for example. The tensile strength, on the other hand, reached a maximum 10 % increase over that of the pure iPP at about 3 wt% MMT, but fell off at higher MMT contents.

iPP/MMT and iPP/CNF fibers were melt-spun using a laboratory-scale industrial spinning line. Processability was consistent with the melt rheology, the maximum MMT content for which fiber spinning was possible being about 5 wt%. The MMT platelets were aligned with the fiber axis over the whole range of MMT loadings and fiber draw ratios. MMT particle aspect ratios of about 150 were observed by TEM in this case, i.e. greater than in the as-compounded iPP/MMT, for which the particle aspect ratios were about 50. An aspect ratio of 150 was found to be consistent with micromechanical modeling of the observed increases in fiber stiffness with MMT content, which reached 170 % for iPP/2 wt% MMT fibers melt-spun with a draw ratio of 1 and a drive-roll velocity of 360 m/min. The tensile strength again reached a maximum at about 3 wt% MMT. The thermal stability of the fibers, determined by thermal mechanical analysis, also increased on MMT addition, the onset of extensive fiber creep shifting from 90 °C for pure iPP fibers to about 110 °C for iPP/1.1 wt% MMT fibers. Moreover, significantly reduced shrinkage was observed in the presence of MMT, which is a potential advantage for textile based composite processing. In the case of iPP/CNF fibers, limited particle orientation and the presence of aggregates in all the formulations led to relatively poor tensile properties, about 50 % lower than those obtained with iPP/MMT fibers melt-spun with the same filler content (4 wt%) and processing conditions. iPP/MMT therefore provided the main focus for subsequent work. iPP/MMT films were produced by extrusion-calendering. Partial orientation of MMT platelets in the melt flow direction resulted in anisotropic stiffness and strength. However, both the tranverse and axial stiffnesses increased with MMT content, with improvements of up to 75 % at 5.9 wt% MMT with respect to those of the pure iPP films, consistent with Halpin-Tsai predictions for composites containing oriented platelets with the observed aspect ratio of 50. The fracture

resistance of the films, determined using modified essential work of fracture (EWF) tests, was likewise strongly dependent on the testing direction. For axial crack propagation, the EWF decreased monotonically with MMT content, but for transverse crack propagation, it reached a maximum at about 3 wt% MMT. This was attributed to orientation dependent cavitation and crack deviation in the presence of the MMT particles.

Rheological measurements indicated increases in the low shear rate melt viscosity by up to two orders of magnitude on MMT addition to the iPP, with a potentially significant influence on the impregnation behavior of composite preforms. For co-woven and co-wound LGF-matrix fiber preforms, impregnation was highly dependent on the fiber bed geometry. For 40 vol% glass fiber co-wound composites, the porosity increased from about 7 vol% for a pure iPP matrix compression molded at 0.6 MPa, to 14 vol% for a iPP/3.4 wt% MMT matrix compression molded at 1.8 MPa. However, the more intimate mixing between the fibers obtained in co-woven preforms led to more consolidated composites in each case (below 2 vol% porosity) with no filtering of the MMT particles. In modeling the impregnation kinetics of glass mat thermoplastic composites (GMT) based on iPP/MMT, the matrix was therefore considered to behave as a continuum and, for simplicity, to show Newtonian behavior. Consistent results were obtained, but in the presence of MMT, higher impregnation times were predicted than observed experimentally in model GMT preforms, owing to the non-linear response of the nanocomposites. Moreover, under experimental conditions corresponding to the industrial process (0.2 MPa at 200 °C), iPP/5.9 wt% MMT-based hybrid composites were fully impregnated (porosity between 11 and 17 vol%) and the glass mat completely relaxed after about 30 s of compression molding, which is consistent with typical GMT industrial process cycle times (20 - 60 s).

Fully consolidated 30 wt% GF - hybrid GMT specimens were prepared for mechanical testing by compression molding at 2 MPa and 200 °C for 10 min, resulting in a porosity of about 2 vol%. At room temperature, the flexural modulus and strength of iPP/MMT-based GMTs increased monotonically with MMT addition, the increases reaching about 45 % and 33 % respectively at 5.9 wt% MMT. The increase in the flexural modulus on MMT addition was greater than predicted on the basis of a conventional rule of mixtures taking into account glass fiber orientation and aspect ratio, and the measured Young's moduli of the matrix. This was tentatively attributed to improvements in the flexural properties of the matrix in the presence of the MMT higher than those observed in tension. Increases in the flexural modulus and strength were also observed at 50 °C and 90 °C, but were less marked than at room temperature. The impact strength of the hybrid composites decreased with increasing MMT content at room temperature owing both to the decrease in matrix fracture resistance inferred from the data for the precursor films, and to an improved fiber-matrix interface as reflected by SEM observations, and argued to be due to the presence of coupling agents. Given that the presence of MMT was shown not to have serious consequences for impregnation, taken as a whole these results are considered highly promising for the implementation of nanocomposite matrices in GMT, and to establish the general feasibility of producing hybrid fiber reinforced thermoplastic nanocomposites by conventional processing routes.

KEYWORDS: nanocomposites**,** montmorillonite, carbon nanofiber, melt-spinning, films, impregnation, hybrid glass fiber reinforced composites

VERSION ABRÉGÉE

Cette thèse a pour but (i) d'évaluer la faisabilité d'intégrer des charges nanométriques dans des composites polypropylène fibres de verre, en utilisant des techniques de mise en œuvre propres aux thermoplastiques, (ii) de vérifier si cet apport pourrait améliorer les propriétés mécaniques du composite final. L'objectif à long terme est d'étendre cette approche à la fabrication de composites hybrides possédant des fonctionnalités non structurelles en complément des propriétés mécaniques usuelles. Cette étude se limite au cas de nano-charges de types montmorillonite (MMT) et nanocarbone, connues pour leur qualité de renfort. Deux grades de polypropylène isotactique (iPP) ont été utilisés pour produire des filaments et des films nanocomposites. Ces précurseurs ont été par la suite tissés, enroulés ou intercalés avec des fibres de verre afin d'obtenir par moulage par compression des composites à fibres longues et des composites estampables. La mise en œuvre et les performances structurelles de ces composites ont été discutées en termes de la morphologie de la matrice, de son influence sur les propriétés rhéologiques et mécaniques de la matrice et de ses interactions avec les fibres de renfort.

Les nanocomposites ont été préparés soit en deux étapes, par voie solvant puis une étape par mélange à l'état fondu, i.e. extrusion, soit directement par extrusion. La méthode combinée a été la plus efficace pour détruire les agglomérats dans le cas des nanofibres de carbone (CNF). Pour les nanocomposites iPP/MMT, les deux procédés ont abouti à une morphologie mixte intercalée-exfoliée avec une MMT présentant une distance interlamellaire 57 % supérieure à celle de la MMT de départ. Cependant le mélange par extrusion était le plus susceptible de répondre aux exigences industrielles et le plus pratique pour la préparation des échantillons à grande échelle. La rigidité des moulages par injection des nanocomposites préparés par extrusion augmentait continuellement avec la quantité de MMT, donnée en pourcentage massique, atteignant par exemple une augmentation de 40 % pour 13.5 % en MMT. En revanche, la contrainte à la rupture pour les mêmes matériaux était jusqu'à 10 % supérieure à celle du iPP pur pour environ 3 % de MMT. Au-delà de cette concentration, la contrainte à la rupture baissait sensiblement.

Des nanocomposites iPP/MMT et iPP/CNF ont été filés en utilisant une ligne de filage de laboratoire. La fenêtre de mise en œuvre pour le filage de ces nanocomposites était en adéquation avec leurs propriétés rhéologiques. Ainsi des filaments ont pu être produits jusqu'à environ 5 % en MMT. Dans ce cas les feuillets de MMT étaient alignés selon l'axe du filament. Le rapport de forme de la MMT, déterminé par microscopie électronique à transmission (MET), était de l'ordre de 150, c'est à dire bien plus grand que celui observé dans les moulages par injection, de l'ordre de 50. Ce rapport de forme était en adéquation avec la modélisation de la rigidité des filaments, celle-ci augmentant de 170 % pour des filaments iPP/2 % MMT filés avec un taux d'étirage de 1 et une vitesse d'enroulement de 360 m/min. Là encore, la contrainte à la rupture atteignait un maximum à environ 3 % en MMT. La stabilité thermique des filaments, déterminée par analyse thermo-mécanique, augmentait aussi du fait de la MMT puisque l'amorçage de leur fluage était décalé de 90 °C pour le iPP jusqu'à environ 110 °C pour iPP/1.1 % MMT. De plus, une réduction du retrait, potentiellement bénéfique pour la mise en œuvre de composites textiles, a été observée. Pour les filaments iPP/CNF, l'orientation partielle des particules et la présence d'agrégats ont conduit à des propriétés en traction typiquement 50 % plus faible que celles obtenues pour des filaments contenant une concentration en MMT identique (4 %) et filés dans les mêmes conditions. La suite de l'étude a donc essentiellement porté sur les nanocomposites iPP/MMT. Des films iPP/MMT ont été fabriqués par extrusion-calandrage. Dans ce cas, l'orientation partielle de la MMT dans le sens de l'écoulement a abouti à un module et une contrainte à la rupture anisotropes. Les modules axiaux et transverses augmentaient continuellement avec la

MMT, jusqu'à 75 % pour 5.9 % en MMT par rapport aux films de iPP pur. Ces valeurs expérimentales corrélaient les prédictions du modèle de Halpin-Tsai dans le cas de particules orientées de rapport de forme 50. La résistance à la fissuration des films, déterminée par des tests modifiés de travail essentiel de la rupture, était aussi anisotropique. Pour une propagation de fissure axiale, le travail essentiel de la rupture diminuait avec la MMT. Par contre, pour une propagation de fissure transversale, ce dernier atteignait un maximum à environ 3% en MMT. Cet effet a été attribué à une cavitation dépendante de l'orientation des films et à des déviations de fissures par la MMT.

La rhéologie a indiqué une augmentation de la viscosité d'environ deux ordres de grandeur pour les faibles vitesses de déformation suite à l'ajout de MMT, potentiellement dommageable pour la cinétique d'imprégnation des préformes composites. Pour les composites tissés et enroulés à base de fibres de verre longues, l'imprégnation était très dépendante de la géométrie des fibres sèches. Pour un composite enroulé contenant 40 % volumique de fibres de verre, la porosité augmentait de 7 % à 14 % volumique dans le cas respectivement d'un composite à matrice iPP pure, moulé par compression à 0.6 MPa et d'un composite ayant une matrice iPP/3.4% MMT moulé par compression à 1.8 MPa. Lorsqu'un mélange plus intime était obtenu entre les filaments et les fibres de verres, dans une préforme tissée, par exemple, le composite était bien consolidé, avec une porosité inférieure à 2 % volumique, et sans filtration des particules par les fibres de verre. Ainsi, pour la modélisation de la cinétique d'imprégnation des composites estampables par une matrice iPP/MMT, la matrice fut considérée comme une entité homogène et par souci de simplicité, newtonienne. Les résultats présentaient une bonne adéquation. Cependant, en présence de MMT, les prédictions surestimaient les temps d'imprégnation par rapport à ceux observés expérimentalement. Cet effet a été attribué au comportement rhéologique non linéaire des nanocomposites. De plus, en utilisant des composites intercalés et des conditions expérimentales proches des conditions industrielles (0.2 MPa à 200 °C), les composites hybrides à base de iPP/5.9 % MMT étaient complètement imprégnés (avec une porosité entre 11 et 17 % volumique) et le lit de fibres de verre complètement relaxé après 30 s de compression, ce qui est dans la tolérance des temps de cycle pour la production industrielle des composites estampables (20 – 60 s).

Des composites estampables hybrides consolidés par moulage par compression à 2 MPa et 200 °C et ayant une porosité d'environ 2 % volumique et 30 % de fibres de verre, ont été fabriqués et testés mécaniquement. A température ambiante, leur module et leur contrainte à la rupture en flexion augmentaient de façon continue avec la MMT jusqu'à environ 45 % et 33 % respectivement pour 5.9 % en MMT. L'augmentation du module en flexion avec la MMT était plus important que les prédictions obtenues en utilisant une loi de mélange classique prenant en compte un facteur de forme et de taille des fibres de verre et en utilisant les rigidités des moulages par injection. Cet effet a été attribué à une augmentation des propriétés en flexion plus importante que celle observée en traction en présence de MMT. Des augmentations du module et de la contrainte à la rupture moins significatives ont aussi été observées à 50 °C et 90 °C. A température ambiante, les contraintes maximales à l'impact des composites hybrides diminuaient avec l'augmentation de la concentration en MMT, non seulement à cause de la réduction de la résistance à la rupture observée dans les films mais aussi à cause de l'amélioration de l'interface fibre-matrice, observée par microscopie électronique à balayage (MEB), dont l'origine pourrait être la présence d'agents de couplage. Cette étude a montré que l'influence de la MMT sur la cinétique d'imprégnation était dans la tolérance des temps de cycle industriels. L'ensemble de ces résultats est donc très prometteur quant à l'implémentation de matrices nanocomposites dans les composites estampables. Ils mettent en évidence la faisabilité de production de nanocomposites thermoplastiques hybrides renforcés par des fibres en utilisant des moyens de mise en œuvre conventionnels.

MOTS CLÉS: nanocomposites, montmorillonite, nanofibre de carbone, filage, films, imprégnation, composites hybrides renforcés par des fibres de verre

TABLE OF CONTENTS

CHAPTER 1

INTRODUCTION

1.1 BACKGROUND

1.1.1 Future challenges for polymer composites

Classical structural polymer composite materials contain a strong load-bearing phase, typically in the form of a reinforcing fiber, embedded in a polymer matrix. The fibers provide the mechanical strength and stiffness, and the polymer matrix ensures the transfer of loads between the fibers, and protects them from environmental degradation. Such materials have traditionally been used in applications where high stiffness/weight and strength/weight ratios are required. However, the next generation of polymer composites may need not only to fulfill structural requirements but also to incorporate one or more non-structural functions such as sensing, actuation, electrical energy absorption or power generation, gas barrier or heat resistance. Multifunctional polymer composites are already of interest for a wide variety of applications. The transport industry represents a large part of this demand[1, 2], but they may also be integrated into sporting goods, for example, such as skis or tennis rackets in order to reduce vibration[3], or into artificial prostheses to restore, repair or replace the structural and functional performance of natural tissues[4].

The performance of polymer composites may be improved and/or expanded by modifying the properties of either the reinforcing fibers or the polymer matrix. The fiber properties may be modified during synthesis or by specific surface treatments, but extensive work has already been carried out in this area, and the perspectives are relatively restricted. Tuning the physical properties of the matrix, on the other hand, offers far greater potential, and the focus in the present work is therefore on improving the polymer matrix properties, whilst maintaining the load bearing function of the fibers. In order to achieve this objective, it is necessary to develop polymer matrices with controlled composition and morphology as well as methods for their incorporation into the final composite. However, to ensure the competitiveness of this approach, it is of interest to exploit conventional manufacturing techniques as far as possible[5-7].

1.1.2 The "nano" route

Over the last two decades, the escalating cost of engineering thermoplastics has renewed incentives to reduce resin consumption by addition of relatively cheap fillers[8]. Nowadays, fillers are also increasingly chosen to improve specific mechanical, thermal and electrical properties in thermoplastic products. For example, when stiffness, strength and dimensional stability are required, polymers are mixed with rigid fillers. For increased toughness, deformable particles are preferred, and asymmetric fillers such as short fibers or flakes are used to improve the modulus and heat distortion temperature. Moreover, unique combinations of physical, mechanical and thermal properties can be obtained by using appropriate fillers. For example, in the tire industry, carbon black in vulcanized rubber acts both as a reinforcing agent, because it enhances the elastic modulus and shear strength, and as a processing aid, because it influences the extrusion characteristics. When processing filled polymer matrices, an improvement in one property may nevertheless lead to the deterioration of others and, consequently, it is the overall performance of the filler in a given formulation that determines its choice.

When the filler consists of microsized particles, a relatively high loading (typically more than 20 vol%) is generally required to produce significant improvements in mechanical properties, and this may compromise other important properties, such as processability, appearance, density or impact resistance. In addition, their use in fiber reinforced composites is restricted by potential filtering of the fillers by the fiber bed. Filled polymers with improved performance at low loading levels are therefore of great interest, and this has provided much of the initial motivation for the development of polymer matrices filled with nanosized particles[9] and the associated hybrid polymer composites. The large specific interfacial area in materials containing nanosized fillers (hundreds of m^2/g) results in a relatively high interphase content. It has been demonstrated that a high interphase content has huge scope for tailoring the mechanical performance of nanocomposite materials, since the properties of the polymer matrix may be significantly modified even at low filler contents[10]. This effect is likely to be most important for the mechanical properties of rubbers and semicrystalline polymers at temperatures above their glass transition temperature, where stiffness is strongly influenced by the rubbery amorphous material, itself dispersed at the nanometric level.

1.1.3 Nanocomposites in practice

Since extensive research began in this area more than 20 years ago, attention has focused on polymer nanocomposites based on a relatively limited range of nanosized fillers, i.e. layered silicates, nanocarbons and, to a lesser extent, fumed silica particles. Exfoliated layered silicates and nanocarbons are expected to provide particularly efficient reinforcement in polymer matrices because of their high aspect ratio[11] and, in the case of nanocarbons, because of their exceptional theoretical mechanical properties[12]. Layered silicates and nanocarbons may also potentially act as multifunctional fillers in polymer marices. Improved barrier properties, thermal stability and flame resistance have been demonstrated for layered silicates, for example. In the case of nanocarbons, significant improvements have also been observed in thermal and electrical conductivity. However,

the full potential of nanofillers has yet to be achieved, at least in part because of un-resolved processing issues, such as the formation of agglomerates, and the optimization of filler-matrix interactions.

1.2 OBJECTIVES

As shown in Figure 1.1, although polymers reinforced with montmorillonite layered silicate (MMT) have demonstrated improved mechanical properties at low loadings, their performance is limited on the one hand by the intrinsic mechanical properties of the polymer matrix and on the other hand by the poor processing characteristics of systems containing more than about 10 vol% nanoparticles. For particulate filled polymers, and glass fiber (GF) reinforced polymers, on the other hand, efficient reinforcement is generally associated with relatively high loadings[13]. It is therefore of interest to combine these two approaches with the aim of producing polymer composites with enhanced mechanical properties at low to intermediate inorganic loadings. The specific objective of the present work is to incorporate nanosized fillers into conventional polymer composites using existing processing techniques and to investigate whether this approach gives rise to significant changes in the mechanical properties of the final composites. Successful preparation of such hybrid polymer composites would nevertheless provide a platform for developing other types of hybrid composites, with the longer term goal of extending the approach to produce composites with added non-structural functionality. The work is based principally on isotactic polypropylene (iPP) matrix filled with montmorillonite layered silicate (MMT), although some consideration is also given to carbon nanotubes or carbon nanofibers. Conventional thermoplastic processing techniques have been used throughout to incorporate the nanocomposite matrix into long glass fiber (LGF) and model glass mat thermoplastic (GMT) composites via fiber and film precursors.

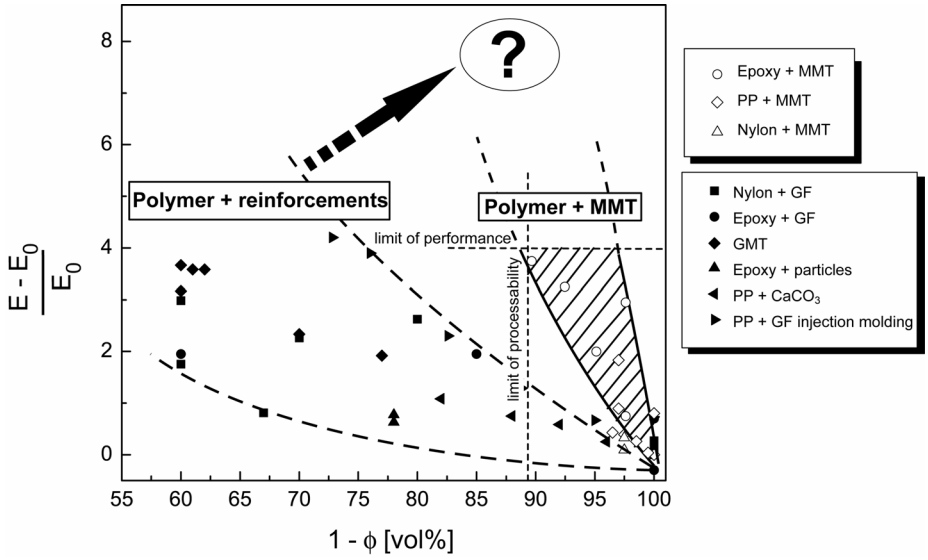

Figure 1.1. Relative tensile modulus vs. filler volume fraction for polymer composites. As indicated by the arrow, the objective is to integrate nanofillers into conventional composites in order to obtain hybrid composites with improved mechanical properties.

A major concern is that the presence of solid additives in thermoplastic melts inevitably influences the processability and performance of composite parts. The extent to which this occurs depends on the amount of filler present, the polymer-filler interactions, the state of dispersion of the filler, and the melt processing conditions. A substantial part of the work has therefore centered on morphology/property and processing/morphology relationships in the composites and their precursors, with the aim of providing a rational framework for process design in hybrid fiber reinforced nanocomposites in general.

1.3 OUTLINE

The research plan is shown schematically in Figure 1.2. Chapter 2 is a literature review of nanoscale fillers, polypropylene-based nanocomposites and hybrid composites. It is followed by a description of characterization techniques and material processing in chapter 3. The main part of the thesis is devoted to the characterization of composite precursors in the form of iPP/MMT (chapter 4) and iPP/CNF (chapter 5) fibers and iPP/MMT films (chapter 6). In Chapter 7, impregnation studies on unidirectional glass fiber and glass mat reinforced nanocomposite-based composites are discussed in terms of the rheological response of the nanocomposite matrix. The mechanical properties of consolidated hybrid composites are then considered in the light of the matrix morphology and properties. Finally, conclusions and perspectives are given in chapter 8.

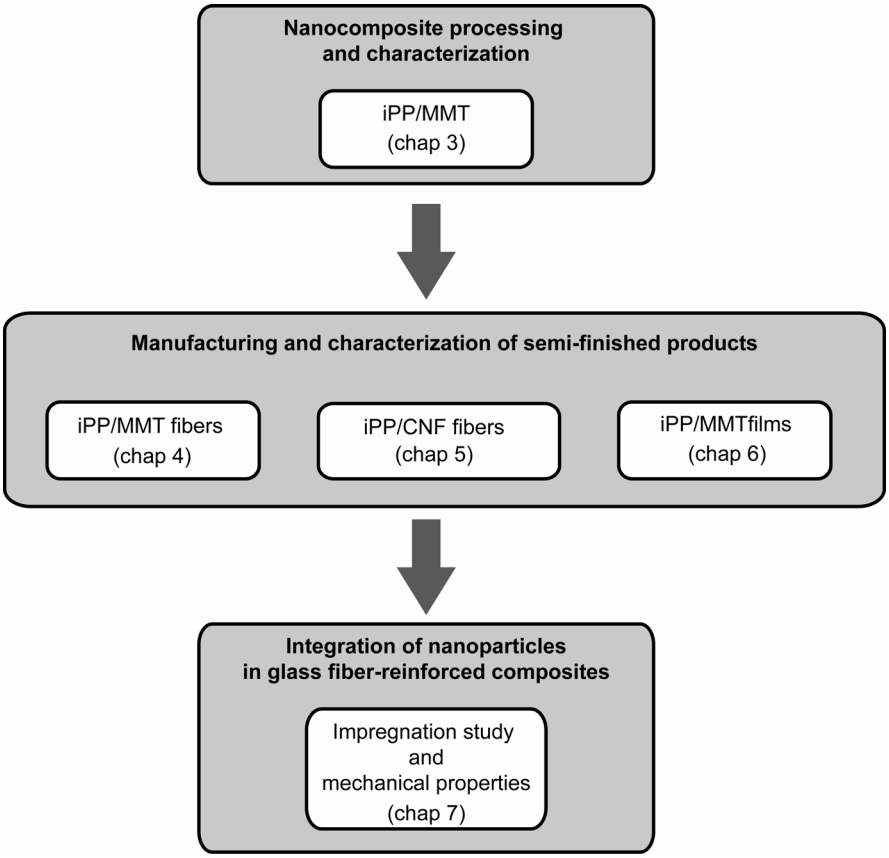

Figure 1.2. Outline of the research plan.

1.4 REFERENCES

1 A. K. Noor, S. L. Venneri, D. B. Paul and M. A. Hopkins, **Structures technology for future aerospace systems**, *Computers & Structures*, 2000; **74** (5): 507-519

2 J. A. Balta, F. Bosia, V. Michaud, G. Dunkel, J. Botsis and J. A. Månson, **Smart composites with embedded shape memory alloy actuators and fibre Bragg grating sensors: activation and control**, *Smart Materials & Structures*, 2005; **14** (4): 457-465

3 C. Fischer, S. A. Braun, P. E. Bourban, V. Michaud, C. J. G. Plummer and J. A. E. Månson, **Dynamic properties of sandwich structures with integrated shear-thickening fluids**, *Smart Materials & Structures*, 2006; **15** (5): 1467-1475

4 L. M. Mathieu, T. L. Mueller, P. E. Bourban, D. P. Pioletti, R. Muller and J. A. E. Månson, **Architecture and properties of anisotropic polymer composite scaffolds for bone tissue engineering**, *Biomaterials*, 2006; **27** (6): 905-916

5 J. Verrey, M. D. Wakeman, V. Michaud and J. A. E. Månson, **Manufacturing cost comparison of thermoplastic and thermoset RTM for an automotive floor pan**, *Composites Part a-Applied Science and Manufacturing*, 2006; **37** (1): 9-22

6 N. Bernet, V. Michaud, P. E. Bourban and J. A. E. Månson, **An impregnation model for the consolidation of thermoplastic composites made from commingled yarns**, *Journal Of Composite Materials*, 1999; **33** (8): 751-772

7 P. E. Bourban, N. Bernet, J. E. Zanetto and J. A. E. Månson, **Material phenomena controlling rapid processing of thermoplastic composites**, *Composites Part a-Applied Science and Manufacturing*, 2001; **32** (8): 1045-1057

8 R. G. Larson, **The Structure and Rheology of Complex Fluids**, Oxford University Press, New York, (1999)

9 M. Rodlert, C. J. G. Plummer, L. Garamszegi, Y. Leterrier, H. J. M. Grunbauer and J. A. E. Månson, **Hyperbranched polymer/montmorillonite clay nanocomposites**, *Polymer*, 2004; **45** (3): 949-960

10 C. L. Wu, M. Q. Zhang, M. Z. Rong and K. Friedrich, **Tensile performance improvement of low nanoparticles filled-polypropylene composites**, *Composites Science and Technology*, 2002; **62** (10-11): 1327-1340

11 M. Alexandre and P. Dubois, **Polymer-layered silicate nanocomposites: preparation, properties and uses of a new class of materials**, *Materials Science and Engineering*, 2000; **28** 1-63

12 O. Breuer and U. Sundararaj, **Big returns from small fibers: A review of polymer/carbon nanotube composites**, *Polymer Composites*, 2004; **25** (6): 630-645

13 M. K. Akkapeddi, **Glass fiber reinforced polyamide-6 nanocomposites**, *Polymer Composites*, 2000; **21** (4): 576-585

CHAPTER 2

STATE OF THE ART

2.1 NANOSCALE FILLERS

2.1.1 Introduction

A large window of opportunity has recently opened up for overcoming the limitations of traditional micrometer-scale polymer composites with polymer nanocomposites, in which the filler has at least one dimension inferior to 100 nm. Although certain nanofilled composites have been known for more than a century, for instance carbon black filled rubber in the automotive industry[1], research and development in the field of nanofilled polymers has greatly increased in recent years. The main reason is that unique combinations of mechanical, electrical, optical, thermal and gas barrier properties have been observed in some polymer nanocomposites. For example, the inclusion of about 70 vol% of MMT in an epoxy reduces oxygen permeability by 2 - 3 orders of magnitude without adverse consequences for the Young's modulus, glass transition temperature and transparency[2]. The incorporation of magnetic iron nanoparticles in shape memory thermoplastics allows the magnetic triggering of shape changes in the polymer as well as improvements in the elastic properties[3]. Another reason for the huge interest in nanocomposites are the significant developments in the chemical processing of nanoparticles, and particularly the achievement of controlled synthesis of carbon nanotubes in the mid-1990s[4]. The properties of nanotubes, e.g. their mechanical and electrical response, are significantly different from those of graphite and offer exciting possibilities for new composite materials[5].

2.1.2 What is unique to nanofillers with respect to micrometer-scale traditional fillers?

The answer to this question resides in the size effect, which influences both particle and composite properties. Typically, single walled carbon nanotubes, essentially composed of defect free molecules and single crystal particles show particular physical properties, i.e., a modulus as high as 1 TPa, demonstrated both experimentally and theoretically[6], and

optical activity. Moreover, compared with micrometer-scale fillers, nanoparticles do not scatter light significantly, and therefore it is possible to obtain composites with altered electrical or mechanical properties that retain their optical clarity. In addition to its effect on particle properties, the small size of the fillers leads to a very large specific interfacial area in composites. As shown in Figure 2.1, in the case of ideally dispersed spherical particles, the surface area of particle per unit volume increases significantly for particles below 100 nm in diameter. As in traditional composites, there exists a region of altered chemistry, polymer chain mobility and crystallinity at the particle surfaces[7]. Beyond this interphase, which controls the degree of interaction between the filler and the polymer, this latter retains its bulk characteristics. The thickness of the interphase has been reported to be in the range 2 to 50 nm, for calcium carbonate ($CaCO_3$) particles in iPP[5, 8] for example. The extremely high specific surface area is one of the most attractive characteristics of nanoparticles because it implies a correspondingly high proportion of interphase[9]. Figure 2.2 shows the interparticle spacing as a function of particle size for an ideally dispersed nanoparticle composite. For 15 nm particles at a loading of 10 vol%, the interparticle spacing is about 10 nm. Thus, even for an interphase of a few nanometers, the matrix response is likely to be dominated by the interphase under these conditions. Reynaud *et al.*[10] have estimated that an interphase of about 1 nm in thickness represents roughly 0.3 % of the total volume of polymer in microparticle filled composites, whereas it reaches about 30 % of the total volume in nanocomposites.

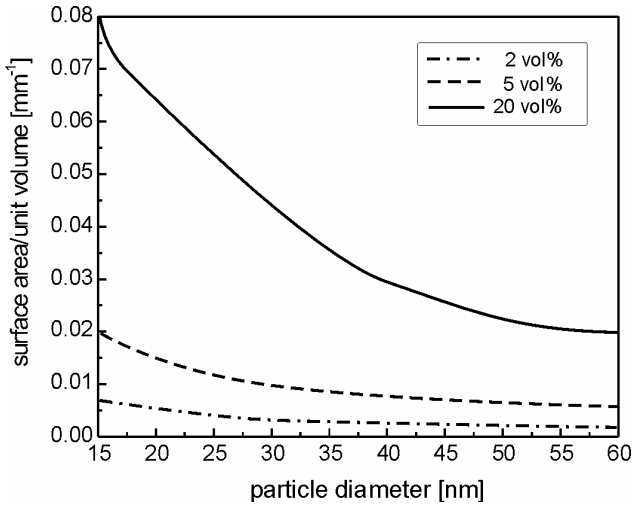

Figure 2.1. Surface area per unit volume versus particle size for spherical particles that are ideally dispersed (reproduced from Schadler[5]).

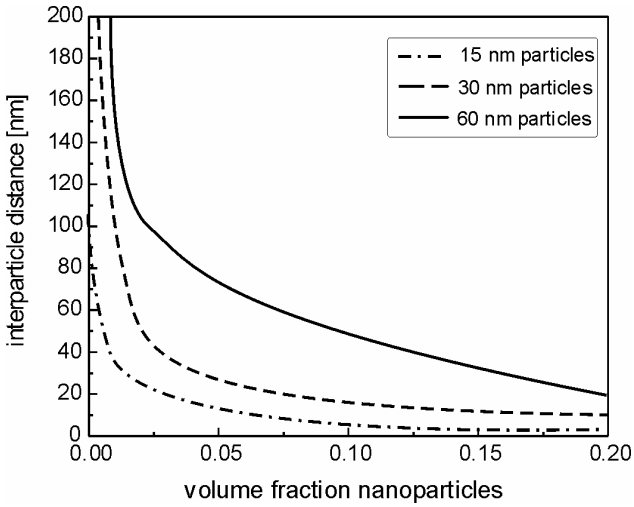

Figure 2.2. Interparticle distance for spherical particles that are ideally dispersed (reproduced from Schadler[5]).

2.1.3 Functional nanoscale fillers

Nanoscale fillers come in many shapes and sizes and there are different ways categorizing them. One pertinent classification is based on particle geometry (Figure 2.3). The geometry of fillers has a significant influence on the processability of filled polymers and on their mechanical properties[5]. When only one particle dimension is in the nanometer range, the filler may be in the form of sheets of up to hundreds to thousands of nanometers in width (layered silicates for example). When two dimensions are at the nanometer scale and the third is larger, forming an elongated structure, one refers to nanotubes or whiskers (for example, carbon nanotubes[11] or cellulose whiskers[12]). The third type of nanocomposites is characterized by three dimensions in the nanometer range (for example, spherical $CaCO_3$ nanoparticle[13] or spherical silica nanoparticles[14]). In this case, one refers to isodimensional nanoparticles. The beneficial attributes of the particles are often further improved when they percolate to form a continuous network throughout the material. A percolating structure can result in dramatic increases in the reinforcement effect of the fillers by providing a continuous backbone of stiff material[15].

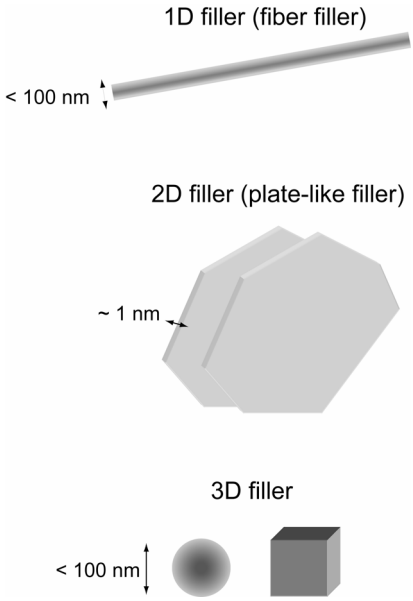

Figure 2.3. Classification of nanoscale fillers according to geometry.

As well as efforts to improve matrix polymer mechanical properties, there has been great interest in the preparation of multifunctional materials based on nanocomposites[16, 17]. If the particles are semiconductors or metals, percolation can significantly increase the electrical conductivity of the system by creating a direct path for electrical transport across the material[18, 19]. Given the range of available nanoparticles, the potential to increase the functionality of the matrix is huge: superconductivity, magnetism, non-linear optics, thermal stability etc., may all be achievable with suitable interfacial region properties. For example, nanocomposite pyroelectric sensors based on nanosized lanthanum powder[20], nanocomposite ultrasonic hydrophones based on nanosized lead zirconate titanate powder[21], shape memory polymer nanocomposites based on silicon carbide nanoparticles[22] or multifunctional nanocomposite coating based on zinc oxide nanoparticles[23] have been fabricated. The potential to increase the matrix functionality is nevertheless currently limited by spatial and compositional precision in nanoparticle fabrication[24].

2.2 POLYPROPYLENE BASED NANOCOMPOSITES

2.2.1 Isotactic polypropylene (iPP)

Polypropylene is a nonpolar semicrystalline thermoplastic with a low surface tension. It is produced by coordination addition polymerization of propylene monomer. The chain configuration of polypropylene is a symmetrical helix molecule with three monomeric units per single revolution (0.65 nm). The methylene side groups are aligned in three columns parallel to the helix axis[25]. Most frequently, strereospecific Ziegler-Natta

catalysts are used in industrial processes to produce either highly crystalline isotactic polypropylene (iPP) or syndiotactic polypropylene (sPP). Under usual solidification conditions, iPP crystallizes in its stable monoclinic α-form[26]. At high undercoolings or at high pressures, the less stable hexagonal β- and triclinic γ-crystal modifications may dominate[27]. Typically, iPP contains 40 – 60 wt% of crystalline phase, with a melting point ranging from 167 °C to 180 °C, depending on the crystal form and lamellar thickness. Neat iPP crystallized from the melt exhibits a spherulitic morphology. Spherulites are typically composed of twisted lamellae, typically 10 nm thick and 1 – 10 μm wide. iPP spherulites exist in five main forms. The three types of α-spherulites are distinguished by their cross-hatched lamellar structure, while β-spherulites exhibit leaf-like lamellae[28].

iPP is an extremely attractive candidate for many engineering applications. Relatively low price, excellent chemical resistance, good processability and the possibility of modifying its mechanical properties over a wide range by adding fillers and dispersions of secondary polymeric inclusions have contributed to the massive expansion of iPP in automotive, land transport, home appliances and other industries[29-31]. Therefore iPP is one of the fastest-growing classes of commodity thermoplastics, with a market share growth of 6 % - 10 % per year[32]. However, brittleness and inadequate stiffness are among its most important deficiencies, so that expensive engineering thermoplastics are generally required in more demanding applications[33]. To reduce cost or enhance physical and mechanical properties, fillers and reinforcements are commonly added in iPP[34, 35]. These include talc[36], $CaCO_3$[37], mica[38], wollastonite[39], glass fiber[40], carbon fiber[41] and jute[42].

2.2.2 Montmorillonite clay (MMT)

Clay minerals are hydrous aluminium silicates. Hectorite, saponite, and montmorillonite are the most commonly used smectite type layered silicates for the preparation of nanocomposites. Montmorillonite (MMT) has the widest acceptability for use in polymers because of its high specific surface area (about 750 m^2/g)[43] and surface reactivity[44]. MMT belongs to the structural familily of 2:1 phyllosilicates. 2:1 phyllosilicates are characterised by two fused silicate tetrahedral sheets sandwiching an edge-shared octahedral sheet of either aluminium or magnesium hydroxide[45] as illustrated in Figure 2.4. The layer thickness is approximately 0.96 nm[46] and the lateral dimensions may vary from 30 nm to several microns and the aspect ratio is about 10 - 1000. These layers organise themselves to form stacks with a regular electrostatic and van der Waals bonded gap, called the interlayer gallery. Isomorphous substitution of Si^{4+} for Al^{3+} in the tetrahedral lattice and of Al^{3+} for Mg^{2+} in the octahedral sheet causes an excess of negative charges. These negative charges are counterbalanced by alkali cations, such as Na^{+} and Ca^{2+}, situated in the interlayer gallery. Due to these interlayer cations, MMT has a high capacity for ion exchange with other cations[2]. In nanocomposite preparation, the MMT is therefore generally treated with a molecule with both an organophilic function compatible with the polymer and a hydrophilic function, typically a cationic group. This has the effect of expanding the interlayer spacing, which facilitates the intercalation of

the matrix polymer or its monomers[44, 47]. In this case one refers to as "organoclays". Alkylamonium ions are commonly used for this purpose. Among layered silicates, MMT is particularly attractive because it is environmentally friendly, readily available in large quantities at relatively low cost and its intercalation chemistry is well understood[6]. Nowadays several grades are commercially available. These include Cloisite® 10A, 15A, 20A and 30B produced from Southern Clay Products (U.S.A.)[48], Bentone® 107, 108, 109 and 2010 from Elementis Specialties Company, Nanomer® 1.30P, 1.31PS, 1.44P, 1.44PS, 1.44PT and 1.28E from Nanocor, Inc. (U.S.A.)[49], Nanofil® 2, 5, 9, SE 3000 and SE 3010 from Sud-Chemie (Germany)[50] and Dellite® 72T from Laviosa Chimica Mineraria (Italy). Synthetic fluoromica clays (Somasif® ME100) are supplied to Asian customers by Co-op Chemicals, Japan.

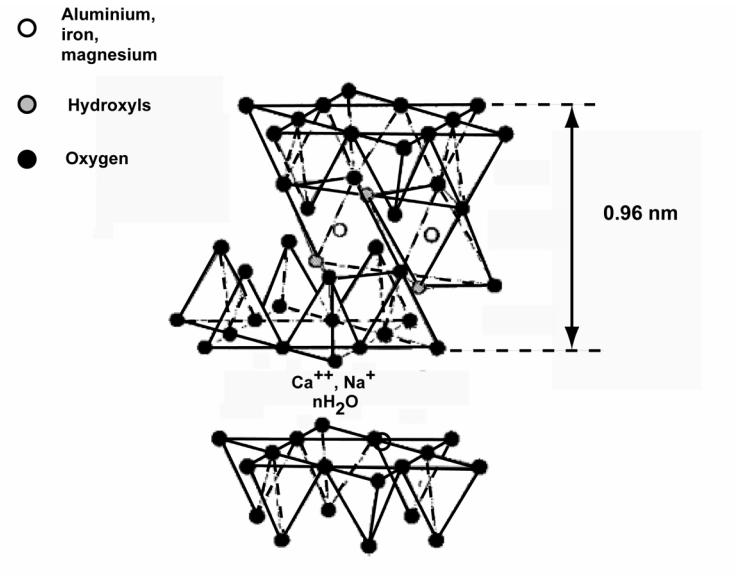

Figure 2.4. Structure of 2:1 phyllosilicates.

MMT was first dispersed in polyamide 6 (PA6) by the Toyota research team[51]. Later, this concept was used for nanocomposites based on epoxies[52], unsaturated polyesters, poly(ε-caprolactone)[53], polystyrene[54], polyimide[55], polypropylene, poly(ethylene terephthalate)[56], and polyurethane[57]. Dispersed MMT in polymeric host show combinations of three morphologies[45, 58, 59], represented in Figure 2.5:

- Phase separated structures, when the polymer and the layered silicate are immiscible.
- Intercalated structures, with well-ordered multilayers in which the polymer chains are inserted in the interlayer galleries.
- Exfoliated structures, with separation of silicate layers sufficiently great for there to be no direct interaction between adjacent layers.

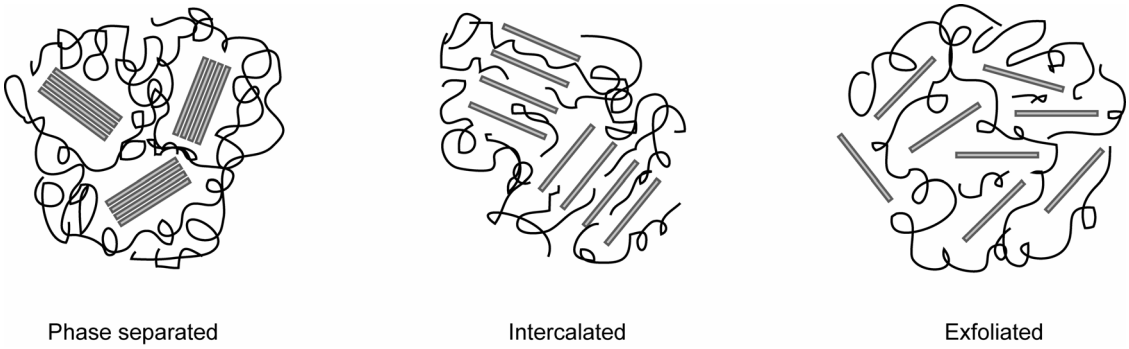

Figure 2.5. Morphologies of layered silicates in a polymeric host.

2.2.3 Nanocarbons

Nanocarbons have long been known as an undesirable by-product of catalytic conversion of carbon-containing gases. The discoveries of fullerenes in 1985[60] and of carbon nanotubes in 1991[4] have opened up a completely different perspective to that of carbon materials based on flat graphite-like hexagonal layers[61]. The terminology for nanocarbons is subjected to many interpretations, and is not always well defined[62]. However, they are usually classified according to their structure and the degree of imperfection of the crystal lattice. Thus three types of nanocarbons are distinguished. These are, from the most perfect to the least ordered structure: (i) single-walled carbon nanotubes (SWNT), (ii) multi-walled carbon nanotubes (MWNT) and (iii) carbon nanofibers (CNF).

Thotenson *et al.*[63], Inagaki *et al.*[64], Maruyama *et al.*[65] and Breuer *et al.*[66] have given extensive reviews on structure and synthesis of nanocarbons. Graphite is formed from 2-D sheets of carbon atoms arranged in a hexagonal array. SWNT can be thought of as sheets of graphite rolled into a cylindrical tube and welded together[63]. The hexagonal carbon array is constituted by aligned C-C sp^3 covalent bonds, which are among the strongest bonds in the nature. The rolling of the lattice into a 1-D tube maximizes the axial mechanical properties of the SWNT, since the covalent bonds are oriented along the axis of the nanotube. This results in an extremely high elastic modulus, of the order of that of diamond (1 TPa), and a tensile strength of about 30 - 60 GPa[65], about one order of magnitude higher than that of current high strength carbon fibers (1.5 – 4.8 GPa). The electronic behavior ranges from high conductivity (10^{-4} Ω-cm) metallic behavior to semiconducting behavior with a large band gap, depending on how the graphite sheet is rolled. The diameter of SWNT's ranges from 0.7 nm to about 3 nm. MWNT are concentric single walled tubes held together by van der Waals bonding. Although nearly as stiff as SWNT and having a similar electrical conductivity, MWNT are not as strong as SWNT, owing to defects in the outer cylinders, as well as internal failure facilitated by the weak van der Waals bonds between the cylinders[6]. The diameter of MWNT ranges from approximately 2 to 20 nm. CNF are a third type of nanonocarbons. They are similar to MWNT[67, 68], but significantly larger, with a typical diameter of the order of 50 to 200 nm, and their length is from 50 to 100 μm. CNF have a tensile strength of about 3 GPa and a tensile modulus of about 100 to 1000 GPa[69]. CNF have much lower production

costs than SWNT and MWNT, and kilogram quantities are readily available, making them commercially attractive. Their main disadvantage is that they contain large amount of microstructural defects, compared with SWNT and MWNT.

Nanocarbons are almost exclusively grown by a metal-catalyzed vapor condensation process[65]. The lack of reliable, large volume production, the high price of the nanotubes, and the fact that there is little selectivity in the properties of the product are the three main factors that have inhibited the commercialization of carbon nanotube technologies[70]. Historically, methods based on the electric arc and laser ablation processes were the first reliable techniques to produce nanocarbons. During nanocarbon synthesis, impurities in the form of catalyst particles, amorphous carbon, and non tubular fullerenes are also produced. Thus, the materials prepared by these techniques have to be purified using chemical and separation methods, with the risk of damaging the tubes through oxidative shortening. However, none of these techniques can currently be scaled up to make the industrial quantities needed for many applications (e.g. composites)[71, 72].

2.2.4 Preparation

There are a wide variety of strategies for preparing polymer/layered silicate and polymer/nanocarbon nanocomposites. They are described in numerous reviews[5, 44, 45, 73], and only the most pertinent will be discussed here. These are in-situ polymerization, melt-mixing and solution processing.

a. In-situ polymerization

In this technique, nanoscale particles are dispersed in the monomer or monomer solution, and the resulting mixture is polymerized by standard polymerization methods. In the case of layered silicates, the dispersion of the particles in the monomer solution results in swelling so that the polymer formation can occur between the intercalated sheets. Toyota research team was the first group to report the preparation of exfoliated nylon-6/MMT nanocomposites by swelling MMT with the ε-caprolactam monomer[51, 74]. The success with nylon-clay nanocomposites has, not so far been extended to making high-performance polyolefin nanocomposites by in-situ methods, probably, because of the chemical sensitivity of current polymerization catalysts. However, this approach has been successfully used with polystyrene[75, 76], poly(methylmetacrylate)[77], polyethylene[78, 79] and to a lower extent to iPP. Sun *et al.*[80] have reported a synthesis approach to make iPP/MMT nanocomposites by in-situ polymerization under mild polymerization conditions. Their method requires no external activators, such as methylaluminoxane and perfluoroarylborates, for initiating the olefin polymerization, or high-pressure and high-temperature process conditions. The organically modified clay powder is suspended in toluene, which acts as a solvent, by mechanical agitation, and is then mixed with hydrolytic scavengers and a highly isotactic metallocene propylene polymerization catalyst. The homogenized slurry is then exposed to a propylene gas stream at ambient to produce the nanocomposites. In the absence of the organoclay nanofillers polymerization does not occur using the same metallocene complexes, suggesting heterogeneous

polymerization in this case. This procedure results in an mixed intercalated/exfoliated morphology of the iPP/MMT nanocomposite.

The main advantage of in-situ polymerization in the context of polymer/nanocarbon nanocomposites is that it enables grafting of polymer macromolecules onto the walls of the nanocarbons. In addition, it is a very convenient processing technique, which allows the preparation of composites with high nanocarbon loading and very good miscibility with almost any polymer type[69]. To our knowledge, the work of Wiemann *et al.*[81] is the only report on in-situ polymerization of iPP/nanocarbon nanocomposites.

b. Melt-mixing

Melt-mixing is the most popular method for thermoplastic polymers. The advantages of this technique are not only its speed and simplicity, but also its compatibility with standard industrial techniques such as injection molding. Typically, twin screw extruders or high shear mixers are used to incorporate the nanofillers in the melted polymer matrix. However melt-mixing techniques may be limited by the significant increase in polymer viscosity with increasing nanofiller concentration. Because of the apolar nature of polymers such as iPP, the dispersion of nanofillers is rather poor. Therefore, organic surfactant and compatibilizer additions are needed and/or surface modification of the nanofillers to enhance the interfacial adhesion between the matrix and the fillers.

In spite of intensive studies of a wide range of thermoplastics, including polystyrene[54, 82] and iPP[83, 84], exfoliated MMT based nanocomposites remain difficult to obtain. Mixed exfoliated/intercalated iPP/MMT morphologies are more readily achieved by means of addition of iPP chains modified with either maleic anhydride (PPMAH) or hydroxyl (PPOH)[85, 86] groups together with an organic modifier for the MMT whose interactions with the MMT are thermodynamically less favorable than the iPP-MMT interactions[84, 87]. There has been considerable effort to enhance to the degree of intercalation of the nanocomposite by optimizing the maleic anhydride and hydroxyl groups content together with the MMT cationic exchange species[84, 88-94]. Improvement in the degree of intercalation has also been obtained by optimizing the processing conditions (the temperature, force and speed of extrusion)[95-97].

The dispersion of nanocarbons in polymers is generally relatively poor, due to the strong tendency of nanocarbons to agglomerate[63]. Physical dispersion in melts include, ball milling, grinding and high speed shearing. Andrews *et al.*[98] have demonstrated the feasibility of iPP/MWNT nanocomposites. iPP was blended with nanotubes at high loading level in a high shear mixer to form masterbatches. These masterbatches were then mixed with pure iPP to form lower mass fraction samples. However, techniques such as shear mixing can induce structural defects such as bending, buckling and fracture of the graphene layers[99]. Therefore chemical functionalization is also often envisaged to improve polymer/nanocarbon interfacial bonding[100].

c. Solution processing

Solution processing is generally performed prior to a melt-processing procedure[101]. It generally involves three steps[102, 103]:

- Dispersion of nanofillers in either a solvent or a polymer solution by energetic agitation.
- Mixing of the nanofillers and polymer in solution by agitation
- Controlled evaporation of the solvent leaving a composite film.

Agitation is generally provided by magnetic stirring, reflux or ultrasonication. This method relies on the efficient dispersion of the nanoparticles in the relevant solvent[104]. The choice of solvent is based on the solubility of the compounding polymer. Hydrocarbon solvents such as xylene, toluene[104] methanol[105] or trichlorobenzene[106]are usually used for this purpose. This processing route is described in detail for iPP/MMT nanocomposites and iPP/CNF nanocomposites in sections 3.3.2 and 5.2.2 respectively.

2.2.5 Characterization methods

Effective characterization tools are crucial for understanding the basic physical and chemical properties of polymer nanocomposites. For structural applications, it facilitates the study of emerging materials by providing information on intrinsic properties. Various techniques have been extensively used in polymer nanocomposite research. Among the most powerful techniques are X-ray diffraction (XRD)[107] measured at wide (WAXS) and small (SAXS) angle, scanning electron microscopy (SEM), and transmission electron microscopy (TEM)[45, 108, 109]. For thermal characterization, the most common techniques are differential scanning calorimeter (DSC), thermogravimetric analysis (TGA), thermomechanical analysis (TMA), and rheology. Details of the experimental techniques used in the present case are given in chapter 3.

2.2.6 Properties

a. iPP/MMT properties

Generally, polymer/MMT are characterized by a range of material improvements which originate from the nature of the organoclay. These include increased tensile/flexural strength, heat deflection temperature, thermal stability, flame retardancy, barrier properties, and so on[44, 45, 73, 110]. iPP/MMT nanocomposites exhibit most of these property enhancements, as will be discussed in what follows.

- *Mechanical properties*

The typical behavior of iPP/MMT nanocomposites is characterized by a sharp increase of Young's modulus for very small inorganic loadings (below 3 wt%)[111, 112] followed by a more gradual increase beyond 4 wt% and a decrease for high MMT content. Depending

on the processing methods and the nature of both iPP and MMT, the improvement observed in the Young's modulus is from about 28 to 50 %[33]. When filled with micrometer sized particles, iPP exhibits more modest increases in tensile modulus. For example, 30 - 60 wt% of talc or mica is needed to achieve comparable results[84]. When the polymer/inorganic particle adhesion is improved by the incorporation of maleic anhydride groups in the polymer chains, the stresses are more effectively transferred from the polymer matrix to the inorganic filler. However, the addition of compatilizer may be detrimental to the fracture toughness of the nanocomposite, so that moderate maleic anhydride contents and higher matrix molar masses may be required to optimize the toughness/stiffness balance[31]. In iPP/MMT nanocomposites, the tensile strength and the impact resistance generally show less improvement (maximum about 30 %) with increasing MMT content than the Young's modulus. Moreover, the elongation at break is significantly lower (about 50 – 90 %) than that of neat iPP [113].

Micromechanical models are commonly used to predict the elastic constant of MMT reinforced polymers. The Voigt and Reuss models provide upper and lower bounds for the composite modulus[114, 115]:

Voigt (Rule of mixture) $$E_c = (1 - V_f)E_m + V_f E_f$$ **Equation 2.1**

Reuss $$\frac{1}{E_c} = \frac{V_f}{E_f} + \frac{1 - V_m}{E_m}$$ **Equation 2.2**

where V_f is the volume fraction of the reinforcing phase and E_c, E_f, E_m, the moduli of the composite, the reinforcing phase and the matrix respectively. The semi-empirical Halpin-Tsai model[113] incorporate further details of the reinforcing phase shape to obtain a more accurate predicted modulus[115, 116]. The Halpin–Tsai equations are detailed in section 4.3.2 together with Mori-Tanaka average stress theory [117].

- *Thermal stability and flame retardancy*

Thermal stability is an important property which depends strongly on the nanocomposite morphology and therefore on the processing conditions[84]. The thermal stability is usually determined by means of TGA where the curves are shifted toward higher temperatures when the thermal stability is increased[118]. The dispersion of MMT in the iPP matrix leads to a higher deflection temperature (HDT). Typically, the HDT increases from about 109 °C for the neat iPP matrix to about 152 °C for the iPP loaded with 6 wt% of MMT[119]. Beyond this loading level, the HDT of the nanocomposite levels off. The improvement of the HDT results from the better mechanical stability of the nanocomposite, compared with the neat iPP[120, 121]. The flame retardancy is commonly measured by cone calorimetry. The cone calorimeter measures the heat release rate (HRR), and in particular the peak HRR[122]. At about 8 wt% MMT loading in iPP, the peak HRR is lower than that of neat iPP by about 57 %[123, 124]. For comparison, if iPP/4 wt% MMT leads to a reduction of the peak HRR of about 44 % compared with that of the neat matrix, the reduction is about 40 % and 32 % for iPP/4 wt% nanosized $CaCO_3$ and iPP/4 wt% microsized $CaCO_3$ respectively[125]. The decrease of the peak HRR is attributed to the delay of thermal-oxidative decomposition of the nanocomposites[119]. The mechanism of this flame

retardancy behavior is believed to be the formation of a protective clay-rich char barrier on the surface of the pyrolyzing polymer during combustion resulting from the migration of particles to the surface of the molten polymer[126].

- *Barrier properties*

In many applications the gas barrier properties of polymers is critical. For example in food packaging, oxygen ingress may determine shelf life, and for carbonated drinks, the egress of carbon dioxide is also an important issue. iPP is widely used in food packaging because of is high distortion temperature and crystallinity. It offers a strong barrier to humidity but suffers from high oxygen permeability[127], and this has been one of the main driving forces for the development of iPP/MMT nanocomposites. The high aspect ratio of MMT layers is expected to improve the oxygen-barrier properties by hindering the penetration of gas molecules and increasing their average diffusion path[128]. Osman *et al.*[129] demonstrated that the oxygen permeation coefficient in iPP/MMT nanocomposites decreased asymptotically with increasing MMT content, and Chaiko and Leyva[130] reported a 62-fold decrease in oxygen permeability at 5 wt% MMT in iPP wax composites.

- *Rheological properties*

The reinforcing effect of fillers increases strongly with the level of dispersion and the anisotropy of the filler, and this also leads to marked differences in rheological behavior between exfoliated polymer nanocomposites and conventional filled polymers[131, 132]. The rheological response of polymer/MMT nanocomposites has been extensively studied by Krishnamoorti, Giannelis and Vaia[133, 134]. As demonstrated by other groups, iPP/MMT nanocomposites generally show similar behavior[83, 91, 113, 135-138] characterized by an increased viscosity and non-terminal behavior of the storage and loss moduli in linear oscillating shear in the limit of low frequencies. This is reflected by a much weaker power-law dependence of the dynamic frequency response than for the unfilled polymer. The increasing solid-like behavior with increasing MMT content is attributed to percolation of interlayer contacts[83]. It follows that application of large strain amplitude oscillating shear and steady state shear lead to a decrease in both the storage and loss moduli owing to shear alignment of the MMT stacks and/or break-up of the percolating network structure[137, 139, 140].

b. iPP/nanocarbon properties

Nanocarbons possess remarkable mechanical and other functional properties, and the main challenge is to exploit these properties in composites at a macroscopic scale by combining a suitable choice of materials with an appropriate processing method. Much of the work on the preparation of nanocarbons/polymer composites has been driven by a desire to exploit their exceptional stiffness and strength. The nanocarbons must be uniformly dispersed in order to achieve efficient stress transfer from the matrix to the nanocarbon network, and minimize the stress concentrations. When the nanocarbons are poorly dispersed, the composite fails by break down of agglomerates rather than by

failure of the nanocarbons themselves, resulting in a substantial decrease in strength[141]. When interfacial adhesion between the matrix and the nanocarbons is poor, the nanocarbons pull-out of the matrix. There are several techniques to improve the dispersion and the interfacial adhesion of nanocarbons including optimized processing routes and chemical functionnalization[100, 142-144]. Finegan *et al.*[145] have studied CNF-iPP adhesion after oxidation of CNF using a carbon dioxide gas. They demonstrated by dynamic mechanical analysis and TEM that the fiber-matrix adhesion was improved, resulting in an increased tensile strength. Similarly, Cortés *et al.*[146] observed an improvement in Young's modulus for iPP/CNF nanocomposites with CNF oxidized in a nitric acid solution compared with samples with un-treated CNF.

- *Mechanical properties*

The mechanical properties of polymer/nanocarbons composites have been extensively described elsewhere[69, 147, 148]. The present section concerns exclusively the incorporation of nanocarbons in a iPP matrix. Low concentrations (lower than 1 wt%) of well dispersed SWNT in iPP result in an increase in Young's modulus (of about 40 %) as well as in tensile strength, followed by a decrease at higher SWNT content[141]. Similar improvements are observed for the Young's modulus of iPP/MWNT nanocomposites prepared by melt-mixing, however accompanied by a decrease in the tensile strength[98]. In this case the low tensile strength is attributed to low interfacial bonding between the MWNT and iPP. As mentioned in the previous section, a modest degree of oxidation may increase adhesion between the nanocarbons and the matrix giving rise to an increase in strength[145]. However, strength may be limited by enhanced crystallization of the iPP due to the nanocarbons acting as additional nucleation sites. This was observed in the case of iPP/CNF nanocomposite where the tensile strength was not significantly altered by an increase in the CNF content[149, 150]. As with other polymer/nanocomposite systems, the extent of mechanical properties is limited by poor dispersion of the nanocarbons[98]

In addition to suitable processing conditions[66], the possibility of making composites with aligned nanocarbons has recently been demonstrated[142, 151-153]. iPP/nanocarbon-based fibers are of particular interest since the stresses applied during spinning can align the nanocarbons along the fiber axis. Because of the high tensile strength and modulus of nanocarbons, a high degree of nanotube alignment in the axial direction can potentially produce a very strong polymer fiber[154]. The composite modulus for random orientation and perfect alignment generally differs by a factor of five[69]. In addition, spinning of the nanocomposite may improve the dispersion of the nanofillers[155]. Kuriger *et al.*[156] have described the mechanism of CNF orientation during the melt-spinning process (Figure 2.6). The die inlet initiates a converging flow pattern that aligns the fibers along the streamline direction. The flow pattern is then transformed into shear flow on entering the annular portion of the die. When passing through the die the fibers suspended in the flowing fluid are subjected to local velocity gradients. These gradients cause fluid elements to stretch and rotate causing the fibers to rotate in the preferred direction[157]. It was observed that the fibers alignment decreased as the fiber content increased, due to increased fiber-fiber interactions that hindered the fibers ability to orient themselves along the preferred direction in the flow field. Kuriger *et al.*[156] also suggested increasing

the residence time of the nanocomposite flow through the die channel to improve the fiber alignment.

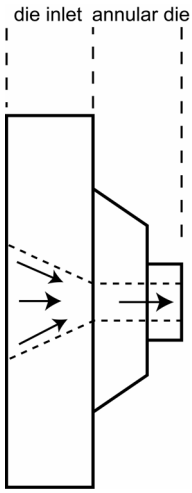

Figure 2.6. Side view of a melt-spinning die (adapted from Kuriger *et al.*[156]).

The mechanical properties of iPP fibers were found to improve with SWNT dispersed using the solvent processing route. For a 1 wt% to 4 wt% loading of SWNT, the fiber tensile strength increased about 40 % and the modulus increased by about 55 %[158, 159]. In the case of iPP/MWNT nanocomposite fibers, a significant increase in Young's modulus was observed but no improvement in the tensile strength[98]. Hassan *et al.*[160] and Kumar *et al.*[161] reported more than 100 % improvement in Young's modulus for iPP/CNF fibers with about 0.5 – 5 wt% well dispersed and aligned CNF. The tensile strength was improved by about 60 % for the same specimens.

The elastic properties of iPP/nanocarbon nanocomposites may be modelled using the Halpin-Tsai equations (detailed in section 4.3.2) as demonstrated in the case of iPP/CNF nanocomposites with a preferential fiber orientation[162]. The stiffness, E_c, of the iPP/nanocarbon composites was also modelled in the present work using a modified rule of mixtures[16, 156, 163]:

$$E_c = (1 - V_f)E_m + n\left[1 - \frac{\tan\beta}{\beta}\right]V_f E_f \qquad \textbf{Equation 2.3}$$

where V_f is the volume fraction of the nanocarbons and E_m is the axial tensile modulus of the iPP matrix. n is an orientation factor such that n = 1/6 for nanocarbons randomly oriented in three dimensions, n = 1/2 for nanocarbons randomly oriented in the plane, and n = 1 for aligned nanocarbons. The factor β is given by

$$\beta = \frac{1}{d}\sqrt{\frac{E_m}{(1+\nu)E_f \ln(\pi / 4V_f)}} \qquad \textbf{Equation 2.4}$$

where *d* is the diameter and *v* the Poisson's ratio of the filler particles.

- *Other properties*

Nanocarbons are expected to improve the dimensional stability of thermoplastics in general[65], and in iPP in particular[164], by lowering the coefficient of thermal expansion, and reducing shrinkage. Nanocarbons have also been shown to improve the electrical properties of iPP and increase its thermal conductivity[61, 156, 165]. Finally, there are numerous reviews of nanocarbon-based multifunctional nanocomposites with different types of polymer matrices[65, 73]. For example, they are used in conducting paints, and Hyperion Catalysis International, Inc. has incorporated carbon nanotubes into a plastic side view mirror housing for the Ford Taurus™ in order to increase conductivity for electrostatic paintability. Nanocarbons can also be used to make efficient, flexible, low-cost sensors for gas-leak detection, medical monitoring, and industrial process control[166]. Actuation and sensing properties are discussed by Baughman in his work on "Carbon Muscle"[167].

2.3 HYBRID COMPOSITES

2.3.1 iPP-based glass fiber reinforced composite processing

As matrix resins, thermoplastics offer a wide range of advantages over thermosets, including almost unlimited shelf life, thermoformability, short process cycle times, recyclability, increased toughness and impact resistance[168]. Despite these various attributes, the disadvantages associated with thermoplastic matrix composites are significant. The processing temperatures are higher than those required to cure epoxy based composites, and the material is supplied in solid form and must be converted into a semi-finished product[169]. To obtain reasonable structural properties, it is desirable to use long reinforcing fibers. However, mixing thermoplastics with continuous fiber tows is a difficult task, mainly because of the high viscosity of the polymer melt, leading to high shear stresses and long residence times for permeation and wetting of the fiber bundle. In what follows, two types of iPP/glass fiber semi-finished products provide the focus: long glass fiber reinforced composites (LGF) and glass mat reinforced thermoplastics (GMT). Typical properties of GMT and LGF based on iPP are reviewed elsewhere[25, 170-173], along with processing issues[174-177].

a. Long glass fiber reinforced composites (LGF)

Two techniques that have been developed for producing continuous fiber reinforced thermoplastic matrix composites are co-mingling and co-weaving[178, 179]. These techniques consist of spinning fibers from the polymer and either co-mingling these fibers with the reinforcing fibers to produce a hybrid yarn or interweaving the two types fibers to produce a fabric that can be melt consolidated[180]. A wide variety of fiber-matrix

combinations are available in co-mingled form[181]. Co-mingling is accomplished by spreading the reinforcing fiber bundles and intermingling them with the thermoplastic fibers. The reinforcement to matrix ratio is controlled closely via the fiber sizes and proportions[182]. Co-mingled yarns can be woven, knitted, or braided into fabrics flexible enough to conform to complex shapes[170, 183, 184]. For example, Vetrotex has patented a semi-finished product, Twintex®[185], made by commingling iPP, PET and PA filaments with glass fibers during the production stage (reinforcement content: 20 – 50 vol%). It is marketed in the form of a fabric, roving or sheet. The main advantage of commingling and coweaving is that they considerably reduce the impregnation distance and can therefore be used with relatively viscous polymer melts. LGF are usual considered for automobile, offshore and marine structures[186].

b. Glass mat reinforced thermoplastics (GMT)

GMT are usually available as semi-finished sheets which can be heated and compression molded. The glass fiber reinforcement is either a swirled mat or chopped fiber mat, held together by a binder[180]. Typical fiber content is about 20 – 50 wt%. The fabrication of a GMT component is characterized by a rapid process cycle (about 20 – 60 s) involving compression molding of heated semi-finished sheets of stacks called blanks. The blanks are heated individually in either an infrared oven or a hot-air convection oven, prior to being placed into the mould, which is rapidly closed. Several continuous melt impregnation sheet forming processes have resulted in commercial products of this type[187, 188]. GMT are essentially used in the automotive industry for floor pans, seat backs, bumper beams and spare wheel covers[189].

2.3.2 Hybrid composites

a. Particulate filled polymers

Microsized inorganic fillers are commonly added to polymers to improved their thermomechanical properties, and the toughness in particular [190, 191]. A typical example of the complexity in mechanical properties of particulate filled polymers is given by Tjong *et al.*[192]. They have shown that the tensile strength of potassium titanate whiskers reinforced PA6 was improved on the addition of the fillers but slightly lower than that predicted from the rule of mixtures whereas the Young's modulus was higher than predicted. Also, impact tests indicated a slight decrease in the impact strength for whisker contents of up to 15 wt%. Moreover, thermogravimetric analysis showed that particulate filled polymers with higher whisker contents (about 35 wt%) to have good heat resistance properties. However the processability of the PA6/potassium titanate whisker composite had to be improved by the incorporation of liquid crystalline polymer (LCP). Usually, the performance of the particulate filled composite requires adequate surface treatment of the filler. For example, Leong *et al.*[193] suggested the treatment of $CaCO_3$ surface with a titanate coupling agent. This treatment resulted in a 20 % improvement in the impact strength of the corresponding iPP/$CaCO_3$ composite.

The typical microsized filler content needed for significant enhancement of thermomechanical properties of polymers can be as high as 10 – 20 vol%. At such volume fractions, the processing of the polymer becomes difficult due to significant increase in viscosity, and since inorganic fillers have a higher density than the base polymer, the density of the filled polymer is also increased. The advantages of polymers, i.e., their ease of processing and lightweight, are therefore lost. To overcome this drawback, a composite with improved properties and lower particle concentration is highly desirable. For comparison, Zhou *et al*.[194] showed that introducing of talc or MMT organoclay into iPP could increase the decomposition temperature, but had no effect on glass transition and melting temperature. In addition, they showed that 40 wt% talc particles could increase the modulus, but decreased the yield strength whereas 5 wt% MMT could improve the modulus and the yield strength by 90 % and 5 % respectively.

b. Hybrid fiber reinforced particulate filled composites

In order to improve their cost efficiency and thermal stability, particulate fillers have been added to glass fiber reinforced iPP composites. Zhao *et al.*[195] prepared mica-filled iPP-based GMT. They found that at 10 wt% mica, the tensile and flexural moduli of the hybrid composite were improved by 58 % and 100 % respectively. However the impact strength was reduced by about 40 %. Similarly, Hartikainen *et al.*[196] showed that the addition of $CaCO_3$ (13 wt%) to LGF iPP increased the stiffness of the composite by about 13 %. On the other hand the toughness was decreased by 11 %.

c. Hybrid fiber reinforced nanofilled composites

Although there are a number of studies on fiber or nanoparticle reinforced systems, hybrid composites with both nanoparticle and fiber reinforcement have rarely been investigated. Preliminary studies have nevertheless demonstrated improved mechanical performance in hybrid polymer composites filled with micro- and nanosized particles. For example, Mahfuz *et al.*[197] studied the tensile response of carbon nanoparticle/whisker reinforced linear low density polyethylene (LLDPE) and observed a 15 – 17 % improvement in the tensile strength and modulus of the LLDPE. Chisholm *et al.*[198] investigated the response of microsized silicon carbide-nanosized silicon carbide/epoxy nanocomposites and reported a 20 to 30 % improvement in flexural and tensile moduli.

Hackman and Hollaway[199] studied the potential applications of organoclay nanocomposite materials in civil engineering structures. They concluded that their ability to increase the service life of materials subjected to aggressive environments could be exploited in increasing the durability of glass and carbon fiber reinforced composites. This has motivated the interest for carbon fiber reinforced composites based on polymer/MMT matrix. A few studies have demonstrated improved mechanical properties in conventional carbon fiber reinforced composites based on epoxy/MMT nanocomposites, generally without any change of the processing parameters[200-202]. Chowdhury *et al.*[203] used MMT as fillers in plain weave carbon fiber reinforced epoxy composite. They found that the optimum MMT loading of about 2 wt% resulted in increases in flexural modulus and strength of 9 % and 14 % respectively. Dean *et al.*[204]

described the successful preparation of a carbon fiber reinforced epoxy/2 wt% MMT hybrid composite using a vacuum assisted resin infusion molding (VARIM) process, in spite of an increase in resin viscosity by a factor of 10 on the addition of MMT. They measured an improvement of 31 % in the flexural modulus and 24 % in the flexural strength. On the other hand, Miyagawa *et al.*[205], who considered a biobased epoxy/MMT nanocomposite as a new matrix for carbon fiber composites, found that in spite of an increase of 0.9 GPa in the epoxy storage modulus on addition of 5 wt% exfoliated MMT, the flexural modulus and strength of the corresponding carbon fiber reinforced epoxy/5 wt% MMT did not change with respect to those of the pure epoxy-based composite. Similarly, Chen *et al.*[206, 207], who prepared epoxy/MMT nanocomposites using an aerospace grade epoxy resin and carbon fibers, reported no improvements in the mechanical properties.

Glass fibers have also been envisaged as reinforcement in epoxy/MMT nanocomposites[208-213]. For example, Haque *et al.*[208, 209] studied the effects of MMT on the improvement of the mechanical and thermal properties of S2-glass reinforced epoxy and S2-glass reinforced vinyl ester composites. They reported that in the presence of 1 wt% MMT, S2-glass reinforced epoxy/MMT nanocomposites showed an improvement of 44 %, 24 % and 23 % in interlaminar shear strength, flexural strength and fracture toughness respectively. To date and to our knowledge, Akkapeddi[214] and Vlasveld *et al.*[138, 215] are the only groups to describe hybrid composites based on a thermoplastic matrix. They manufactured glass-fiber reinforced PA6/MMT nanocomposites and reported no major changes in processing characteristics. Vlasveld *et al.*[216] also observed a 40 % increase in flexural and compressive strength at elevated temperatures in a hybrid glass fiber reinforced PA6 composite containing 10 wt% of MMT.

2.4 CONCLUSION

Progress in the synthesis of nanosized particles has opened the up the potential to integrate new functionalities in polymers in general and in polymer composites in particular. Nanosized particles are commonly classified according to their functionality, their shape and their size. The difference between micro- and nanoparticles is essentially the extent of the interphase relative to the overall matrix volume. The main preparation routes for polymer nanocomposites are now well established and are divided in three categories: in-situ polymerization, melt-mixing and solvent processing. These result in different nanocomposite morphologies depending on the matrix polymer and the type of nanofiller. In the particular case of iPP/MMT and iPP/nanocarbon nanocomposites, the melt-mixing and the solvent processing routes are of most practical interest. They result methods result in a mixed intercalated/exfoliated morphology in the case of MMT, and a wide variation in homogeneity in the case nanocarbons.

The main challenge in producing hybrid fiber reinforced nanofilled composites is to process them so as to take advantage of the potential of the nanofillers. Structure - processing and structure - property relationships are well documented for iPP/MMT and iPP/nanocarbons nanocomposites. In particular, the mechanical properties, which are

highly dependent on the morphology, are found to be improved on addition of MMT and nanocarbons to a much greater extent and at much lower nanofiller contents than for microsized fillers or conventional carbon and glass fibers. Moreover, they may also bring additional specific functionalities, such as flame resistance for iPP/MMT and thermal conductivity and thermal conductivity in the case of iPP/nanocarbon nanocomposites.

Few studies have so far been made of hybrid composites with a nanocomposite matrix, although improvements in mechanical properties have been reported in carbon fiber and glass fiber reinforced epoxy/MMT composites at low MMT loadings. In either case, the rheological properties of the nanocomposite matrices are expected to be a major issue in the context of processing. Significant changes in viscosity have already been observed in epoxy-based matrices. However, the question of the importance of any such changes for thermoplastic matrix based hybrid composite processing, in which the viscosities of the pure matrices are already relatively high, remains substantially open, and is one of the key aspects of the present work.

2.5 REFERENCES

1 J. K. W. Sandler, S. Pegel, M. Cadek, F. Gojny, M. van Es, J. Lohmar, W. J. Blau, K. Schulte, A. H. Windle and M. S. P. Shaffer, **A comparative study of melt spun polyamide-12 fibres reinforced with carbon nanotubes and nanofibres**, *Polymer*, 2004; **45** (6): 2001-2015

2 K. S. Triantafyllidis, P. C. LeBaron, I. Park and T. J. Pinnavaia, **Epoxy-clay fabric film composites with unprecedented oxygen-barrier properties**, *Chemistry of Materials*, 2006; **18** (18): 4393-4398

3 R. Mohr, K. Kratz, T. Weigel, M. Lucka-Gabor, M. Moneke and A. Lendlein, **Initiation of shape-memory effect by inductive heating of magnetic nanoparticles in thermoplastic polymers**, *Proceedings of the National Academy of Sciences of the United States of America*, 2006; **103** (10): 3540-3545

4 S. Iijima, **Helical Microtubules Of Graphitic Carbon**, *Nature*, 1991; **354** (6348): 56-58

5 L. S. Schadler, **Polymer-based and polymer-filled nanocomposites** in *Nanocomposite science and technology*, pp 230, Wiley-VCH, Weinheim (2003)

6 S. C. Tjong, **Structural and mechanical properties of polymer nanocomposites**, *Materials Science & Engineering R-Reports*, 2006; **53** (3-4): 73-197

7 R. Rothon, **Particulate-filled polymer composites**, Longman, Harlow, (1995)

8 B. Pukanszky, **Interfaces and interphases in multicomponent materials: past, present, future**, *European Polymer Journal*, 2005; **41** (4): 645-662

9 C. L. Wu, M. Q. Zhang, M. Z. Rong and K. Friedrich, **Tensile performance improvement of low nanoparticles filled-polypropylene composites**, *Composites Science and Technology*, 2002; **62** (10-11): 1327-1340

10 E. Reynaud, C. Gauthier and J. Perez, **Nanophases in polymers**, *Revue De Metallurgie-Cahiers D Informations Techniques*, 1999; **96** (2): 169-176

11 B. Fiedler, F. H. Gojny, M. H. G. Wichmann, M. C. M. Nolte and K. Schulte, **Fundamental aspects of nano-reinforced composites**, *Composites Science and Technology*, 2006; **66** (16): 3115-3125

12 Y. J. Choi and J. Simonsen, **Cellulose nanocrystal-filled carboxymethyl cellulose nanocomposites**, *Journal of Nanoscience and Nanotechnology*, 2006; **6** (3): 633-639

13 C. M. Chan, J. S. Wu, J. X. Li and Y. K. Cheung, **Polypropylene/calcium carbonate nanocomposites**, *Polymer*, 2002; **43** (10): 2981-2992

14 C. A. R. Costa, C. A. P. Leite and F. Galembeck, **Size dependence of Stober silica nanoparticle microchemistry**, *Journal of Physical Chemistry B*, 2003; **107** (20): 4747-4755

15 G. A. Buxton and A. C. Balazs, **Predicting the mechanical and electrical properties of nanocomposites formed from polymer blends and nanorods**, *Molecular Simulation*, 2004; **30** (4): 249-257

16 H. Ma, J. Zeng, M. L. Realff, S. Kumar and D. A. Schiraldi, **Processing, structure, and properties of fibers from polyester/carbon nanofiber composites**, *Composites Science and technology*, 2003; **63** 1617-1628

17 G. Schmidt and M. M. Malwitz, **Properties of polymer-nanoparticle composites**, *Current Opinion in Colloid & Interface Science*, 2003; **8** (1): 103-108

18 Y. Brechet, J. Y. Y. Cavaille, E. Chabert, L. Chazeau, R. Dendievel, L. Flandin and C. Gauthier, **Polymer based nanocomposites: Effect of filler-filler and filler-matrix interactions**, *Advanced Engineering Materials*, 2001; **3** (8): 571-577

19 R. Gangopadhyay and A. De, **Conducting polymer nanocomposites: A brief overview**, *Chemistry of Materials*, 2000; **12** (3): 608-622

20 Q.-Q. Zhang, H. Chan, B. Ploss and C. L. Choy, **PCLT/P(VDF-TrFE) Nanocomposite Pyroelectric Sensors**, *IEEE Transactions on ultrasonics, ferroelectrics, and frequency control*, 2001; **48** (1): 154-160

21 H. L. W. Chan, S. T. Lau, K. W. Kwok, Q. Q. Zhang, Q. F. Zhou and C. L. Choy, **Nanocomposite ultrasonic hydrophones**, *Sensors and Actuators*, 1999; **75** 252-256

22 K. Gall, M. L. Dunn, Y. P. Liu, D. Finch, M. Lake and N. A. Munshi, **Shape memory polymer**

nanocomposites, *Acta Materialia*, 2002; **50** (20): 5115-5126
23 H. Li, Y. Chen, C. Ruan, W. Gao and Y. Xie, **preparation of organic-inorganic multifunctional nanocomposite composite via sol-gel routes**, *Journal of nanoparticle research*, 2001; **3** 157-160
24 R. A. Vaia and H. D. Wagner, **Framework for nanocomposites**, *Materials Today*, 2004; **7** (11): 32-37
25 J. Karger-Kocsis, **Polypropylene structure, blends and composites**, Chapman & Hall, London etc., (1995)
26 X. Wang, W. M. Hou, J. J. Zhou, L. Li, Y. Li and C. M. Chan, **Melting behavior of lamellae of isotactic polypropylene studied using hot-stage atomic force microscopy**, *Colloid and Polymer Science*, 2007; **285** (4): 449-455
27 K. Mezghani and P. J. Phillips, **The gamma-phase of high molecular weight isotactic polypropylene .2. The morphology of the gamma-form crystallized at 200 MPa**, *Polymer*, 1997; **38** (23): 5725-5733
28 J. Karger-Kocsis, **Polypropylene an a-z reference**, Kluwer Academic Publ., Dordrecht etc., (1999)
29 J. Jancar, **Structure-Property relationships in Thermoplastic Matrices**, *Advances in Polymer Science*, 1999; **139**
30 J. R. Fried, **Polymer science and technology**, Prentice Hall, Englewood Cliffs, NJ, (1995)
31 C. H. Hong, Y. B. Lee, J. W. Bae, J. Y. Jho, B. U. Nam and T. W. Hwang, **Preparation and mechanical properties of polypropylene/clay nanocomposites for automotive parts application**, *Journal of Applied Polymer Science*, 2005; **98** (1): 427-433
32 S. M. Zebarjad, M. Tahani and S. A. Sajjadi, **Influence of filler particles on deformation and fracture mechanism of isotactic polypropylene**, *Journal Of Materials Processing Technology*, 2004; **155-56** 1459-1464
33 Q. Yuan and R. D. K. Misra, **Impact fracture behavior of clay-reinforced polypropylene nanocomposites**, *Polymer*, 2006; **47** (12): 4421-4433
34 A. V. Shenoy, **Rheology of filled polymer systems**, Kluwer Academic Publishers, Dordrecht, (1999)
35 R. N. Rothon, **Mineral fillers in thermoplastics: filler manufacture and characterization**, *Advances in Polymer Science*, 1999; **139**
36 P. M. McGenity, J. J. Hooper, C. D. Paynter, A. M. Riley, C. Nutbeem, N. J. Elton and J. M. Adams, **Nucleation and Crystallization of Polypropylene by Mineral Fillers - Relationship to Impact Strength**, *Polymer*, 1992; **33** (24): 5215-5224
37 W. C. J. Zuiderduin, C. Westzaan, J. Huetink and R. J. Gaymans, **Toughening of polypropylene with calcium carbonate particles**, *Polymer*, 2003; **44** (1): 261-275
38 Z. Demjen, B. Pukanszky and J. Nagy, **Evaluation of interfacial interaction in polypropylene surface treated CaCO3 composites**, *Composites Part a-Applied Science and Manufacturing*, 1998; **29** (3): 323-329
39 L. Jilken, G. Malhammar and R. Selden, **The Effect of Mineral Fillers on Impact and Tensile Properties of Polypropylene**, *Polymer Testing*, 1991; **10** (5): 329-344
40 P. F. Bright, R. J. Crowson and M. J. Folkes, **Study of Effect of Injection Speed on Fiber Orientation in Simple Moldings of Short Glass Fiber-Filled Polypropylene**, *Journal of Materials Science*, 1978; **13** (11): 2497-2506
41 M. Drubetski, A. Siegmann and M. Narkis, **Electrical properties of hybrid carbon black/carbon fiber polypropylene composites**, *Journal of Materials Science*, 2007; **42** (1): 1-8
42 J. Gassan and A. K. Bledzki, **The influence of fiber-surface treatment on the mechanical properties of jute-polypropylene composites**, *Composites Part a-Applied Science and Manufacturing*, 1997; **28** (12): 1001-1005
43 S. M. Auerbach, **Handbook of layered materials**, Marcel Dekker, New York, (2004)
44 S. S. Ray and M. Okamoto, **Polymer/layered silicate nanocomposites: a review from preparation to processing**, *Progress in Polymer Science*, 2003; **28** (11): 1539-1641
45 M. Alexandre and P. Dubois, **Polymer-layered silicate nanocomposites: preparation, properties and uses of a new class of materials**, *Materials Science and Engineering*, 2000; **28** 1-63
46 T. J. Pinnavaia, **Polymer-clay nanocomposites**, John Wiley, Chichester, (2000)
47 P. C. LeBaron, Z. Wang and T. J. Pinnavaia, **Polymer-layered silicate nanocomposites: an**

overview, *Applied Clay Science*, 1999; **15** (1-2): 11-29
48 http://www.nanoclay.com
49 http://www.nanocor.com
50 http://www.sud-chemie.com
51 A. Usuki, Y. Kojima, M. Kawasumi, A. Okada, Y. Fukushima, T. Kurauchi and O. Kamigaito, **Synthesis of Nylon 6-Clay Hybrid**, *Journal of Materials Research*, 1993; **8** (5): 1179-1184
52 X. Kornmann, H. Lindberg and L. A. Berglund, **Synthesis of epoxy-clay nanocomposites: influence of the nature of the clay on structure**, *Polymer*, 2001; **42** (4): 1303-1310
53 D. Homminga, B. Goderis, I. Dolbnya and G. Groeninckx, **Crystallization behavior of polymer/montmorillonite nanocomposites. Part II. Intercalated poly (epsilon-caprolactone)/montmorillonite nanocomposites**, *Polymer*, 2006; **47** (5): 1620-1629
54 X. Fu and S. Qutubuddin, **Polymer-clay nanocomposites: exfoliation of organophilic montmorillonite nanolayers in polystyrene**, *Polymer*, 2001; **42** (2): 807-813
55 Y. Yang, Z. K. Zhu, J. Yin, X. Y. Wang and Z. E. Qi, **Preparation and properties of hybrids of organo-soluble polyimide and montmorillonite with various chemical surface modification methods**, *Polymer*, 1999; **40** (15): 4407-4414
56 J. H. Chang, S. J. Kim, Y. L. Joo and S. Im, **Poly(ethylene terephthalate) nanocomposites by in situ interlayer polymerization: the thermo-mechanical properties and morphology of the hybrid fibers**, *Polymer*, 2004; **45** (3): 919-926
57 X. M. Zhang, R. J. Xu, Z. G. Wu and C. X. Zhou, **The synthesis and characterization of polyurethane/clay nanocomposites**, *Polymer International*, 2003; **52** (5): 790-794
58 R. A. Vaia, K. D. Jandt, E. J. Kramer and E. P. Giannelis, **Microstructural evolution of melt intercalated polymer-organically modified layered silicates nanocomposites**, *Chemistry of Materials*, 1996; **8** (11): 2628-2635
59 R. Krishnamoorti, R. A. Vaia and E. P. Giannelis, **Structure and dynamics of polymer-layered silicate nanocomposites**, *Chemistry of Materials*, 1996; **8** (8): 1728-1734
60 H. W. Kroto, J. R. Heath, S. C. Obrien, R. F. Curl and R. E. Smalley, **C-60 - Buckminsterfullerene**, *Nature*, 1985; **318** (6042): 162-163
61 E. Hammel, X. Tang, M. Trampert, T. Schmitt, K. Mauthner, A. Eder and P. Pötschke, **Carbon nanofibers for composite applications**, *Carbon*, 2004; **42** (5-6): 1153-1158
62 C. X. Pan, Y. L. Liu and F. Cao, **Novel solid-cored carbon nanofiber grown on steels substrates in ethanol flames**, *Journal Of Materials Science*, 2005; **40** (5): 1293-1295
63 E. T. Thostenson, Z. Ren and T.-W. Chou, **Advances in the science and technology of carbon nanotubes and their composites: a review**, *Composites Science and technology*, 2001; **61** 1899-1912
64 M. Inagaki and L. R. Radovic, **Nanocarbons**, *Carbon*, 2002; **40** (12): 2279-2282
65 B. Maruyama and H. Alam, **Carbon nanotubes and nanofibers in composite materials**, *Sampe Journal*, 2002; **38** (3): 59-70
66 O. Breuer and U. Sundararaj, **Big returns from small fibers: A review of polymer/carbon nanotube composites**, *Polymer Composites*, 2004; **25** (6): 630-645
67 I. A. Merkulov, A. V. Meleshko, J. C. Wells, H. Cui, V. I. Merkulov, M. L. Simpson and D. H. Lowndes, **Two growth modes of graphitic carbon nanofibers with herring-bone structure**, *Physical Review B*, 2005; **72** (4):
68 R. L. Vander Wal, A. J. Tomasek and J. D. King, **A method for structural characterization of the range of cylindrical nanocarbons: Nanotubes to nanofibers**, *Carbon*, 2005; **43** (14): 2918-2930
69 J. N. Coleman, U. Khan, W. J. Blau and Y. K. Gun'ko, **Small but strong: A review of the mechanical properties of carbon nanotube-polymer composites**, *Carbon*, 2006; **44** (9): 1624-1652
70 R. Andrews, D. Jacques, D. L. Qian and T. Rantell, **Multiwall carbon nanotubes: Synthesis and application**, *Accounts Of Chemical Research*, 2002; **35** (12): 1008-1017
71 Z. E. Horvath, K. Kertesz, L. Petho, A. A. Koos, L. Tapaszto, Z. Vertesy, Z. Osvath, A. Darabont, P. Nemes-Incze, Z. Sarkozi and L. P. Biro, **Inexpensive, upscalable nanotube growth methods**, *Current Applied Physics*, 2006; **6** (2): 135-140
72 P. J. F. Harris, **Carbon nanotube composites**, *International Materials Reviews*, 2004; **49** (1): 31-43

73 F. Hussain, M. Hojjati, M. Okamoto and R. E. Gorga, **Review article: Polymer-matrix nanocomposites, processing, manufacturing, and application: An overview**, *Journal of Composite Materials*, 2006; **40** (17): 1511-1575

74 A. Okada and A. Usuki, **The chemistry of polymer-clay hybrids**, *Materials Science & Engineering C-Biomimetic Materials Sensors and Systems*, 1995; **3** (2): 109-115

75 Y. Zhong, Z. Y. Zhu and S. Q. Wang, **Synthesis and rheological properties of poly styrene/layered silicate nanocomposite**, *Polymer*, 2005; **46** (9): 3006-3013

76 J. G. Doh and I. Cho, **Synthesis and properties of polystyrene organoammonium montmorillonite hybrid**, *Polymer Bulletin*, 1998; **41** (5): 511-518

77 l. D. Choo; and J. L. Wook, **Preparation and Characterization of PMMA-Clay Hybrid Composite by Emulsion Polymerization**, *Journal of Applied Polymer Science*, 1996; **61** 1117-1122

78 J. S. Bergman, H. Chen, E. P. Giannelis, M. G. Thomas and G. W. Coates, **Synthesis and characterization of polyolefin-silicate nanocomposites: a catalyst intercalation and in situ polymerization approach**, *Chemical Communications*, 1999; (21): 2179-2180

79 J. Heinemann, P. Reichert, R. Thomann and R. Mulhaupt, **Polyolefin nanocomposites formed by melt compounding and transition metal catalyzed ethene homo- and copolymerization in the presence of layered silicates**, *Macromolecular Rapid Communications*, 1999; **20** (8): 423-430

80 T. Sun and J. M. Garces, **High-performance polypropylene-clay nanocomposites by in-situ polymerization with metallocene/clay catalysts**, *Advanced Materials*, 2002; **14** (2): 128-+

81 K. Wiemann, W. Kaminsky, F. H. Gojny and K. Schulte, **Synthesis and properties of syndiotactic poly (propylene)/carbon nanofiber and nanotube composites prepared by in situ polymerization with metallocene/MAO catalysts**, *Macromolecular Chemistry and Physics*, 2005; **206** (15): 1472-1478

82 A. Sorrentino, R. Pantani and V. Brucato, **Injection molding of syndiotactic polystyrene/clay nanocomposites**, *Polymer Engineering and Science*, 2006; **46** (12): 1768-1777

83 G. Galgali, C. Ramesh and A. Lele, **A rheological study on the kinetics of hybrid formation in polypropylene nanocomposites**, *Macromolecules*, 2001; **34** (4): 852-858

84 E. Manias, A. Touny, L. Wu, K. Strawhecker, B. Lu and T. C. Chung, **Polypropylene/Montmorillonite nanocomposites. Review of the synthetic routes and materials properties**, *Chemistry of Materials*, 2001; **13** (10): 3516-3523

85 M. Kawasumi, N. Hasegawa, M. Kato, A. Usuki and A. Okada, **Preparation and mechanical properties of polypropylene-clay hybrids**, *Macromolecules*, 1997; **30** (20): 6333-6338

86 N. Hasegawa and A. Usuki, **Silicate layer exfoliation in polyolefin/clay nanocomposites based on maleic anhydride modified polyolefins and organophilic clay**, *Journal of Applied Polymer Science*, 2004; **93** 464-470

87 M. Kato, A. Usuki and A. Okada, **Synthesis of Polypropylene Oligomer-Clay Intercalation Compounds**, *Journal of Applied Polymer Science*, 1997; **66** 1781-1785

88 Z. M. Wang, H. Nakajima, E. Manias and T. C. Chung, **Exfoliated PP/clay nanocomposites using ammonium-terminated PP as the organic modification for montmorillonite**, *Macromolecules*, 2003; **36** (24): 8919-8922

89 D. Marchant and K. Jayaraman, **Strategies for optimizing polypropylene-clay nanocomposite structure**, *Industrial & Engineering Chemistry Research*, 2002; **41** (25): 6402-6408

90 P. Reichert, H. Nitz, S. Klinke, R. Brandsch, R. Thomann and R. Mulhaupt, **Poly(propylene)/organoclay nanocomposite formation: Influence of compatibilizer functionality and organoclay modification**, *Macromolecular Materials And Engineering*, 2000; **275** (2): 8-17

91 C. M. Koo, M. J. Kim, M. H. Choi, S. O. Kim and I. J. Chung, **Mechanical and rheological properties of the maleated polypropylene-layered silicate nanocomposites with different morphology**, *Journal Of Applied Polymer Science*, 2003; **88** (6): 1526-1535

92 M. L. Lopez-Quintanilla, S. Sanchez-Valdes, L. F. R. de Valle and F. J. Medellin-Rodriguez, **Effect of some compatibilizing agents on clay dispersion of polypropylene-clay nanocomposites**, *Journal of Applied Polymer Science*, 2006; **100** (6): 4748-4756

93 V. K. Nguyen, S. H. Jin, S. H. Lee, D. S. Lee and S. Choe, **Polypropylene/clay nanocomposites prepared with masterbatches of polypropylene ionomer and organoclay**, *Composite Interfaces*, 2006; **13** (2-3): 299-310

94 Y. Wang, F. B. Chen and K. C. Wu, **Melt intercalation and exfoliation of maleated polypropylene modified polypropylene nanocomposites**, *Composite Interfaces*, 2005; **12** (3-4): 341-363

95 L. Zhu and M. Xanthos, **Effects of process conditions and mixing protocols on structure of extruded polypropylene nanocomposites**, *journal of Applied Polymer Science*, 2004; **93** 1891-1899

96 P. Peltola, E. Valipakka, J. Vuorinen, S. Syrjala and K. Hanhi, **Effect of rotational speed of twin screw extruder on the microstructure and rheological and mechanical properties of nanoclay-reinforced polypropylene nanocomposites**, *Polymer Engineering and Science*, 2006; **46** (8): 995-1000

97 L. J. Zhao, J. Li, S. Y. Guo and Q. Du, **Ultrasonic oscillations induced morphology and property development of polypropylene/montmorillonite nanocomposites**, *Polymer*, 2006; **47** (7): 2460-2469

98 R. Andrews, D. Jacques, M. Minot and T. Rantell, **Fabrication of carbon multiwall nanotube/polymer composites by shear mixing**, *Macrmolecular Materials and Engineering*, 2002; **287** 395-403

99 P. Pötschke, T. D. Fornes and D. R. Paul, **Rheological behavior of multiwalled carbon nanotube/polycarbonate composites**, *Polymer*, 2002; **43** (11): 3247-3255

100 S. B. Sinnott, **Chemical functionalization of carbon nanotubes**, *Journal Of Nanoscience And Nanotechnology*, 2002; **2** (2): 113-123

101 M. Kato, M. Matsushita and K. Fukumori, **Development of a new production method for a polypropylene-clay nanocomposite**, *Polymer Engineering and Science*, 2004; **44** (7): 1205-1211

102 L. Jin, C. Bower and O. Zhou, **Alignment of carbon nanotubes in a polymer matrix by mechanical stretching**, *Applied Physics Letters*, 1998; **73** (9): 1197-1199

103 Y. Zhong and S.-Q. Wang, **Exfoliation and yield behavior in nanodispersions of organically modified montmorillote clay**, *Journal of Rheology*, 2003; **47** (2): 483-494

104 Y. S. Ding, C. Y. Guo, J. Y. Dong and Z. G. Wang, **Novel organic modification of montmorillonite in hydrocarbon solvent using ionic liquid-type surfactant for the preparation of polyolefin-clay nanocomposites**, *Journal of Applied Polymer Science*, 2006; **102** (5): 4314-4320

105 M. Mravcakova, M. Omastova, P. Pötschke, A. Pozsgay, B. Pukanszky and J. Pionteck, **Poly(propylene)/montmorillonite/polypyrrole composites: structure and conductivity**, *Polymers for Advanced Technologies*, 2006; **17** (9-10): 715-726

106 F. C. Chiu and P. H. Chu, **Characterization of solution-mixed polypropylene/clay nanocomposites without compatibilizers**, *Journal of Polymer Research*, 2006; **13** (1): 73-78

107 A. B. Morgan and J. W. Gilman, **Characterization of Polymer-Layered Silicate (Clay) nanocomposites by transmission Electron Microscopy and X-ray Diffraction: A Comparative Study**, *Journal of Applied Polymer Science*, 2003; **87** 1329-1338

108 T. Belin and R. Epron, **Characterization methods of carbon nanotubes: a review**, *Materials Science and Engineering B-Solid State Materials for Advanced Technology*, 2005; **119** (2): 105-118

109 Q. H. Zeng, A. B. Yu, G. Q. Lu and D. R. Paul, **Clay-based polymer nanocomposites: Research and commercial development**, *Journal of Nanoscience and Nanotechnology*, 2005; **5** (10): 1574-1592

110 R. Krishnamoorti and K. Yurekli, **Rheology of polymer layered silicate nanocomposites**, *Current Opinion In Colloid & Interface Science*, 2001; **6** (5-6): 464-470

111 K. Wang, S. Liang, J. N. Deng, H. Yang, Q. Zhang, Q. Fu, X. Dong, D. J. Wang and C. C. Han, **The role of clay network on macromolecular chain mobility and relaxation in isotactic polypropylene/organoclay nanocomposites**, *Polymer*, 2006; **47** (20): 7131-7144

112 E. Moncada, R. Quijada and J. Retuert, **Comparative effect of metallocene and Ziegler-Natta polypropylene on the exfoliation of montmorillonite and hectorite clays to obtain nanocomposites**, *Journal of Applied Polymer Science*, 2007; **103** (2): 698-706

113 W. Gianelli, G. Ferrara, G. Camino, G. Pellegatti, J. Rosenthal and R. C. Trombini, **Effect of matrix features on polypropylene layered silicate nanocomposites**, *Polymer*, 2005; **46** (18): 7037-7046

114 Y. Fan, J. Lou and D. M. Shinozaki, **Microstructure dependent properties of polypropylene-**

clay nanocomposites, *Journal of Applied Polymer Science*, 2007; **103** (1): 204-210
115 C. J. G. Plummer, M. Rodlert, J. L. Bucaille, H. J. M. Grunbauer and J. A. E. Månson, **Correlating the rheological and mechanical response of polyurethane nanocomposites containing hyperbranched polymers**, *Polymer*, 2005; **46** (17): 6543-6553
116 J. Bicerano, J. F. Douglas and D. A. Brune, **Model for the viscosity of particle dispersions**, *Rev. Macromol. chem. phys.*, 1999; **C39** (4): 561-642
117 G. P. Tandon and G. J. Weng, **The Effect Of Aspect Ratio Of Inclusions On The Elastic Properties Of Unidirectionally Aligned Composites**, *Polymer Composites*, 1984; **5** (4): 327-333
118 J. D. He, M. K. Cheung, M. S. Yang and Z. N. Qi, **Thermal stability and crystallization kinetics of isotactic polypropylene/organomontmorillonite nanocomposites**, *Journal Of Applied Polymer Science*, 2003; **89** (12): 3404-3415
119 H. L. Qin, S. M. Zhang, C. G. Zhao, M. Feng, M. S. Yang, Z. J. Shu and S. S. Yang, **Thermal stability and flammability of polypropylene/montmorillonite composites**, *Polymer Degradation And Stability*, 2004; **85** (2): 807-813
120 F. C. Chiu, S. M. Lai, J. W. Chen and P. H. Chu, **Combined effects of clay modifications and compatibilizers on the formation and physical properties of melt-mixed polypropylene/clay nanocomposites**, *Journal of Polymer Science Part B-Polymer Physics*, 2004; **42** (22): 4139-4150
121 F. Bertini, M. Canetti, G. Audisio, G. Costa and L. Falqui, **Characterization and thermal degradation of polypropylene-montmorillonite nanocomposites**, *Polymer Degradation and Stability*, 2006; **91** (3): 600-605
122 J. W. Gilman, **Flammability and thermal stability studies of polymer layered-silicate (clay) nanocomposites**, *Applied Clay Science*, 1999; **15** (1-2): 31-49
123 J. W. Gilman, C. L. Jackson, A. B. Morgan, R. Harris, E. Manias, E. P. Giannelis, M. Wuthenow, D. Hilton and S. H. Phillips, **Flammability properties of polymer - Layered-silicate nanocomposites. Polypropylene and polystyrene nanocomposites**, *Chemistry of Materials*, 2000; **12** (7): 1866-1873
124 Y. Tang, Y. Hu, B. G. Li, L. Liu, Z. Z. Wang, Z. Y. Chen and W. C. Fan, **Polypropylene/montmorillonite nanocomposites and intumescent, flame-retardant montmorillonite synergism in polypropylene nanocomposites**, *Journal Of Polymer Science Part A-Polymer Chemistry*, 2004; **42** (23): 6163-6173
125 Y. Hu, Y. Tang and L. Song, **Poly (propylene)/clay nanocomposites and their application in flame retardancy**, *Polymers for Advanced Technologies*, 2006; **17** (4): 235-245
126 M. Lewin, **Reflections on migration of clay and structural changes in nanocomposites**, *Polymers for Advanced Technologies*, 2006; **17** (9-10): 758-763
127 M. Sirousazar, M. Yari, B. F. Achachlouei, J. Arsalani and Y. Mansoori, **Polypropylene/montmorillonite nanocomposites for food packaging**, *E-Polymers*, 2007;
128 C. E. Powell and G. W. Beall, **Physical properties of polymer/clay nanocomposites**, *Current Opinion in Solid State & Materials Science*, 2006; **10** (2): 73-80
129 M. A. Osman, V. Mittal and U. W. Suter, **Poly(propylene)-layered silicate nanocomposites: Gas permeation properties and clay exfoliation**, *Macromolecular Chemistry and Physics*, 2007; **208** (1): 68-75
130 D. J. Chaiko and A. A. Leyva, **Thermal transitions and barrier properties of olefinic nanocomposites**, *Chemistry of Materials*, 2005; **17** (1): 13-19
131 J. Ren, A. S. Silva and R. Krishnamoorti, **Linear viscoelasticity of disordered polystyrene-polyisoprene block**, *Macromolecules*, 2000; **33** 3739-3746
132 M. Rodlert, C. J. G. Plummer, H. J. M. Grunbauer and J. E. Manson, **Hyperbranched polymer/clay nanocomposites**, *Advanced Engineering Materials*, 2004; **6** (9): 715-719
133 R. Krishnamoorti and E. P. Giannelis, **Rheology of end-tethered polymer layered silicate nanocomposites**, *Macromolecules*, 1997; **30** (14): 4097-4102
134 R. krishnamoorti, R. A. Vaia and E. P. Giannelis, **Structure and dynamics of polymer-layered Silicate nanocomposites**, *Chem. Mater.*, 1996; **8** 1728-1734
135 S. Y. Gu, J. Ren and Q. F. Wang, **Rheology of poly(propylene)/clay nanocomposites**, *Journal Of Applied Polymer Science*, 2004; **91** (4): 2427-2434
136 L. Jian, C. Zhou, W. Gang, Y. Wei and T. Ying, **Preparation and linear rheological behavior of Polypropylene/MMT nanocomposites**, *Polymer Composites*, 2003; **24** (3): 323-331
137 M. J. Solomon, A. S. Almusallam, K. F. Seefeldt, A. Somwangthanaroj and P. Varadan, **Rheology**

of polypropylene/clay hybrid materials, *Macromolecules*, 2001; **34** (6): 1864-1872
138 D. P. N. Vlasveld, M. de Jong, H. E. N. Bersee, A. D. Gotsis and S. J. Picken, **The relation between rheological and mechanical properties of PA6 nano- and micro-composites**, *Polymer*, 2005; **46** (23): 10279-10289
139 E. P. Giannelis, Krishnamoorti and E. Manias, **Polymer-silicate nanocomposites: model systems for confined Polymers and polymer brushes**, *Advances in Polymer Science*, 1999; **138** 107-147
140 A. Abranyi, L. Szazdi, B. Pukanszky, G. J. Vancso and B. Pukanszky, **Formation and detection of clay network structure in poly (propylene)/layered silicate nanocomposites**, *Macromolecular Rapid Communications*, 2006; **27** (2): 132-135
141 M. A. L. Manchado, L. Valentini, J. Biagiotti and J. M. Kenny, **Thermal and mechanical properties of single-walled carbon nano tubes-polypropylene composites prepared by melt processing**, *Carbon*, 2005; **43** (7): 1499-1505
142 X. L. Xie, Y. W. Mai and X. P. Zhou, **Dispersion and alignment of carbon nanotubes in polymer matrix: A review**, *Materials Science & Engineering R-Reports*, 2005; **49** (4): 89-112
143 C. Velasco-Santos, A. L. Martinez-Hernandez, M. Lozada-Cassou, A. lvarez-Castillo and V. M. Castano, **Chemical functionalization of carbon nanotubes through an organosilane**, *Nanotechnology*, 2002; **13** 495-498
144 D. McIntosh, V. N. Khabashesku and E. V. Barrera, **Nanocomposite fiber systems processed from fluorinated single-walled carbon nanotubes and a polypropylene matrix**, *Chemistry of Materials*, 2006; **18** (19): 4561-4569
145 I. C. Finegan, G. G. Tibbets, D. G. Glasgow, J.-M. Ting and M.-L. Lake, **Surface treatments for improving th emechanical properties of carbon nanofiber/thermoplastic composites**, *Journal of materials science*, 2003; **38** 3485-3490
146 P. Cortes, K. Lozano, E. V. Barrera and J. Bonilla-Rios, **Effects of nanofiber treatments on the properties of vapor-grown carbon fiber reinforced polymer composites**, *Journal of Applied Polymer Science*, 2003; **89** (9): 2527-2534
147 E. T. Thostenson, C. Y. Li and T. W. Chou, **Nanocomposites in context**, *Composites Science And Technology*, 2005; **65** (3-4): 491-516
148 V. A. Buryachenko, A. Roy, K. Lafdi, K. L. Anderson and S. Chellapilla, **Multi-scale mechanics of nanocomposites including interface: Experimental and numerical investigation**, *Composites Science and Technology*, 2005; **65** (15-16): 2435-2465
149 L. Valentini, J. Biagiotti, M. A. Lopez-Manchado, S. Santucci and J. M. Kenny, **Effects of carbon nanotubes on the crystallization behavior of polypropylene**, *Polymer Engineering and Science*, 2004; **44** (2): 303-311
150 K. Lozano and E. V. Barrera, **Nanofiber-reinforced thermoplastic composites. I. Thermoanalytical and mechanical analyses**, *Journal of Applied Polymer Science*, 2001; **79** (1): 125-133
151 P. Pötschke, H. Brunig, A. Janke, D. Fischer and D. Jehnichen, **Orientation of multiwalled carbon nanotubes in composites with polycarbonate by melt spinning**, *Polymer*, 2005; **46** (23): 10355-10363
152 B. vigolo, P. Poulin, M. Lucas, P. Launois and P. Bernier, **Improved structure and properties of single-wall carbon nanotube spun fibers**, *Applied Physics Letters*, 2002; **81** (7): 1210-1212
153 H. G. Chae, T. V. Sreekumar, T. Uchida and S. Kumar, **A comparison of reinforcement efficiency of various types of carbon nanotubes in poly acrylonitrile fiber**, *Polymer*, 2005; **46** (24): 10925-10935
154 E. M. Moore, D. L. Ortiz, V. T. Marla, R. L. Shambaugh and B. P. Grady, **Enhancing the strength of polypropylene fibers with carbon nanotubes**, *Journal of Applied Polymer Science*, 2004; **93** (6): 2926-2933
155 W. H. Ruan, X. B. Huang, X. H. Wang, M. Z. Rong and M. Q. Zhang, **Effect of drawing induced dispersion of nano-silica on performance improvement of poly(propylene)-based nanocomposites**, *Macromolecular Rapid Communications*, 2006; **27** (8): 581-585
156 R. J. Kuriger, M. K. Alam, D. P. Anderson and R. L. Jacobsen, **Processing and characterization of aligned vapor grown carbon fiber reinforced polypropylene**, *Composites Part A-Applied Science And Manufacturing*, 2002; **33** (1): 53-62
157 Z. H. Fan and S. G. Advani, **Characterization of orientation state of carbon nanotubes in shear flow**, *Polymer*, 2005; **46** (14): 5232-5240

158 T. E. Chang, L. R. Jensen, A. Kisliuk, R. B. Pipes, R. Pyrz and A. P. Sokolov, **Microscopic mechanism of reinforcement in single-wall carbon nanotube/polypropylene nanocomposite**, *Polymer*, 2005; **46** (2): 439-444

159 J. C. Kearns and R. L. Shambaugh, **Polypropylene fibers reinforced with carbon nanotubes**, *Journal of Applied Polymer Science*, 2002; **86** (8): 2079-2084

160 M. M. Hasan, Y. X. Zhou and S. Jeelani, **Thermal and tensile properties of aligned carbon nanofiber reinforced polypropylene**, *Materials Letters*, 2007; **61** (4-5): 1134-1136

161 S. Kumar, H. Doshi, M. Srinivasarao, J. O. Park and D. A. Schiraldi, **Fibers from polypropylene/nano carbon fiber composites**, *Polymer*, 2002; **43** (5): 1701-1703

162 I. C. Finegan, G. G. Tibbets and R. F. Gibson, **Modeling and characterization of damping in carbon nanofiber/polypropylene composites**, *Composites Science and technology*, 2003; **63** 1629-1635

163 J. J. Zeng, B. Saltysiak, W. S. Johnson, D. A. Schiraldi and S. Kumar, **Processing and properties of poly(methyl methacrylate)/carbon nanofiber composites**, *Composites Part B-Engineering*, 2004; **35** (3): 245-249

164 A. Chatterjee and B. L. Deopura, **Thermal stability of polypropylene/carbon nanofiber composite**, *Journal of Applied Polymer Science*, 2006; **100** (5): 3574-3578

165 K. Lozano, J. Bonilla-Rios and E. V. Barrera, **A study on nanofiber-reinforced thermoplastic composites (II): Investigation of the mixing rheology and conduction properties**, *Journal of Applied Polymer Science*, 2001; **80** (8): 1162-1172

166 J. Ouellette, **Building the nanofuture with carbon tubes**, *The industrial physicist*, 2003; (12/02): 18-21

167 R. H. Baughman, C. Z. Cui, A. A.; , Z. Iqbal, J. N. Barisci, G. M. Spinks, W. G. G.;, A. Mazzoldi, D. De Rossi, A. G. Rinzler, O. Jaschinski, S. Roth and M. Kertesz, **Carbon nanotube actuators**, *science*, 1999; **284** 1340-1344

168 M. Reyne, **Composite solutions thermosets and thermoplastics**, JEC Publications, Paris, (2006)

169 R. A. Ford, **Semi-finished thermoplastic composites-realising their potential**, *Materials & Design*, 2004; **25** (7): 631-636

170 M. D. Gilchrist, N. Svensson and R. Shishoo, **Fracture and fatigue performance of textile commingled yarn composites**, *Journal Of Materials Science*, 1998; **33** (16): 4049-4058

171 E. Mäder and K. Skop-Cardarella, **Tailored Thermoplastic Composites Based on New Hybrid Yarns**, *Key Engineering Materials*, 1998; **137** 24-31

172 M. D. Wakeman, T. A. Cain, C. D. Rudd and A. C. Long, **Compression Moulding of Glass and Polypropylene Composites for Optimised Macro- and Micro- Mechanical Properties II. Glass-Mat-Reinforced Thermoplastics**, *Composites Science and Technology*, 1999; **59** 709-726

173 M. N. Bureau and J. Denault, **Fatigue resistance of continuous glass fiber/polypropylene composites: consolidation dependence**, *Composites Science and technology*, 2004; **64** 1785-1794

174 S. K. Kim, G. M. Kim, H. J. Kim and W. Il Lee, **An experimental study on the thermoplastic filament winding process using commingled yarns**, *Advanced Composites Letters*, 2002; **11** (2): 67-71

175 R. P. Chhabra, J. Comiti and I. Machac, **Flow of non-Newtonian fluids in fixed and fluidised beds**, *Chemical Engineering Science*, 2001; **56** (1): 1-27

176 J. L. Thomason, **The influence of fibre length and concentration on the properties of glass fibre reinforced polypropylene. 6. The properties of injection moulded long fibre PP at high fibre content**, *Composites Part A-Applied Science And Manufacturing*, 2005; **36** (7): 995-1003

177 S. G. Advani, **Flow and rheology in polymer composites manufacturing**, Elsevier, Amsterdam etc., (1994)

178 R. Kamiya, B. A. Cheeseman, P. Popper and T.-W. Chou, **Some recent advances in the fabrication and design of three-dimensional textile preforms: a review**, *Composites Science and technology*, 2000; **60** 33-47

179 A. P. Mouritz, M. K. Bannister, P. J. Falzon and K. H. Leong, **Review of applications for advanced three-dimensional fibre textile composites**, *Composites Part a-Applied Science and Manufacturing*, 1999; **30** (12): 1445-1461

180 J. Karger-Kocsis, **Polypropylene structure, blends and composites**, Chapman & Hall, London etc., (1995)

181 H. Brunig, R. Beyreuther, R. Vogel and B. Tandler, **Melt spinning of fine and ultra-fine PEEK-filaments**, *Journal Of Materials Science*, 2003; **38** (10): 2149-2153

182 R. Beyreuther, H. Brunig and R. Vogel, **Preferable filament diameter ratios of hybrid yarn components for optimized longfiber reinforced thermoplastics**, *International Polymer Processing*, 2002; **17** (2): 153-157

183 N. Svensson, R. Shishoo and M. Gilchrist, **Manufacturing of thermoplastic composites from commingled yarns - A review**, *Journal Of Thermoplastic Composite Materials*, 1998; **11** (1): 22-56

184 N. Bernet, V. Michaud, P.-E. Bourban and J.-A. E. Månson, **Commingled yarn composites for rapid processing of complex shapes**, *Composites: Part A*, 2001; **32** 1613-1626

185 http://www.twintex.com

186 K. Ogi, T. Shiraishi and H. Murayama, **Effect of temperature and after-cure on fatigue fracture behavior of a glass/phenol composite**, *International Journal of Fatigue*, 2006; **28** (10): 1290-1296

187 http://www.quadrant.ch

188 http://www.azdel.com

189 J. Karger-Kocsis, **Swirl mat- and long discontinuous fiber mat-reinforced polypropylene composites - Status and future trends**, *Polymer Composites*, 2000; **21** (4): 514-522

190 H. Tolonen and S. G. Sjolind, **Effect of mineral fillers on properties of composite matrix material**, *Mechanics Of Composite Materials*, 1995; **31** (4): 317-324

191 P. E. J. Babu, S. Savithri, U. T. S. Pillai and B. C. Pai, **Micromechanical modeling of hybrid composites**, *Polymer*, 2005; **46** (18): 7478-7484

192 S. C. Tjong and Y. Z. Meng, **Properties and morphology of polyamide 6 hybrid composites containing potassium titanate whisker and liquid crystalline copolyester**, *Polymer*, 1999; **40** (5): 1109-1117

193 Y. W. Leong, M. B. Abu Bakar, Z. A. M. Ishak and A. Ariffin, **Effects of filler treatments on the mechanical, flow, thermal, and morphological properties of talc and calcium carbonate filled polypropylene hybrid composites**, *Journal Of Applied Polymer Science*, 2005; **98** (1): 413-426

194 Y. X. Zhou, V. Rangari, H. Mahfuz, S. Jeelani and P. K. Mallick, **Experimental study on thermal and mechanical behavior of polypropylene, talc/polypropylene and polypropylene/clay nanocomposites**, *Materials Science And Engineering A-Structural Materials Properties Microstructure And Processing*, 2005; **402** (1-2): 109-117

195 R. Zhao, J. Huang, S. Bin and G. Dai, **Study of the mechanical properties of mica-filled polypropylene-based GMT composite**, *Journal Of Applied Polymer Science*, 2001; **82** (11): 2719-2728

196 J. Hartikainen, P. Hine, J. S. Szabo, M. Lindner, T. Harmia, R. A. Duckett and K. Friedrich, **Polypropylene hybrid composites reinforced with long glass fibres and particulate filler**, *Composites Science And Technology*, 2005; **65** (2): 257-267

197 H. Mahfuz, A. Adnan, V. K. Rangari, S. Jeelani and B. Z. Jang, **Carbon nanoparticles/whiskers reinforced composites and their tensile response**, *Composites Part A-Applied Science And Manufacturing*, 2004; **35** (5): 519-527

198 N. Chisholm, H. Mahfuz, V. K. Rangari, A. Ashfaq and S. Jeelani, **Fabrication and mechanical characterization of carbon/SiC-epoxy nanocomposites**, *Composite Structures*, 2005; **67** (1): 115-124

199 I. Hackman and L. Hollaway, **Epoxy-layered silicate nanocomposites in civil engineering**, *Composites Part a-Applied Science and Manufacturing*, 2006; **37** (8): 1161-1170

200 E. N. Gilbert, B. S. Hayes and J. C. Seferis, **Variable density composite systems constructed by metal particle modified prepregs**, *Journal of Composite Materials*, 2002; **36** (17): 2045-2060

201 E. N. Gilbert, B. S. Hayes and J. C. Seferis, **Metal particle modification of composite matrices for customized density applications**, *Polymer Composites*, 2002; **23** (1): 132-140

202 J. F. Timmerman, B. S. Hayes and J. C. Seferis, **Nanoclay reinforcement effects on the cryogenic microcracking of carbon fiber/epoxy composites**, *Composites Science and Technology*, 2002; **62** (9): 1249-1258

203 F. H. Chowdhury, M. V. Hosur and S. Jeelani, **Studies on the flexural and thermomechanical properties of woven carbon/nanoclay-epoxy laminates**, *Materials Science and Engineering a-Structural Materials Properties Microstructure and Processing*, 2006; **421** (1-2): 298-306

204 D. Dean, A. M. Obore, S. Richmond and E. Nyairo, **Multiscale fiber-reinforced nanocomposites: Synthesis, processing and properties**, *Composites Science and Technology*, 2006; **66** (13): 2135-2142

205 H. Miyagawa, R. J. Jurek, A. K. Mohanty, M. Misra and L. T. Drzal, **Biobased epoxy/clay nanocomposites as a new matrix for CFRP**, *Composites Part a-Applied Science and Manufacturing*, 2006; **37** (1): 54-62

206 B. P. Rice, C. G. Chen, L. Cloos and D. Curliss, **Carbon fiber composites: Organoclay-aerospace epoxy nanocomposites, Part I**, *Sampe Journal*, 2001; **37** (5): 7-9

207 C. G. Chen and D. Curliss, **Resin matrix composites: Organoclay-aerospace epoxy nanocomposites, Part II**, *Sampe Journal*, 2001; **37** (5): 11-18

208 A. Haque, M. Shamsuzzoha, F. Hussain and D. Dean, **S2-glass/epoxy polymer nanocomposites: Manufacturing, structures, thermal and mechanical properties**, *Journal Of Composite Materials*, 2003; **37** (20): 1821-1837

209 F. Hussain, D. Dean, A. Haque and A. M. Shamsuzzoha, **S2 glass/vinylester polymer nanocomposites: Manufacturing, structures, thermal and mechanical properties**, *Journal of Advanced Materials*, 2005; **37** (1): 16-27

210 O. Becker, R. J. Varley and G. P. Simon, **Use of layered silicates to supplementarily toughen high performance epoxy-carbon fiber composites**, *Journal Of Materials Science Letters*, 2003; **22** (20): 1411-1414

211 X. Kornmann, M. Rees, Y. Thomann, A. Necola, M. Barbezat and R. Thomann, **Epoxy-layered silicate nanocomposites as matrix in glass fibre-reinforced composites**, *Composites Science And Technology*, 2005; **65** (14): 2259-2268

212 J. L. Tsai, J. C. Kuo and S. M. Hsu, **Organoclay effect on transverse compressive strength of glass/epoxy nanocomposites**, *Journal of Materials Science*, 2006; **41** (22): 7406-7412

213 J. L. Tsai, J. C. Kuo and S. M. Hsu, **Fabrication and mechanical properties of glass fiber/epoxy nanocomposites** in *Progress on Advanced Manufacture for Micro/Nano Technology 2005, Pt 1 and 2*, pp 37-42, (2006)

214 M. K. Akkapeddi, **Glass fiber reinforced polyamide-6 nanocomposites**, *Polymer Composites*, 2000; **21** (4): 576-585

215 D. P. N. Vlasveld, H. E. N. Bersee and S. J. Picken, **Nanocomposite matrix for increased fibre composite strength**, *Polymer*, 2005; **46** (23): 10269-10278

216 D. P. N. Vlasveld, W. Daud, H. E. N. Bersee and S. J. Picken, **Continuous fibre composites with a nanocomposite matrix: Improvement of flexural and compressive strength at elevated temperatures**, *Composites Part a-Applied Science and Manufacturing*, 2007; **38** (3): 730-738

CHAPTER 3

MATERIALS AND METHODS

3.1 PROCESSING TECHNIQUES

3.1.1 Melt compounding

Two different types of equipment were used to compound the materials in the melt state. Melt compounding of the masterbatch with the pure matrix material was mainly carried out using a conventional 16 × 15D twin screw extruder (Prism) which is suitable for production of large quantities of material. The screw speed was 40 rpm and three temperatures had to be set in the successive zones. The standard temperature setting was 180 °C, 200 °C, and 200 °C respectively, from the feeder to the die. The temperatures of the last two zones could be adjusted to up to 220 °C, depending on the materials. The polymer strand at the exit of the extruder die was cooled on a conveyor belt and then pelletized for subsequent processing. For in house preparation masterbatches and smaller quantities of compounded material, a DSM micro-extruder was used. The capacity of the micro-extruder was 5 cm^3 per cycle. And it was possible to pass the polymer through the twin-screws several times during each cycle, so that it was possible to vary the time of extrusion. The standard operating conditions for the micro-extruder were 180 °C, 200 °C, and 200 °C for the temperatures of the different extruder zones and the screw speed was set to 80 rpm. Masterbatches were obtained directly at the exit of the micro extruder. The micro-extruder was also coupled with a DSM micro-injection molding machine to produce dumbbell-shaped specimens corresponding to the ISO 527-2 type 5A norm. The temperature of the injection molding feeder was set to 200 °C, the temperature of the mold was 80 °C, and the specimens were injection molded at 0.2 MPa.

3.1.2 Melt-spinning

a. Fiber melt-spinning principles

The melt spinning process is commonly used for polymer resins and inorganic glasses. The process involves the melting and the extrusion of the material to be processed through multi orifice capillary die, followed by cooling and solidification of the filaments, which can be wound on a bobbin or otherwise processed[1].

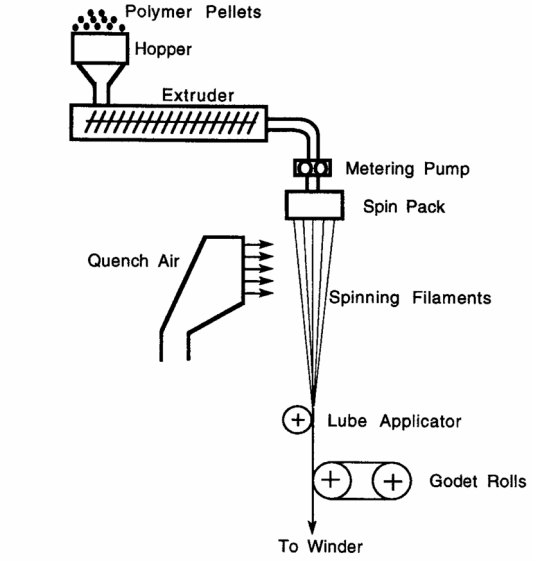

Figure 3.1. Schematic description of the melt spinning process.

A basic form of the melt spinning process is illustrated in Figure 3.1. The polymer, in the form of dried granules is fed into the extruder where it is melted and conveyed to a metering pump. The metering pump ensures a steady flow of polymer to the spin pack where the polymer is filtered and forced through the capillaries of the spinneret. The filaments are then cooled and solidified by blowing air into the quench chamber, while being drawn down by the action of heated godet rolls and then wound onto a bobbin. The winding speed corresponds to the spinning speed and is called the drive-roll velocity.

b. Experimental parameters

The present work has made use of a “Laboratory Melt-spinntester” from Fourné Polymertechnik GmbH. This is essentially a scaled down version of a standard industrial fiber spinning line, and comprises a (18 × 25D) single screw extruder with a spinneret containing 36 circular dies with a diameter of 0.4 mm, two heated godets, and a Comoli winding apparatus. The lubricant, Limanol BF2 from Schill+Seilacher, was spread onto

the "as-spun" filaments prior to the drawing. The major process variables for melt spinning are:

- Extrusion temperature (T_0),
- Mass flow rate of polymer through each spinneret hole (W),
- Drive-roll velocity of the wound up filaments (V_L),
- The spinline cooling conditions,
- Spinneret channel dimensions (diameter (d_0), length (l_0)),
- The length of the spinline (L).

The spinline cooling conditions and the spinneret channel dimensions were fixed by the equipment. Several trials were carried out in order to establish suitable spinning conditions for pure iPP. Based on these, certain independent variables were set constant for all material formulations. These are: T_0, W (controlled by the spin pump), and L (given by the cooling conditions). A systematic procedure was used to determine the processing window for each formulation. The speed of the first godet (V_{g1}) was maintained constant and the speed of the second godet (V_{g2}) was increased step by step, along with (V_L). A relevant parameter is the deformation ratio, or "melt draw ratio", defined as $V_L \backslash V_0$, where[2]

$$V_0 = \frac{4W}{n\rho_0 \pi d_0^2}, \qquad \textbf{Equation 3.1}$$

with n the number of filaments in the spinline and ρ_0 the density of the melt. The hot draw ratio DR is defined as DR= V_{g2}/V_{g1}. The standard spinning conditions are given in Table 3.1. It is also possible to define a global draw ratio λ, such that $\lambda = (d_0/d)^2$, where d is the diameter of a single filament in the yarn.

Table 3.1 Standard spinning conditions

Temperature zone 1	210 °C
Temperature zone 2	245 °C
Temperature zone 3	245 °C
Extruder speed (melt pressure)	25 rpm (60 bars)
Spin pump	12 rpm
V_{g1}	300 rpm
V_{g2}	300 rpm - 900 rpm
Comoli drive-roll velocity, V_L	360 rpm – max. 1500 rpm

The fibers were characterized in terms of their fineness. In the SI system, the units of fineness are kg/m. However, in the textile industry, the DIN 60905 specification is commonly used, that is the TEX system, where 1 tex = 1 g/10000 m. This was the specification used in this work. The fineness T was hence calculated as follows:

$$T = \frac{output\ in\ 10\ \min}{drive\ roll\ velocity} \times 100$$ **Equation 3.2**

The diameter of single filaments was measured by optical microscopy under reflected light[3]. In each yarn, at least 7 different fibers were measured and 3 measurements were made every 10 cm. The calculation of the yarn diameter assumed a circular cross-section. Thus, for a yarn containing 36 fibers, the diameter D (μm) was given by:

$$D = 6 * d$$ **Equation 3.3**

where d (μm) is the mean diameter of a single filament. This approximation was validated using the relationship between the fineness and the equivalent yarn diameter:

$$d = 20\sqrt{\frac{T}{\rho\pi}}$$ **Equation 3.4**

3.1.3 Film extrusion-calendering

The calendering of thermoplastics is an operation used for the production of continuous sheets or films of uniform thickness by squeezing the molten material between a pair of heated driven rolls[4].

A schematic of the extrusion-calendering process is given Figure 3.2. Films of about 75 mm wide and 0.7 μm thick were produced by this method using a standard Prism twin-screw extruder (described in section 3.1.1) and a Prism TSE system calender. The experimental settings are given in Table 3.2.

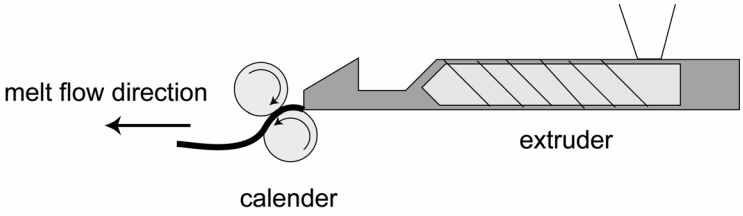

Figure 3.2. Schematic description of the extrusion-calendering process.

Table 3.2. Standard operating conditions for the extrusion-calendering process.

Temperature zone 1	180 °C
Temperature zone 2	200 °C
Temperature zone 3 (die temperature)	200 °C
Extruder speed	40 rpm
Calender temperature	25 °C
Calender speed	1 rpm

3.1.4 Compression molding

Two presses were used for the compression molding of different types of specimens: a Fontjine press and an Interlaken Press. The Fontjine press was used for the compression molding of polymer granulates to produce rheology specimens, for consolidation experiments on co-woven and co-wound specimens, and for processing of fully consolidated GMT parts. The specimens were placed in the press prior to the heating. The standard process cycle of the Fontjine involved applying a temperature ramp to the two halves of the press by holding the maximum temperature for a certain time and finally cooling down to room temperature. A constant pressure was used for the whole cycle. The heating and the cooling times for the press plates were about 20 min. For rheology specimens, the polymer was held at 200 °C for 10 min and the pressure was set to 5 KN. For consolidation experiments on LGF, the holding temperature was 220 °C and the pressure was varied from 5 KN to 10 KN. Finally, fully consolidated GMT 140 × 60 mm^2 parts were prepared using a holding time of 10 min at 200 °C and a pressure of 10 KN.

The Interlaken hydraulic press was used with a 70 × 30 mm^2 mold for infiltration-consolidation experiments on dry glass-mats. The temperature, the pressure and the time at pressure were carefully controlled and the samples were placed in the mold once a constant temperature had been reached in the two halves of the mold. For infiltration-consolidation experiments, the temperature was set to 200 °C. The glass mats and the polymer layers were placed together in the mold and allowed to heat for 5 min. When the temperature was uniform in the whole system, the mold was closed in two steps: 200 mm/min and 50 mm/min until the desired pressure of 0.2 MPa was reached. The instant at which the mold reached the final pressure was taken to be t = 0 s. The pressure was kept constant during the impregnation. When the desired impregnation time was reached, the mold was rapidly cooled down by means of circulating water. During the cooling step the pressure was maintained constant and equal to 0.2 MPa.

3.2 CHARACTERIZATION TECHNIQUES

3.2.1 Morphology

The dispersion of nanofillers and intercalation of MMT in the nanocomposites were evaluated by a combination of XRD and TEM. The experimental methodologies are described below.

a. X-ray Diffraction (XRD)

XRD is a convenient method to determine the interlayer spacing, *d*, of ordered stacks of silicate layers. Intercalation of polymer chains between silicate sheets usually increases the interlayer spacing, resulting in a shift of the XRD peak towards lower angles. The diffraction angle is related to the silicate layer spacing through the Bragg relationship:

$$\lambda = 2d\sin\theta \qquad \textbf{Equation 3.5}$$

where λ corresponds to the wavelength of the X-ray radiation, d is the spacing between the silicate layers, and θ is the measured diffraction angle. A limitation of this method is that it provides no information on the spatial distribution of the silicate layers or inhomogeneities (TEM is a complementary method in this respect). For compression molding specimens, $\theta/2\theta$ diffraction patterns were recorded at room temperature with a Siemens Kristalloflex 805 diffractometer with a Cu Kα radiation (λ = 1.54 Å). Samples were prepared by hot pressing at between 200 °C and 220 °C using the Fontjine press. XRD data were collected between 1 ° and 10 ° in steps of 0.02 ° using a generator voltage of 45 kV and a generator current of 100 mA. Wide Angle X-ray diffraction (WAXS) and Small Angle X-ray diffraction (SAXS) patterns were recorded simultaneously on melt-spun filaments using a Molecular Metrology, Inc. SAXS system with Cu Kα radiation at a maximum power of 30 W.

b. Transmission Electron Microscopy (TEM)

TEM allows qualitative analysis of the internal structure and spatial distribution of various phases[5]. The observations were performed with a Philips CM-20 apparatus equipped with a LaB_6 filament at an acceleration voltage of 200 kV. The specimens were embedded in a polymerized epoxy resin (Electron Microscopy Sciences), stained with a ruthenium tetroxide (RuO_4) solution, and ultrathin sections (70 - 50 nm) were cut at room temperature with a Reichert Jung ultramicrotome equipped with a diamond knife (Diatome), and deposited on copper grids.

c. Optical microscopy

The measurements of filament diameters and localized sections of glass fiber reinforced composite specimens were carried out using an Olympus light microscope model BX60, under reflected light. In order to observe the glass fiber distribution and the porosity in glass-mat reinforced composites, 15 × 10 mm^2 specimens were cut from partially and fully consolidated parts with a diamond saw. The specimens were embedded in an Epofix

resin (Struers) colored with a fluorescent dye (Epodye, Struers) to increase the contrast between the iPP matrix and the embedding medium. The embedding step was performed under depressurization to ensure maximum infiltration of the porosity. After a curing time of about 24h, the embedded specimens were polished. A correct polishing procedure is essential to obtain reliable optical micrographs. The procedure adopted here using a Struers polishing machine is as follows:

- 500 grit silicon carbide grinding paper for 2 - 5 min with a transverse force of 25N,
- 1000 grit silicon carbide grinding paper for 10 min with a transverse force of 10N,
- 2400 grit silicon carbide grinding paper for 30 min with a transverse force of 10N,
- 4000 grit silicon carbide grinding paper for 30 min with a transverse force of 10N.

Images of large transverse sections of glass reinforced composite were then recorded using an Olympus light microscope, model BX61 equipped with a motorized plate, and image analysis software (Soft Imaging System Gmbh) was used to measure the fiber and void volume fractions.

3.2.2 Differential Scanning Calorimetry (DSC)

Non-isothermal analysis was performed using a Thermal Analysis Instruments Q100 DSC calibrated using indium. All experiments were carried out in a nitrogen atmosphere. The standard procedure for compounded specimens was as follows: specimens of about 3 mg were heated to 220 °C at a scan rate of 10 K/min and held for 1 min in order to eliminate any thermal history of the material. The specimens were then cooled to - 50 °C at a scan rate of 5 K/min. The melting peak after crystallization was obtained by reheating the specimen to 200 °C at 10 K/min.

The crystallization peak (T_c), the apparent melting temperatures of the crystallized specimens (T_m), and the crystallization and the melting enthalpies (H_c and H_m respectively) were recorded. The degree of crystallinity X_c was calculated from the melting enthalpy, H_m, using

$$X_c = \frac{\Delta H_m}{(1 - W_{fillers})\,\Delta H_f^0} \qquad \textbf{Equation 3.6}$$

where H_f^0 is the heat of fusion of a 100 % crystalline iPP, taken to be equal to 146.5 J/g[6] and $W_{fillers}$ the weight fraction of fillers. For the filaments, specimens were cut into small pieces using a razor blade, and the crystallinity was calculated from H_m measured during the first heating scan.

3.2.3 Rheology

The flow behavior of the nanocomposites was investigated by shear and capillary rheometry in order to establish the extent to which it was necessary to modify the processing window for fiber spinning in the presence of the fillers, and to assess the

effect of the fillers on subsequent processing operations. For the shear rheometry, the pre-compounded granulates were compression molded into 0.9 mm thick disks of 25 mm in diameter. Oscillating and steady-state shear measurements were then performed with an ARES rheometer (Rheometrics Scientific) in the cone-plate geometry (0.1 rad) in the temperature range 180 to 240 °C. Dynamic strain sweeps were used to determine the extent of linear viscoelastic regime and all subsequent dynamic measurements were consequently carried out at shear strains below 0.5 %. Capillary flow measurements were made using a twin-bore Rosand capillary rheometer RH7 (Rosand Precision Ldt, Sturbridge, UK). Melt fracture (pressure drop) and stress relaxation tests were made using a single bore and a capillary die with a length ratio of 1:16 and an entrance angle of 180 °. Each test was preceded by an initial pre-compression run up to 0.5 bar and a 5 min heat treatment at the final test temperature of 220 °C. For elongationnal shear viscosities, constant shear tests were performed using a capillary die in one bore and an orifice die with zero length in the other, to allow use of the Bagley correction, 5 stages of constant shear rate were applied from 10 s^{-1} to 10^4 s^{-1}. In this case, the shear stress at the channel wall (τ_w) is defined as[7]:

$$\tau_w = \frac{(\Delta P - \Delta P_0) R}{2L} \qquad \textbf{Equation 3.7}$$

where P is the pressure drop over the capillary, P_0 the pressure drop over the zero length die and L and R are the die length and radius respectively. The apparent shear rate at the channel wall ($\dot{\gamma}_a$) is defined as:

$$\dot{\gamma}_a = \frac{4Q}{\pi R^3} \qquad \textbf{Equation 3.8}$$

where Q is the volume flow rate.

According to the Rabinowitsch shear rate correction method, the true shear rate at the wall ($\dot{\gamma}_W$) for a power law fluid is given by:

$$\dot{\gamma}_W = \frac{3n+1}{4n}\dot{\gamma}_a \qquad \textbf{Equation 3.9}$$

where n is the power law index. Finally, the true melt shear viscosity can be expressed as:

$$\eta = \frac{\tau_w}{\dot{\gamma}_W} \qquad \textbf{Equation 3.10}$$

For extensional measurements and to simulate the fiber spinning process, use was made of a 2 mm diameter die with a length ratio of 1:10, equipped with a haul-off apparatus. A schematic description of the haul-off apparatus is given in Figure 3.3.

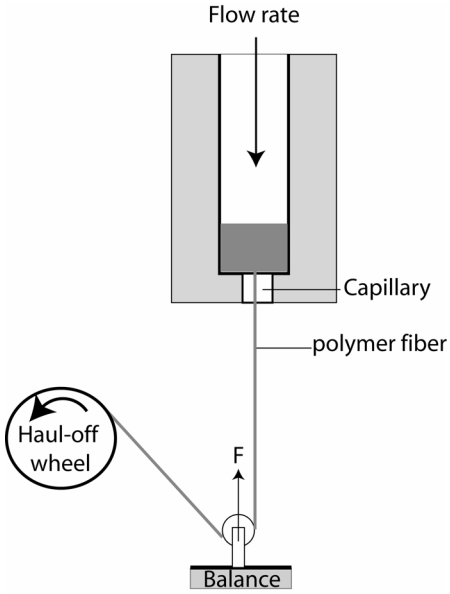

Figure 3.3. Schematic description of the haul-off apparatus.

The Hencky strain, ε_H, the melt stress, σ, and the apparent uniaxial elongational viscosity, μ, were calculated from[7]:

$$\varepsilon_H = \ln \frac{R_0^2}{R_f^2} = \ln \frac{V_f}{V_0} \qquad \textbf{Equation 3.11}$$

and

$$\sigma = \frac{FV_f}{Q} \qquad \textbf{Equation 3.12}$$

$$\mu = \frac{FL_f}{Q} \qquad \textbf{Equation 3.13}$$

respectively, assuming the effects of shear history, extrudate swell, gravity, air drag and surface tension to be negligible, and where F is the tensile force, Q is the flow rate, V_f and R_f are the haul-off wheel velocity and final radius of the filament, and L_f is the fiber length. V_0 and R_0 are the velocity and radius of the filament at the die exit. The piston speed was maintained constant at 2 mm/min and Q was calculated from the filament mass after 10 min of extrusion. V_f was increased continuously from 10 m/min up to about 200 m/min, depending on the formulation. The melt strength σ_{max} was defined as the maximum melt stress. A minimum of 4 measurements were carried out on each material.

3.2.4 Thermo-mechanical characterization

A screw driven UTS tensile testing machine (Testsystem Gmbh) was used to perform tensile tests on dumbbell-shaped specimens produced from the DSM micro-injection molding equipment, on fibers, produced by melt-spinning and on films produced with extrusion-calendering. A three point bending test fixture was also used on the same equipment to performed three-point bending test on fully impregnated GMT parts. For measurements performed above room temperature (50 °C and 90 °C), the whole test fixture was placed into an oven (Noske-Kaeser) set to the desired temperature. Tensile moduli were determined from linear fits to the elastic part of the force-displacement curves.

a. Tensile tests on injection molded specimens

For the ISO 527-2 type 5A dumbbell-shaped injection molded specimens, the UTS was equipped with a 1 KN load cell, and the samples were tested at 8 mm/min.

b. Tensile tests on melt-spun fibers

The load-elongation characteristics of the drawn yarns were investigated using the UTS equipped with a 100 N load cell. The specimen length was 100 mm. The extension rate was chosen to be consistent with DIN 53 834: 2 mm/min up to 5 % elongation, 20 mm/min up to 100 % and 80 mm/min over 100 % with a preload of about 2 – 5 N. Four specimens of each composition were tested. Several types of sample fixture were tested in order to reduce stress concentration at the clamping points as far as possible. One of the methods was to glue the ends of the yarn to be tested between two pieces of sandpaper such that the rough sides of the sandpaper were in contact with the clamp, as shown in Figure 3.4(a). In this particular case, the load-elongation characteristics of the yarns were recorded using a miniature tensile test machine (Minimat 2000, Rheometrics Scientific) with a 1 KN load cell and a yarn gauge length of 10 – 20 mm. The other test fixture was directly adapted to the standard tensile test fixture of UTS apparatus and permitted use of a displacement sensor, which avoided errors due to the finite compliance of the UTS. In this case the fibers were fixed at the end by two screws and passed through two godets. A schematic description of the fiber test fixture is given Figure 3.4(b). The results obtained with the two methods were in good agreement.

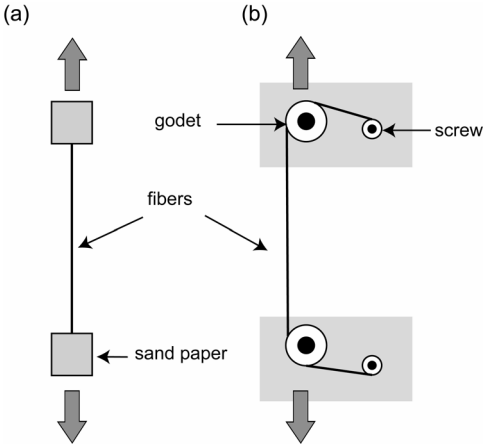

Figure 3.4. Schematic of the test fixture used to perform tensile test on yarns.

c. Tensile tests on films

For notched tensile testing, rectangular coupons of width, *W*, of 40 mm, and an overall specimen length, *H*, of 100 mm and 80 mm were cut from extrusion-calendered specimens in the flow direction and in the transverse direction. The thickness *t* of the specimens was that of the films, i.e. 0.7 mm. Double edge notched tensile (DENT) geometry specimens were prepared from the coupons by razor notching giving ligament lengths, *l*, ranging from 0 mm to 15 mm. The ligament length was measured after testing with the help of a magnifying glass. The tests were performed on the UTS. The cross-head speed was set to 0.2 *H*, following to the ESIS protocol[8].

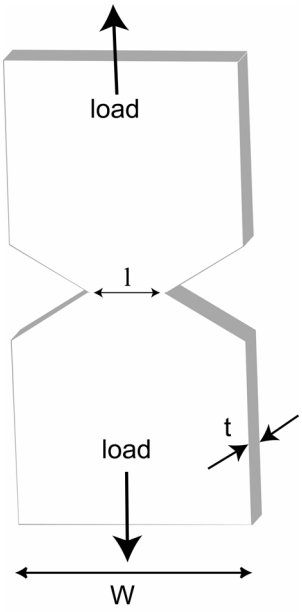

Figure 3.5. DENT specimen for notched tensile testing.

d. Three point bending tests on GMT

Flexural testing was carried out using a three point flexure test set-up equipped with a 1 KN load cell, at room temperature, 50 °C and 90 °C. Specimens with a width of 25 mm and a length of 50 mm were cut from the compression molded plates and a minimum of 6 tests were performed for each specimen type. The span length between the two supportings was 32 mm and the crosshead displacement speed was 2 mm min^{-1}. The test procedure followed The ASTM 790 standard method.

e. Impact tests on GMT

70 × 70 mm^2 rectangle specimens were cut from compression molded plaques and subjected to instrumented falling weight impact (IFWI) using a Rosand IFW 8. The clamped diameter was 40 mm. The speed of the indenter, which was equipped with an instrumented hemispherical tip of diameter 10 mm, was 4 ms^{-1}, and the incident impact energy was 30 J. The experiments were carried out at room temperature and 90 °C. For the high temperature measurements, the samples were placed in a oven set to 90 °C for 15 min and then tested in air immediately. The following data were recorded from IFWI traces:

- at maximum load (F_{peak}): energy (E_{peak}), impact strength = 2.5 F_{peak}/t^2; where t is the specimen thickness.
- at perforation: energy (E_{tot}).

The impact energy was defined as the energy absorbed up to the peak force.

f. Thermo-Mechanical Analysis (TMA)

Thermo-mechanical analysis was carried out on fibers using a Perkin Elmer TMA 7. A 20 mm length of fiber was submitted to a constant force of 50 mN and a temperature ramp of 5 K/min from 25 °C to 260 °C. The deformation was recorded as a function of temperature.

g. Dynamic thermal mechanical analysis (DTMA) on fibers

For DTMA measurements, a fiber and film test fixture was mounted on a Rheometrics RSA II. The temperature was ramped from - 40 °C to 80 °C at a constant rate of about 2 K/min. For fibers, the specimens were about 27 mm in length and the diameter was taken to be equal at 210 μm according to the mean diameter of the filaments and Equation 3.3. The scans were carried out at a frequency of 1 Hz and a strain of 0.2 %. The scans were carried out at a frequency of 10 Hz and a strain of 0.1 %.

3.2.5 Wetting

Wetting expresses how well a polymer melt spreads on a fiber surface. In the context of polymer composites, good wettability is characterized by spontaneous spreading of the polymer onto the fiber surface, minimizing the time and the pressure required for the impregnation of a fiber network. This effect is particularly desirable when using thermoplastic matrices since these require much higher pressures and longer cycle times than thermosets, owing to their high viscosity. Generally, the contact angle of a polymer drop on a fiber gives a good indication of the wetting behavior of a given polymer/fiber system.

The contact angle of iPP2/MMT nanocomposite on glass fibers was measured from axisymmetrical unduloid drops of polymer formed on the glass fibers. The glass fibers used were from Glasseide-Oschatz and hence similar to those used for the co-wound and co-woven composites (section 6.3.1). The technique for forming an unduloid drop on a fiber has been described elsewhere[9], and a typical drop is shown in Figure 3.6. A minimum of 10 drops per polymer were observed by optical microscopy and the critical parameters were measured. The details of the calculation relating the geometry of the drop to the contact angle have been given by Caroll[10, 11]. The method involves measuring the length L and the diameter D of several drops with different dimensions. From these measurements, (D/r) may be plotted against (L/r), where r is the radius of the glass fibers (r = 15 μm - 20 μm), and the curve is fitted with a second order polynomial of the form:

$$\frac{D}{r} = a\left(\frac{L}{r}\right)^2 + b\left(\frac{L}{r}\right) \qquad \textbf{Equation 3.14}$$

where a and b are constant. Finally, the contact angle θ is given by:

$$\theta = 2\arctan(2b) \qquad \textbf{Equation 3.15}$$

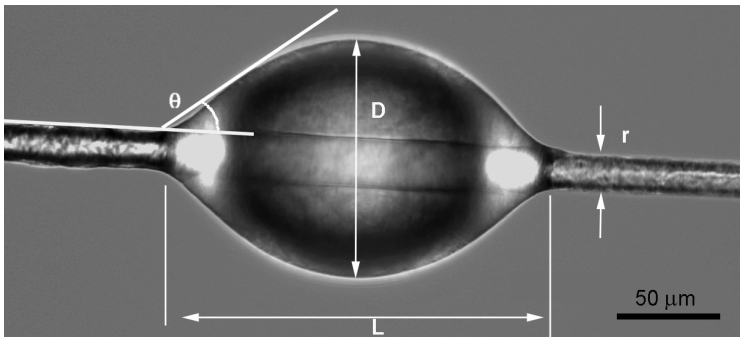

Figure 3.6. Optical microscope picture of an asymmetrical unduloid drop of iPP on a glass fiber.

3.3 MATERIALS

3.3.1 Starting materials

Chapters 4, 6 and 7 of this report are devoted to the characterization and the processing of iPP/MMT-based fibers, films and fiber reinforced composite systems. Therefore this section concentrates on the description of the iPP/MMT nanocomposites. Two grades of iPP were available for this study. These were: (i) a low polydispersity fiber spinning grade from Borealis (HH 450 FB), with a melt flow index of 37 g/10min, and (ii) a film extrusion grade kindly provided by a major GMT producer. In the next sections, these two iPP grades will be referred to as iPP1 (the fiber melt-spinning grade) and iPP2 (the film extrusion grade). The MMT was obtained from two sources. First an alkyl quaternary ammonium modified MMT, Cloisite® 20A, provided by Southern Clay Products. Second, a premixed concentrate (C.44PA Nanomer®), provided by Nanocor. The latter consists of 40 – 50 wt% surface-modified MMT, iPP and a iPP compatibilizer. Two synthetic routes for iPP/MMT nanocomposites were investigated. These are described in the following section.

3.3.2 iPP/MMT nanocomposite preparation

a. Investigation of a masterbatch process

- *Synthesis of iPP1/MMT*

Following Wang *et al.*[12] , organically modified MMT was dispersed in a solvent for iPP and submitted to sonication[13]. In the present work, the synthesis of iPP1/MMT concentrates was carried out using Cloisite 20A and three dispersing solvents: xylene, decahydronapthalin (decalin) and chloroform. The Cloisite 20A was weighed and dissolved in 250 ml of solvent. The solution was then submitted to sonication (Sonopulse) for 15 min. At this stage the solution had a gel-like appearance owing to wetting of the silicate layers by the solvent and possible further intercalation. The solutions were then heated to 100 °C and PPMAH granulates (Fusabond MD 353D, Dupont) were added under stirring together with iPP1 granulates. These were dosed such that the organically modified MMT, Cloisite 20A to iPP1 weight ratio was 0.1 and the PPMAH to Cloisite 20A ratio was 0.02 or 0.5. When polymer granulates were completely dissolved, the temperature was increased to above the boiling temperature of the solvent to allow its evaporation. The obtained slurries were then dried in a vacuum oven at 100 °C. The dried powders were submitted to mechanical shear at 200 °C in a twin-screw micro-extruder (DSM) at 80 rpm for different durations. The resulting samples were characterized by XRD and TEM. Results from this combined solvent and melt-mixing procedure are given below.

- *XRD*

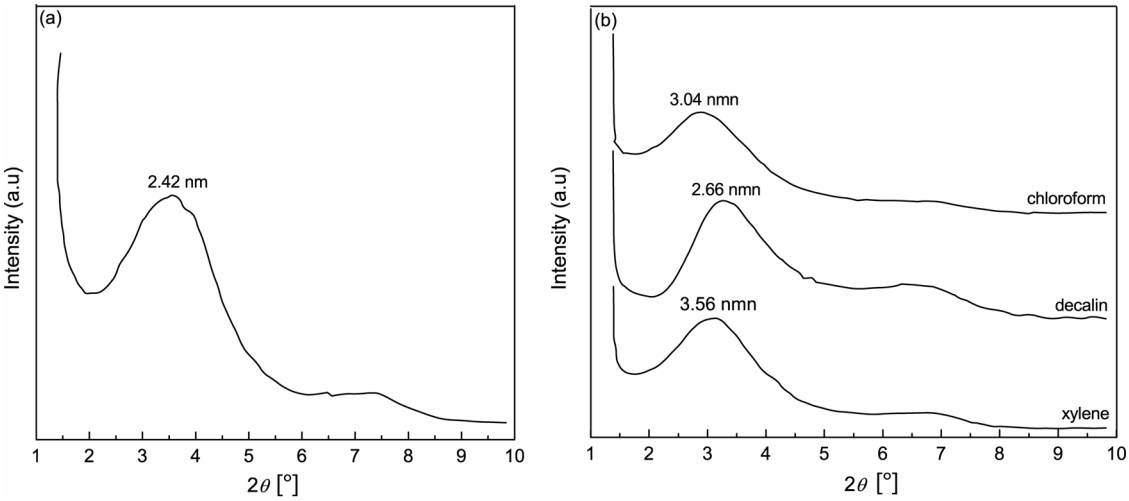

Figure 3.7. (a)XRD diffraction pattern of Cloisite 20A powder. (b) XRD diffraction patterns of iPP1/10 wt% Cloisite 20A prepared by the combined solvent and melt-mixing procedure with 2 wt% of PPMAH.

Cloisite 20A is a natural MMT modified with a quaternary ammonium salt. As observed in the XRD pattern in Figure 3.7(a), the observed interlayer spacing was 2.42 nm. Figure 3.7(b) showed the influence of the solvent on the state of intercalation of the MMT in iPP1/MMT specimens containing 10 wt% of Cloisite 20A after 10 min of melt-mixing in the micro-extruder. The shift of the peaks to the left indicated an increase in the degree of intercalation. Compared with the pure Cloisite 20A powder, the degree of intercalation increased on compounding with iPP1. The intercalation of the polymer chains increased in the order decalin, chloroform, and xylene. The strong dark brown coloration observed in specimens produced by dissolution of iPP1 in decalin suggested partial degradation of iPP1 subsequent to processing. This would explain a lower interlayer spacing compared with specimens produced in chloroform and xylene. It was also found to be difficult to dissolve completely the iPP1 in chloroform even at high temperatures and solvent volumes. This may have contributed to a lower degree of intercalation for this solvent.

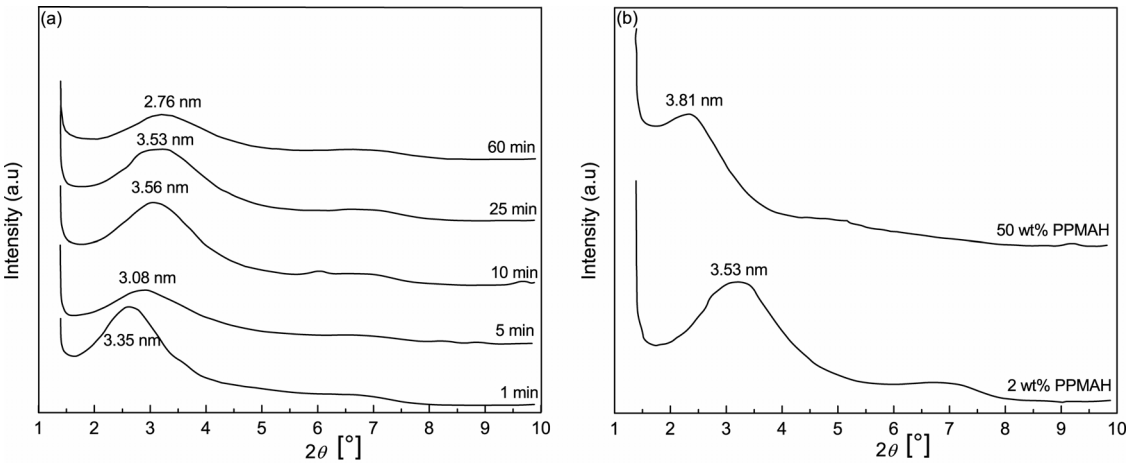

Figure 3.8. XRD diffraction patterns of iPP1/10 wt% Cloisite 20A prepared by the combined solvent and melt-mixing procedure in xylene (a) with different melt-mixing times, and (b) with different concentrations of PPMAH after 25 min of melt-mixing.

The influence of the melt-mixing time on the state of intercalation is shown in Figure 3.8(a) for iPP1/10 wt% Cloisite 20A specimens prepared with xylene. From 1 min to 25 min of melt-mixing a slight increase in the interlayer spacing was observed. Beyond 25 min, a significant decrease of the interlayer spacing was observed, probably resulting from the degradation of the iPP1 due to processing at high temperature beyond a critical time. Thus, melt-mixing only appeared to have a minor influence on the state of intercalation, and the morphology was mainly determined during the solvent phase, indicating the importance of achieving a high level of intercalation at this point in the process. It was therefore suggested to increase the time of sonication or to increase the shear forces in the micro-extruder by reducing the temperature of the melt. Figure 3.8(b) shows the influence of the PPMAH content on the nanocomposites. As expected, the layer spacing was greater at higher PPMAH contents since it is known to interact with silicate layer to a greater extent than iPP, increasing the level of intercalation. However, a balance has to be achieved between the amount of PPMAH added to improve intercalation and its detrimental effect on the mechanical properties of the nanocomposite. Plasticization of the iPP1 and polymer chain scission have both been observed on addition of PPMAH[14].

- *TEM*

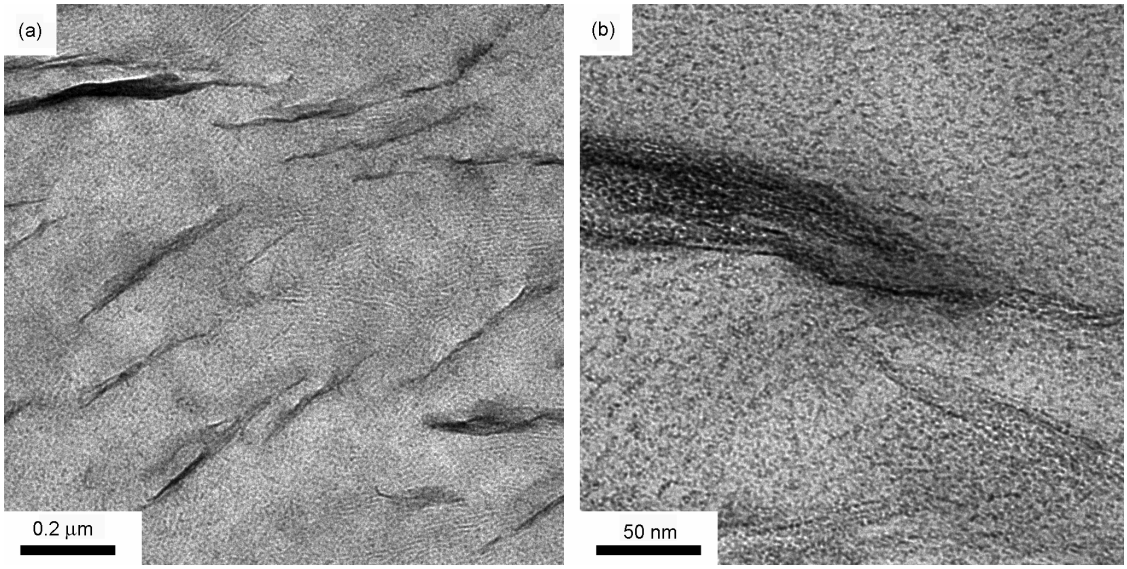

Figure 3.9. (a) and (b)TEM micrographs of iPP1/ 10 wt% Cloisite 20A prepared in xylene, after 10 min of melt-mixing.

Figure 3.9 and Figure 3.10 are TEM images of iPP1/10 wt% Cloisite 20A prepared in xylene, after 10 min of melt-mixing, and Figure 3.11 and Figure 3.12 are images of iPP1/10 wt% Cloisite 20A prepared in decalin, under the same processing conditions. In both cases, the dispersion of the clay was homogeneous (Figure 3.9(a) and Figure 3.11 (a)) and intercalated clay stacks were observed throughout (Figure 3.9(b) and Figure 3.11 (b). In the case of specimen prepared in xylene, Figure 3.9(a), Cloisite 20A, particles had a mean aspect ratio of about 20. However, large particles (Figure 3.10) were also visible in the micrographs indicating a certain level of dispersion in the size of the stacks. When a large particle was observed at higher magnification, single silicate layers were visible, showing the extent of the intercalation directly.

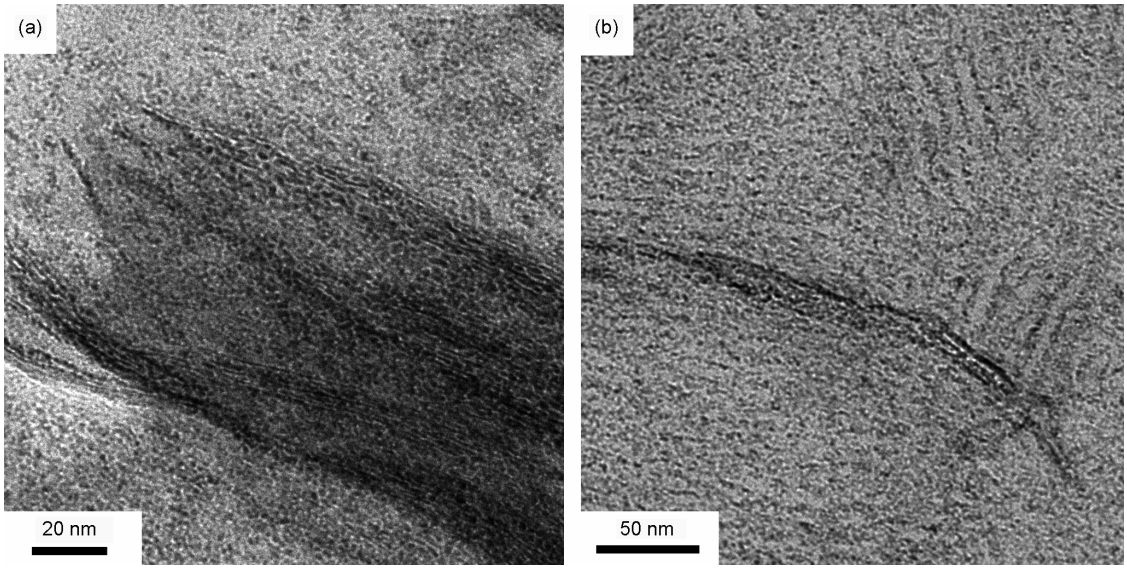

Figure 3.10. (a) and (b)TEM micrographs of iPP1/10 wt% Cloisite 20A prepared in xylene, after 10 min of melt-mixing.

Simirlarly, in the case of specimens prepared with decalin, large (Figure 3.12(a)) and thinner (Figure 3.12(b)) particles were visible, and the dispersion in the particle size was relatively large compared with specimens prepared in xylene. Thus it appeared that in the case of a combined solvent and melt-mixing procedure, the morphology was directly dependent on the solvent.

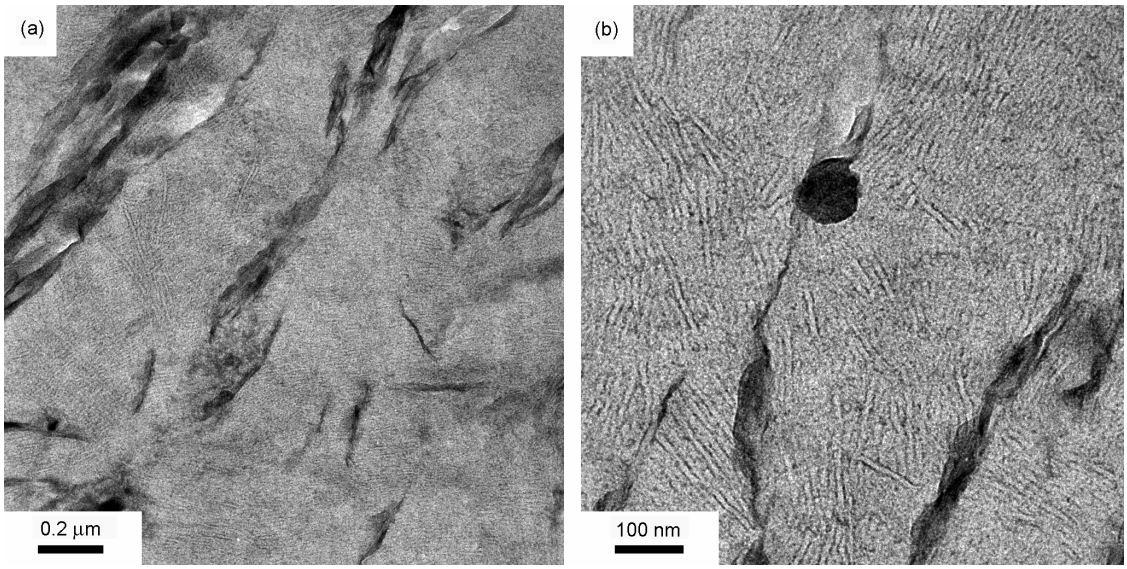

Figure 3.11. (a) and (b)TEM micrographs of iPP1/ 10 wt% Cloisite 20A prepared in decalin, after 10 min of melt-mixing.

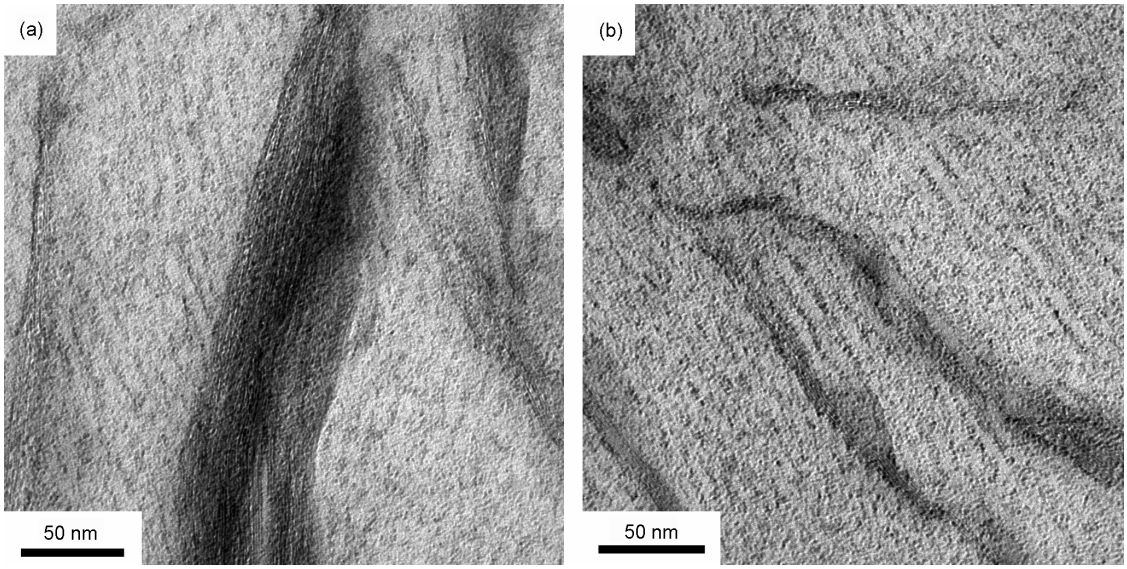

Figure 3.12. (a) and (b)TEM micrographs of iPP1/10 wt% Cloisite 20A prepared in decalin, after 10 min of melt-mixing.

The combined solvent and melt-mixing procedure allowed homogenous iPP1/Cloisite 20A nanocomposites to be prepared into a well intercalated structure with an interlayer spacing up to 57 % greater than the as-received powder. However, from a commercial point of view, this method has the disadvantage of requiring organic solvents, which is not viable economically. However, it provides for a useful comparison with the commercial masterbatches.

b. Direct melt-mixing from a masterbatch precursor

- *Synthesis of iPP1/MMT*

Melt-mixing is a standard method for preparing iPP/MMT nanocomposites. Its major advantages are the absence of solvent and its compatibility with current industrial processes such as extrusion and injection moulding. In the present work, iPP1/MMT formulations (1 wt%, 2.4 wt%, 3.4 wt%, 5.9 wt% and 13.5 wt%) were prepared using iPP1 granulates and Nanocor concentrate. The different concentrations were calculated according to the manufacturer's recommendations. However, pyrolysis of compounded granulates suggested that the effective MMT content was about half the nominal content. This difference is attributed to the presence of organic cations in the modified MMT.

- *FTIR*

A preliminary study was carried out with the objective of characterizing the different components of the Nanocor concentrates. It was of particular interest to verify the presence of compatibilizers in the compound (PPMAH for example). Indeed, as seen in the previous section, PPMAH may have a significant effect on the state of intercalation of

MMT, and may degrade mechanical properties in the final iPP1/MMT nanocomposite. Therefore, fourier transform infrared (FTIR) spectra of compression molding sheets of iPP1/MMT and Nanocor concentrates were recorded using a Perkin-Elmer 580B spectrometer from 4000 to 400 cm^{-1}.

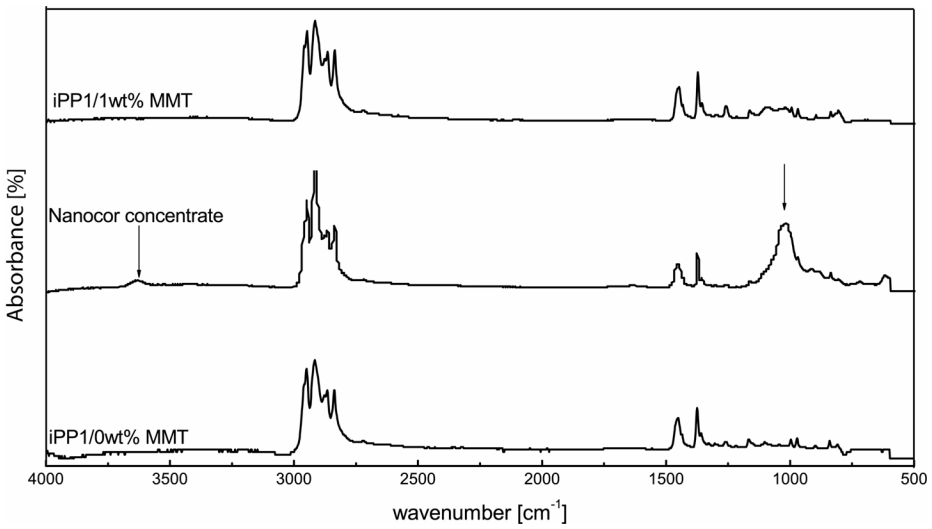

Figure 3.13. FTIR spectra of pure iPP1, Nanocor concentrate and iPP1/1 wt% MMT nanocomposite (4000 cm^{-1} to 400 cm^{-1}). Black arrows indicate specific –OH absorption peak at 3630 cm^{-1} and Si-O absorption peak at 1050 cm^{-1}.

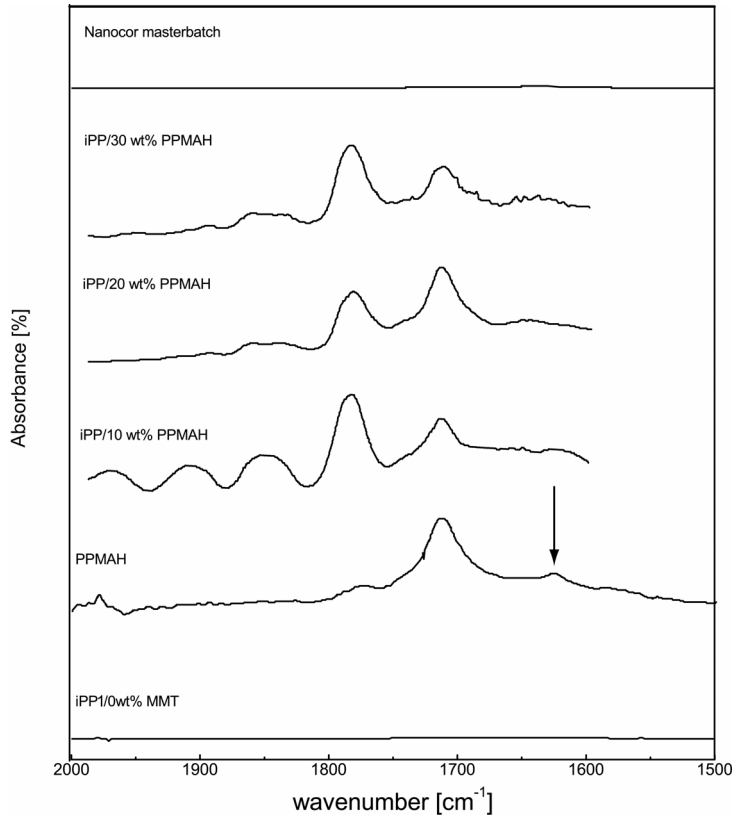

Figure 3.14. FTIR spectra of pure iPP1, PPMAH, and different compositions of iPP/MD 353 D (2000 cm^{-1} to 1500 cm^{-1}).

Figure 3.13 compares the FTIR spectra of the pure iPP1 with those of Nanocor concentrate and iPP1/1 wt% MMT. According to Yoon *et al.*[15], the absorptions at 3630 and 1050 cm^{-1} in the Nanocor concentrate spectrum, indicated by the arrows, are associated with -OH stretching of the lattice and Si-O stretching of MMT respectively. The latter absorption bands were not detected in the case of iPP1/1 wt% MMT due to the small amount of MMT in the nanocomposite. In Figure 3.14, pure iPP1, PPMAH, and different compositions of iPP1/PPMAH are compared between 2000 cm^{-1} and 1500 cm^{-1}. An absorption band at 1750 cm^{-1} corresponding to the C=O stretching was expected in specimens containing detectable amounts of PPMAH. This absorption band is clearly visible in Figure 3.14 in the spectrum of PPMAH, and in the iPP/PPMAH compounds. This characteristic PPMAH band was absent from the pure iPP1 spectrum, as expected, but also from the Nanocor concentrate spectrum. It was therefore not possible to conclude anything further about the nature of the compatibilizer. The presence of PPMAH cannot be excluded, but in too a low concentration to be detectable by FTIR.

- *XRD*

XRD of the compression molded sheets from the masterbatch and compounded iPP1/3.4 wt% MMT, Figure 3.15, showed clear reflections corresponding to the regular stacking

of the individual MMT platelets within the particles. Compression molded sheets from the compounded iPP1/3.4 wt% MMT showed a basal spacing of 3.17 nm, for example, i.e. a slight increase with respect to the value of 2.98 nm observed in the iPP1/MMT concentrate before compounding, indicating some additional intercalation.

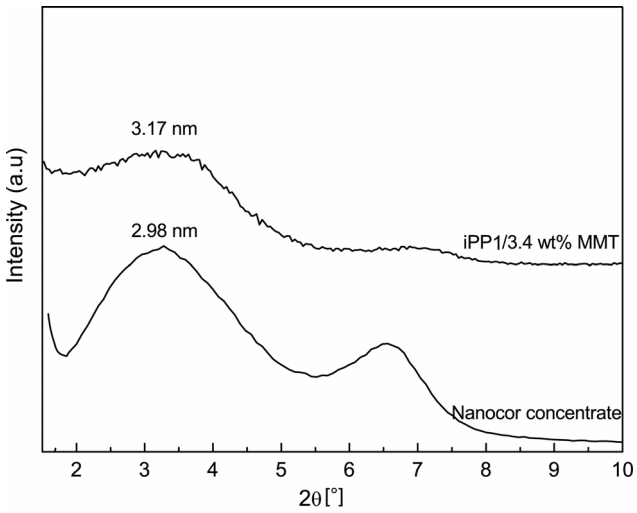

Figure 3.15. XRD patterns of the Nanocor concentrate and iPP1/3.4 wt% MMT prepared by melt-mixing.

- *TEM*

Figure 3.16, Figure 3.17, Figure 3.18 and Figure 3.19 are representative TEM micrographs of compounded iPP1/3.4 wt% MMT, iPP1/5.9 wt% MMT and iPP1/13.5 wt% MMT respectively, showing well dispersed MMT particles typical of an intercalated-exfoliated nanocomposite microstructure. The sections through the particles were roughly oval, and globally oriented in the extrusion direction, although the orientation remained partial. The particules aspect ratio was estimated to 20 – 50 for melt-mixing iPP1/MMT formulations, independently of the MMT content in the range considered.

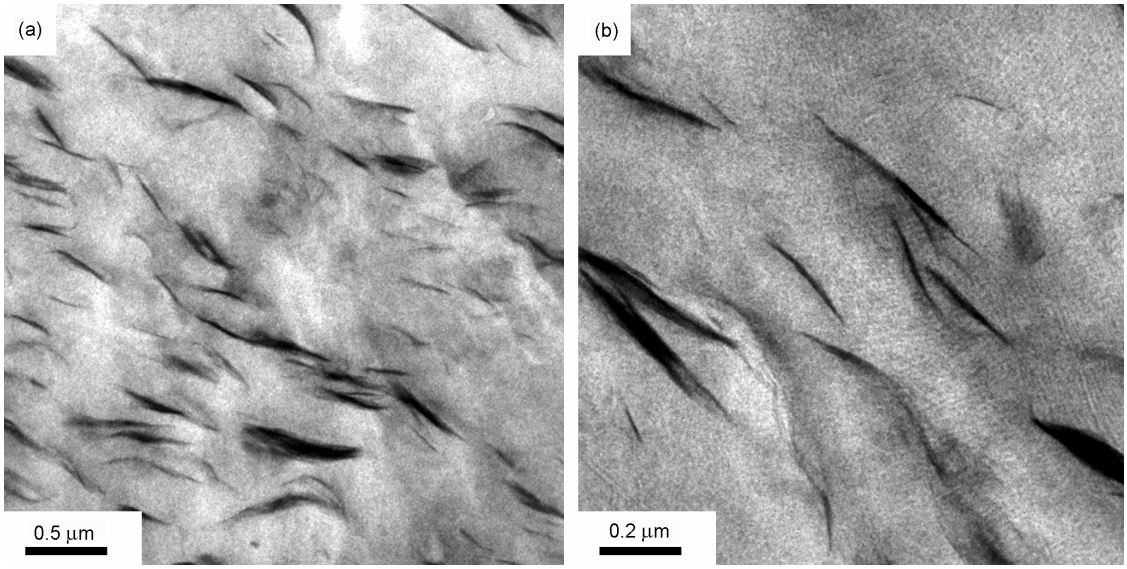

Figure 3.16. (a) and (b) TEM micrographs of compounded iPP1/3.4 wt% MMT nanocomposite granulates.

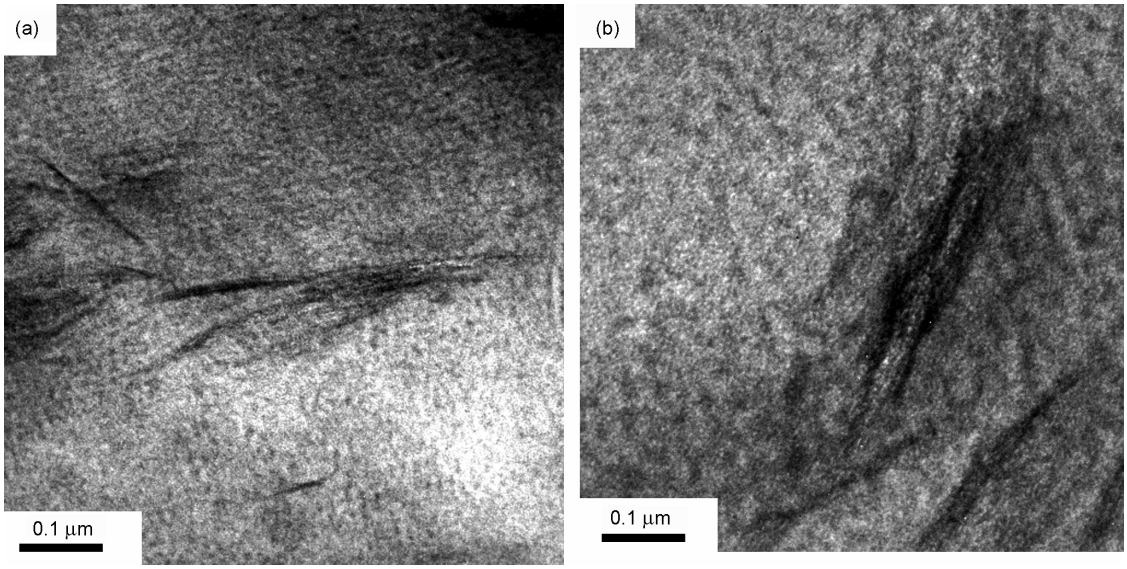

Figure 3.17. (a) and (b) TEM micrographs of compounded iPP1/3.4 wt% MMT nanocomposite granulates.

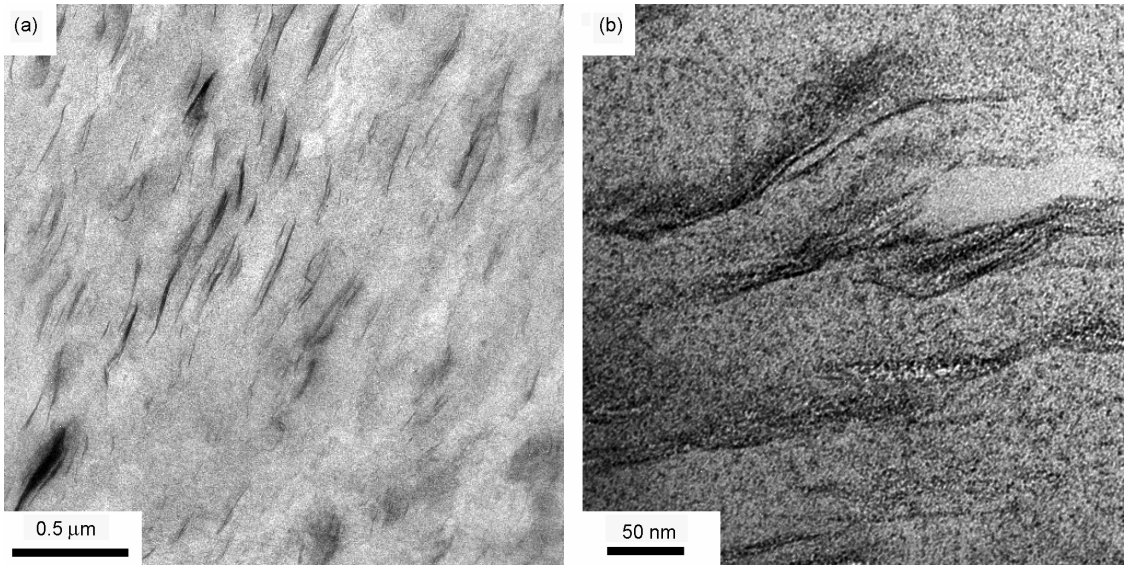

Figure 3.18. (a) and (b) TEM micrographs of compounded iPP1/5.9 wt% MMT nanocomposite granulates.

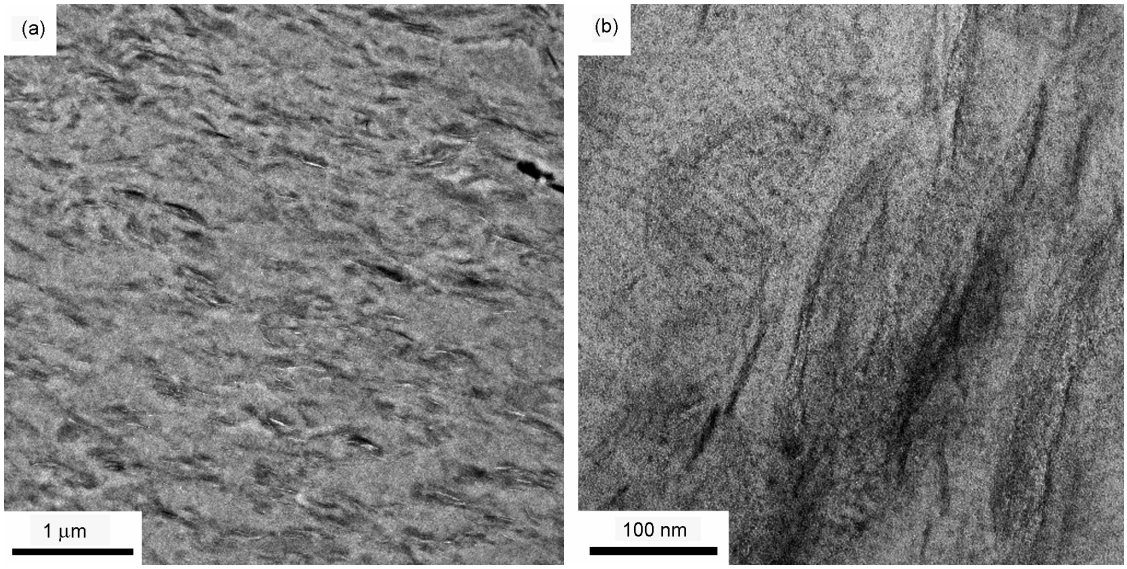

Figure 3.19. (a) and (b) TEM micrographs of compounded iPP1/13.5 wt% MMT nanocomposite granulates.

3.3.3 Rheological characterization of melt-compounded fiber grade iPP/MMT

The viscoelastic nature of a material is an important parameter in many industrial processing routes, including extrusion, injection moulding, blow moulding, thermoforming and fiber spinning. Generally, the appropriate range of deformation or stress must be used in obtaining relevant parameters for a given process[16]. The purpose of the present rheological measurements was twofold. First, rheological properties are indicative of the melt behaviour and hence processability, and second, they are sensitive to particle size, shape, surface characterization and therefore potentially offer a means to assess the state of dispersion of nanocomposites directly in the melt state, and to understand the structure-property relationships in these materials. Understanding the effects of particle loading on the structure of the iPP1/MMT nanocomposites was of particular interest.

Dynamic strain sweeps were first conducted to determine the extent of the linear viscoelastic regime. Figure 3.20 shows the strain dependence of the normalized storage modulus for iPP1/5.9 wt% MMT and pure iPP1. The behavior was sensitive to the presence of MMT. Deviation from linear behavior in the nanocomposite occured at strains approximately 2 orders of magnitude less than for pure iPP1. Therefore, the dynamic shear measurements were performed at a shear strain of 0.5 %.

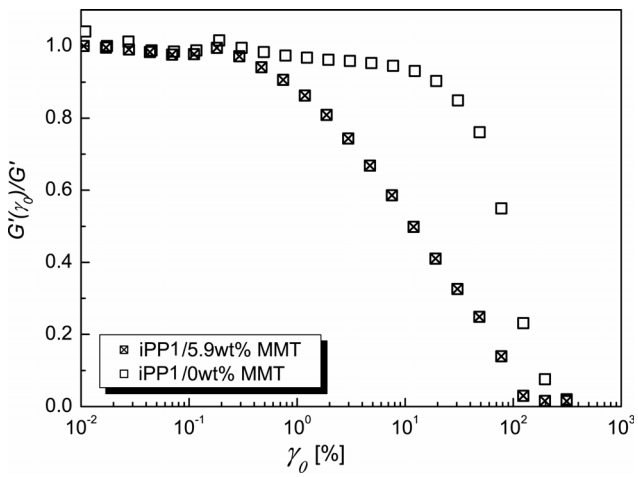

Figure 3.20. Dynamic strain sweep at 180 °C of pure iPP1 and iPP1/5.9 wt% MMT performed at a frequency of 100 rad/s.

Figure 3.21(a) and (b) show the effect of MMT content on the storage modulus *G'* and the loss *G''* modulus in dynamic shear measurements on compression molded specimens prepared from the melt compounded iPP1/MMT nanocomposites as described in section 3.3.2(b). As has been extensively reported elsewhere for similar materials [17-19], addition of MMT resulted in increasingly non-terminal behavior within the accessible range of angular frequencies, ω, i.e. a transition from the $G' \sim \omega^2$ and $G'' \sim \omega$, scaling shown by

the unmodified iPP1 at low ω [20], to solid-like behavior, with an apparently finite limiting value of *G'* and *G''* as $\omega \rightarrow 0$. Thus, the apparent dynamic shear viscosity at low ω increased strongly with the MMT content. Frequency-temperature superposition was nevertheless found to remain possible for concentrations of up to about 3.4 wt% and the flow activation energies, showed in Table 3.3, determined by assuming an Arrhenius temperature dependence for the shift factors (Figure 3.22) were found to be close to that of the pure iPP1[17, 21]. The influence of the MMT was also most marked at low rates in steady-state shear tests. As shown in Figure 3.23(a), η increased by approximately an order of magnitude on addition of 2.4 wt% MMT. At high effective shear rates, on the other hand, the matrix dominated the response in both types of measurement, although there was considerable non-systematic scatter in the steady state data. Tests using the capillary rheometer, for which results are given in Figure 3.23(b), nevertheless confirmed the MMT to have relatively little effect on η at shear rates above about 100 s^{-1}.

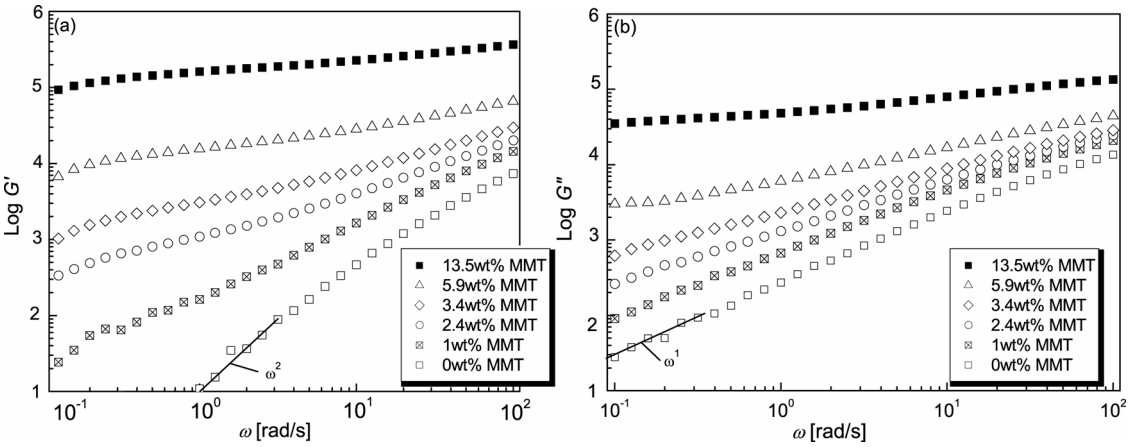

Figure 3.21. (a) *G'* vs ω and (b) *G'* vs ω at 220 °C in iPP1/MMT nanocomposites for different MMT contents.

Table 3.3. Flow activation energies determined from time-temperature superposition of *G'* vs ω data at 180 °C, 220 °C and 240 °C.

Materials	E_0 [KJ/mol]
iPP1/0 wt% MMT	39.2 ± 1.6
iPP1/1 wt% MMT	41.1 ± 5.4
iPP1/3.4 wt% MMT	35.5 ± 3.7

The melt response of the iPP1/MMT might be attributed to increasing physical contacts between the individual MMT particles as their concentration increases, which result in a weak agglomerated network of multi-platelet particulate domains that can break down on shear, with subsequent orientation and possibly deformation of the individual domains during flow[20]. This is typical behavior for systems filled with clay in the non-Newtonian

region[22] but may not occur in other nanocomposite systems[23]. Network formation may take place at very low MMT volume fractions if the aspect ratio of the MMT particles is sufficiently large, and the strong dependence of the linear viscoelastic data on MMT content at low flow rates may be a consequence of the percolation of inter-particle contacts above some critical threshold as opposed to confinement of polymer chains[24]. On the other hand, for a weak network, the shear stresses tend to be dominated by the viscous response of the matrix at high flow rates, consistent with the observed behavior. Moreover, if the formation of the MMT network is assumed to be essentially due to frictional interactions between the MMT particles, it follows that the flow activation energy should be dominated by the matrix, again consistent with the observed behavior. The non-terminal dynamic behavior also implies a transition to yielding-type behavior, i.e. a high viscosity at low stresses with a sharp decrease over a narrow range of stresses.

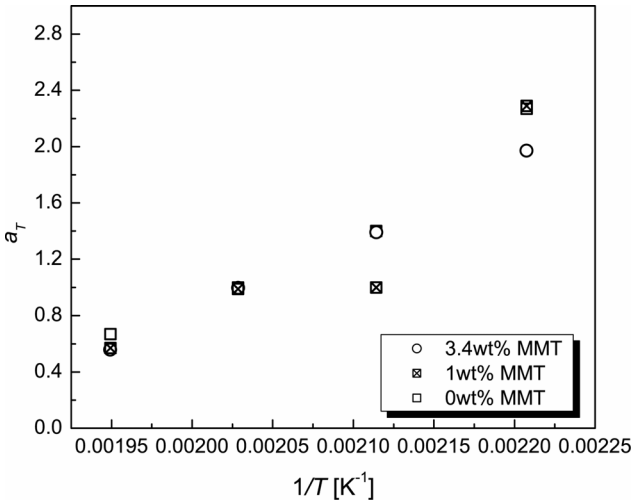

Figure 3.22. Shift factors determined from time-temperature superposition of *G'* vs *ω* data at 180 °C, 220 °C and 240 °C.

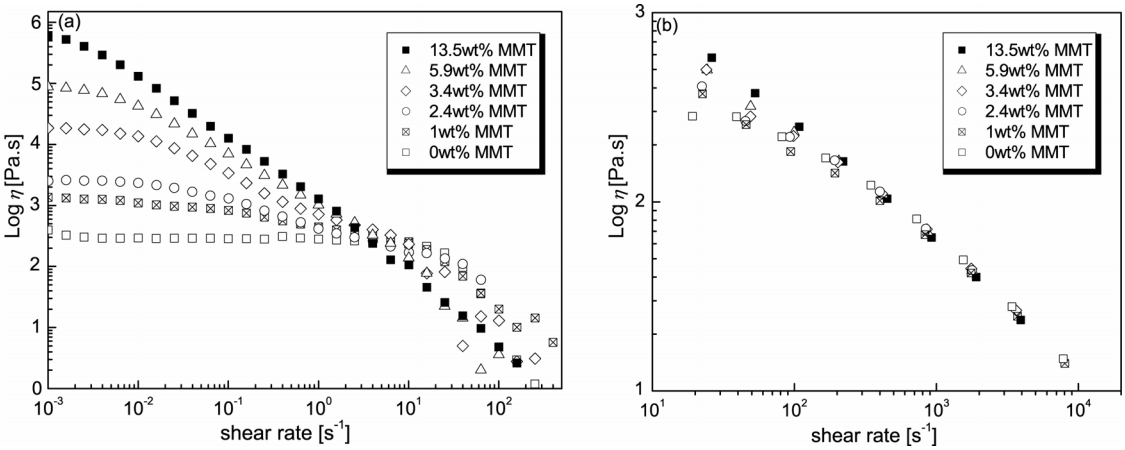

Figure 3.23. η vs. shear rate in iPP1/MMT nanocomposites measured at 220 °C for different MMT contents in (a) cone-plate geometry and (b) capillary rheometer.

As pointed out by Solomon *et al.*[19], rheological measurements allow indirect probing of the melt-state structure of iPP1/MMT. The particulate domains of ordered platelet stacks are non-Brownian and anisotropic; they reconstitute the network after cessation of the flow[19]. The nonterminal dynamic behaviour is consistent with a yielding process in which the viscosity is high at low stresses and undergoes a sharp drop over a narrow range of stresses as observed here. Indeed, the alignment of the silicate layers along the flow direction causes the material to flow to an increasingly greater extent. The yield stress of the materials was determined by fitting the low shear rate data to Casson's equation[25, 26]:

$$\sigma^{1/2} = \sigma_0^{1/2} + \beta\dot{\gamma}^{1/2} \qquad \textbf{Equation 3.16}$$

where σ is the steady state shear stress, $\dot{\gamma}$ the shear rate, σ_0 is the yield stress and β is an arbitrary constant. The results are shown in Figure 3.24, where the dependence of σ_0 on MMT loading above 4 wt% MMT is apparent. The yield stress determined in this way was typically of the order of 10 – 500 Pa even up to much higher MMT contents.

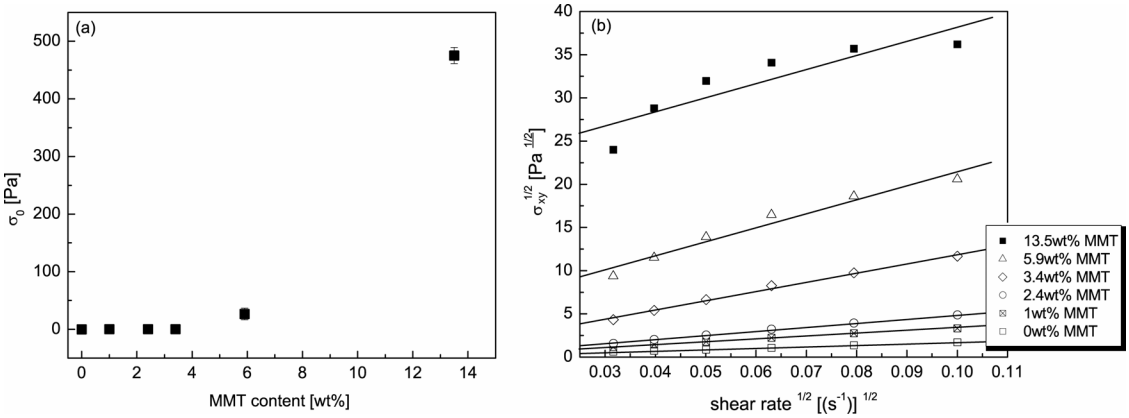

Figure 3.24. (a) Concentration dependence of the yield stress σ_0, determined by application of Equation 3.14 to the low shear rate steady data as shown in (b).

These two specific rheological characteristics of the nanocomposites i.e. non terminal behavior and yielding, have been observed for microscopic filled systems. The difference between nanocomposites and these latter is that they require typically 20 - 50 wt% filler for these effects to be observable[27], whereas iPP1/MMT nanocomposites showed a solid-like behavior at much lower loadings.

3.3.4 Rheological characterization of film grade iPP/MMT

Rheological characterization of iPP2/MMT was performed on melt-compounded specimens prepared following the procedure described in section 3.3.2(b). Figure 3.25(a) and (b) show the effect of MMT content on *G'* and on *G"* in dynamic shear measurements in the linear elastic range of iPP2/MMT. As discussed in section 3.3.3, for iPP1/MMT, addition of MMT resulted in a transition from $G' \sim \omega^2$ and $G'' \sim \omega$, shown by the unmodified iPP2 at low ω, to solid-like behavior as $\omega \rightarrow 0$ characterized by finite limiting values of *G'* and *G"*. This was also reflected by the steady shear viscosity measurements shown in Figure 3.26. Between 10^{-3} s^{-1} and 10^{3} s^{-1}, the iPP2 melt was Newtonian. With increasing MMT content, however, the melts began to show shear thinning behavior at moderate to high ω.

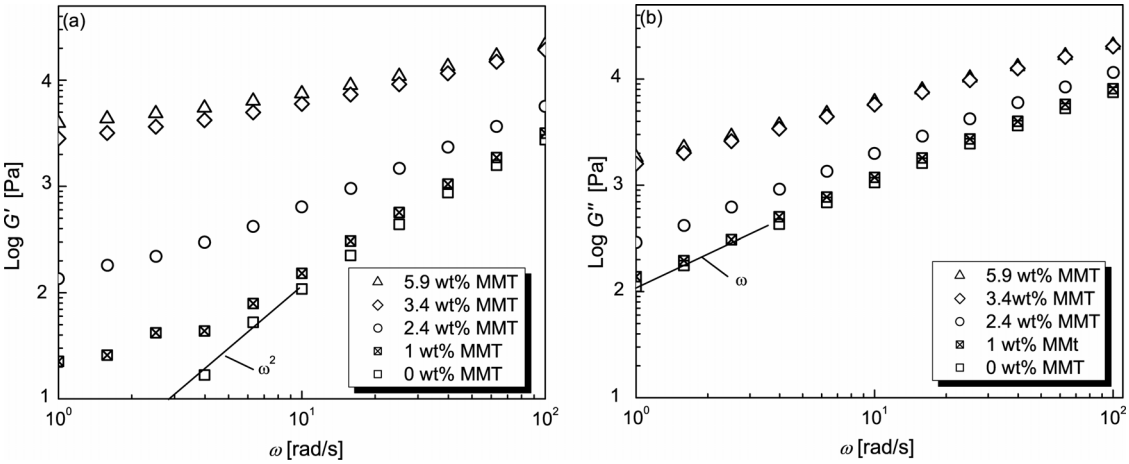

Figure 3.25. (a) *G'* vs ω and (b) *G"* vs ω at 200 °C in iPP2/MMT nanocomposites for different MMT contents.

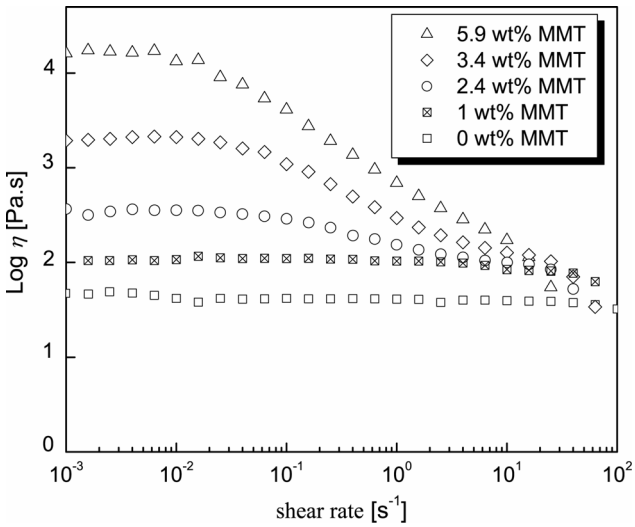

Figure 3.26. η vs shear rate in iPP2/MMT nanocomposites measured at 200 °C in the cone-plate geometry for different MMT contents.

3.4 CONCLUSION

Two preparation routes for iPP1/MMT nanocomposites were investigated. Both methods resulted in mixed intercaled-exfoliated morphologies with well-dispersed MMT stacks, as shown by XRD and TEM. The combined solvent and melt-mixing procedure provided better results in terms of intercalation degree compared with the simple melt-mixing from the masterbatch precursor. The final morphologies of the nanocomposites were found to be dependent on the intercalation level achieved in the solvent phase and increasing the

melt-mixing shear force and time marginally improved the intercalation level. However, combined solvent and melt-mixing was not convenient for large production scale due to the large amount of solvent involved, the number of processing steps and the significant process time. Therefore, direct melt-mixing was used to prepare iPP1/MMT and iPP2/MMT precursors for composite processing.

The rheological characterization of iPP1/MMT and iPP2/MMT revealed behaviour typical of filled thermoplastics i.e. a non-terminal behaviour with increasing MMT concentration and shear-thinning with increasing shear rate. Moreover, this rheological response was achieved at much lower MMT loadings than for microfillers.

3.5 REFERENCES

1 D. R. Salem, **Structure formation in polymeric fibers**, Hanser, Munich, (2001)

2 B. V. Gupta and K. V. Kothari, **Manufactured fibre technology**, Chapman & Hall, London, (1997)

3 G. P. Meshcheryakova and K. E. Perepelkin, **Compararative analysis of methods of measuring fibre and filamnet diameters**, *Fibre chemistry*, 2001; **33** (6): 509-516

4 J. Vlachopoulos and D. Strutt, **Polymer processing**, *Materials Science And Technology*, 2003; **19** (9): 1161-1169

5 S. S. Ray and M. Okamoto, **Polymer/layered silicate nanocomposites: a review from preparation to processing**, *Progress in Polymer Science*, 2003; **28** (11): 1539-1641

6 M. N. Huda, H. Dragaun, S. Bauer, H. Muschik and P. Skalicky, **A Study Of The Crystallinity Index Of Polypropylene Fibers**, *Colloid And Polymer Science*, 1985; **263** (9): 730-737

7 C. W. Macosko, **Rheology principles, measurements, and applications**, VCH, New York etc., (1994)

8 D. R. Moore, **Fracture mechanics testing methods for polymers, adhesives and composites**, Elsevie, Amsterdam, (2001)

9 N. Bernet, **Commingled yarn composites for rapid processing of complex shapes**, Thesis, EPFL, Lausanne, (2000)

10 B. J. Carroll, **Accurate Measurement of Contact-Angle, Phase Contact Areas, Drop Volume, And Laplace Excess Pressure In Drop-On-Fiber Systems**, *Journal Of Colloid And Interface Science*, 1976; **57** (3): 488-495

11 B. J. Carroll, **Deposition of Liquid-Drops on A Long Cylindrical Fiber**, *Textile Research Journal*, 1988; **58** (9): 495-500

12 Y. Zhong and S.-Q. Wang, **Exfoliation and yield behavior in nanodispersions of organically modified montmorillote clay**, *Journal of Rheology*, 2003; **47** (2): 483-494

13 E. C. Lee, D. F. Mielewski and R. J. Baird, **Exfoliation and dispersion enhancement in polypropylene nanocomposites by in-situ melt phase ultrasoniaction**, *Polymer Engineering and Science*, 2004; **44** (9): 1773-1781

14 Y. Fan, J. Lou and D. M. Shinozaki, **Microstructure dependent properties of polypropylene-clay nanocomposites**, *Journal of Applied Polymer Science*, 2007; **103** (1): 204-210

15 M. J. Chung, L. W. Jang, J. H. Shim and J. S. Yoon, **Preparation and characterization of maleic anhydride-g-polypropylene/diamine-modified clay nanocomposites**, *Journal Of Applied Polymer Science*, 2005; **95** (2): 307-311

16 M. Gahleitner, **Melt rheology of polyolefins**, *Progress in Polymer science*, 2001; **26** 895-944

17 G. Galgali, C. Ramesh and A. Lele, **A rheological study on the kinetics of hybrid formation in polypropylene nanocomposites**, *Macromolecules*, 2001; **34** (4): 852-858

18 S. Y. Gu, J. Ren and Q. F. Wang, **Rheology of poly(propylene)/clay nanocomposites**, *Journal Of Applied Polymer Science*, 2004; **91** (4): 2427-2434

19 M. J. Solomon, A. S. Almusallam, K. F. Seefeldt, A. Somwangthanaroj and P. Varadan, **Rheology of polypropylene/clay hybrid materials**, *Macromolecules*, 2001; **34** (6): 1864-1872

20 R. Krishnamoorti and K. Yurekli, **Rheology of polymer layered silicate nanocomposites**, *Current Opinion In Colloid & Interface Science*, 2001; **6** (5-6): 464-470

21 M. Fujiyama and H. Inata, **Rheological properties of metallocene isotactic polypropylenes**, *Journal of Applied Polymer Science*, 2002; **84** 2157-2170

22 F. P. La Mantia, S. Lo Verso and N. T. Dintcheva, **EVA copolymer based nanocomposites**, *Macromolecular Materials and Engineering*, 2002; **287** 909-914

23 J.-Z. Liang, **Melt rheology of nanometer-calcium-carbonate-filled acrylonitrile-butadiene-styrene (ABS) copolymer composites during capillary extrusion**, *Polymer International*, 2002; **51** 1473-1478

24 J. Bicerano, J. F. Douglas and D. A. Brune, **Model for the viscosity of particle dispersions**, *Rev. Macromol. chem. phys.*, 1999; **C39** (4): 561-642

25 J. X. Ren and R. Krishnamoorti, **Nonlinear viscoelastic properties of layered-silicate-based**

intercalated nanocomposites, *Macromolecules*, 2003; **36** (12): 4443-4451
26 M. A. Treece and J. P. Oberhauser, **Processing of polypropylene-clay nanocomposites: Single-screw extrusion with in-line supercritical carbon dioxide feed versus twin-screw extrusion**, *Journal of Applied Polymer Science*, 2007; **103** (2): 884-892
27 Y. Wang and J. J. Wang, **Shear yield behavior of calcium carbonate-filled polypropylene**, *Polymer Engineering And Science*, 1999; **39** (1): 190-198

CHAPTER 4

MELT-SPUN iPP/MMT FILAMENTS

4.1 INTRODUCTION AND OBJECTIVES

Industrial polymer fibers are characterized by an extremely high length to thickness ratio and outstanding flexibility. They are produced as continuous filaments, which may subsequently be cut into shorter lengths. They may be classified as natural or manufactured fibers. The present work is directed towards manufactured fibers and particularly towards fibers produced from synthetic polymers, as opposed to fibers produced from inorganic materials. Synthetic fibers are mostly made from polyamides, polyesters, polyacrylonitrile, polyolefins, polyurethane and polyvinyl alcohol[1]. They are widely used for producing household textiles, but they are also used in diverse applications such as filters, protective clothing or reinforcement for tyres, rubber goods and composites. Two principal routes are used to convert fiber-forming polymers into filaments. These are (i) melt spinning, described in section 3.1 of this document, and (ii) solution spinning, which involves the extrusion of a solution to form the fibers. In both cases, after the spinning process, the fibers are generally subjecting to drawing followed by heat-setting to increase their dimensional stability.

The primary aim of the work describes in this chapter has been to produce melt spun iPP1 and iPP1/MMT filaments for use in hybrid yarns. A further aim is to understand the influence of the melt spinning process on the morphology of the nanocomposites and the resulting physical properties. During melt spinning and subsequent drawing operations, the polymer is subjected to high shear forces that tend to align the polymer chains along the filament axis. This raises the question of the influence of these forces on the intercalation and dispersion of the MMT platelets.The limitations and constraints on the melt spinning of iPP1/MMT filaments compared with pure iPP1 have been studied in order to assess the extent to which iPP1/MMT can be produced on an industrial level. Attention is given to how the MMT platelets influence the physical properties of the filaments, depending on their morphology and concentration, in order to understand the characteristics of the final hybrid composite part. To summarize, the objectives of this chapter are to compare neat iPP1 with iPP1/MMT filaments from the points of view of: (i) ease of processing and (ii) physical properties.

4.2 PROCESSING OF iPP/MMT FILAMENTS

4.2.1 Introduction to spinnability criteria

In this section, different criteria that affect the spinnability of polymer melts are defined and discussed in the context of iPP1/MMT nanocomposites. They are divided into two categories:

- Mechanisms of filament breakage; these depend on processing parameters and melt viscosity and include:
  - Cohesive brittle fracture
  - Capillary waves
- Flow instabilities; these cause non-uniformity in the filament diameter:
  - Die swell
  - Melt fracture
  - Draw resonnance

A fluid is spinnable under a given set of deformation conditions if steady-state, continuous elongation of the fluid jet proceeds without rupture of any kind[2]. Thus, a lack of spinnability is usually manifested by filament breakage, and the maximum elongation of the fluid thread is a measure of spinnability. Two principal physical mechanisms control the breakage of the fluid threads. These are (i) cohesive, brittle fracture, and (ii) capillary waves. A schematic description of these two failure mechanisms is given Figure 4.1.

Cohesive brittle fracture occurs when the tensile stress in the jet exceeds a critical value (the tensile strength). In this case, the elasticity of the fluid plays a determinant role. Whereas an ideally viscous fluid would deform to an infinite extent, the deformation energy being dissipated instantaneously, a viscoelastic polymer melt stores part of this energy. When the stored energy reaches a critical value, depending on the deformation rate and the relaxational characteristics of the polymer melt, cohesive, brittle fracture occurs. The probability of failure is reduced when the relaxation of the stored energy is rapid[3]. A similar failure mode has been identified by Ide and White[4], called ductile failure. The latter mode of failure is due to the growth of a neck generated in the filament by high local stresses.

Capillary waves are associated with the viscosity and the surface tension of the fluid. They correspond to the growth of distortions of the jet surface that lead to the formation of droplets.

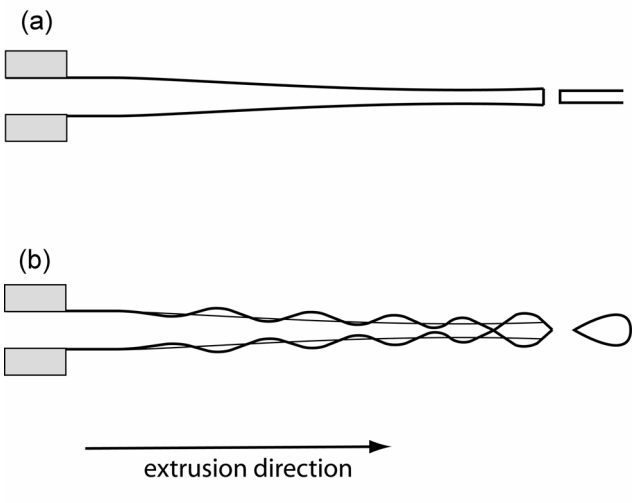

Figure 4.1. Schematic description of (a) cohesive fracture and (b) capillary break-up failure mechanisms.

To obtain a qualitative idea of how the spinnability i.e. the maximum filament length is affected by these two modes of fracture, it is useful to consider the ideal case of a linear viscoelastic polymer subjected to a steady–state, isothermal stress distribution during melt spinning. Ziabicki[2] has shown that if only the cohesive fracture mode is considered, the maximum filament length increases linearly with the product $V_0\eta$, where V_0 is the extrusion velocity and η is the melt viscosity. For the same conditions, he has also shown that for the capillary wave failure mode, the dependence is more complex and that the maximum filament length increases monotonically with η, and decreases with the surface tension of the liquid.

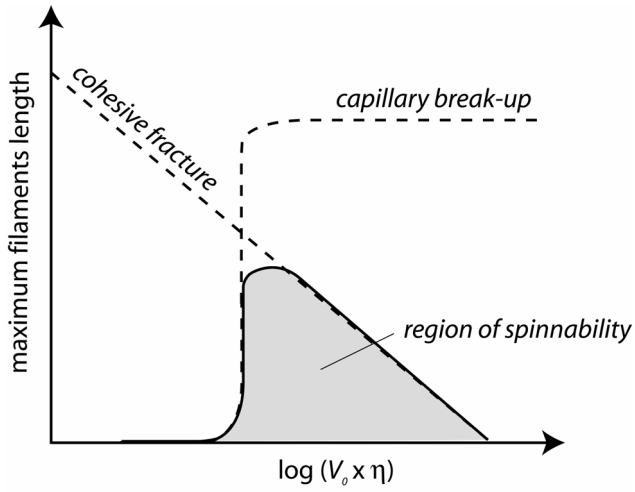

Figure 4.2. Maximum filament length predicted for the capillary break and cohesive fracture mechanisms.

In practice, neither isothermal nor steady state conditions are encountered in the melt spinning process. Moreover, the variation of the maximum filament length in the cohesive and capillary wave failure mode would be much more complex in the case of a viscoelastic polymer melt. However, the above analysis, summarized in Figure 4.2, highlights factors that may be used to assess the spinnability of polymer melts. These include not only experimental variables (the extrusion temperature and velocity, the dimensions and number of the spinneret orifices, the fluid flow rate, etc.), but also the intrinsic properties of the fluid. In order to compare the ease of processing of the different iPP1/MMT formulations, it is assumed here that the processing variables, except for V_L, are constant. Thus, the parameters pertinent to the spinnability may be divided in two groups: (i) those that affect the intrinsic rheological properties of the polymer melt and (ii) the spinning conditions. This chapter focuses on the rheological properties of the melt, and, in particular on their dependence on MMT concentration. Spinning conditions are discussed in terms of drive-roll velocity and the physical characteristics of the filaments.

4.2.2 Rheological properties of iPP/MMT fiber-forming melts

The melt spinning process involves the flow of polymer within the extruder and the spin pack, where it experiences essentially shear deformations. After exiting the spinneret the polymer cools down and undergoes uniaxial extension. Whereas the flow of the melt in the spinneret and the potential instabilities are controlled by the shear flow characteristics of the melt, the dynamics of the deformation occurring well below the spinneret are dependent on its extensional characteristics, typically expressed by the elongational behavior[2]. Therefore, the spinnability of the iPP1/MMT melts was studied by both shear and elongational measurements.

a. Linear shear viscoelasticity

The Cole-Cole plot approach was used to represent the viscoelastic properties of the melts[5]. A logarithmic plot of the storage modulus *G'* versus the loss modulus *G"* measured at 0.5 % of strain is shown in Figure 4.3(a) for different iPP1/MMT formulations. Pure iPP1 gave a linear curve with a slope close to 2 in the terminal region as expected for a homogeneous polymer[6]. The curves tended to shift upward with increasing MMT content. This deviation from the curve for pure iPP1 suggested that iPP1/MMT nanocomposites, even at low loadings, had longer relaxation times than pure iPP1[7]. In addition, the reduced slope with increasing MMT content indicated increasingly solid-like behavior in the nanocomposite[8, 9]. For a given iPP1/MMT formulation, the slope of the curve changed with frequency, particularly in the low frequency regime and at high MMT contents. This was attributed to the formation of a MMT platelet network in the melt.

The value of tan δ is a quantitative measure of the solid-like or liquid-like behavior of a polymer melt. The liquidlike character is dominant when *G"* is greater than *G'*, and the solid-like character is dominant when *G'* is greater than *G"*, tan δ = 1 representing the

transition[9]. In Figure 4.3(b), iPP1/MMT exhibited exclusively liquid-like character up to 1 wt% MMT. Beyond this MMT concentration, the behavior was either liquid-like or solid-like depending on the shear rate (2.4 and 3.4 wt%) or exclusively solid-like for 5.9 and 13.5 wt%. This result was confirmed by results from melt pressure relaxation measurements in elongational shear (described in section 3.2.3) shown in Figure 4.4. The relaxation time constants increased significantly with MMT addition (by about 140 % on addition of 13.5 wt% MMT), indicating that the elastic energy of the melt was increased on addition of MMT[5, 10].

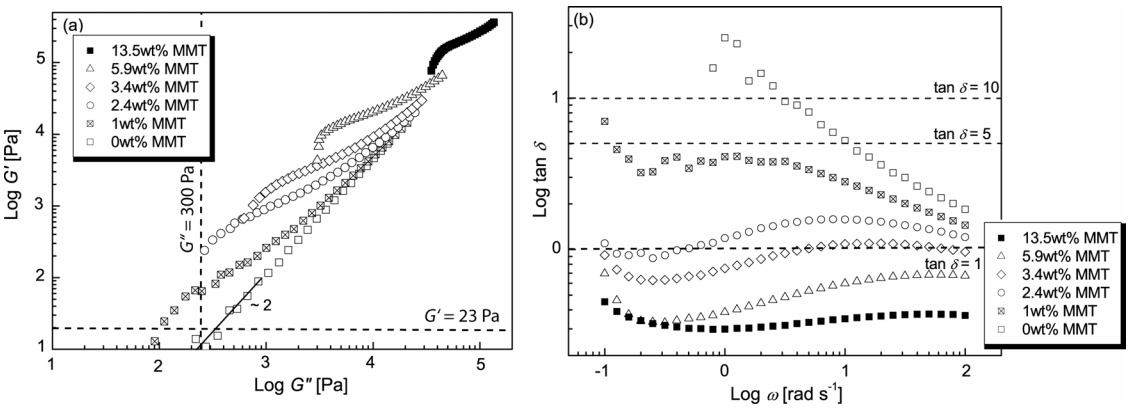

Figure 4.3. (a) Storage (*G'*) versus loss (*G"*) modulus and (b) loss factor (tan δ) as a function of shear rate (ω) for a range of iPP1/MMT concentrations.

An important consideration in the present work is how to assess the spinnability of the melt quantatively. Beyreuther *et al.*[11] have attempted to express spinnability in terms of the loss factor, tan δ and they advanced a structural rheological model in support of this approach. Spinnable and a non-spinnable regimes were defined from plots of *G'* versus *G"*, for different thermoplastics (polyesters and polyamides) and *G'* 100 Pa, they found that for a spinnable melt, tan δ = *G"*/*G'* > 10. For a non-spinnable melt, on the other hand, tan δ < 5, according to these authors. These two criteria are represented in Figure 4.3(b), where tan δ is plotted as a function of ω for different iPP1/MMT formulations. According to the above criterion, only pure iPP1 and iPP1/1 wt% MMT could be spinnable. Christiani *et al.*[12] have established somewhat different criteria for iPP. They suggested that *G"* 300 Pa and *G'* 23 Pa for the melt to be spinnable. Comparison with Figure 4.3(a) indicates this criterion to be met for the all range of MMT concentrations considered here. The establishment of a quantitative criterion for spinnability does not therefore appear to be straightforward. However, the decreasing slope of the curves with increasing MMT content (Figure 4.3(a)) suggested *G'* to dominate *G"* with increasing MMT content. Thus, the relative elasticity of the melt increased with increasing MMT content, and, following to Gupta *et al*[3], who stated that the elasticity of the melt is detrimental to its spinnability, the addition of MMT to iPP1 may be concluded to be at least qualitatively detrimental.

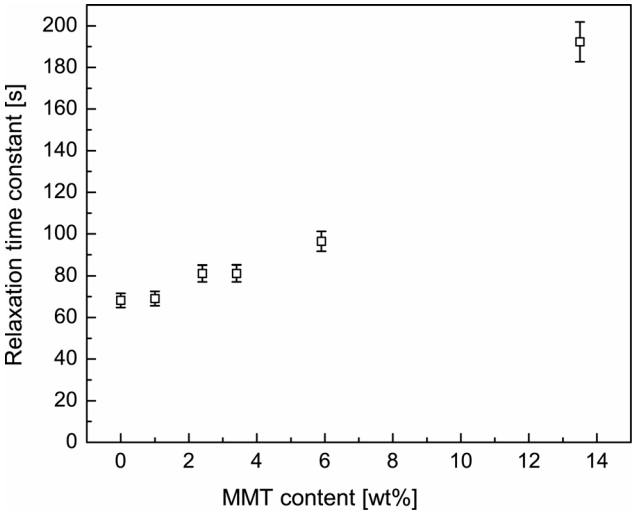

Figure 4.4. Relaxation time constants from capillary relaxation tests at 220°C, as a function of MMT concentration.

b. Elongational viscosity (Haul-off test)

The processability of a melt into a fiber is not only dependent on the spinnability in the molten state, but also on stretching in the solid sate, so drawability of the melt must also be investigated[12].

Extensional deformations are involved in many processing operations, including fiber spinning, thermoforming and film blowing. However, few data are available for the extensional properties of fluids because it is relatively difficult to obtain homogeneous extensional flow in practice[13]. It is particularly difficult to eliminate shear stresses and to control the deformation simultaneously. The extensional behavior of polymer melts is therefore often observed by means of extensional indexers[14, 15]. These instruments provide flows with a mixture of extension and shear and a resulting apparent extensional viscosity.

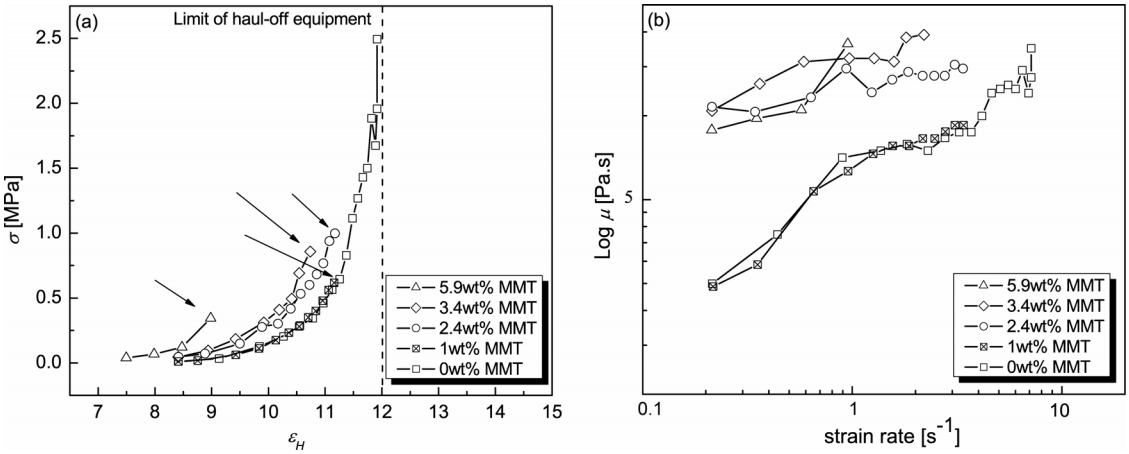

Figure 4.5. (a) Melt stress σ of extruded iPP1/MMT versus Hencky strain ε_h for different MMT concentrations at 220 °C. (b) Apparent transient elongational viscosity μ versus strain rate at 220 °C for different MMT concentrations.

In the present case, the elongational behavior of the polymer melts was measured by means of a haul-off set-up (see section 3.2.3). Its principle is relatively simple: the polymer is continuously extruded from a tube and stretched by a rotating wheel. The force on the polymer strand is measured together with its diameter and the flow rate, allowing the calculation of the stress applied to the strand σ, and the apparent elongational viscosity, μ. These calculations assume that the inertial, drag, gravitational and surface tension forces are negligible and that the strain rate is constant (section 3.2.3). In addition to these approximations, certain parameters differed from those associated with the practical melt spinning operation. In particular, the deformation rates involved in the haul-off measurements (maximum 10 s^{-1}) are much lower than those in melt spinning (about 10^4 s^{-1}). Also, the process is non-isothermal and the temperature gradient of the melt along the spinline is not controlled. However, the analysis gives a qualitative comparative indication of the spinnability of the different iPP1/MMT formulations, and, importantly, it allows assessement of the drawability of the melt as a function of MMT concentration. The validity of such measurements has been discussed further by Salem[16].

The overall force balance on a single filament of the spinline at distance z from the spinneret may be written as:

$$F_{rheo}(z) = F_0 + F_{inert}(z) + F_{drag}(z) - F_{grav}(z) + F_{surf}(z) \qquad \textbf{Equation 4.1}$$

where F_{rheo} is the rheological force in the fiber at a distance z from the spinneret, F_0 is the force at the exit of the spinneret, F_{inert} is the inertial force produced by the acceleration of the polymer mass along the spinline, F_{drag} is the drag force caused by the fiber moving through the cooling air, F_{grav} is the gravitational force acting on the spinline, and F_{surf} is the surface tension force at the fiber/air interface. The surface tension of polymer melts is often small compared to other forces and can be neglected. If the tension in the spinline at a distance L from the spinneret, F_L (for example close to the take-up device), is measured,

then the spinline force, F_{rheo}, at any point in the spinline may be written:

$$F_{rheo}(z) = F_L - \int_Z^L F_{inert}(z)dz - \int_z^L F_{drag}(z)dz + \int_z^L F_{grav}(z)dz \qquad \textbf{Equation 4.2}$$

Thus, in the context of the haul-off test where the inertial, drag and gravitational forces are neglected, it is also assumed that F_{rheo} on the polymer strand is constant over its length and can be measured.

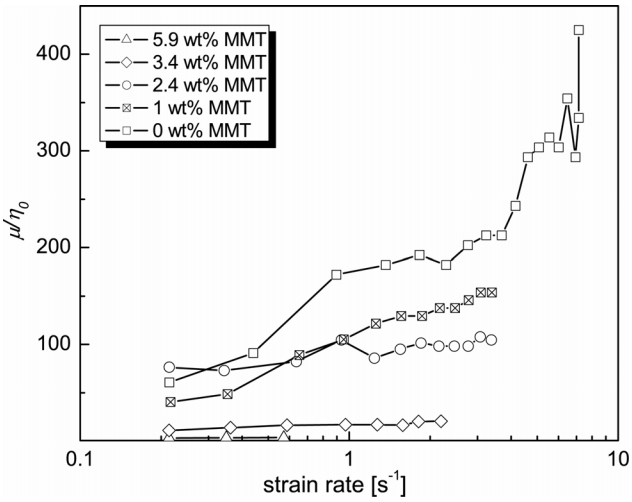

Figure 4.6. Troughton's ratio μ/η_0 as a function of strain rate.

Results from the haul-off tests are shown in Figure 4.5(a) and (b). As stated previously in section 4.2.1, the limit of spinnability is reached when the stress applied to the polymer filament reaches a critical value, σ_{max}, which corresponds to rupture of the filament. σ_{max} is also called the melt strength. The dependence of the stress applied to the polymer filament, σ, on the Hencky strain ε_h is shown in Figure 4.5(a). For the pure iPP1 polymer melt, the strand could be extruded to deformation levels beyond the limits of the equipment, and σ_{max} was about 2.5 MPa, which is similar to reported values for the melt strength of iPP (about 2 MPa)[17]. For the different iPP1/MMT formulations, the polymer strands broke after a certain critical deformation. The corresponding stress, σ_{max} indicated by the arrows in Figure 4.5(a), provided an indication on the limit of spinnability of the polymer melt. σ_{max} decreased as the MMT content increased, i.e. thepresence of MMT reduced the spinnability of iPP1.

Figure 4.5(b) shows the evolution of the apparent transient elongational viscosity, μ, as a function of the strain rate. μ increased as the MMT concentration increased. The data for iPP1/5.9 wt% MMT were out of range, owing to the adherence of the melt to the surface of the bore of the capillary rheometer, which became significant at high MMT concentrations. Most studies involving an extensional indexer are limited to the determination of the melt strength given by the maximum melt stress before failure of the

filaments owing to the difficulty of obtaining a constant elongation rate experimentally[18], as assumed for the haul-off apparatus. Indeed, the elongational viscosity is more often measured using a convergent flow die in a capillary rheometer in conjunction with the Cogswell and Binding approach[19, 20], for example. The converging flow method for determining elongational viscosity is a low strain experiment whereas much higher deformation strains are achieved with extensional indexers[21]. It is therefore difficult to compare the present experimental data with literature values. However, one generally expects a correlation between μ and the maximum draw ratio applicable to the polymer strand[22]. Thus, a material with low μ should show better drawing behavior than a material with high μ. It is also useful to consider the apparent value of Troughton's ratio, μ/η_0, where η_0 is the zero-shear rate viscosity determined from steady-state shear tests (section 3.3.3), for the different iPP1/MMT formulations (Figure 4.6). In general, polymer melts show hardening under uniaxial elongation at constant strain rate. This behavior is called elongational thickening[23], and it has been shown that an increasing elongational thickening behavior of a polymer melt leads to both an enhancement of the processing stability and a decrease in the drawability of the melt[21]. An increasing Troughton's ratio is indicative of a decreasing elongational thickening in polymer melts[24]. At all shear rates, μ/η_0 decreased on addition of MMT. For pure iPP1, μ/η_0 increased markedly with increasing strain rate. However, this trend was less marked on the presence of MMT, and μ/η_0 was almost constant for iPP1/5.9 wt% MMT. Thus, addition of MMT and increasing strain rate are again concluded to reduce the drawability of iPP1.

It has also been observed for various polymers filled with micro-sized fillers, $CaCO_3$-filled iPP[22] or short glass fiber-iPP[25], for example, that the melt strength and the drawability of the melts decrease with increasing filler concentration. Moreover, Koyama *et al.*[23] have shown that the smaller the fillers and the larger their aspect ratio, the weaker the elongational thickening behavior, and hence the lower the drawability. Relatively few studies concern the elongational behavior and the drawability of nanocomposites. Moreover, as pointed out by Zhu *et al.*[26], the processability in such materials may be limited by the dispersion and the morphology of the fillers. In the particular case of ethylene vinyl acetate (EVA) copolymer/MMT and polyethylene/MMT nanocomposites, La Mantia *et al.*[27] and Wang *et al.*[28] respectively, have nevertheless found that a high degree of intercalation or exfoliation has either no influence on, or is beneficial to the extensional properties and the drawability of the melt. This clearly contradicts the results of the present study. This difference may be attributed to a relatively low degree of intercalation in the present study compared with that of the above mentioned studies .

4.2.3 Melt-spinning and flow instabilities

In practice, iPP1/MMT fibers could be successfully melt-spun and drawn from pre-compounded nanocomposites for MMT contents up to about 5 wt%. Melts with higher MMT contents could also be extruded, but, as anticipated from the elongational rheology measurements, drawing was found to be limited regardless of other processing parameters.

The hot draw ratio DR was defined in section 3.1.2(b). It corresponds to the ratio between

the velocities of the two heated godets. As shown in Figure 4.7, at lower MMT contents, the maximum drive roll velocity, V_L, before fiber breakage decreased with increasing MMT content for fixed hot draw ratios. Similarly, the maximum DR decreased with increasing MMT content, so that it was limited to 1 for specimens containing 3.4 wt% MMT for V_L = 500 m/min, for example.

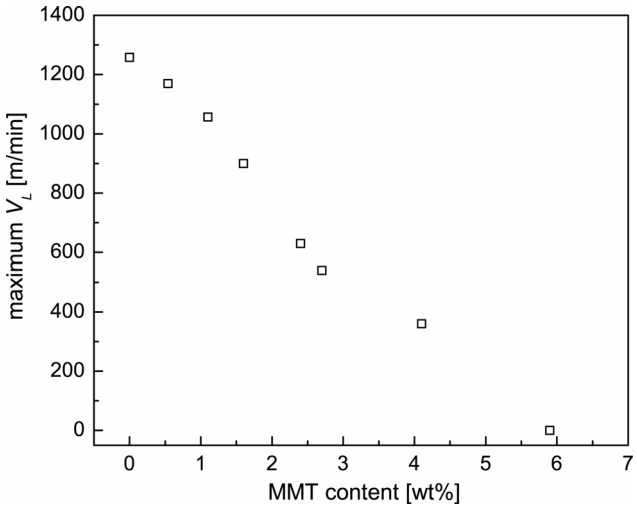

Figure 4.7. Maximum drive-roll velocity, V_L, for fiber spinning of iPP1 with different MMT concentrations (DR = 1).

As observed previously for industrial melt-spinning processes[1], spinnability limited by fiber breakage was mainly attributed to cohesive failure since capillary break-up was not observed in the present work. To develop the analysis of the spinnability and to complement the elongational rheology measurements, it was of interest to consider other types of melt instability that may contribute to the breakage of filaments during melt spinning.

From the industrial point of view, a primary concern is to produce filaments with uniform cross-sections. The flow instabilities of particular interest are therefore those that introduce non-uniformity into the filament. These can be divided into two categories: the first covers instabilities whose origin is in the spinneret channel, die swell and melt fracture, and the second covers those that occur when the draw ratio reaches a critical value, referred to as draw resonance.

Draw resonance, which appears in the form of periodic fluctuations in the thread diameter, was not observed in the present melt-spinning trials. However, no systematic analysis of the filament diameters was conducted beyond simple inspection in the optical microscope so it could not be concluded that the phenomenon did not occur over relatively long lengths of filament. On the other hand, die swell was initially of major concern. Attempts to spin fibers from iPP1/MMT nanocomposites without pre-compounding resulted not only in excessive die swell but also in irregular output at the

spinneret, as is often the case with filled iPP [29]. The yarns also showed a pronounced yellow coloration when the MMT was poorly dispersed. Figure 4.8 shows typical diameter variations due to die swell. This instability was overcome by pre-compounding the nanocomposites, after which regular diameters were obtained. However, although good homogeneity is indispensable for the spinnability of the polymer melt, additional extrusion steps may lead to chemical, oxidative or molecular weight degradation[30].

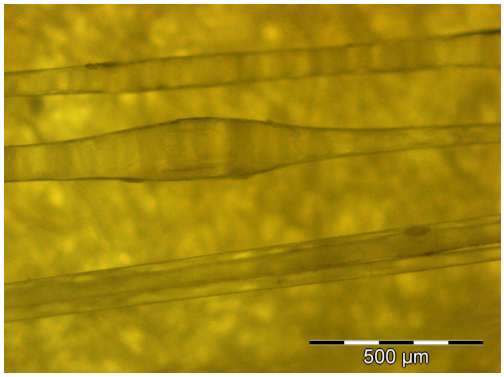

Figure 4.8. Typical swelling in spun filaments resulting from a poor dispersion of the MMT in the nanocomposite.

Melt fracture is a more complex phenomenon. It can be of two types. At low shear rates, as the flow rate increases, the extrudate develops a small amplitude high frequency disturbance on its surface called sharkskin. At higher shear rates, however, severe, irregular distortions of the filament may occur. In a system with a controlled piston speed, it may result in both large amplitude oscillations of the extrudate cross-section and discontinuities in pressure drop versus flow rate[31]. Pressure drop is characteristic of elastic properties during die extrusion of polymeric fluids[32]. In the case of iPP, the pressure oscillation regime is generally not seen[33] so that the surface of the extrudate must be monitored visually to detect signs of melt fracture. Figure 4.9 shows the results obtained for a range of MMT concentrations. No discontinuities or oscillations in the curves were observed and the surface of the extrudates was regular (cf. Huang *et al.*[34]). The pressure drop increased non-linearly with the shear rate as well as with the MMT content. No melt fracture was observed for neat iPP1 in the range of deformation rate of interest in the context of melt-spinning (10^{-4} s^{-1}), and it has been observed elsewhere that organically modified nanoclays may significantly delay the onset of melt fracture to higher shear rates, even at low loadings[35].

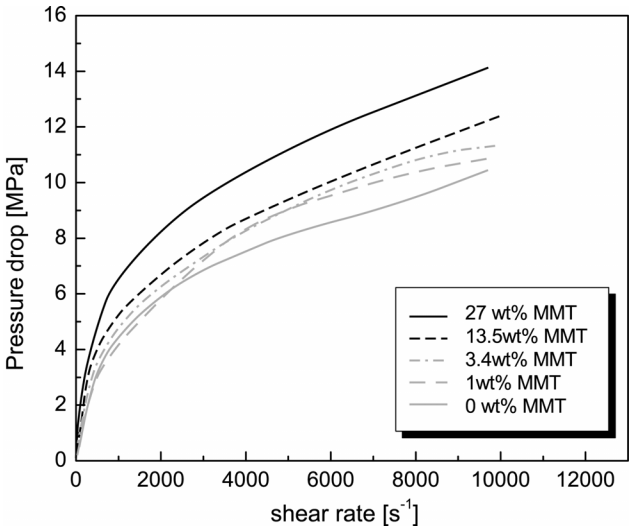

Figure 4.9. Melt pressure drop at the entrance of the capillary die as a function of shear rate at 220°C for different MMT concentrations.

4.3 FILAMENT CHARACTERIZATION

At the industrial level, the testing of the filaments is a necessary and integral part of the production process, to ensure certain quality standards and to investigate how the textile articles behave in service. Indeed, during further processing, such as weaving or knitting, the process variables, namely tension and temperature, may have a significant influence on the filament and its derived products. The requirements of industrial fiber testing standards imply the use of several meters of filaments for each test to avoid scatter in the data resulting from fluctuations associated with the melt spinning process. On a laboratory scale, tests involving such large quantities of material are not envisageable. However, the purpose of the laboratory characterization is not a quality control, it is rather to gain an understanding of the factors that influence filament properties. The central issue in the present study is microstructure/property relationships in iPP1/MMT melt-spun fibers. Thus, the influence of the processing parameters on the morphology of the fibers has been considered, as well as their influence on global physical properties.

4.3.1 Physical structure characterization

a. Microstructure

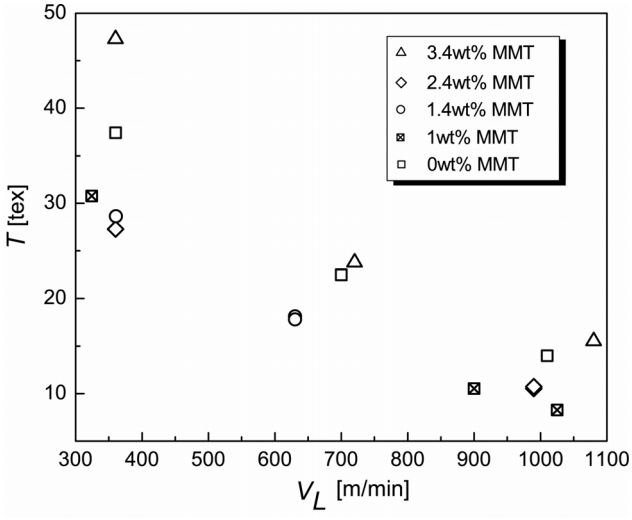

Figure 4.10. Yarn fineness, *T*, of melt-spun filaments with DR = 1 as a function of drive-roll velocity, V_L for different MMT concentrations.

Optical microscopy observations and measurements revealed that the surface of the filaments was smooth, their cross-section was circular and that the diameter, *d*, of a single filament was between 50 μm and 20 μm, corresponding to a fineness *T* (defined in section 3.1.2) of between 10 tex and 50 tex. The cross-section of the filaments was not influenced by DR. On the other hand, as shown in Figure 4.10, the influence of V_L was significant. The diameter decreased with increasing drive-roll velocity for all MMT concentrations. Moreover, using Equation 3.4, it was found that the measured filament diameters were consistent with *T* derived from Equation 3.2, although the agreement was less good at high MMT concentrations, as shown in Table 4.1. The die swell discussed in section 4.2, as well as variations in the melt flow rate inherent in the melt spinning process, imply any diameter variations to increase with MMT concentration. Moreover, in spite of efforts to obtain a good statistical sample of filament diameter measurements, i.e. 7 filament diameters measured every 10 cm, systematic errors may still be present in the optical measurements.

Table 4.1. iPP1/MMT filament fineness and diameters for different drawing conditions.

MMT concentration [wt%]	DR	V_L [m/min]	Measured *T* [tex]	Calculated *d* [μm] (Equation 3.4)	Measured *d* [μm]
0	1	360	37.4	39.7	41.1
0	1	700	22.5	30.8	29.5
0	1	1010	14.0	24.3	26.4
1	1	324	30.7	35.6	38.9
1	1	900	10.5	20.8	20
1	1	1025	8.2	18.4	18.3
1.3	1	360	27.2	18.4	35.5
1.3	1	990	10.5	33.3	20.7
1.3	2	990	10.7	20.7	21.4
2.4	1	360	28.6	33.9	34.6
2.4	1	630	18.1	27.0	28.1
2.4	1.5	630	17.8	26.7	28.1
3.4	1	360	47.2	43.1	46.0
3.4	1	720	23.7	30.5	39.1
3.4	1	1080	15.5	24.7	26.1
7.5	1	360	44.2	41.2	50.3

b. Crystallinity

In semicrystalline polymeric filaments, the differences in molecular organization, resulting from the processing parameters can lead to significant differences in physical properties. These differences are mainly related to the proportions and roles of the crystalline and the amorphous phases. The crystalline phase contributes to the macroscopic stiffness, strength, durability, thermal resistance and stability of the filaments. The amorphous phase is more loosely packed and contributes mainly to the extensibility, pliability and recovery of the filaments[3]. As a result it was of interest to determine the degree of crystallinity in the filaments. This was performed by DSC.

- *DSC*

Since spinning was carried out above the melting point of the polymer, the filament was cooled continuously through the temperature range where crystallization is possible. Relatively little information is available on the effect of spinning conditions on the crystallinity of melt spun fibers. It has generally been observed that the degree of crystallinity increases with the draw ratio in iPP[36]. In addition, the incorporation of MMT platelets in iPP is known to significantly influence crystallization kinetics, crystal structure and crystallinity of the semicrystalline polymer. Two particular effects of the MMT platelets have drawn attention: (i) the MMT layers act as nucleating agents for the crystallization of iPP[37, 38] which increase the nucleation and crystallization rate and (ii) physical hindrance due to the presence of the MMT layers results in a decrease in crystallinity[39, 40]. Nowacki *et al.*[41] reported only a weak nucleating effect of MMT during crystallization under static conditions. However, it was greatly enhanced during shear-induced crystallization. Similarly, Solomon *et al.*[42] observed a flow-induced acceleration of the crystallization kinetics in iPP1/MMT nanocomposites, but only a modest effect of

shear strain on crystallization in pure iPP.

During cooling from the melt in the absence of flow, as is the case for the melt compounded iPP1/MMT granulates, the iPP adopts a semi-crystalline structure dominated by the α crystalline form. A second possible crystal type is the β form. The α form is more stable and shows a melting temperature of the order of 165 °C. The β form is less stable and melts at lower temperature[43]. Only melting of the α form was detected in the DSC scans.

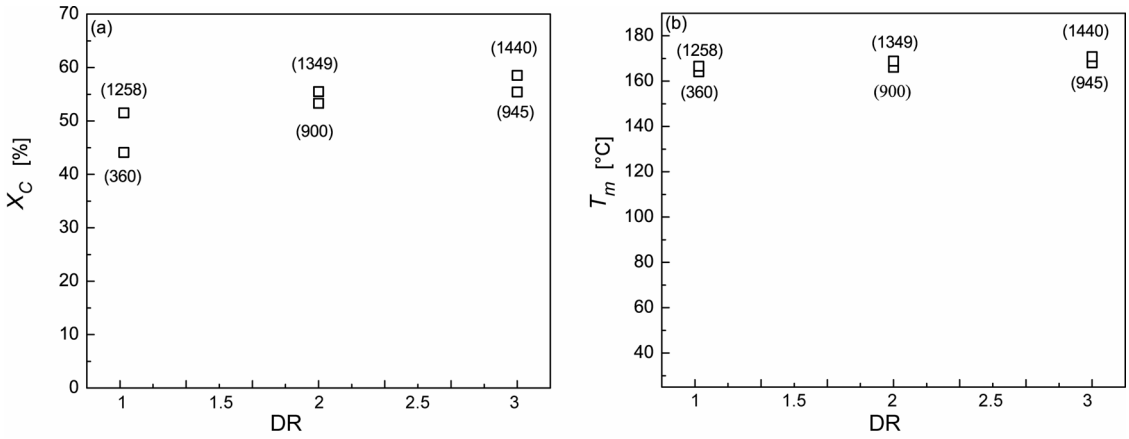

Figure 4.11. (a) Degree of crystallinity, X_C, and (b) melting temperature, T_m, of pure iPP1 fibers as a function of DR. The corresponding V_L are given in brackets.

Figure 4.11(a) and (b) show the influence of DR and V_L (in brackets) on the crystallinity and the melting temperature of iPP1 fibers. Figure 4.11(a) shows that DR = 3 and V_L = 1440 m/min led to an increase in crystallinity of about 10 % compared with that of fibers melt-spun with DR = 1 and V_L = 360 and 1258 m/min. Thus, for pure iPP1 fibers, the degree of crystallinity increased with DR. This enhancement was attributed to an increased crystallization rate on stretching[36]. On the other hand, the melting temperature was almost unchanged on drawing (Figure 4.11(b)).

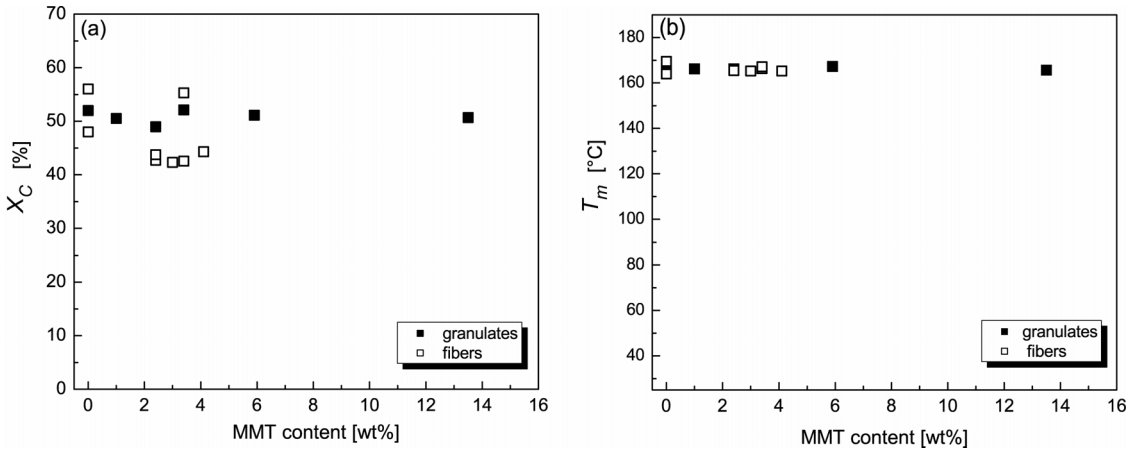

Figure 4.12. (a) crystallinity and (b) melting temperature of the matrix iPP1/MMT granulates and fibers with DR=1 as a function of MMT concentration.

For iPP1/MMT filaments melt-spun and drawn under similar conditions (Figure 4.12(a) and Figure 4.12(b)), the MMT had no influence on the crystallinity nor on the melting temperature for both the melt compounded samples and the fibers, as observed elsewhere for similar materials[44]. It has been observed in iPP/MMT[45] and PA6/MMT[46] that MMT may act as a nucleating agent, resulting in increased crystallinity in the nanocomposite compared with the neat matrix. This was not verified here. However, Pozsgay *et al.*[47] have argued that the ability of MMT to nucleate iPP crystallization depends on the organo-treatment of the clay, this latter acting not only through modification of the clay surface tension but also alteration of the interlayer distance. They concluded that the nucleation occurs in the interlayer galleries of the clay particles. Thus, no nucleating effect is observed with well dispersed clay[48]. Another feature of the DSC scans was that the crystallinity of the less drawn fibers was lower than that of melt compounded samples at all MMT concentrations. This behavior may be attributed to a high cooling rate and physical disruption of crystallization and crystal orientation in the fibers during drawing in the presence of the MMT.

c. Molecular orientation

The molecular orientation in a fiber arises from the alignment and stretching of the molecular chains along the fiber axis in both the crystalline and non-crystalline regions of the filaments. Its development occurs in 3 stages during melt-spinning: first in the spinneret channel, then during the elongation of the filament and finally during the cold drawing, the latter stage being the most important. In the particular case of iPP1/MMT nanocomposites, the solid state properties of the filaments may depend not only on the size, the shape and the amount of filler, but also on their possible orientation with respect to the applied loads. Some studies have been made on the orientation of clay in the melt processed nanocomposite products, such as injection-molded specimens[49, 50], blown films[51], or melt-extruded specimens[52], and it has been shown, using rheo-XRD techniques, that the average orientation of clay increases with shear rate up to a saturation value. Thus some flow induced clay orientation may be expected to be retained during

solidification of the melt and it was therefore of interest to investigate the orientation of the MMT platelets in iPP1/MMT filaments. Three methods of investigation were used to investigate the molecular orientation, these are TEM, WAXS and SAXS. All these techniques are described in chapter 3 section 3.2.1.

- *TEM*

TEM is particularly suited to observation of the MMT platelet morphology in the filaments. Specimens were prepared from iPP1/MMT filaments with the same DR but stretched at different drive-roll velocities, since it was observed previously that the drive-roll velocity was a more important factor for the fineness than DR, and various MMT concentrations. The filaments were sectioned in the directions parallel to the fiber axis and perpendicular to the fiber axis.

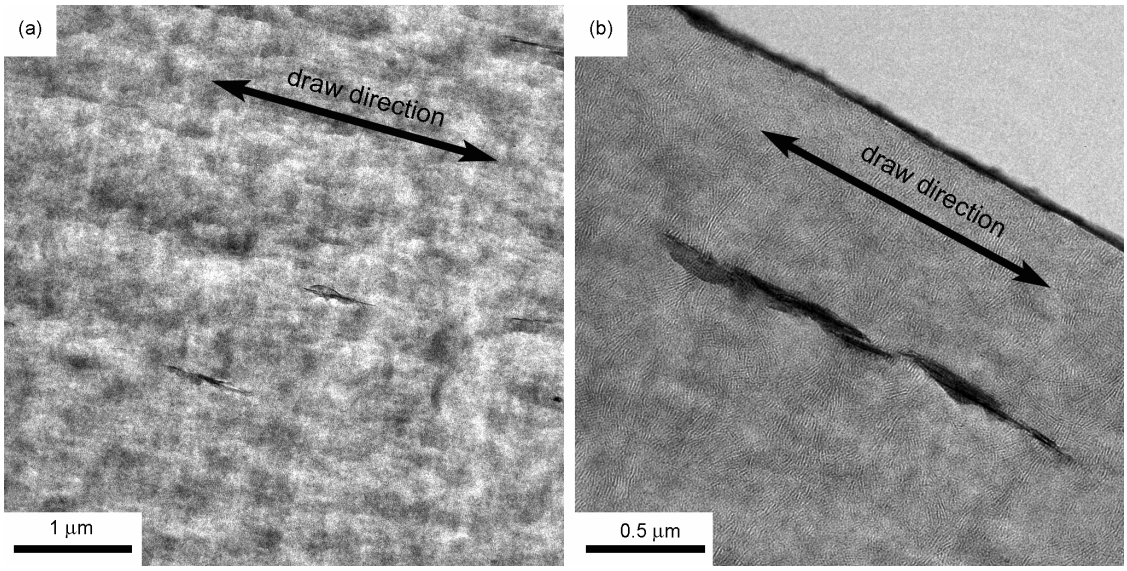

Figure 4.13. (a) and (b):TEM micrographs of longitudinal sections of iPP1/1 wt% MMT filaments with DR = 1 and V_L = 360 m/min . The arrows indicate the direction of drawing.

In the case of iPP1/1 wt% MMT fibers spun with a relatively low drive-roll velocity of 360 m/min and sectioned parallel to the fiber axis (Figure 4.13(a)), relatively few MMT particles were observed. They were homogeneously dispersed in the iPP1 matrix and oriented along the filament axis. A higher magnification (Figure 4.13(b)) indicated that the particles were typically 900 nm in length and their width was of the order of a few nanometers. Even at low spin draw ratios, the MMT particles showed a strong orientation in the fiber direction.

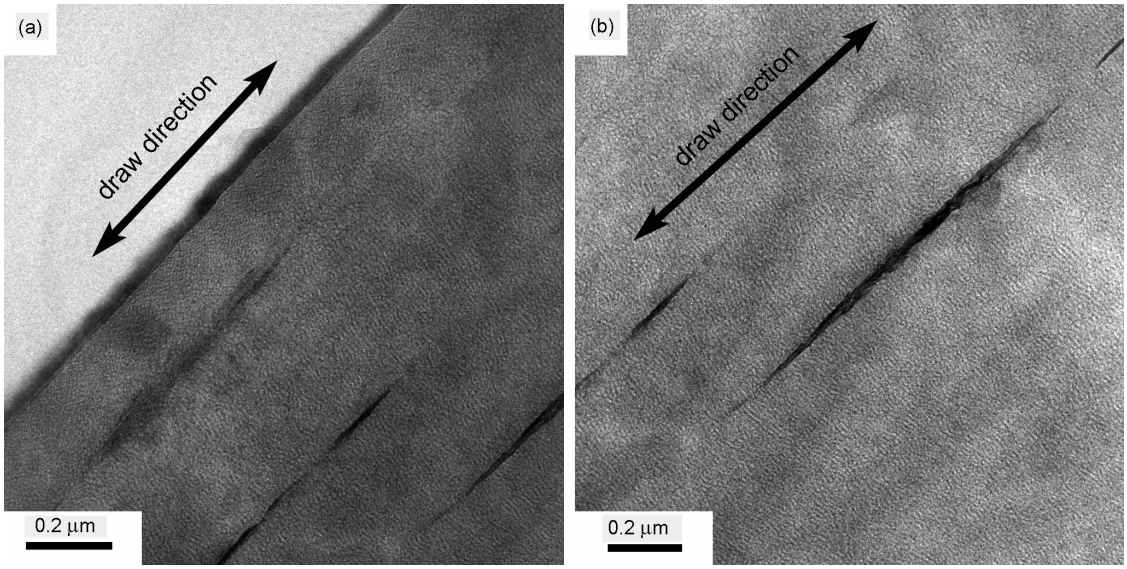

Figure 4.14. (a) and (b):TEM micrographs of longitudinal sections of iPP1/1 wt% MMT filaments with DR = 1 and V_L = 1080 m/min. The arrows indicate the direction of drawing.

At higher drive-roll velocities (Figure 4.14), the MMT particles were longer (~1.5 μm) and thinner. The MMT stacks underwent elongation in the orientation direction. Thus the stretching effect of cold drawing on the particles morphology was significant[53, 54], resulting in increased particle aspect ratios. The lamellar structure of the iPP1 is also visible in Figure 4.13(b) and Figure 4.14(b), showing a stacked structure with the lamellar trajectories running perpendicular to the draw direction. The microstructure became finer with increasing drive-roll velocity.

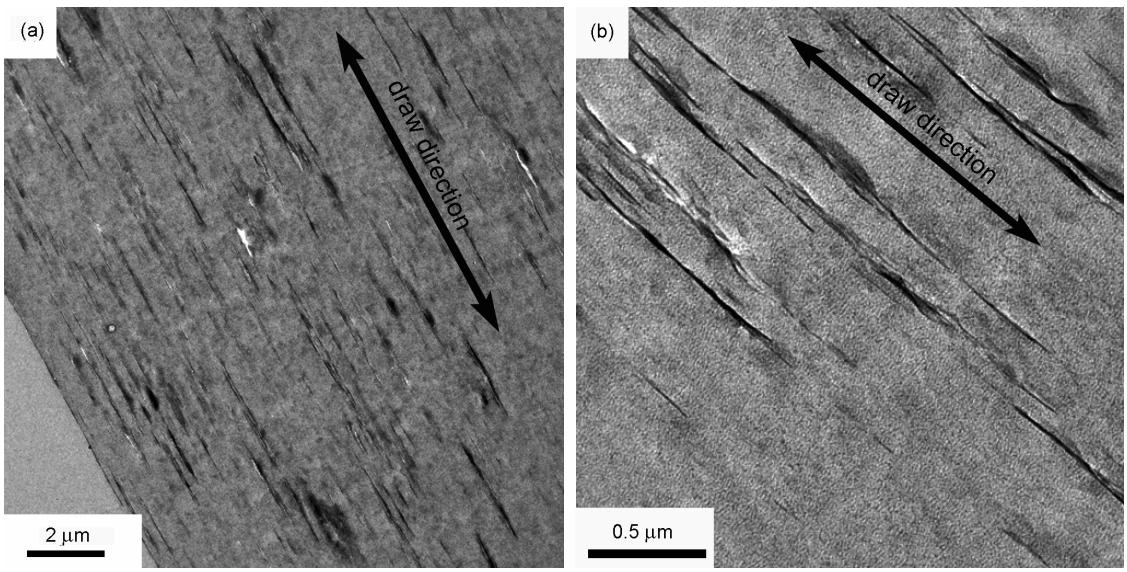

Figure 4.15. (a) and (b): TEM micrographs of longitudinal sections of iPP1/3.4 wt% MMT filaments with DR = 1 and V_L = 1080 m/min. The arrows indicate the direction of drawing.

The morphology of iPP1/MMT filaments with higher MMT concentrations are shown in Figure 4.15. The dispersion of the silicate stacks was homogeneous and the orientation of the platelets was isotropic in the direction of the fiber axis. In transverse sections, Figure 4.16(a) and (b), on the other hand, the orientation of the platelets appeared random and there was substantial curvature in the platelet cross-sections. The same observation was made for filaments with a higher MMT content as shown on Figure 4.18 for iPP1/5.9 wt% MMT filaments. Thus, whereas the particle aspect ratio was estimated to be 20 to 50 for the pre-compounded iPP1/MMT, it was at least between 100 and 150 in the longitudinal direction of the drawn filaments even at low drive-roll velocity.

Figure 4.17 shows the microstructure in an as-extruded filament containing 5.9 wt% MMT. The much lower anisotropy of this nanocomposite confirms that the cold drawing is essential for achieving high degrees of MMT particle orientation.

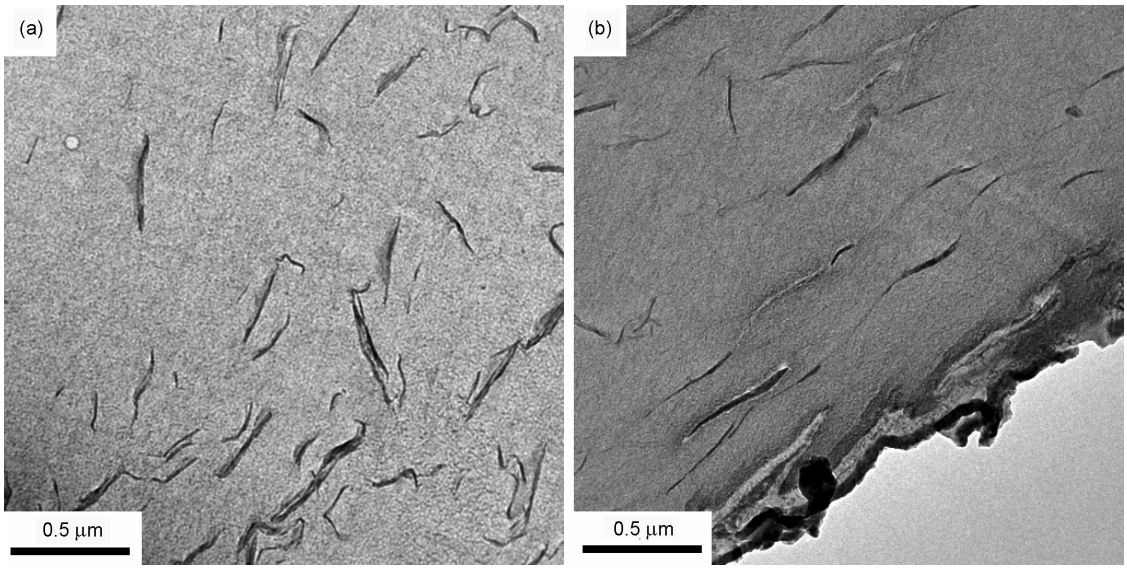

Figure 4.16. (a) and (b): TEM micrographs of transverse sections of iPP1/3.4wt% MMT filaments with DR = 1 V_L = 1080 m/min.

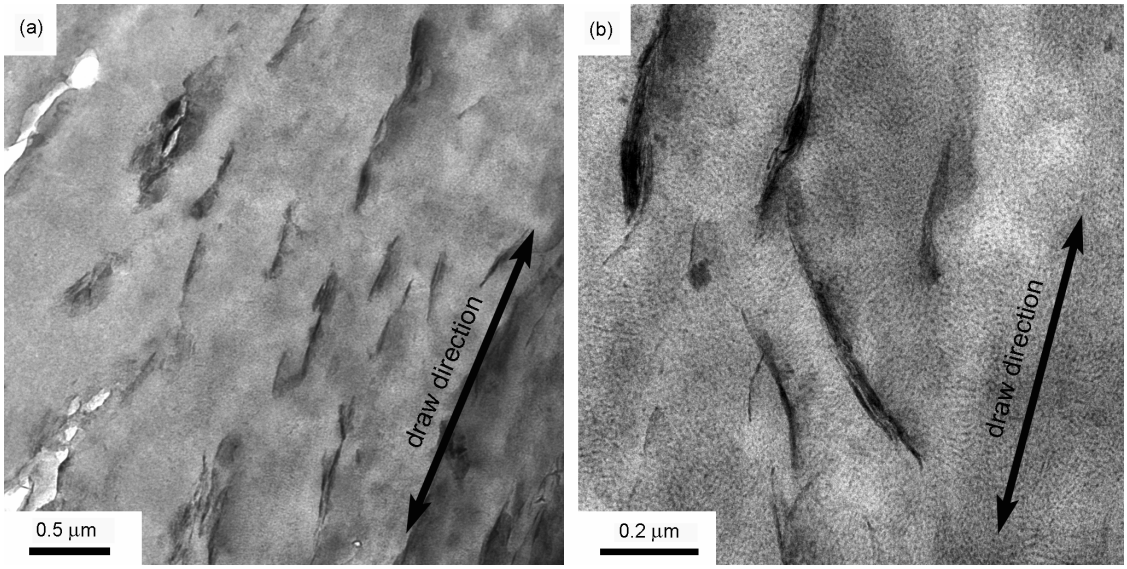

Figure 4.17. (a) and (b): TEM micrographs of longitudinal sections of as-extruded iPP1/5.9 wt% MMT filaments. The arrows indicate the direction of drawing.

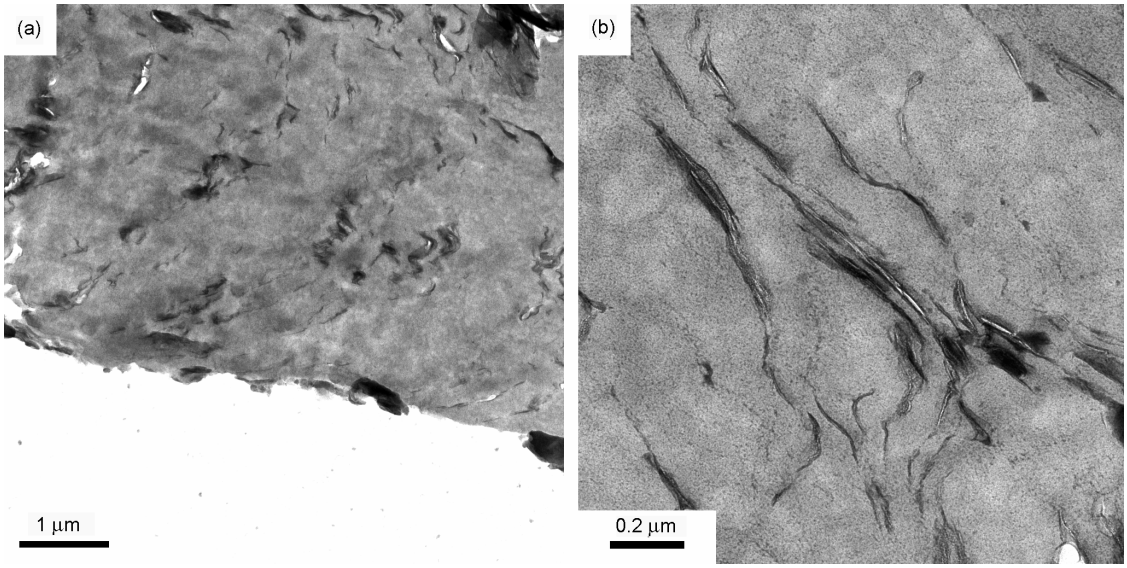

Figure 4.18. TEM micrographs of transverse sections of as-extruded iPP1/5.9 wt% MMT filaments.

A preferential orientation of iPP lamellae perpendicular to the surface of MMT platelets and the orientation of the MMT platelets in the drawing direction (i.e. the normal to the surface is oriented perpendicularly to the drawing direction) observed in this study are not universal phenomena. Indeed, although similar behavior has also been observed by Maiti *et al.*[55] and Kim *et al.*[56] in PA/MMT nanocomposites, where a typical "shish-kebab" crystalline structure, associated with an increase of orientation of polymer crystallites with increasing MMT content, but a constant degree of crystallization[57], some contradictory observations are also found to be in literature. Kojima *et al.*[49] pointed out, in the case of PA6/MMT nanocomposites, that the orientation of the polymer chains

relative to the silicate platelets surface was dependent on the shear applied during the process. They found that the chain axes of the polymer crystallites were perpendicular to the silicate layers for low shear forces and parallel to them for high shear forces. In addition, the orientation of the MMT platelets relative to the direction of the extensional flow may depend on the nature of this latter. Thus, in the case of an uniaxial extensional flow, Okamoto *et al.*[58], showed that the silicate layers were aligned perpendicular to the stretching direction, whereas the same group[59] observed that the silicate layers were mainly oriented in the flow direction in the case of biaxial stretching.

- *XRD*

External flow causes orientation and extension of molecular chains in a polymer melt[60]. The resulting bulk polymer consists of two distinct morphologies: spherulites and flow induced morphologies such as shish-kebabs[61]. Qualitative and quantitative studies of molecular orientation were made by measuring the intensity distribution around the Debye rings of iPP1/MMT filaments.

Table 4.2 compares the basal spacings of extruded iPP1/MMT and iPP1/MMT filaments from WAXS scans performed between 0 ° and 10 °. In this case, the iPP1/MMT filaments were compression molded at 200 °C for 2 min. Extrusion molded iPP1/3.4 wt% MMT showed a slight increase of about 6 % with respect to the basal spacing of iPP1/MMT concentrate before pre-compounding, indicating some additional intercalation. After melt spinning, the intercalation level increased further to about 25 % as measured by WAXS. It has already been observed that further intercalation may occur during melt spinning because of the strong shear flows[62].

Table 4.2. MMT basal plane spacings for different processing conditions and MMT concentrations determined by XRD.

Material	Basal plane spacing [nm]
iPP1/MMT concentrate as-received	2.98
iPP1/3.4wt% MMT compression molded sheet	3.17
iPP1/1 wt% MMT filament	3.81
iPP1/2.4wt% MMT filament	4.02
iPP1/4.1 wt% MMT filament	4.02

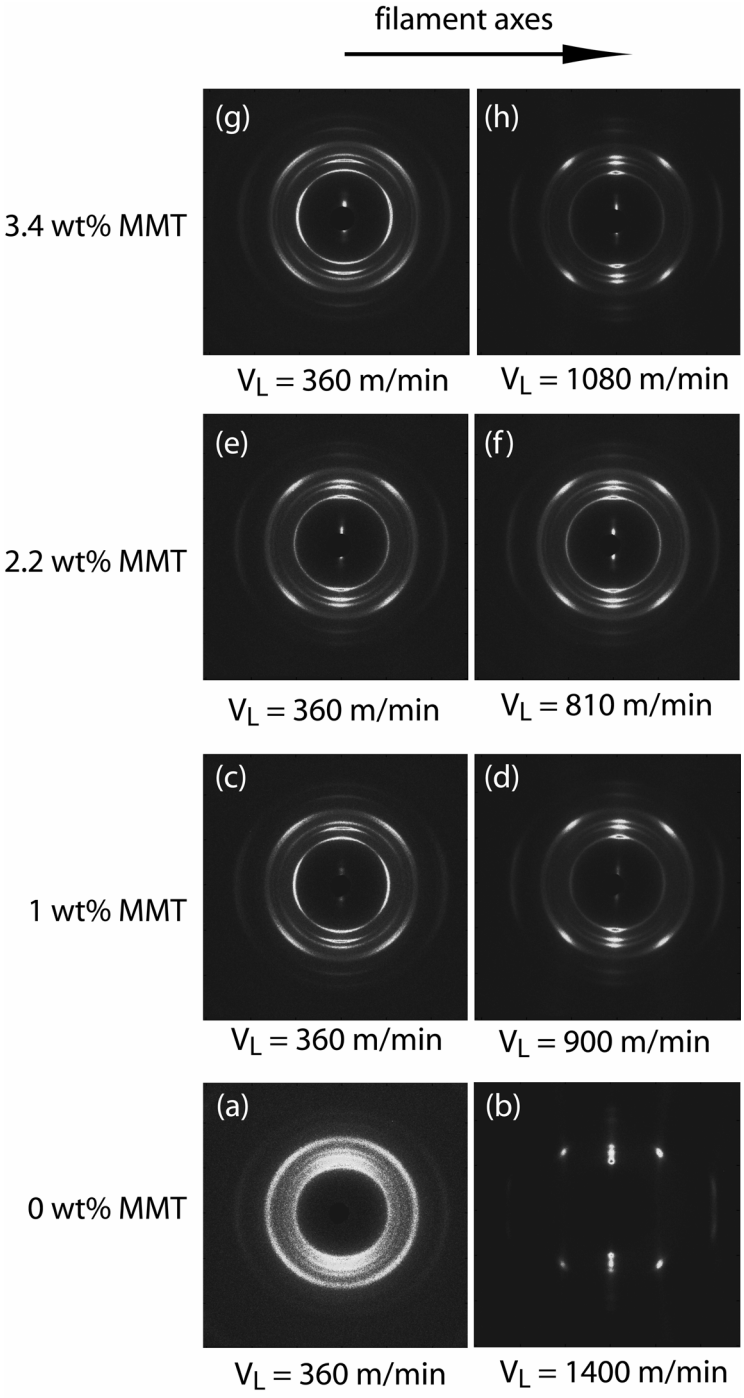

Figure 4.19. 2D-WAXS photographs of iPP1/MMT filaments, DR = 1, with different MMT content and drawn at DR = 1 with different drive-roll velocity. The filaments axis laid in the equator and V_L is indicated below each micrograph.

Figure 4.19 shows the 2D-WAXS photographs of iPP1/MMT filaments with different MMT contents and drawn at different drive-roll velocities. The corresponding intensity versus 2θ curves are shown Figure 4.20 and Figure 4.21. Four distinct reflections were

observed for pure iPP1 filaments drawn at 360 m/min (Figure 4.21(a)), corresponding to a α monoclinic unit cell with: (110) at 2θ = 14.1 °, (040) at 2θ = 16.9 °, (130) at 2θ = 18.5 °, (111) at 2θ = 22.1 ° and (220) at 2θ = 28.5 °. It was found (Figure 4.21(b)) that the α-crystalline form also dominated in the iPP1/MMT filaments, so that the addition of MMT did not affect the crystal form of iPP1 in the filament[38]. However, for higher MMT concentrations (2.2 wt% MMT and 3.4 wt% MMT), an additional reflection peak was observed at 2θ = 16° (Figure 4.19), corresponding to the (300) reflection of the trigonal β unit cell. The presence of the β phase, even in amounts, not detected in the DSC scans, suggested that the MMT acted as a nucleating agent in iPP1[63] and that the β phase was induced by the crystalline orientation. The WAXS pattern from iPP1 filaments drawn at low velocity (360 m/min), Figure 4.19(a), showed rather diffuse crystal reflections. These crystal reflections became sharper with increasing drive-roll velocity, and, for iPP1 filaments drawn at 1400 m/min Figure 4.19(b), the reflections were reduced to spots along the meridian, indicating highly oriented crystals. In Figure 4.21(a), the corresponding peaks were less distinct owing to a lack of intensity in the signal.

For iPP1/MMT filaments and for a given MMT concentration, an increase in crystal orientation with increasing drive-roll velocity was also observed, as indicated by the increasing sharpness of the Debye rings (Figure 4.19(c) to Figure 4.19(d)), from Figure 4.19(e) to Figure 4.19(f) and from Figure 4.19(g) to Figure 4.19(h). Figure 4.20 compares the intensity versus 2θ of iPP1/MMT filaments drawn under similar conditions. A significant increase of the sharpness of the rings was also observed on addition of MMT, as seen in the 2D patterns (Figure 4.19(a) to Figure 4.19(c)) for example. However, under similar drawing conditions, neither the intensity of the peaks (Figure 4.19) nor the appearance of the 2D-WAXS patterns (Figure 4.19) from the iPP1/MMT filaments changed with increasing MMT content.

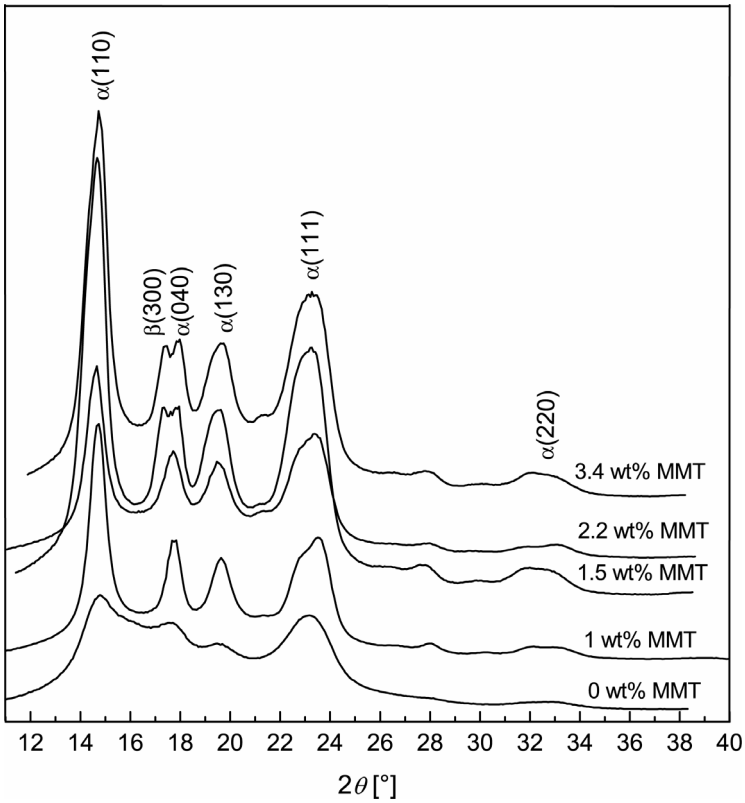

Figure 4.20. Average WAXS intensity profiles of iPP1/MMT filaments, DR = 1, drawn at 360 m/min with various MMT concentration. The crystallographic indices are indicated in brackets.

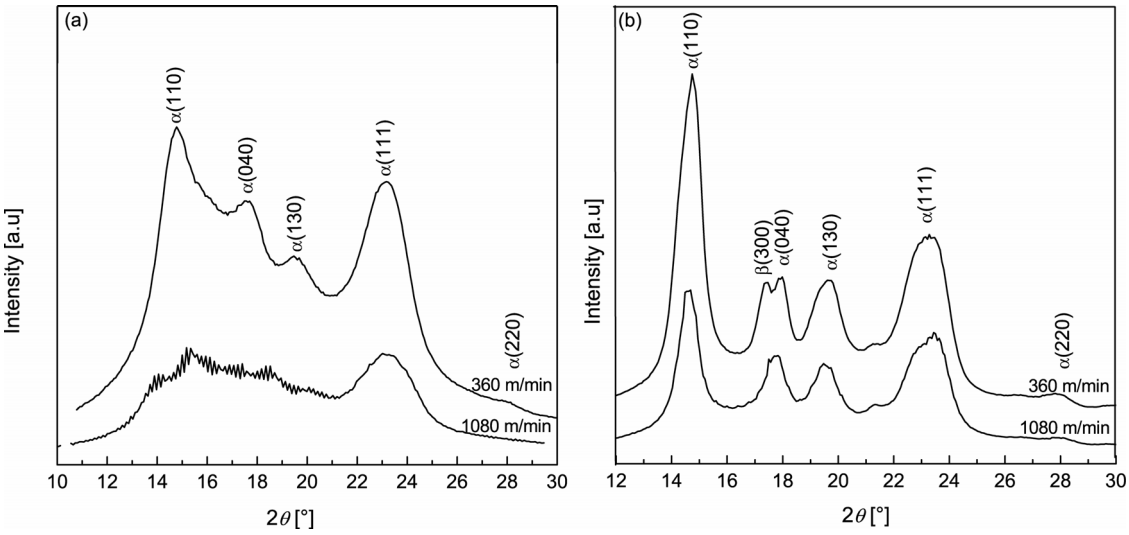

Figure 4.21. Average WAXS intensity profiles of (a) iPP1 filaments, DR = 1, drawn at 360 m/min and 1400 m/min and (b) iPP1/ 3.4 wt% MMT filaments, DR = 1, drawn at 360 m/min and 1080 m/min. The crystallographic indices are indicated in brackets.

The SAXS patterns from a pure iPP1 filament (Figure 4.22(a) and (b)) showed a large-

scale oriented structure. The meridional maxima perpendicular to the fiber axis are the signature of crystalline lamellae oriented perpendicular to the flow direction[61, 64]. The intensity of the equatorial scattering generally tended to diminish for iPP1 filaments drawn at higher drive-roll velocities, indicating that the orientation of the lamellae perpendicular to the flow direction was increased[65]. This tendency was also observed for iPP1/MMT filaments at fixed MMT content. On the other hand the intensity of the meridional maxima significantly increased on the addition of MMT platelets. This reinforcement of the meridional reflection is attributed to the MMT platelets themselves and implied that MMT were aligned parallel to the flow direction[66, 67], consistent with the TEM observations.

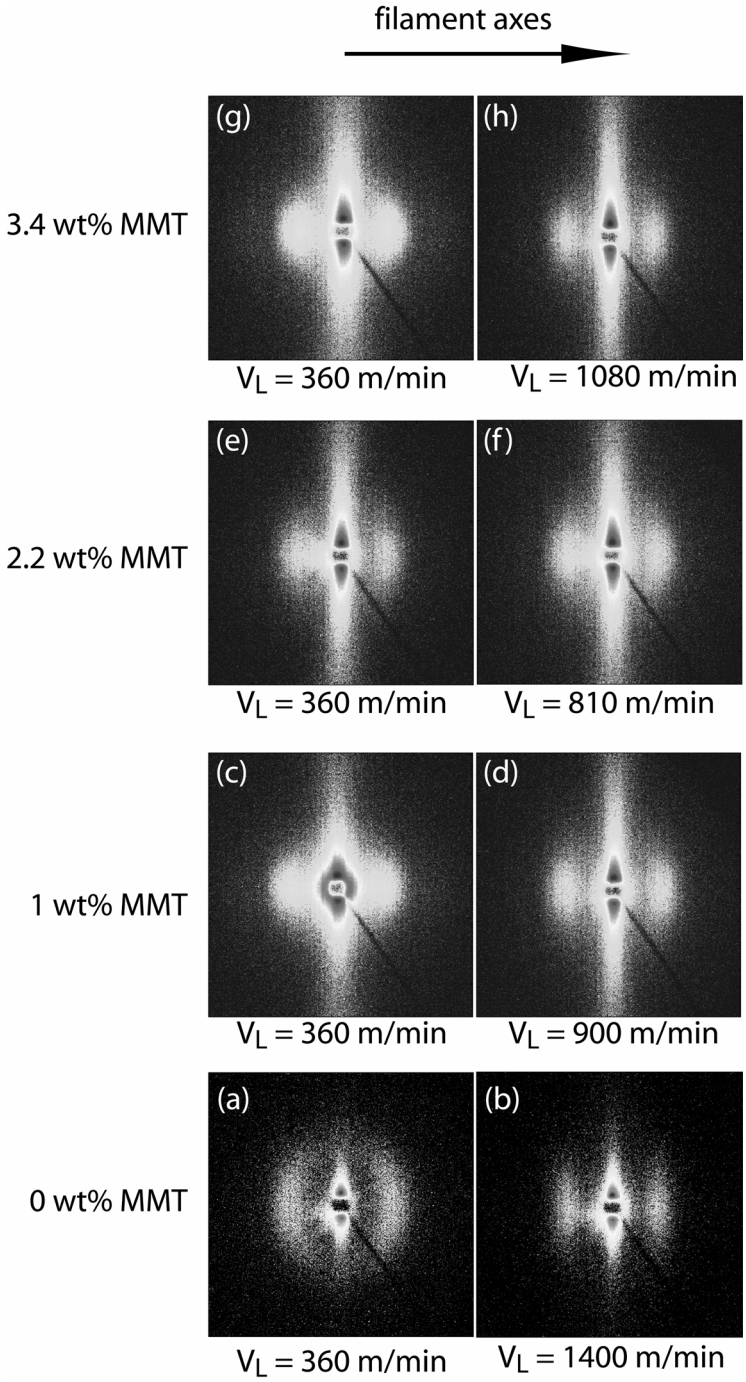

Figure 4.22. 2D-SAXS patterns of iPP1/MMT filaments with different MMT contents and drawn at different drive-roll velocity. The filament axis direction is along the equator and the drive-roll velocity is indicated below each micrograph.

The quantitative degree of lamellae crystal orientation in the iPP1/MMT filaments was estimated using the Herman-Stein method[68]. In this method, the crystalline orientation is characterized by average orientation of the normal to the crystalline plane with respect to an external reference frame. Here, the filament axis was taken to be the reference

direction. For a set of *hkl* planes, the average orientation, is expressed as $\langle\cos^2\phi\rangle_{hkl}$, calculated according to:

$$\langle\cos^2\phi\rangle_{hkl} = \frac{\int_0^{\frac{\pi}{2}} I(\phi)\cos^2\phi\sin\phi\,d\phi}{\int_0^{\frac{\pi}{2}} I(\phi)\sin\phi\,d\phi} \qquad \textbf{Equation 4.3}$$

where ϕ is the azimuthal angle and $I(\phi)$ is the scattered intensity along the angle ϕ. Herman-Stein's orientation factors, f_j, where j represents the **a**, **b** or **c** crystallographic axes of the unit cell, indicates the orientation of the crystallographic axis with respect to the fiber axis. There are defined as:

$$f_j = \frac{3\langle\cos^2\phi\rangle_{hkl} - 1}{2} \qquad \textbf{Equation 4.4}$$

where f_j = -0.5, when the crystals are oriented parallel to the filament axis, f_j = 1, when the crystals are oriented perpendicularly to the filament axis, and f_j = 0, when the orientation is random. f_b was determined from the intensity distribution in the (040) reflection. In monoclinic iPP, the chains are helices whose axes lie along the **c**-crystallographic axis. There is no convenient set of diffraction planes perpendicular to the **c**-axis, therefore (110) and (040) reflections were used to determine f_c from $\langle\cos^2\phi\rangle_{00l}$ according to[65]:

$$\langle\cos^2\phi\rangle_{00l} = 1 - 1.099\langle\cos^2\phi\rangle_{110} - 0.901\langle\cos^2\phi\rangle_{040} \qquad \textbf{Equation 4.5}$$

For orthogonal crystal axes,

$$f_a + f_b + f_c = 0 \qquad \textbf{Equation 4.6}$$

In the case of iPP, the **a**-axis is not perpendicular to the **c**-axis, but makes an angle of 99.3°. It is therefore convenient to define an **a***-axis, which is not a true crystallographic axis, but is perpendicular to both the **b**- and **c**-crystallographic axes and whose orientation factor is determined using Equation 4.6. The results of the calculation are shown in Table 4.3.

Table 4.3. iPP1/MMT filament Herman-Stein orientation factors as a function of drive roll velocity and MMT concentration.

	0 wt% MMT 360 m/min	1 wt% MMT 360 m/min	2.2 wt% MMT 360 m/min	3.4 wt% MMT 360 m/min
f_{a*}	- 0.10	- 0.020	- 0.12	0.05
f_b	- 0.09	- 0.20	- 0.19	- 0.17
f_c	0.19	0.22	0.31	0.12
	0 wt% MMT 1400 m/min	1 wt% MMT 900 m/min	2.2 wt% MMT 1500 m/min	3.4 wt% MMT 1080 m/min
f_{a*}	- 0.3	- 0.23	- 0.12	0.18
f_b	- 0.3	- 0.24	- 0.20	- 0.23
f_c	0.6	0.47	0.32	0.41

Under similar processing conditions, the orientation factors, f_{a*} and f_b, of iPP1/MMT filaments were negative and close to 0, indicating that there is no preferential orientation for these crystallographic axes. For a given MMT concentration, f_{a*} and f_b, decreased substantially due to a progressive orientation of **a*** and **b**-axes in the filament direction. Since the molecular chains of iPP1 lie along the **c**-axis**,** the latter is normal to iPP1 lamellae layers. According to Table 4.3, for iPP1/MMT filaments drawn at 360 m/min, f_c increased with MMT content up to 2.4 wt% but then decreased. Here again, it was verified that for a given MMT content, f_c increased with increasing drive-roll velocity.

d. Thermal characterization

Filaments are expected to undergo change in structure and properties as a function of temperature, duration of temperature exposure, composition of the environments, and other factors. These changes are characteristic of the polymer involved and thermal processes. They can interfere in post production processing operations for example. The thermal characteristics of the filaments were therefore determined by TMA and DTMA.

- *TMA*

In the spinning and drawing processes, randomly oriented polymer chains are aligned with the filament axis. When heat is applied to the filament, it provides mobility to the oriented molecular chains, which tend to return to their original randomly oriented state. This results in changes in length (usually a reduction), refered to as shrinkage. Shrinkage is not directly measurable by conventional thermomechanical analysis (TMA), since it is superimposed onto the thermal expansion of the filament[69]. However, this technique provides a useful indication of the influence of MMT platelets on the shrinkage and the thermal stability of the filaments.

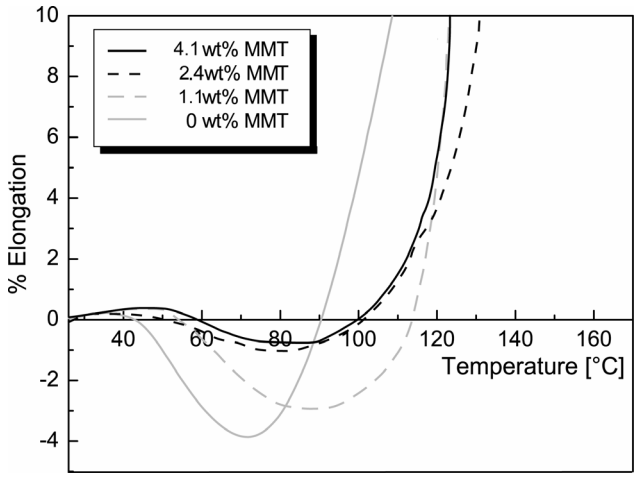

Figure 4.23. Percent elongation under tension as a function of temperature of fibers with different MMT concentration (DR = 1, V_L = 360 m/min).

The TMA curves in Figure 4.23 show changes in specimen length versus temperature for iPP1 and iPP1/MMT filaments produced under identical drawing conditions. The TMA curve is load-dependent and is the result of the balance between the applied load and the resistance to elongation of the sample[70]. During heating from room temperature, all the yarns initially underwent shrinkage, but then expanded abruptly at high temperatures. The expansion corresponded to the melting of the α-crystallites, causing a rapid decrease in fiber dimensional stability[71]. The small extension observed for all the yarns between 40 °C and 60 °C was attributed to the presence of non-oriented polymer chains in the samples. The temperature onset of shrinkage increased with MMT concentration. It was about 40 °C for pure iPP1 and about 55 °C for iPP1/4.1 wt% MMT. The extent of shrinkage, which was relatively large for pure iPP1 fibers, decreased with MMT concentration, and the stability of the fibers with respect to higher onset of creep temperature.

- *DTMA*

Although the addition of rigid inorganic particles to semicrystalline polymers results in stiffness reinforcement, other materials properties may also be altered, e.g. the response to time-dependant loads or deformations. The purpose of DTMA tests was to investigate the effect of drawing on the relaxation process and to understand the changes in viscoelastic behavior induced by MMT platelets.

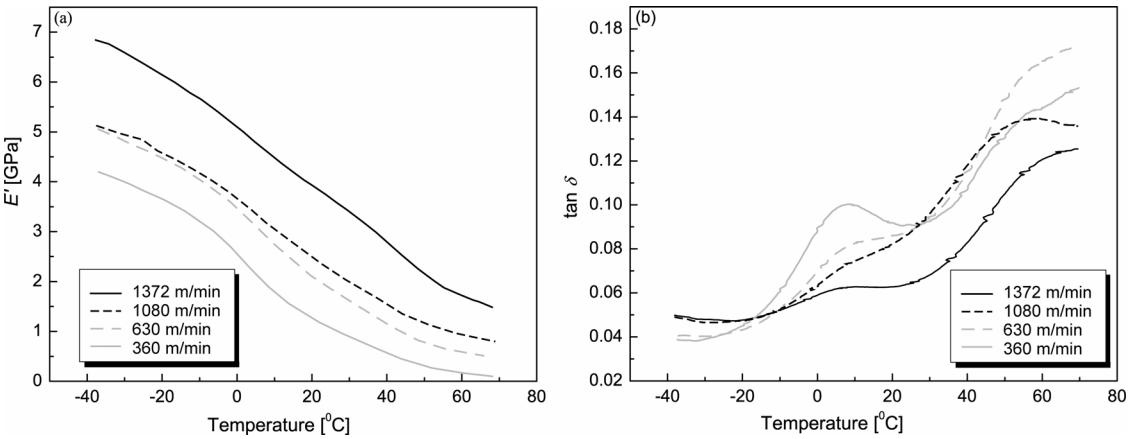

Figure 4.24. (a) Dynamic storage modulus *E'* and (b) loss factor tan *δ* as a function of temperature for pure iPP1 fibers with DR = 1. The drive roll velocities are given in brackets.

The dynamic mechanical properties of the fibers were measured in the temperature range -40 °C – 65 °C. In Figure 4.24(a), the storage modulus *E'* is plotted against temperature for pure iPP1 fibers for different drive-roll velocities. The increase in storage modulus *E'* as a function of the drive-roll velocity is typical of pure iPP1 fibers. Such behavior is explained by the transformation of the lamellar structure of iPP1 into a fibrillar structure. This process gives rise to constraints on the molecular mobility[72, 73]. Figure 4.24(b) shows the loss tangent (tan δ) as a function of temperature for the same specimens. The β-relaxation peak, corresponding to the glass transition temperature, was clearly discernible between 0 °C and 10 °C[74]. The β-relaxation peak intensity decreased with increasing draw ratio. Generally, the peak intensity is proportional to the volume fraction of the corresponding phase. The β-relaxation peak has been attributed to the transformation of the amorphous regions into a "pseudocrystalline" form[74, 75].This "pseudocrystalline" form is similar to the α crystalline form since only one peak of fusion was observed in DSC scans. It more difficult to assess the effect of drawing on iPP/MMT fibers due to large inhomogeneities in the specimens compared with the specimens length. Therefore unexpected results are observed in Figure 4.25(a). However, in Figure 4.25(b), the position of glass transition temperature of iPP1 filaments remained unchanged on drawing although it is possible to shift this transition to lower temperatures with higher draw ratios than those achieved in the present study[74].

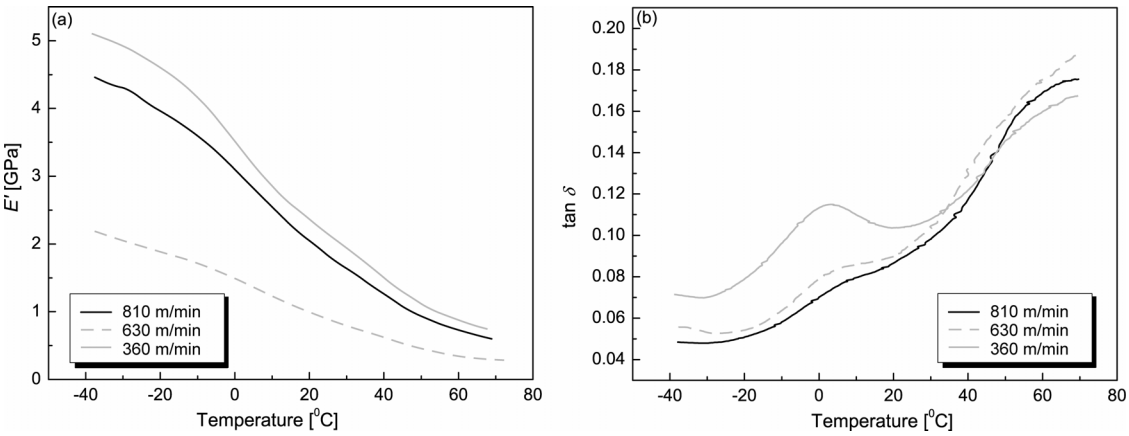

Figure 4.25. (a) Dynamic storage modulus *E'* and (b) loss factor tan *δ* as a function of temperature for iPP1/2.4wt% MMT fibers with DR = 1. The drive roll velocities are given in brackets.

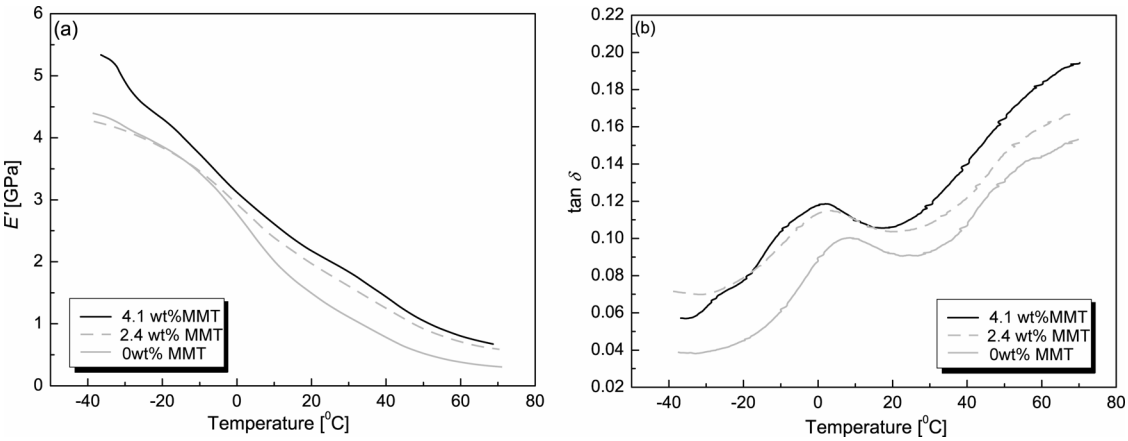

Figure 4.26.(a) Dynamic storage modulus *E'* and (b) loss factor tan *δ* as a function of temperature for iPP1/MMT fibers with DR = 1 and different MMT concentrations.

Dispersing MMT within iPP1 resulted in increased stiffness over a wide range of temperatures, shown in Figure 4.27(a) for filaments produced under the same processing conditions, and in Figure 4.26(a) for compression molded specimens. In the case of the filaments, the effect of the MMT was greater above the glass transition temperature of the matrix. This was thought to be primarily due to the increased difference in modulus between the filler and the matrix as the matrix passes from the glassy to the rubbery state. The filler, on the other hand, remains rigid over the entire temperature range.

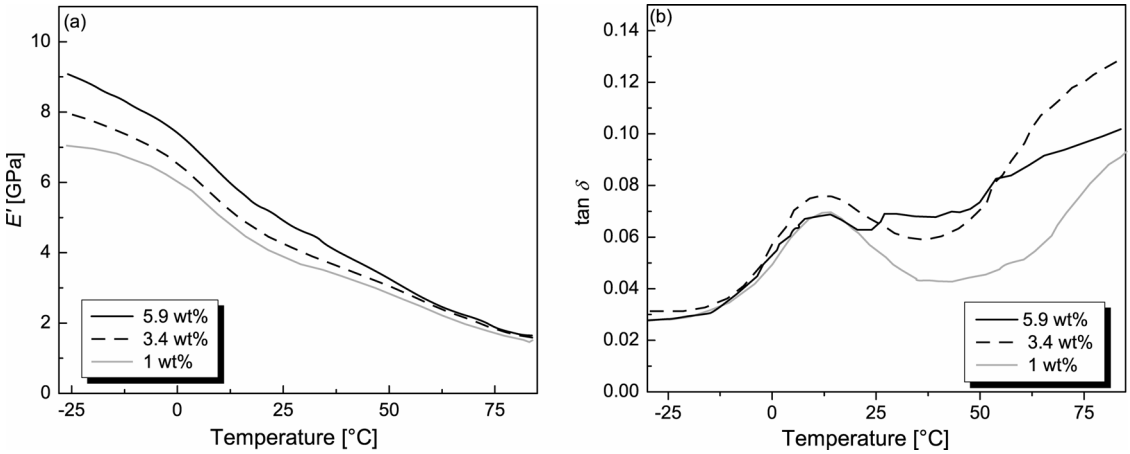

Figure 4.27. (a) Dynamic storage modulus *E'* and (b) loss factor tan δ as a function of temperature for iPP1/MMT compression moldings at different MMT concentrations.

In Figure 4.26(b), tan δ has been plotted for different MMT concentrations. The β relaxation in filaments with relatively high MMT concentrations (4.1 wt% MMT) occurred at lower temperatures and with higher peak intensities. The shift of the β relaxation to lower temperatures on the addition of MMT has been reported previously, for example, for the case of microsized sepiolite in iPP[76]. Masenelli-Varlot *et al.*[77] attribute a similar shift in the glass transition temperature of PA6/MMT nanocomposites prepared by melt compounding to a plasticizing effect due to the use of a compatibilizer. Their observations were in accordance with those of Vlasveld *et al.*[78] who did not observe any change in glass transition temperature for PA6-surface treated/MMT nanocomposites produced in absence of compatibilizer. In addition, Masenelli-varlot *et al.*[77] suggested that the filler geometry and orientation may be linked to mechanical coupling between the different phases, which could give rise to a modification in matrix behavior. The effect is also often attributed to the reduction of the segmental motions of iPP chains as a consequence of an intercalated microstructure[79],or to the existence of a complex interphase with a packing density that differs from that of unfilled iPP[76]. On the other hand, it is observed in Figure 4.26(b) that the glass transition temperature remained unchanged in the case of iPP1/MMT compression molded specimens.

4.3.2 Mechanical characterization

a. Tensile tests

The objectives of the tensile tests were to evaluate the influence of the MMT clay platelets on the mechanical properties of the iPP1 matrix and the relationships between the mechanical properties and the particle morphology induced by the processing route.

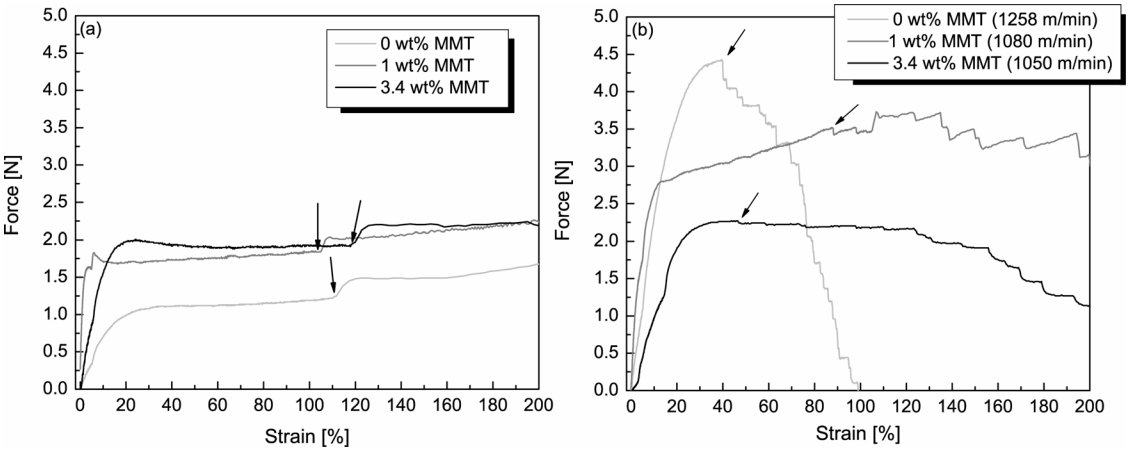

Figure 4.28. Typical force vs strian curves of (a) iPP1/MMT fibers melt-spun with DR =1 and V_L = 360 m/min and (b) iPP1/MMT fibers melt-spun with DR =1, the drive-roll velocity is indicated in bracket. The arrows indicate the first fiber break.

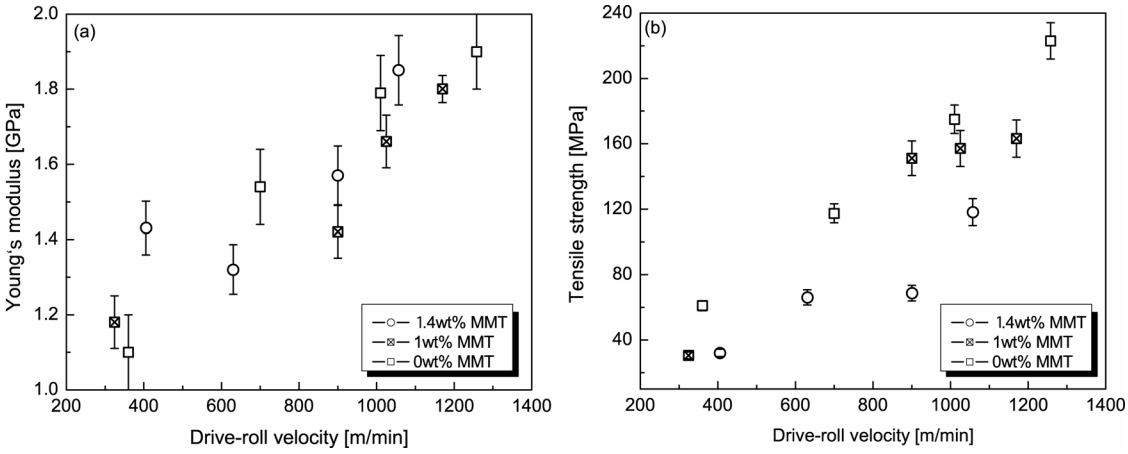

Figure 4.29. **(a) Young's modulus and (b) tensile strength of melt-spun filaments with DR = 1.**

Typical force versus strain curves of iPP1/MMT fibers are shown in Figure 4.28. The stiffness and the tensile strength of the fibers increased monotonically with drive-roll velocity for all MMT contents as shown in Figure 4.29(a) and (b). These nominal values of Young's modulus were consistent with those observed by DTMA at room temperature. DR had relatively little influence on the mechanical properties, even though the maximum attainable drive-roll velocity diminished significantly as discussed previously (Figure 4.7).

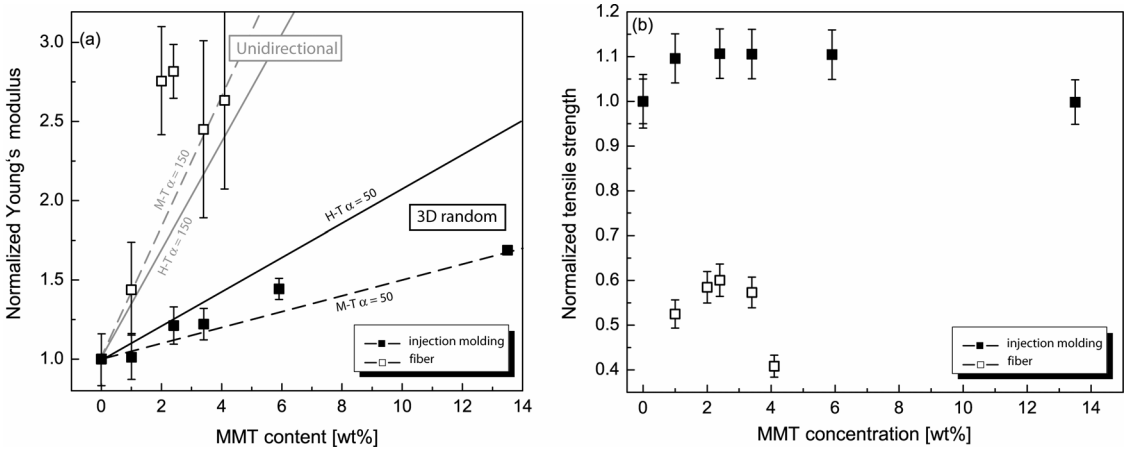

Figure 4.30. (a) Normalized Young's modulus E/E_0 of melt-spun filaments (DR = 1, V_L = 360 m/min) and specimens injection molded from the pre-compounded resin as a function of MMT content (E_0 = 1.4 GPa and E_0 = 1.1 GPa for the injection molded specimens and the filaments respectively); (b) normalized tensile strength for the same specimens. The curves in (a) correspond to Halpin-Tsai (H-T) and Mori-Tanaka (M-T) predictions for an isotropic composite with α = 50 and a uniaxially oriented composite with α = 150.

The Young's modulus increased monotonically with MMT content in injection moldings from the pre-mixed iPP1/MMT precursors Figure 4.30(a). This is a typical response for polymer/layered-inorganic particle nanocomposite materials. However, higher relative Young's moduli have been observed elsewhere for iPP/MMT (up to 2 for a 10 wt% loading)[80]. Indeed, Luo and Daniel[81] have pointed out that in the case of a random orientation of the platelets, among several parameters, including the exfoliation ratio, the clay aspect ratio, the interlayer spacing and the matrix modulus, a high degree of exfoliation is the most effective in enhancing the nanocomposite stiffness, along with the clay aspect ratio. Thus, for a given weight fraction, exfoliation is more favorable than intercalation in terms of mechanical properties. However, a very high aspect ratio of clay platelets places restrictions on the amount of clay that can be exfoliated and still remain dispersed and randomly oriented. Improvements of mechanical properties can also be obtained by optimization of the iPP1/compatibilizer ratio[82].

Results obtained from filaments produced under constant processing conditions (DR = 1, V_L = 360 m/min) with different MMT contents are also given Figure 4.30(a), indicating a far stronger relative increase in stiffness on MMT addition than in injection moldings. This follows from the higher degree of MMT particle orientation and the increased particle aspect ratios of the filaments. Beyond about 2 wt% of MMT, the Young's modulus of the fibers increased less. However, this may be due to the presence of the compatibilizer, which is usually of lower molecular weight and crystallinity than the iPP1 matrix, and has been shown previously to degrade the mechanical properties of iPP1 filaments[53, 83]. For injection moldings, as well as for the filaments, the tensile strength reached a maximum and then started to decrease[84] with further increase in MMT content.

The moduli of MMT reinforced nanocomposites are frequently modeled using scale independent micromechanical approaches developed for macroscopic particle reinforced

composites[81, 85-87]. Here the experimental results were compared with the approaches of Mori-Tanaka and Halpin-Tsai. The later have been chosen because they have been widely employed to model MMT-based nanocomposites[88]. The general assumptions are that the polymer and the inclusions are well bonded to each other, and that both show linear, isotropic and homogeneous elastic properties. It is also assumed that the particles, idealized as circular or ellipsoidal disks, are uniformly distributed in the matrix.

In the approach of Halpin and Tsai, the axial stiffness of a nanocomposite containing uniaxially aligned identical planar disc-shaped isotropic platelets may be obtained from[89],

$$E_{11} = E_0 \frac{1+\zeta \eta \phi_1}{1-\eta \phi_1} \qquad \textbf{Equation 4.7}$$

$$\eta = \frac{E_1 / E_2 - 1}{E_1 / E_0 + \zeta} \qquad \textbf{Equation 4.8}$$

derived by interpolating numerical solutions for aligned composites, where E_0 is the Young's modulus of the matrix, E_1 is the Young's modulus of the particles (usually taken to be equal to the in-plane modulus of mica (178 GPa)[86]), ϕ_1 is the particle volume fraction and $\zeta = 2\alpha$, where α is the aspect ratio of the platelets. Van Es *et al.*[85] have shown that the Young's modulus of a composite that contains randomly oriented platelets may be approximated by

$$E = 0.49E_{11} + 0.51E_{33} \qquad \textbf{Equation 4.9}$$

for small ϕ_1, where E_{33} is the modulus perpendicular to the planes of the platelets, which is approximately equal to E_0 for the range of compositions under consideration[23].

Mori-Tanaka average stress theory considers a non-dilute composite consisting of many identical spheroidal particles that cause the matrix to experience an average stress different from that of the applied stress. Tandon and Weng[90] used this theory to derive complete analytical solutions for the elastic moduli of an isotropic matrix filled with aligned spheroidal inclusions. Thus,

$$E_{11} = \frac{E_0 A}{A + \phi_1 (A_1 + 2\nu_0 A_2)} \qquad \textbf{Equation 4.10}$$

where v_0 is the Poisson's ratio of the matrix, and A_1, A_2 and A are functions of Eshelby's tensor given by Tandon *et al.*[90]. For small ϕ_1, the Mori-Tanaka predictions for randomly oriented speroids are well approximated by the expressions of Norris[91] for the bulk modulus, K, and the effective shear modulus, μ,

$$K = K_0 + \frac{4}{9}\phi_1 \left[\frac{\pi}{8\alpha} \frac{3-4\nu_0}{\mu_0(1-\nu_0)} + \frac{1}{\mu_1} \frac{1-\nu_1}{1+\nu_1} \right]^{-1} \qquad \textbf{Equation 4.11}$$

$$\mu = \mu_0 + \frac{1}{15}\phi_1\left[\frac{\pi}{8\alpha}\frac{3-4\nu_0}{\mu_0(1-\nu_0)} + \frac{1}{\mu_1}\frac{1-\nu_1}{1+\nu_1}\right]^{-1} + \frac{2}{5}\phi_1\left[\frac{\pi}{16\alpha}\frac{7-8\nu_0}{\mu_0(1-\nu_0)} + \frac{1}{\mu_1}\right]^{-1} \quad \textbf{Equation 4.12}$$

where K_0 is the bulk modulus of iPP1, ν_1 is the Poisson ratio of the MMT, and μ_0 and μ_1, the shear moduli of iPP1 and MMT respectively. For an isotropic material, the elastic constants are related by:

$$K = \frac{E}{3(1-2\nu)}, \qquad \mu = \frac{E}{2(1+\nu)}, \qquad E = \frac{9K\mu}{3K+\mu} \quad \textbf{Equation 4.13}$$

Halpin-Tsai and Mori-Tanaka approaches were compared with the data for the injection molded pre-compounded iPP1/MMT in Figure 4.30(a). Taking into account experimental scatter, these data suggest a value of α between about 10 and 50. This range of values is consistent with the morphological investigations of melt compounded iPP1/MMT described in section 3.3.2. Figure 4.30(a) also shows the reduced axial modulus, E_{11}/E_0, for the corresponding uniaxially oriented composite and the model E_{11}/E_0 ratio for α = 150. α = 150 accounted well for the behavior of filaments at low and high MMT contents and was consistent with the significant increase in α on fiber drawing implied by the morphological data. The axial modulus leveled off at around 2 wt% suggesting much higher values for α, but this may also be accounted for experimental scatter. Indeed, TEM images have shown that the MMT in the iPP1 have irregular shape, which may not be well approximated by a single aspect ratio[92].

As observed elsewhere[57], the Mori-Tanaka approach predicted significantly lower tensile stiffness than the Halpin-Tsai equations at intermediate α. However, both theories are very sensitive to filler aspect ratio for unidirectional reinforcement, and the data are generally in closer agreement in the aligned case[86]. Given the inconsistencies between, the theoretical assumptions and the real material, such as the potentially imperfect bonding between the filler and the matrix or a more or less wide distribution of lengths and thicknesses of the silica platelets, it appears that the two theories are effective in predicting the stiffness of the nanocomposite, especially in the random case.

As discussed above, the aspect ratio of the silica platelets has an important effect on the tensile modulus of the nanocomposite. However, this effect cannot be dissociated from the effect of the alignment in the present tests. Thus, the morphological changes induced by the melt-spinning process, i.e. a strong alignment of the platelets and an increase in intercalation are believed to be the main factors responsible for the increase in tensile modulus.

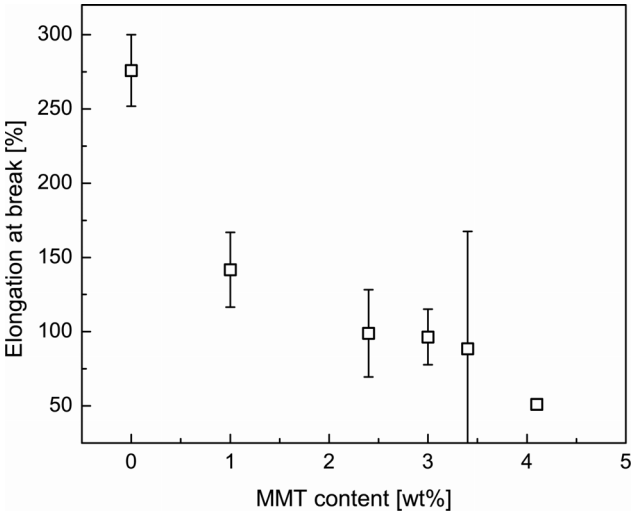

Figure 4.31. Ultimate strain as a function of MMT concentration for iPP1/MMT fibers with a DR = 1 and a drive-roll speed of 360m/min.

The ultimate elongation at break decreased monotonically with MMT content in fibers from about 300 % at 0 wt% to 50 % at 4.1 wt% of MMT. This decrease may be imputed to alteration of the matrix properties and/or reduced homogeneity in the MMT dispersion leading to agglomerates.

4.4 CONCLUSION

In this chapter, the influence of MMT on the spinnability of iPP1 melts has been investigated. It appeared difficult to establish a range of spinnability based only on simple steady-state shear rheology measurements. On the other hand, such measurements indicated a significant increase in the ratio of the elastic modulus to storage modulus on addition of MMT, which was argued to be a relevant parameter. Elongational measurements, involving deformations similar to those observed during melt-spinning were better suited to comparing the different MMT formulations. They indicated two contradictory effects of the MMT on the processability of iPP1/MMT formulations. On the one hand, the stability of the melts was increased and on the other hand the drawability of the filaments was decreased. These effects were well correlated with experimental results. Under identical processing conditions, the maximum content of MMT at which melt-spinning was possible was about 5 wt%, the major limitation being the maximum attainable drive-roll velocity. Among melt instabilities, only die swell was significantly detrimental for the nanocomposite spinnability. Its occurrence was directly related to the homogeneity of the nanocomposite and an additional pre-processing melt compounding operation is therefore recommended.

The melt-spinning operation induced significant changes in the nanocomposite morphology. Melt-spun filaments showed a significant orientation of both the iPP1 chains and the MMT platelets in the filament direction, associated with a slight increase

in the level of intercalation level and an increase in aspect ratio by about three times compared with injection molding specimens. The parameter responsible for the neat significant changes in morphology was identified to be the cold drawing provided by the drive-roll. However, highly drawn fibers are of limited interest for composite technology because they become highly dimensionnaly unstable during subsequent thermoforming operations, although MMT was found to increase the thermal stability and reduce the extent of shrinkage in the filaments. Moreover, any advantages from increased matrix orientation in the fibers is unlikely to be maintained in the final composites.

The presence of MMT platelets induced significant changes in the iPP1 matrix properties. For example the polymer chains arranged themselves perpendicularly to the platelet surfaces, as observed in TEM images. However, these changes were most relevant when associated with the oriented morphology observed in the filaments. The increase of stiffness in the filaments was linked to the presence, alignment and the aspect ratio of the silica platelets, all these parameters acting in the same way.

iPP1/MMT filaments could be produced using the same processing parameters as for pure iPP1 filaments. However, in industrial production, additional processing costs may need to be envisaged due to the necessary pre-processing operations. On the other hand, in terms of product quality and post-processing operations, MMT platelets may be beneficial, since they improve the thermal and dimensional stability of the filaments. Therefore, there are no major technical limitations for their use in co-mingled performs. Moreover, in addition to opening up a convenient route for introducing MMT platelets into conventional composites, the melt-spinning process increased the MMT particles with high aspect ratio, which should be favorable for the mechanical properties of the nanocomposite, even if the particle orientation is lost during subsequent processes.

4.5 REFERENCES

1 F. Fourné, **Synthetic Fibers. Machines and Equipment, Manufacture, Properties**, Hanser Publishers, Munich, (1998)

2 A. Ziabicki, **Fundamentals of fibre formation the science of fibre spinning and drawing**, Wiley, London a.o., (1976)

3 B. V. Gupta and K. V. Kothari, **Manufactured fibre technology**, Chapman & Hall, London, (1997)

4 Y. Ide and J. L. White, **Investigation of failure during elongational flow of polymer melts**, *Journal of Non-Newtonian Fluid Mechanics*, 1977; **2** 281-298

5 A. Abranyi, L. Szazdi, B. Pukanszky, G. J. Vancso and B. Pukanszky, **Formation and detection of clay network structure in poly (propylene)/layered silicate nanocomposites**, *Macromolecular Rapid Communications*, 2006; **27** (2): 132-135

6 K. M. Lee and C. D. Han, **Rheology of organoclay nanocomposites: Effects of polymer matrix/organoclay compatibility and the gallery distance of organoclay**, *Macromolecules*, 2003; **36** (19): 7165-7178

7 J. H. Tian, W. Yu and C. X. Zhou, **The preparation and rheology characterization of long chain branching polypropylene**, *Polymer*, 2006; **47** (23): 7962-7969

8 D. W. Chae, K. H. Lee and Y. C. Kim, **Rheological properties of ferrite nanocomposites based on nylon-66**, *Journal Of Polymer Science Part B-Polymer Physics*, 2006; **44** (2): 371-377

9 E. J. Lee, N. H. Kim, K. S. Dan and B. C. Kim, **Rheological properties of solutions of general-purpose poly(vinyl alcohol) in dimethyl sulfoxide**, *Journal Of Polymer Science Part B-Polymer Physics*, 2004; **42** (8): 1451-1456

10 B. Seyfzadeh and J. R. Collier, **Elongational Rheology of Polyethylene Melts**, *Journal of Applied Polymer Science*, 2001; **79** 2170-2184

11 R. Beyreuther and R. Vogel, **Spinnability of polymer melts - A complex problem in basic research**, *International Polymer Processing*, 1996; **11** (2): 154-158

12 C. Christiani, C. Klason and R. Shishoo, **The efffect of reprocessing of polypropylene on fiber spinning**, *Journal of Applied Polymer Science*, 1999; **73** 1859-1867

13 C. W. Macosko, **Rheology principles, measurements, and applications**, VCH, New York etc., (1994)

14 S. Muke, I. Ivanov, N. Kao and S. N. Bhattacharya, **The melt extensibility of polypropylene**, *Polymer International*, 2001; **50** (5): 515-523

15 M. Zatloukal, P. Stach, R. Liu and R. Saha, **Tensile strength characteristics of polymer melts**, *International Polymer Processing*, 2002; **17** (3): 223-227

16 D. R. Salem, **Structure formation in polymeric fibers**, Hanser, Munich, (2001)

17 A. Ghijsels, C. H. C. Massardier and R. M. Bradley, **Brittle melt rupture phenomena in polymer processing - An overview**, *International Polymer Processing*, 1997; **12** (2): 147-154

18 K. Feigl, F. Tanner, B. J. Edwards and J. R. Collier, **A numerical study of the measurement of elongational viscosity of polymeric fluids in a semihyperbolically converging die**, *Journal Of Non-Newtonian Fluid Mechanics*, 2003; **115** (2-3): 191-215

19 J. C. Huang and K. S. Leong, **Shear viscosity, extensional viscosity, and die swell of polypropylene in capillary flow with pressure dependency**, *Journal Of Applied Polymer Science*, 2002; **84** (6): 1269-1276

20 M. A. Couch and D. M. Binding, **High pressure capillary rheometry of polymeric fluids**, *Polymer*, 2000; **41** (16): 6323-6334

21 P. Micic and S. N. Bhattacharya, **Rheology of LLDPE, LDPE and LLDPE/LDPE blends and its relevance to the film blowing process**, *Polymer International*, 2000; **49** (12): 1580-1589

22 C. D. Han and Y. W. Kim, **Studies on melt spinning. V. Elongational viscosity and spinnability of two -phase systems**, *Journal of Applied Polymer Science*, 1974; **18** 2589-2603

23 T. Takahashi, J. I. Takimoto and K. Koyama, **Uniaxial elongational viscosity of various molten**

polymer composites, *Polymer Composites*, 1999; **20** (3): 357-366

24 S. B. Kil, T. Augros, Y. Leterrier, J. A. E. Månson, A. Christel and C. Borer, **Rheological properties of hyperbranched polymer/poly(ethylene terephthalate) reactive blends**, *Polymer Engineering And Science*, 2003; **43** (2): 329-343

25 C. Mobuchon, P. J. Carreau, M. C. Heuzey, M. Sepehr and G. Ausias, **Shear and extensional properties of short glass fiber reinforced polypropylene**, *Polymer Composites*, 2005; **26** (3): 247-264

26 M. F. Zhu, Q. Xing, H. K. He, Y. Zhang, Y. M. Chen, P. Potschke and H. J. Adler, **Preparation of PA6/nano titanium dioxide (TiO2) composites and their spinnability**, *Macromolecular Symposia*, 2004; **210** 251-261

27 F. P. La Mantia, S. Lo Verso and N. T. Dintcheva, **EVA copolymer based nanocomposites**, *Macromolecular Materials and Engineering*, 2002; **287** 909-914

28 K. H. Wang, M. Xu, Y. S. Choi and I. J. Chung, **Effect of aspect ratio of clay on melt extensional process of maleated polyethylene/clay nanocomposites**, *Polymer Bulletin*, 2001; **46** (6): 499-505

29 J. Z. Liang, **The melt elastic behavior of polypropylene/glass bead composites in capillary flow**, *Polymer Testing*, 2002; **21** (8): 927-931

30 R. Beyreuther, B. Tandler, M. Hoffmann and R. Vogel, **Reactive extrusion and melt spinning - A new technological route to special fibres**, *Journal Of Materials Science*, 2001; **36** (13): 3103-3111

31 Z. H. Tao and J. C. Huang, **Observation of melt fracture of polypropylene resins in capillary flow**, *Polymer*, 2003; **44** (3): 719-727

32 J. Z. Liang, **Estimation of die-swell ratio for polymer melts from exit pressure drop data**, *Polymer Testing*, 2001; **20** (1): 29-31

33 M. Mika, **Dispersive mixing oh high viscosity ratio polymer blends**, Thesis, EPFL, Lausanne, (2000)

34 J.-C. Huang and Z. Tao, **Melt Fracture, Melt Viscosities, and Die Swell of Polypropylene Resin in Capillary Flow**, *Journal of Applied Polymer Science*, 2003; **87** 1587-1594

35 S. G. Hatzikiriakos, N. Rathod and E. B. Muliawan, **The effect of nanoclays on the processibility of polyolefins**, *Polymer Engineering And Science*, 2005; **45** (8): 1098-1107

36 S. Chand, G. S. Bhat, J. E. Spruiell and S. Malkan, **Structure and properties of polypropylene fibers during thermal bonding**, *Thermochimica Acta*, 2001; **367-368** 155-160

37 J. Y. Nam, S. S. Ray and M. Okamoto, **Crystallization behavior and morphology of biodegradable polylactide/layered silicate nanocomposite**, *Macromolecules*, 2003; **36** (19): 7126-7131

38 X. Q. Zhang, M. S. Yang, Y. Zhao, S. M. Zhang, X. Dong, X. X. Liu, D. J. Wang and D. F. Xu, **Polypropylene/montmorillonite composites and their application in hybrid fiber preparation by melt-spinning**, *Journal Of Applied Polymer Science*, 2004; **92** (1): 552-558

39 J. S. Ma, S. M. Zhang, Z. N. Qi, G. Li and Y. L. Hu, **Crystallization behaviors of polypropylene/montmorillonite nanocomposites**, *Journal Of Applied Polymer Science*, 2002; **83** (9): 1978-1985

40 K. Wang, S. Liang, J. N. Deng, H. Yang, Q. Zhang, Q. Fu, X. Dong, D. J. Wang and C. C. Han, **The role of clay network on macromolecular chain mobility and relaxation in isotactic polypropylene/organoclay nanocomposites**, *Polymer*, 2006; **47** (20): 7131-7144

41 R. Nowacki, B. Monasse, E. Piorkowska, A. Galeski and J. M. Haudin, **Spherulite nucleation in isotactic polypropylene based nanocomposites with montmorillonite under shear**, *Polymer*, 2004; **45** (14): 4877-4892

42 A. Somwangthanaroj, E. C. Lee and M. J. Solomon, **Early stage quiescent and flow-induced crystallization of intercalated polypropylene nanocomposites by time-resolved light scattering**, *Macromolecules*, 2003; **36** (7): 2333-2342

43 J. Karger-Kocsis, **Polypropylene structure, blends and composites**, Chapman & Hall, London etc., (1995)

44 J. D. He, M. K. Cheung, M. S. Yang and Z. N. Qi, **Thermal stability and crystallization kinetics of isotactic polypropylene/organomontmorillonite nanocomposites**, *Journal Of Applied*

Polymer Science, 2003; **89** (12): 3404-3415

45 S. Hambir, N. Bulakh and J. P. Jog, **Polypropylene/clay nanocomposites: Effect of compatibilizer on the thermal, crystallization and dynamic mechanical behavior**, *Polymer Engineering And Science*, 2002; **42** (9): 1800-1807

46 L. Razafimahefa, S. Chlebicki, I. Vroman and E. Devaux, **Effect of nanoclay on the dyeing ability of PA6 nanocomposite fibers**, *Dyes And Pigments*, 2005; **66** (1): 55-60

47 A. Pozsgay, T. Frater, L. Papp, I. Sajo and B. Pukanszky, **Nucleating effect of montmorillonite nanoparticles in polypropylene**, *Journal Of Macromolecular Science-Physics*, 2002; **B41** (4-6): 1249-1265

48 P. Svoboda, C. C. Zeng, H. Wang, L. J. Lee and D. L. Tomasko, **Morphology and mechanical properties of polypropylene/organoclay nanocomposites**, *Journal Of Applied Polymer Science*, 2002; **85** (7): 1562-1570

49 Y. Kojima, A. Usuki, M. Kawasumi, A. Okada, T. Kurauchi, O. Kamigaito and K. Kaji, **Novel Preferred Orientation In Injection-Molded Nylon 6-Clay Hybrid**, *Journal Of Polymer Science Part B-Polymer Physics*, 1995; **33** (7): 1039-1045

50 K. Wang, P. Zhao, H. Yang, S. Liang, Q. Zhang, R. N. Du, Q. A. Fu, Z. Q. Yu and E. Q. Chen, **Unique clay orientation in the injection-molded bar of isotactic polypropylene/clay nanocomposite**, *Polymer*, 2006; **47** (20): 7103-7110

51 A. Bafna, G. Beaucage, F. Mirabella and S. Mehta, **3D Hierarchical orientation in polymer-clay nanocomposite films**, *Polymer*, 2003; **44** (4): 1103-1115

52 G. Galgali, S. Agarwal and A. Lele, **Effect of Clay Orientation on the Tensile Modulus of Polypropylene-Nanoclay Composites**, *Polymer*, 2004; **45** 6059-6069

53 S. Pavlikova, R. Thomann, P. Reichert, R. Mulhaupt, A. Marcincin and E. Borsig, **Fiber spinning from poly(propylene)-organoclay nanocomposite**, *Journal Of Applied Polymer Science*, 2003; **89** (3): 604-611

54 Z. Mlynarcikova, D. Kaempfer, R. Thomann, R. Mulhaupt, E. Borsig and A. Marcincin, **Syndiotactic poly(propylene)/organoclay nanocomposite fibers: influence of the nano-filler and the compatibilizer on the fiber properties**, *Polymers For Advanced Technologies*, 2005; **16** (5): 362-369

55 P. Maiti and M. Okamoto, **Crystallization controlled by silicate surfaces in nylon 6-clay nanocomposites**, *Macromolecular Materials And Engineering*, 2003; **288** (5): 440-445

56 G. M. Kim, D. H. Lee, B. Hoffmann, J. Kressler and G. Stoppelmann, **Influence of nanofillers on the deformation process in layered silicate/polyamide-12 nanocomposites**, *Polymer*, 2001; **42** (3): 1095-1100

57 N. Sheng, M. C. Boyce, D. M. Parks, G. C. Rutledge, J. I. Abes and R. E. Cohen, **Multiscale micromechanical modeling of polymer/clay nanocomposites and the effective clay particle**, *Polymer*, 2004; **45** (2): 487-506

58 M. Okamoto, P. H. Nam, P. Maiti, T. Kotaka, N. Hasegawa and A. Usuki, **A house of cards structure in polypropylene/clay nanocomposites under elongational flow**, *Nano Letters*, 2001; **1** (6): 295-298

59 M. Okamoto, P. H. Nam, P. Maiti, T. Kotaka, T. Nakayama, M. Takada, M. Ohshima, A. Usuki, N. Hasegawa and H. Okamoto, **Biaxial flow-induced alignment of silicate layers in polypropylene/clay nanocomposite foam**, *Nano Letters*, 2001; **1** (9): 503-505

60 A. Keller and H. W. H. Kolnaar, **Processing of polymers** in *Processing of polymers*, pp 189, Wiley-VCH, Weinheim etc. (1997)

61 R. H. Somani, L. Yang, L. Zhu and B. S. Hsiao, **Flow-induced shish-kebab precursor structures in entangled polymer melts**, *Polymer*, 2005; **46** (20): 8587-8623

62 G. H. Guan, C. C. Li and D. Zhang, **Spinning and properties of poly(ethylene terephthalate)/organomontmorillonite nanocomposite fibers**, *Journal Of Applied Polymer Science*, 2005; **95** (6): 1443-1447

63 G. Machado, E. L. G. Denardin, E. J. Kinast, M. C. Goncalves, M. A. de Luca, S. R. Teixeira and D. Samios, **Crystalline properties and morphological changes in plastically deformed isotatic polypropylene evaluated by X-ray diffraction and transmission electron microscopy**, *European Polymer Journal*, 2005; **41** (1): 129-138

64 S. F. Ran, C. Burger, I. Sics, K. Yoon, D. F. Fang, K. S. Kim, C. Avila-Orta, J. Keum, B. Chu, B. S. Hsiao, D. Cookson, D. Shultz, M. Lee, J. Viccaro and Y. Ohta, **In situ synchrotron SAXS/WAXD studies during melt spinning of modified carbon nanofiber and isotactic polypropylene nanocomposite**, *Colloid and Polymer Science*, 2004; **282** (8): 802-809

65 C. H. Choi and J. L. White, **Comparative study of structure development in melt spinning polyolefin fibers**, *International Polymer Processing*, 1998; **13** (1): 78-87

66 W. Ke, X. Yan, N. Bing, T. Hong, Z. Qin and F. Qiang, **Shear amplification and re-crystallization of isotactic polypropylene from an oriented melt in presence of oriented clay platelets**, *Polymer*, 2005; **46** (21): 9022-9032

67 C. M. Koo, M. J. Kim, M. H. Choi, S. O. Kim and I. J. Chung, **Mechanical and rheological properties of the maleated polypropylene-layered silicate nanocomposites with different morphology**, *Journal Of Applied Polymer Science*, 2003; **88** (6): 1526-1535

68 H. P. Nadella, H. M. Henson, J. E. Spruiell and J. L. White, **Melt Spinning Of Isotactic Polypropylene - Structure Development And Relationship To Mechanical-Properties**, *Journal Of Applied Polymer Science*, 1977; **21** (11): 3003-3022

69 R. Riesen and J. E. K. Schawe, **Expansion and shrinkage of fibers. Load- and temperature modulated TMA measurements temperature calibration of fiber attachments**, *Journal Of Thermal Analysis And Calorimetry*, 2000; **59** (1-2): 337-350

70 J. N. Cao and A. Y. Bhoyro, **Structural characterization of wool by thermal mechanical analysis of yarns**, *Textile Research Journal*, 2001; **71** (1): 63-66

71 Y. C. Bhuvanesh and V. B. Gupta, **Interaction between viscoelastic and structural relaxation in drawn polypropylene yarn**, *Polymer*, 1995; **36** (19): 3669-3674

72 O. Fricova, D. Olcak, L. Sevcovic and O. Durcova, **NMR and dynamic mechanical studies of the drwan polypropylene fibers**, *Acta polym.*, 1998; **49** 495-501

73 J. Hautojärvi and A. Leijala, **A morphological study of melt-spun polypropylene filaments by atomic force microscopy**, *Journal of Applied Polymer Science*, 1999; **74** 1242-1249

74 S. K. Roy, T. Kyu and R. St. J. Manley, **Physical and dynamic mechanical properties of ultradrawn polypropylene films**, *Macromolecules*, 1988; **21** 499-504

75 M. B. Elias, R. Machado and S. V. Canevarolo, **Thermal and dynamic-mechanical characterization of uni-and biaxially oriented polypropylene films**, *Journal of thermal analysis and calorimetry*, 2000; **59** 143-155

76 E. Morales, M. C. Ojeda, A. Linares and J. L. Acosta, **Dynamic Mechanical Analysis Of Polypropylene Composites Based On Surface-Treated Sepiolite**, *Polymer Engineering And Science*, 1992; **32** (12): 769-772

77 K. Masenelli-Varlot, E. Reynaud, G. Vigier and J. Varlet, **Mechanical properties of clay-reinforced polyamide**, *Journal Of Polymer Science Part B-Polymer Physics*, 2002; **40** (3): 272-283

78 D. P. N. Vlasveld, H. E. N. Bersee and S. J. Picken, **Nanocomposite matrix for increased fibre composite strength**, *Polymer*, 2005; **46** (23): 10269-10278

79 C. Ding, D. M. Jia, H. He, B. C. Guo and H. Q. Hong, **How organo-montmorillonite truly affects the structure and properties of polypropylene**, *Polymer Testing*, 2005; **24** (1): 94-100

80 E. Manias, A. Touny, L. Wu, K. Strawhecker, B. Lu and T. C. Chung, **Polypropylene/Montmorillonite nanocomposites. Review of the synthetic routes and materials properties**, *Chemistry of Materials*, 2001; **13** (10): 3516-3523

81 J. J. Luo and I. M. Daniel, **Characterization and modeling of mechanical behavior of polymer/clay nanocomposites**, *Composites Science And Technology*, 2003; **63** (11): 1607-1616

82 D. Marchant and K. Jayaraman, **Strategies for optimizing polypropylene-clay nanocomposite structure**, *Industrial & Engineering Chemistry Research*, 2002; **41** (25): 6402-6408

83 P. Reichert, H. Nitz, S. Klinke, R. Brandsch, R. Thomann and R. Mulhaupt, **Poly(propylene)/organoclay nanocomposite formation: Influence of compatibilizer functionality and organoclay modification**, *Macromolecular Materials And Engineering*, 2000; **275** (2): 8-17

84 Z. Mlynarcikova, E. Borsig, J. Legen, A. Marcincin and P. Alexy, **Influence of the composition of polypropylene/organoclay nanocomposite fibers on their tensile strength**, *Journal Of*

Macromolecular Science-Pure And Applied Chemistry, 2005; **A42** (5): 543-554

85 M. Van Es, F. Xiqiao, J. Van Turnhout and E. Van der Giessen, **Comparing Polymer-Clay Nanocomposites with Conventional Composites using Composite Modeling** in *Specialty polymer additives principles and applications*, pp 484, Blackwell Science, Oxford (2001)

86 T. D. Fornes and D. R. Paul, **Modeling properties of nylon 6/clay nanocomposites using composite theories**, *Polymer*, 2003; **44** (17): 4993-5013

87 J.-I. weon and H.-J. Sue, **Effects of clay orientation and aspect ratio on mechanical behavior of nylon-6 nanocomposite**, *Polymer*, 2005; **46** (6325-6334):

88 C. J. G. Plummer, M. Rodlert, J. L. Bucaille, H. J. M. Grunbauer and J. A. E. Månson, **Correlating the rheological and mechanical response of polyurethane nanocomposites containing hyperbranched polymers**, *Polymer*, 2005; **46** (17): 6543-6553

89 J. C. Halpin and J. L. Kardos, **Halpin-Tsai Equations - Review**, *Polymer Engineering And Science*, 1976; **16** (5): 344-352

90 G. P. Tandon and G. J. Weng, **The Effect Of Aspect Ratio Of Inclusions On The Elastic Properties Of Unidirectionally Aligned Composites**, *Polymer Composites*, 1984; **5** (4): 327-333

91 J. Wang and R. Pyrz, **Prediction of the overall moduli of layered silicate-reinforced nanocomposites-part I: basic theory and formulas**, *Composites Science and technology*, 2004; **64** 925-934

92 K. Y. Lee and D. R. Paul, **A model for composites containing three-dimensional ellipsoidal inclusions**, *Polymer*, 2005; **46** (21): 9064-9080

CHAPTER 5

MELT-SPUN iPP/CNF FILAMENTS

5.1 INTRODUCTION

The discovery of nanocarbons has opened up new possibilities, not only for reinforcement, but also for introducing new functionalities into polymer composites. However, the limited availability of nanocarbons and their high price have restricted implementation of polymer/nanocarbon composites. Nowadays CNF produced by a catalytic vapor deposition process from hydrocarbons are available on the market at a relatively low price compared with other nanocarbon products. It is therefore of interest to assess their use in composite materials.

In the previous chapter it has been demonstrated that iPP/MMT nanocomposites can successfully be melt-spun. The objective of the present chapter is to use the guidelines developed in the previous chapter to assess the melt-spinning of iPP/nanocarbons. Achieving a satisfactory degree of homogeneity in the nanocomposites is one of the major challenges involved in the use of nanocarbons as fillers in thermoplastics. Two simple methods are described here along with the corresponding morphological results. The different melt-spinning trials are discussed in terms of the nanocomposite morphology and tensile properties. Therefore iPP1/CNF yarns have been produced by melt spinning in order to (i) assess melt-spinning as a simple tool for aligning nanocarbons and further to (ii) incorporate nanocarbons into conventional composites with a satisfactory degree of dispersion and in a form suited to large scale production.

5.2 MATERIALS AND METHODS

5.2.1 Materials

Two types of nanocarbons have been used in this study: vapor grown carbon nanofibers (VGCF) and multi-walled carbon nanotubes (MWNT). Both were melt-compounded with iPP1.

a. Vapor grown nanofibers (VGCF)

The VGCF used for this study are catalytically grown by a vapour deposition process and purchased from Applied Sciences. Inc. (ASI, Cedarville, OH). They are referred to as Pyrograf™ III, PR-24-LHT. In this study they are denoted CNF.

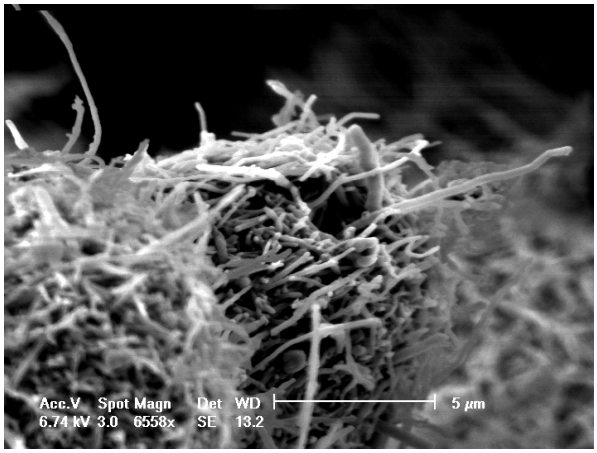

Figure 5.1. SEM micrograpf of as-received PR-24-LHT carbon nanofibers

As seen inFigure 5.1, the as-received fibers were entangled in a loosely packed fibrous matrix of interwoven bundles and aggregates, making handling and fiber dispersion a major challenge. The bundles were up to several tens of microns in diameter. For further morphological investigations, the as-received fibers were dispersed in acetone and several drops of the mixture were poured into an Epofix embedding medium. After curing of the resin, thin utramicrotomed sections were observed by TEM. CNF showed a wide range of diameters and lengths. It had a hollow structure and a mean diameter of about 100 nm (Figure 5.2(a)). A systematic study of CNF length indicated the fiber length to be comprised between 10 and 80 μm^1. Figure 5.2(b) shows a detail of a CNF wall. The regular fringes corresponded to concentric graphitic layers indicating that the CNF were multi-walled.

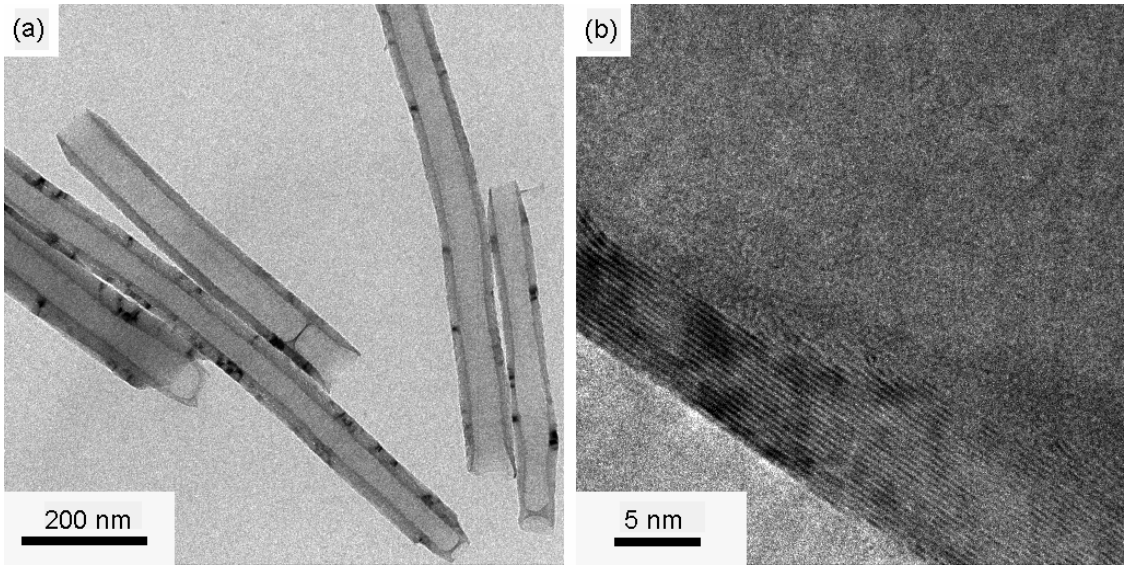

Figure 5.2. TEM micrographs of as-received CNF at different magnifications.

Figure 5.3 shows a CNF embedded in iPP1. The specimen was prepared by melt-blending with a twin-screw extruder as described in section 7.2.2. It was shown that the CNF are flexible objects that are easily bent during processing. This flexibility makes it difficult to overcome entanglements formed during production, and to align the CNF.

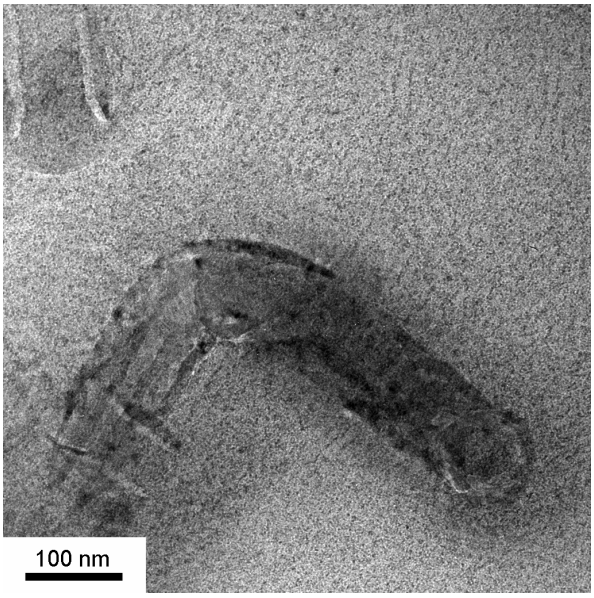

Figure 5.3. TEM micrograph of a CNF in a iPP1 matrix.

b. Multi-walled nanotubes (MWNT)

MWNTs were produced by a CVD laboratory process[2]. In the present study they are denoted CNT. Typical images of a CNTs embedded in iPP1, prepared by melt-blending as described in section 7.2.2, are shown in Figure 5.4(a) and at a higher magnification in Figure 5.4(b). The CNTs showed a more narrow distribution in size and diameter than the CNFs. Their length was about 0.5 μm and their diameter was about 50 nm.

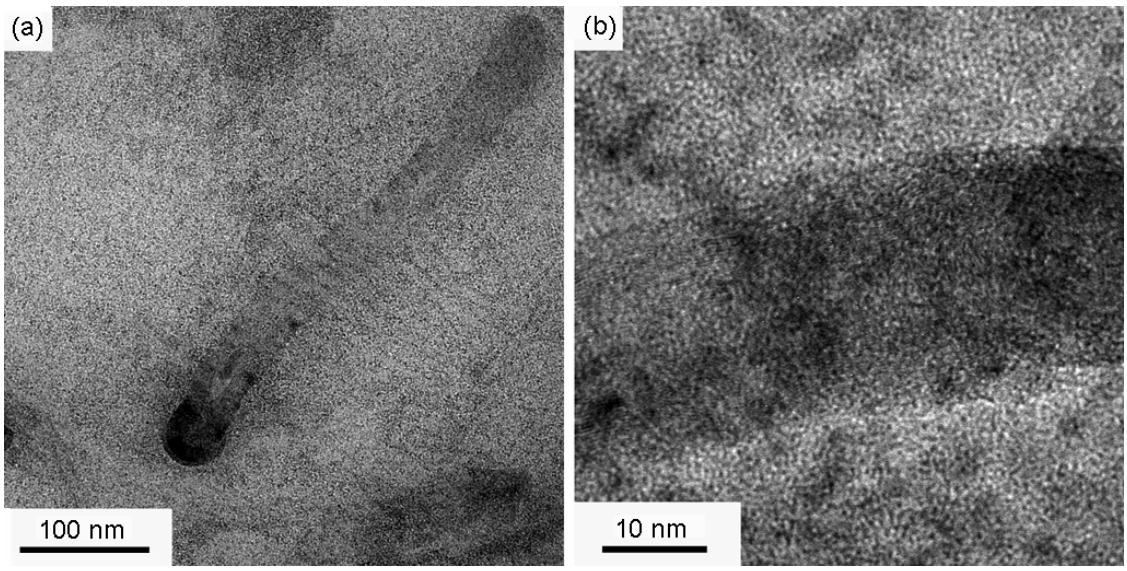

Figure 5.4. TEM micrographs of CNT in iPP1 matrix.

5.2.2 Preparation

a. Direct melt-mixing

The first attempt to prepare a iPP1/CNF composite was a one step extrusion process to give a iPP1/3.5 wt% CNF masterbatch. The iPP1 pellets and the as-received CNF were weighed and mixed manually. PPMAH granulates were added at 2 wt% relative to the CNF. The mixture was then directly fed into the Prism twin-screw extruder described in section 3.1.1. The extruder temperatures were set to 180 °C, 180 °C and 200 °C respectively from the entrance to the die. Composites of iPP1/ 0.35, 0.4, 0.87, 1.75 wt% CNF were produced by diluting the extruded masterbatch of 3.5 wt% CNF with the unmodified iPP1 granulates to obtain the desired concentrations.

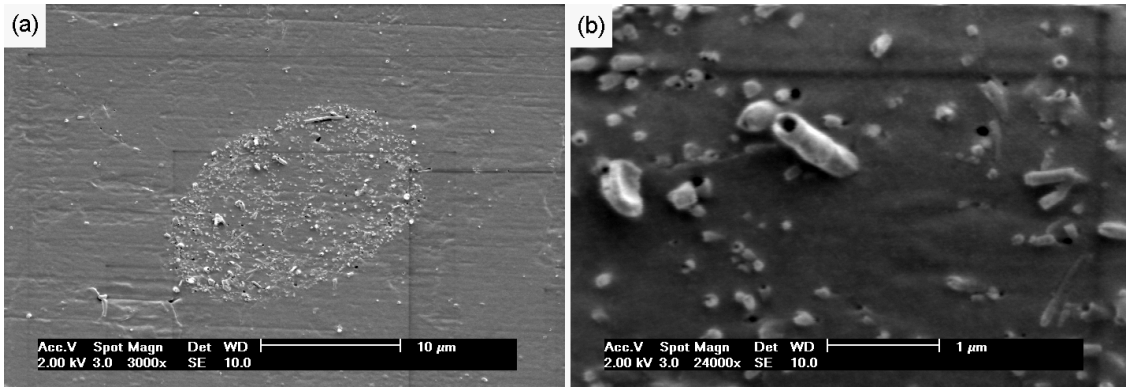

Figure 5.5. SEM micrographs of an iPP1/0.4 wt% CNF agglomerate.

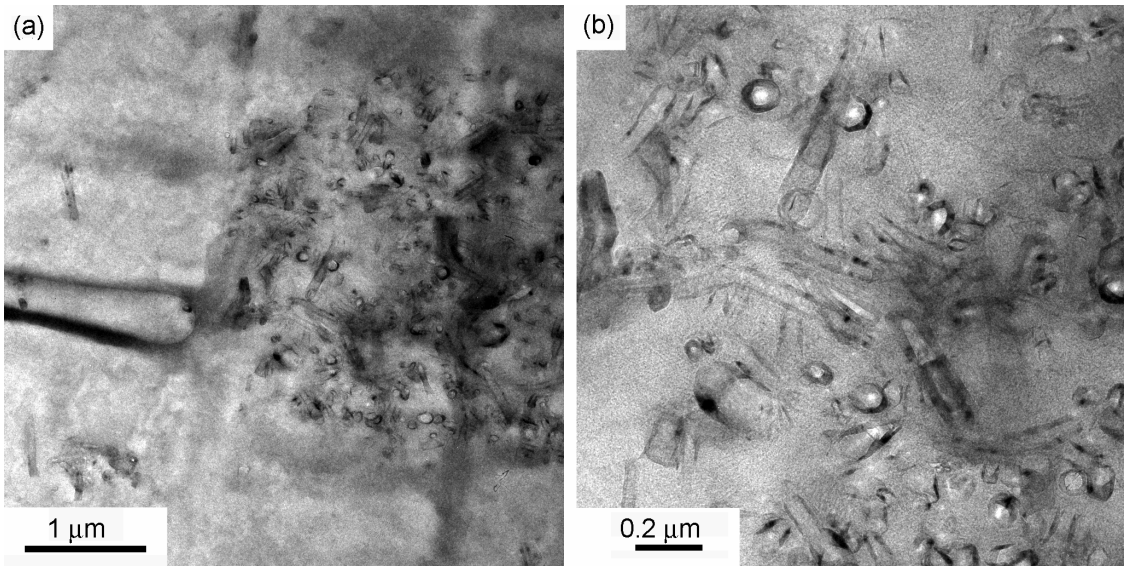

Figure 5.6. TEM micrographs of a iPP1/0.4 wt% CNF agglomerate.

It was expected that applying shear to the aggregates during the compounding process would destroy most of the aggregates. However, SEM images of extrusion compounded samples (Figure 5.5(a)) showed that large aggregates still existed in the nanocomposite even at low loading levels (0.4 wt% CNF). The aggregates were randomly distributed throughout the composite and their diameter was about 10 μm. From the higher magnification image of the aggregate (Figure 5.5(b)), the CNF appeared to be randomly oriented. Figure 5.6(a) shows a TEM image of an aggregate in the same iPP1/0.4 wt% CNF. The aggregate was about 2 μm in diameter and the entanglement of the CNF is visible in Figure 5.6(b), as well as the large dispersion in diameters of the CNF. These observations indicated that the shear forces developed during extrusion were not sufficient to break up all CNF bundles. Another drawback of the single step melt extrusion process is that large quantities of as-received CNF need to be handled to

produce the masterbatch. Hand mixing of the iPP1 granulates with the CNF results in a significant amount of dust, which requires sealing of the twin-screw feeder to avoid extensive contamination of the surrounding air[3, 4].

b. Combined dilution in solvent and melt-mixing

Due to the unsatisfactory levels of dispersion provided by the single melt-mixing procedure, a different route was investigated for the preparation of iPP1/CNF nanocomposites. Haggenmuller *et al.*[5] have demonstrated the potential of a combined solvent and extrusion process, and a similar procedure was therefore adopted. The idea is (i) to break up the CNF agglomerates in the liquid phase by sonication and (ii) to promote the interaction between the CNF and the iPP1 chains in the liquid state by magnetic stirring.

The detailed procedure was as follows: the CNF were weighed and dissolved in 250 ml of xylene. The solution was then subjected to sonication (Sonopulse stick) for 15 min. After sonication, the appearance of the solution changed from a light grey suspension with large precipitates to a dark macroscopically homogeneous solution. Thus destruction of the largest aggregates was confirmed visually. iPP1 and PPMAH were immediately added to the solution in desired concentration. The CNF to PPMAH weight ratio was maintained constant at 0.02. The solution was then stirred and heated at 250 °C, above the boiling point of xylene. After about 5 h to 6 h the solvent was almost completely evaporated and the resulting slurry was placed in a vacuum oven at 100 °C for several days for further removal of the solvent. After complete drying, the remaining solid was roughly chopped under liquid nitrogen and fed into a DSM 5 twin-screw micro-extruder, at 80 rpm at 220 °C for 5 min, and pelletelized. The following weight fractions were prepared; 1 wt%, 4 wt%, 6 wt% and 10 wt % CNF. The same procedure was used to produce iPP1/CNT composites.

Figure 5.7 shows a TEM picture of the typical morphology of iPP1/CNF composites produced by the combined solvent and melt-mixing procedure. The CNF showed less entanglement and were randomly oriented. However the homogeneity was not optimum and the specimen still contained regions with a relatively high concentration of CNF.

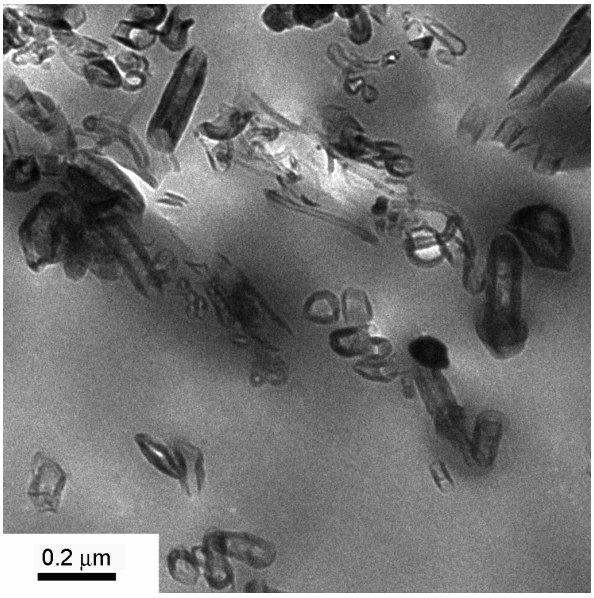

Figure 5.7. Typical TEM micrograph of iPP1/10 wt% CNF synthesized by the combined solvent and melt-mixing procedure.

This processing route was more successful for the CNT. As seen in Figure 5.8(a), regions of well dispersed CNT were observed throughout the specimen, even at high CNT loadings. However, Figure 5.8(b) shows that small aggregates persisted (about 0.2 μm in diameter).

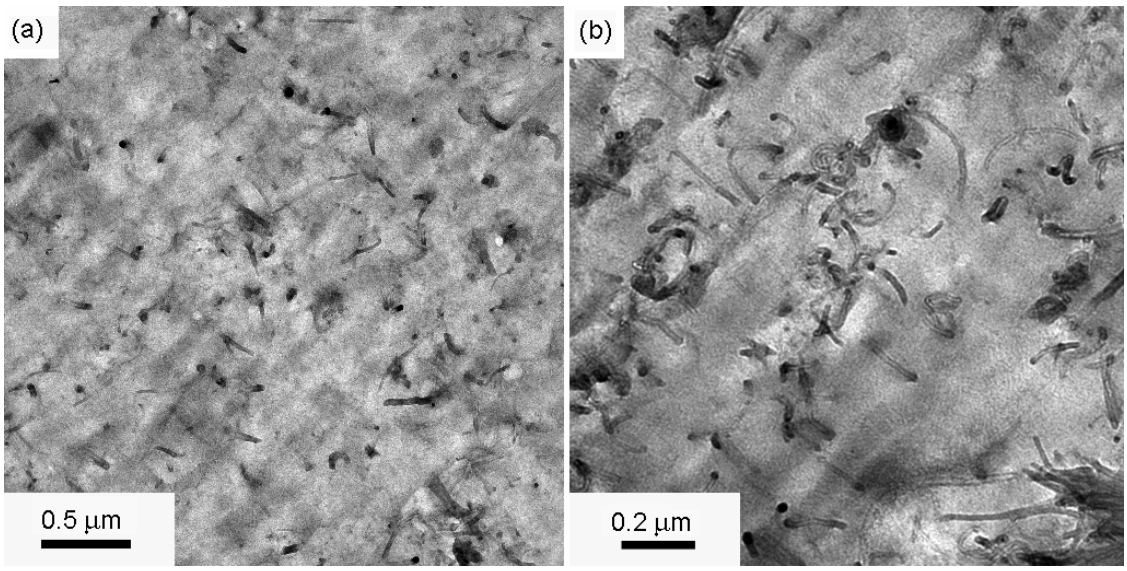

Figure 5.8. Typical TEM micrograph of iPP1/10 wt% CNT prepared by the combined solvent and melt-mixing procedure.

5.2.3 Melt-spinning by flow through a capillary die

First melt-spinning trials were performed on iPP1/CNT formulations prepared by the combined solvent and melt-mixing procedure, by means of piston driven flow through a single aperture die, 0.4 mm in diameter, using a Rosand capillary rheometer. The polymer was heated at 220 °C for 10 min before the piston was started. The speed of the piston was set to 0.2 mm/min. The resulting filament was cooled down by ambient circulating air and no drawing forces were applied. The strand had a diameter of about 200 μm as determined by optical microscopy, corresponding to DR = 2. Thin sections, longitudinal and transverse to the filament axis were obtained by ultramicrotomy and observed by TEM using the experimental procedure described in chapter 3, section 3.2.1.

5.2.4 Melt-spinning using Fourné "Laboratory Melt-Spinntester"

The experimental conditions were the same as used to produce pure iPP1 yarns, described in section 3.1.2. The melt-spinning equipment requires relatively large amounts of material (kilograms) as opposed to the few grammes used in the experiments described section 7.2.3. Therefore a masterbatch approach was used for these melt-spinning trials. A iPP1/4 wt% CNF masterbatch was produced using the combined solvent and melt-mixing process. iPP1/1 wt%, 2 wt%, and 4 wt% CNF were then prepared by diluting the masterbatch with pure iPP1 in the desired proportions. The compounding of the masterbatch with pure iPP1 granulates was carried out using a standard twin-screw extruder, again as described in the experimental chapter (chapter 3, section 3.1.1). DR was varied between 1 and 3 and cold drawing with the winding apparatus was performed at different drive-roll velocities, V_L = 360 m/min, 720 m/min and 1500m/min (the maximum speed allowed by the equipment). The resulting fibers were then subjected to morphological analysis by means of TEM and XRD, mechanical testing and DSC.

5.2.5 Characterization

The experimental procedures for TEM, XRD and DSC were as described in section 3.2.

a. Rheology

The melt rheological properties of unmodified iPP1 and iPP1/CNF composites synthesized by the single melt-mixing procedure were investigated using (i) the ARES oscillatory rheometer (Rheometric Scientific) for steady-state measurements, and (ii) the twin-bore Rosand Capillary rheometer RH7 (Rosand Precision) for elongational shear measurements at high shear rates. The experimental conditions are described in section 3.2.3. Steady-state shear measurements were also performed on iPP1/CNF composites produced by the combined solvent and melt-mixing procedure.

b. Tensile tests

Mechanical characterization of the specimens was performed by standard tensile testing. Two types of specimen were tested: (i) iPP1/CNF fibers at different CNF concentrations and drive-roll speeds, and (ii) injection molding specimens. Injection molded specimens were produced from iPP1/CNF composites produced by the combined solvent and shear mixing method using the DSM micro-injection molding machine. The tensile test equipment and experimental testing conditions for the filaments and injection molded specimens were described in the experimental section 3.2.4.

5.3 RHEOLOGY

The results of the steady state and elongational shear measurements for specimens produced by the single melt-mixing procedure are given in Figure 5.9. At low shear rates (up to 10^2 s^{-1}, Figure 5.9(a)), the neat iPP1 and the iPP1/CNF composites with intermediate CNF contents showed a Newtonian plateau. The Newtonian plateau was somewhat more extensive for the iPP1/CNF composites than for the pure iPP1. Shear thinning generally characteristic of filled thermoplastics, appeared at low shear rates only at the highest CNF content of 3.5 wt%. The viscosity of iPP1/CNF composites was systematically lower than that of iPP1. This behaviour is quite unusual[6, 7]. However, a sudden drop in viscosity, even at low CNF concentrations, might be attributed to a lubricating effect of CNF bundles. This effect is well known for carbon black, which is used as a lubricating agent in numerous applications. Moreover, the CNF were compounded "as-received" and were not purified, so that significant quantities of carbonaceous by-products of the synthesis may still have been present within the CNF. In Figure 5.9(b), it appears that at high shear rates, the flow behaviour of the iPP1/CNF composites was dominated by that of the iPP1 matrix, behaviour that is observed for other fillers and nanofillers, including MMT platelets. This is encouraging for the future integration of iPP1/CNF composites in conventional composites, although the dispersion issues remain.

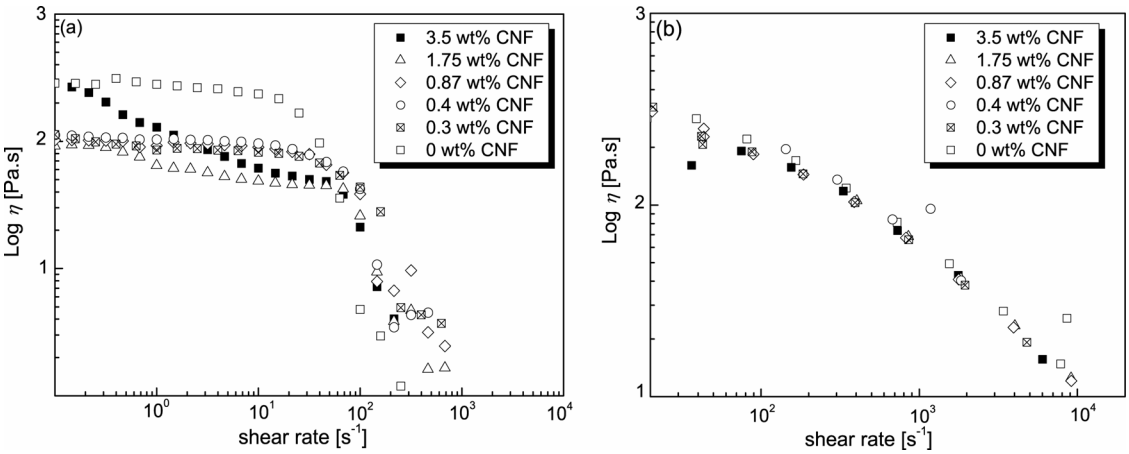

Figure 5.9. Flow curves at 220 °C of iPP1/CNF composites produced by the single step melt-mixing procedure at different CNF concentration, (a) at low shear rates determined by steady shear measurements and (b) at high shear rates determined by capillary rheometry.

Results from steady-state shear measurements on iPP1/CNF composites produced by the combined solvent and melt-mixing procedure are shown in Figure 5.10. Consistent with Figure 5.9(a), at 1 wt% CNF the viscosity of the nanocomposite was lower than that of the pure iPP1 and the Newtonian plateau extended towards higher shear rates. Strong shear thinning appeared for CNF contents above 4 wt% CNF and the viscosity showed an increase by about one order of magnitude between 1 wt% and 4 wt% CNF at the lowest strain rates. At 4 wt% CNF or above, the strong shear thinning suggests that difficulty of processing is not an issue for processes that involve shear rates down to 10^{-1} s^{-1}. Indeed, for iPP1/CNF composites containing 1 wt% CNF, processing may even be easier than for pure iPP1, since the viscosity is lower. The marked viscosity increase between 1 wt% CNF and 4 wt% CNF may be associated with a percolation threshold. This concentration range is nevertheless low compared with that observed by Lozano *et al.*[8] for similar materials. They report a percolation threshold at around 10 wt% CNF, although in their study, the CNF were purified by a dichloromethane refluxing. Balberg *et al.*[9] have shown that for randomly distributed cylinders, the critical volume fraction for percolation is proportional to the inverse of the aspect ratio. The difference in percolation threshold might therefore be attributed to the presence of by-products and impurities in significant amount. Another possibility is that the grade of CNF used by Lozano *et al.*[8] (not specified) did not have the same morphological characteristics as those used here.

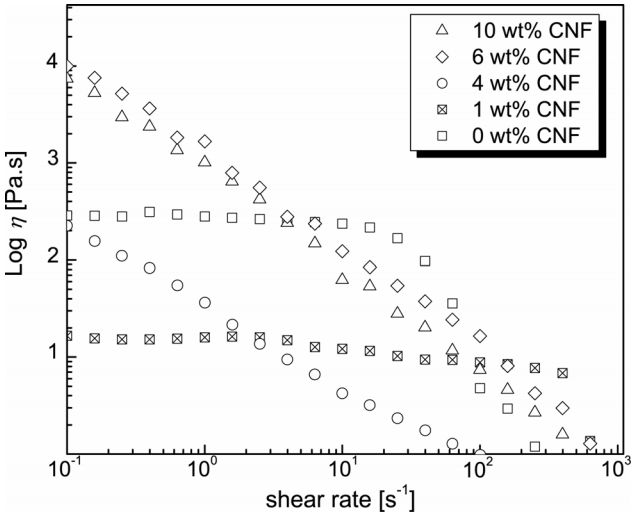

Figure 5.10. Flow curves at 220 °C of iPP1/CNF composites produced by the combined solvent and melt-mixing procedure, at different CNF concentration, determined by steady shear measurements.

5.4 iPP/CNF MELT-SPINNING

5.4.1 Introduction

The mechanical properties of filled polymer matrices are a function not only of the reinforcing fibers and polymeric matrix materials, but also of the state of fiber orientation. It is well known from conventional fiber reinforcement that unidirectional composites show the highest improvements in axial strength and modulus. In the present work, melt spinning served the dual purpose of orienting the CNF and of producing yarns suitable for co-mingling with glass fibers to produce a hybrid composite part. Two melt-spinning trials were conducted, the first one using the flow of the polymer through a die, and the second one using the Fourné "Laboratory Melt-spinntester". The two methods differ in the amount of drawing of the polymer strands at the exit of the die and on the final filament diameter. The first trial did not involve any cold drawing of the filament, whose diameter was relatively large compared to that of the yarns that were drawn at relatively high speeds (up to V_L = 1500 m/min).

5.4.2 Spinnability of iPP1/CNF nanocomposites

Cole-Cole plots are usually used to probe structural differences between pure matrices and filled systems[10]. However, as discussed in 4.2.2, they can also be used to assess the spinnability of polymer melts. Dynamic shear measurements on unmodified iPP1 and iPP1/CNF composites synthesized by the single melt-mixing procedure were performed within the linear elastic range (0.2 % of deformation).

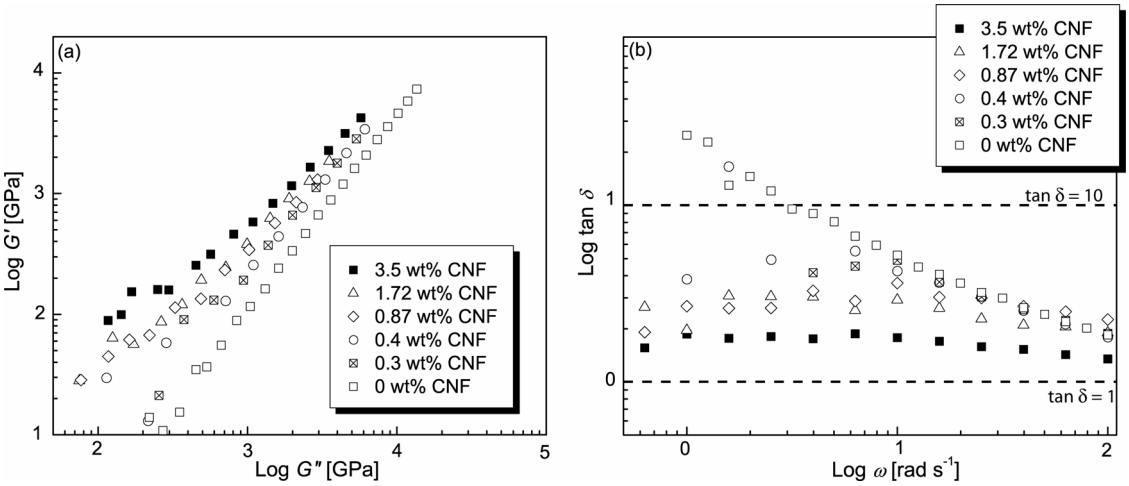

Figure 5.11. (a) *G'* vs *G"* and (b) tan δ versus ω for a range of iPP1/CNF composites produced by the single melt-mixing procedure.

In Figure 5.11, the storage modulus *G'* has been plotted against the loss modulus *G"* for iPP1/CNF nanocomposites produced. It was observed that the slopes of log *G'* versus log *G"* plots for iPP1/CNF nanocomposites were slightly lower than that observed for pure iPP1, indicating that only minor changes in morphology occurred in iPP1/CNF nanocomposites as the concentration in CNF increased. The melt-spinning criterion established in 4.2.2 is verified for iPP1/CNF nanocomposites up to 3.5 wt% CNF, namely that the nanocomposites are spinnable as long as tan δ is between 1 and 10. Therefore it was predicted that iPP1/CNF nanoccomposites should be spinnable under the present conditions. The highest CNF content considered here (3.5 wt%), corresponds to 1.5 vol% CNF. For comparison, 1.5 vol% MMT corresponds to 4.5 wt% MMT in iPP1. According to Figure 4.3(b), 4.5 wt% MMT is above the limit of spinnability for iPP1/MMT nanocomposites whereas iPP1/3.5 wt% CNF lies well with the range of spinnability for iPP1/CNF nanocomposites (Figure 5.11(b)). Therefore, for a given filler volume fraction, the processing window for melt-spinning was larger for iPP1/CNF than for iPP1/MMT nanocomposites.

5.5 iPP/CNF FILAMENT CHARACTERIZATION

5.5.1 Morphological analysis

a. Melt-spinning by flow through a capillary die

Figure 5.12(a) and (b) show typical TEM images of the iPP1/10 wt% CNT in the direction parallel to the filament axis. The CNT showed a good level of dispersion, as was already observed in the as-compounded iPP1/CNT specimens. However no preferential orientation of the CNT was observed in the micrographs. Indeed, it appears from Figure 5.12(b) that some CNT adopted a coiled morphology.

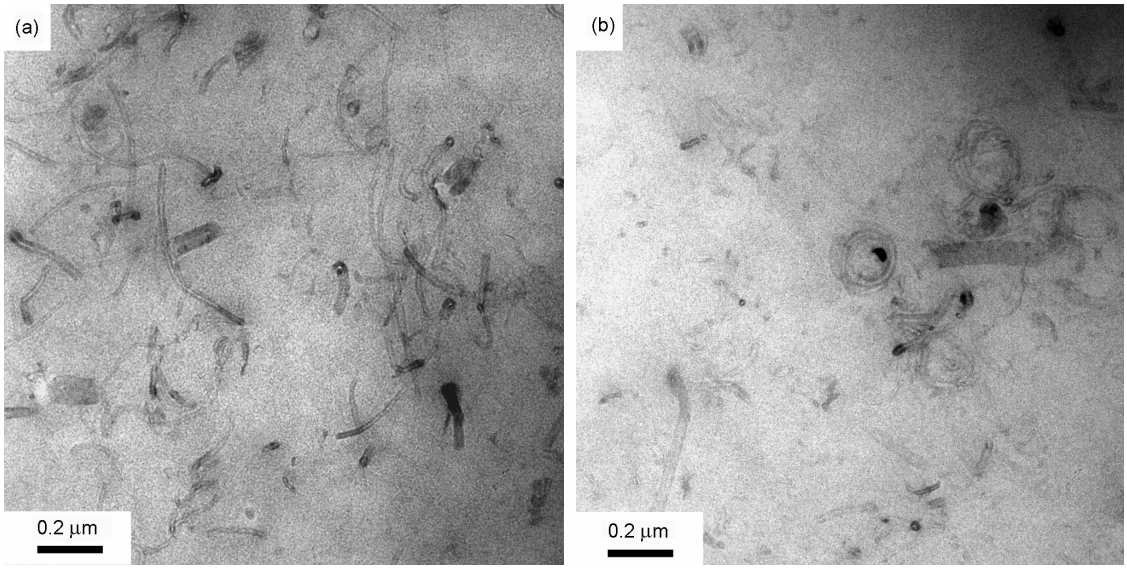

Figure 5.12. Representative TEM micrographs of longitudinal sections of iPP1/10 wt% CNF filament obtained by the piston driven extrusion.

Another method used to observe the CNT morphology was to burn the filament at 350 °C for 2 hour under an Argon flow in order to destroy the iPP1 matrix. The specimens were then observed by SEM. Figure 5.13(a) shows an image of a burnt filament, and Figure 5.13(b) is a higher magnification of the same filament. The CNT were randomly oriented and formed bundles of about 2.5 µm in diameter.

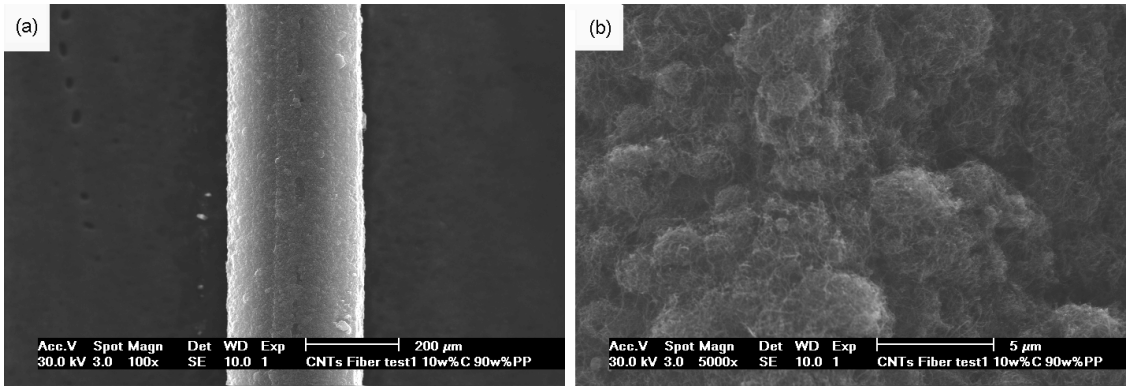

Figure 5.13. SEM pictures of a iPP1/10 wt% CNT filament obtained by the piston driven extrusion after burning at 350 °C under circulating argon, (a) at low magnification and (b) at high magnification.

b. Melt-spinning using Fourné "Laboratory Melt-Spinntester"

As inferred from the rheological measurements, spinning and winding were possible for all the iPP1/CNF concentrations under the same conditions as for iPP1. Macroscopically, all the iPP1/CNF fibers appeared to be of good quality, with a smooth surface finish and no die swell[7], as observed by optical microscopy (Figure 5.14). The mean diameter of single filaments measured by optical microscopy are shown in Table 5.1 along with the global draw ratio, λ, defined in 3.1.2. The diameters ranged from 17 μm to 38 μm, depending on the drawing conditions and, for a given CNF concentration, the filament diameter decreased with increasing V_L. This behavior was also observed for iPP1/MMT yarns (section 4.3.1).

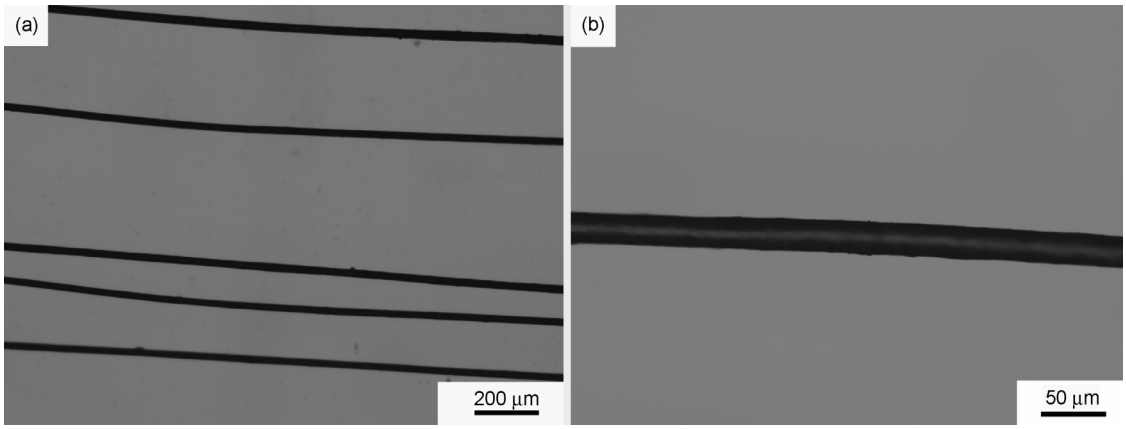

Figure 5.14. Optical micrographs of iPP1/4 wt% CNF filaments at different magnifications melt-spun with DR = 1 and V_L = 720 m/min.

Table 5.1.Single filament diameters and corresponding global draw ratio λ for iPP1/CNF yarns produced by melt-spinning and drawing (DR = 1).

wt% CNF	V_L [m/min]	Single filament diameter d [μm]	λ
0	360	34.6	133.6
	630	28.20	201.2
	1258	22.7	310.5
1	360	38.5	107.9
	720	20.5	380.7
	1500	18.7	457.5
2	360	34.4	135.2
	720	24.6	264.4
	1500	18.7	457.5
4	360	30.4	173.13
	720	24.7	262.2
	1500	17.2	540.8

Longitudinal sections of iPP1/1 wt% CNF filament are shown in Figure 5.15. Few CNF were visible on the TEM micrographs, suggesting that aggregates may be present in the iPP1/1 wt% CNF precursor. Short sections of CNF are visible in Figure 5.15(a) as well as iPP1 lamellae. Figure 5.15(b) shows that the CNF were not aligned with the filament axis.

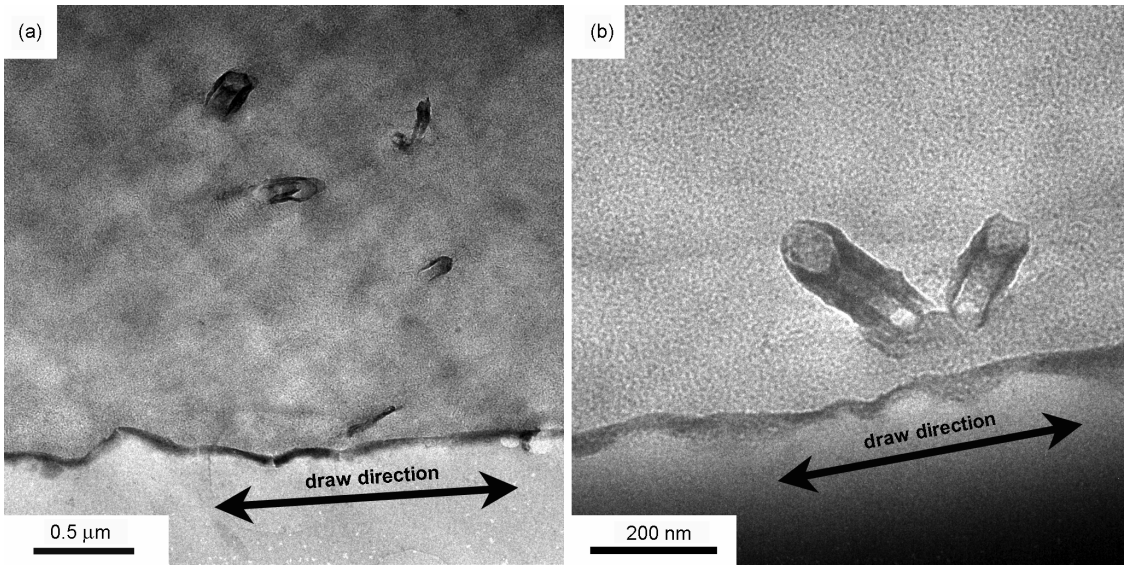

Figure 5.15. TEM micrographs of longitudinal sections from a iPP1/1 wt% CNF filament melt-spun with DR = 1 and V_L = 360 m/min.

Figure 5.15(a), is a representative micrograph of a longitudinal section of iPP1/1 wt% CNF filament melt-spun with DR = 1 and V_L = 1500 m/min. The CNF sections observed were generally longitudinal, but the distribution in length was wide, ranging from about 10 nm to about 800 nm, i.e. much lower than the nominal length of the CNF (about 10 to 80 μm). Only small portions of CNF were observed by TEM because the specimens are cut in thin films of about 50 nm in thickness[11]. It was observed in Figure 5.15(b) that sections of CNF aligned with the filament axis were present in the specimen. However, transverse sections were also observed, Figure 5.16(a) as well as curved CNF (Figure 5.16(b))[12].

Relatively homogeneous dispersions were observed in TEM micrographs of transverse sections of iPP1/1 wt% CNF filaments melt-spun with DR = 1 and V_L = 1500 m/min, as shown in Figure 5.18(a). Close to perpendicular sections of CNF were mainly present, but also some longitudinal sections, as seen in Figure 5.18(b). Similar features were observed in iPP1/1 wt% CNF filaments melt-spun with DR = 3 and V_L = 1500 m/min (Figure 5.18). Figure 5.19(a) shows a homogeneous distribution of CNF and Figure 5.19(b) shows mainly transverse sections. As mentioned in section 4.3.1, DR had little influence on the morphology of the melt-spun filaments, no improvement of CNF alignment being observed with increasing DR. Also, small CNF aggregates of about 0.2 μm in diameter were visible in the filaments (Figure 5.18(b)), indicating that despite an improvement in nanocomposite homogeneity with the melt-spinning process, the dispersion of CNF was still limited.

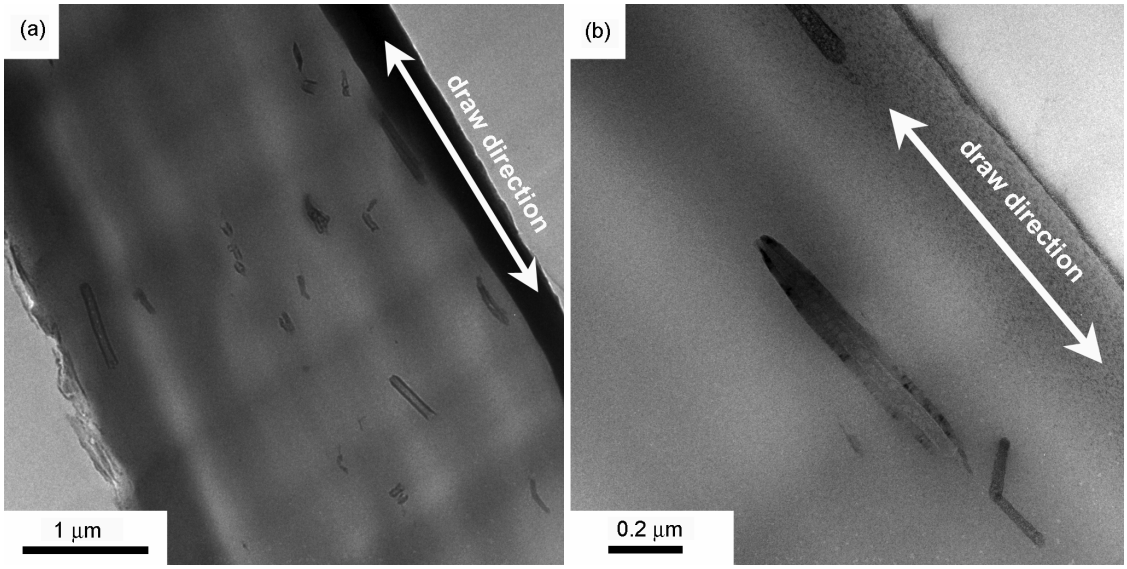

Figure 5.16. TEM micrographs of longitudinal sections from a iPP1/1 wt% CNF filament melt-spun with DR = 1 and V_L = 1500 m/min.

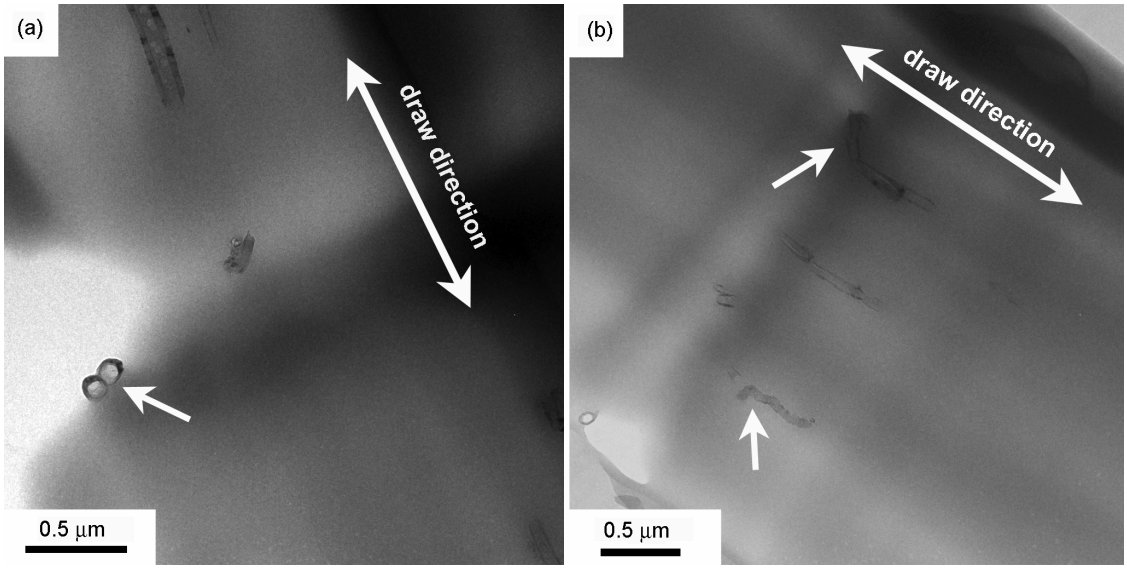

Figure 5.17. TEM micrographs of longitudinal sections from a iPP1/1 wt% CNF filament melt-spun with DR = 1 and V_L = 1500 m/min.

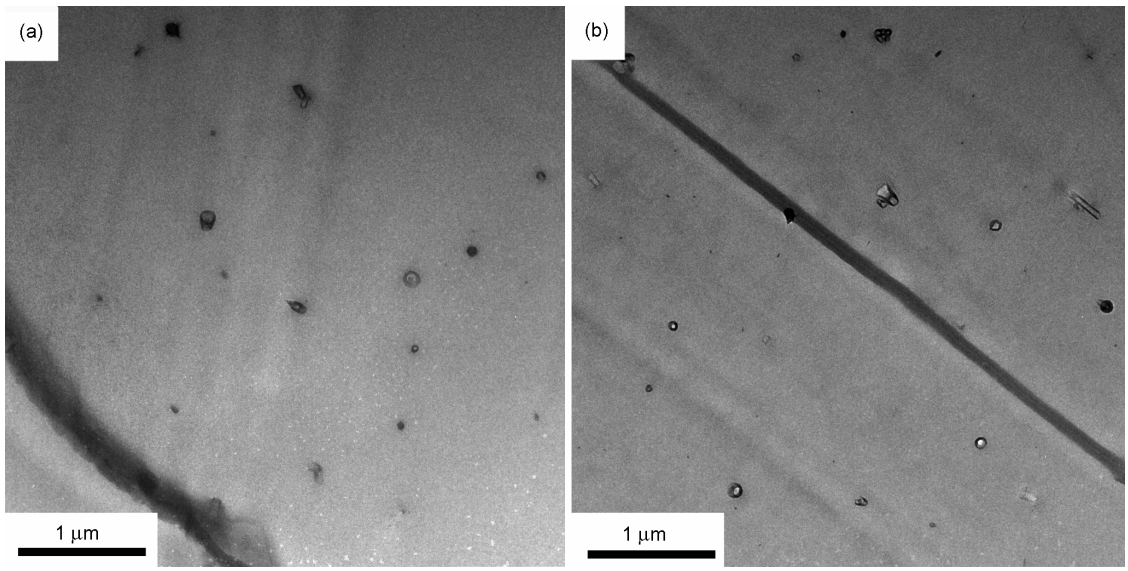

Figure 5.18. TEM micrographs of transverse sections from a iPP1/1 wt% CNF filament melt-spun with DR = 1 and V_L = 1500m/min.

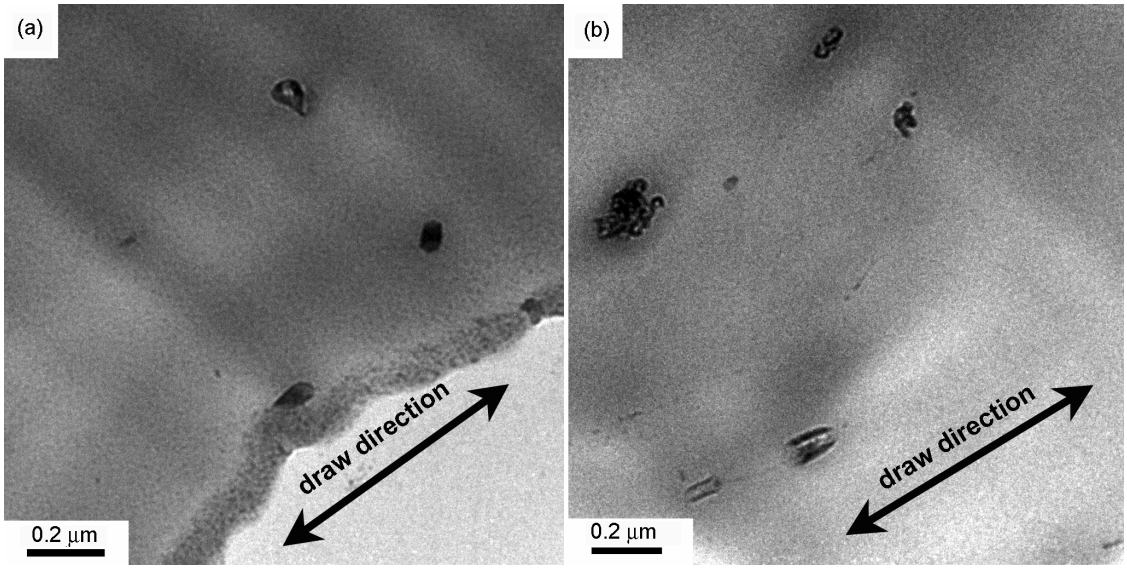

Figure 5.19. TEM micrographs of longitudinal sections from a iPP1/1 wt% CNF with DR = 3 and V_L = 1500 m/min.

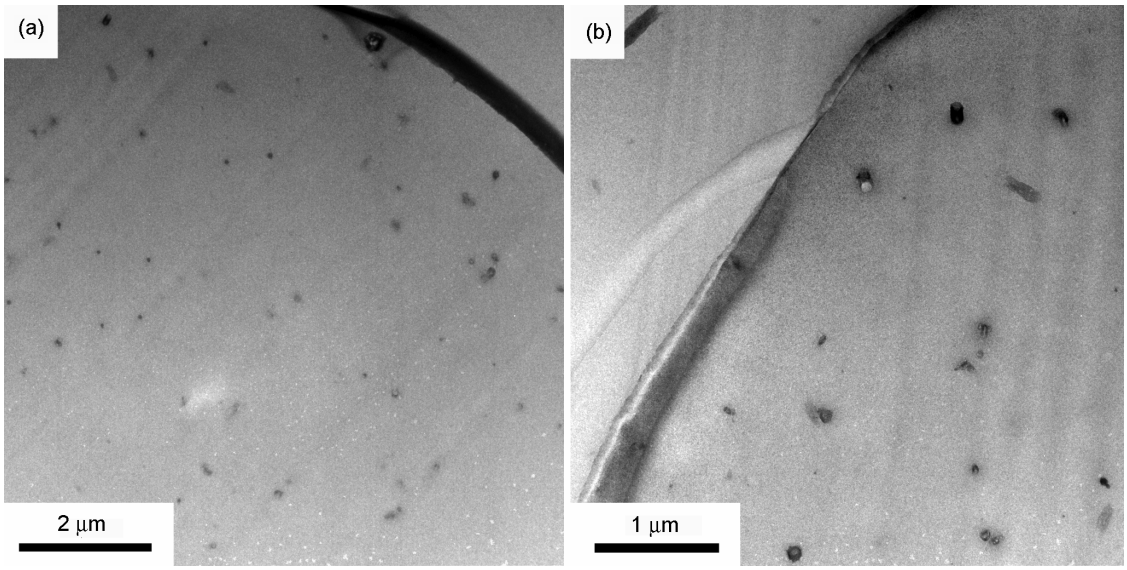

Figure 5.20. TEM micrographs of transverse sections from a iPP1/1 wt% CNF filament melt-spun with DR = 3 and V_L = 1500 m/min.

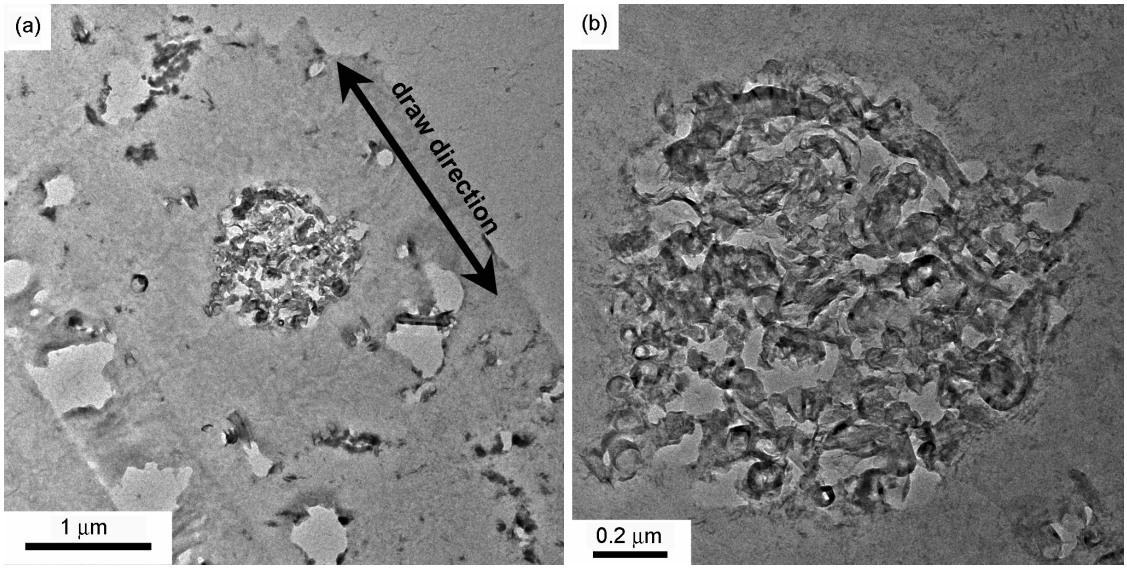

Figure 5.21. TEM micrographs of longitudinal sections from a iPP1/4 wt% CNF as-spun filament showing a CNF agglomerate.

In the case of filaments with higher CNF content (typically 4 wt%), large inhomogeneities were present in the as-spun filaments (about 1 μm in diameter) and ultramicrotomed thin films cut parallel to the filament axis contained large holes (Figure 5.21). Transverse sections of as-spun iPP1/4 wt% CNF revealed a relatively isotropic morphology. Figure 5.21(b) is a higher magnification of an aggregate showing entangled CNF.

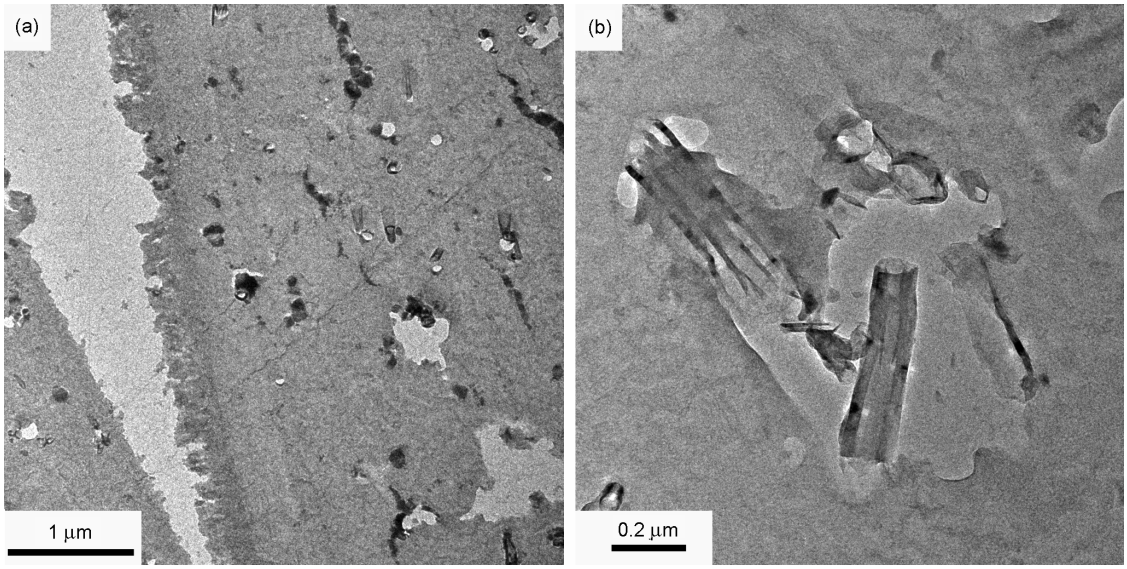

Figure 5.22. TEM micrographs of transverse sections from iPP1/4 wt% CNF as-spun filament.

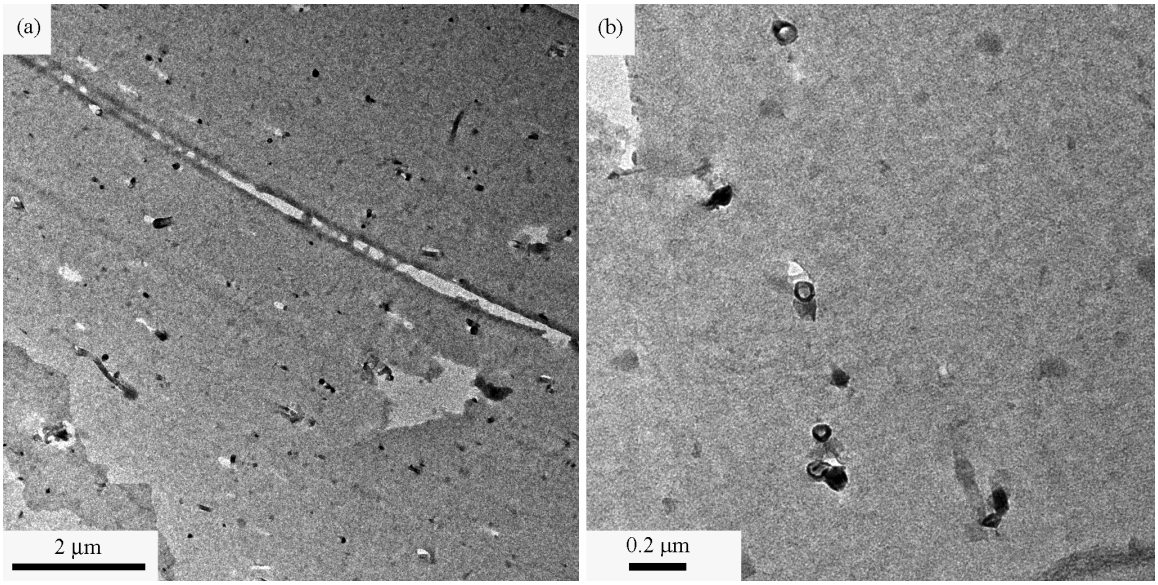

Figure 5.23. TEM micrographs of transverse sections from a iPP1/4 wt% CNF with DR = 1 and V_L = 1500 m/min.

It was only possible to observe transverse sections of iPP1/4 wt% CNF filaments melt-spun with DR = 1 and V_L = 1500 m/min. The micrographs are given in Figure 5.23. CNF were mainly observed in nearly perpendicular sections and the numerous holes in the film suggested the presence of smaller aggregates than those in Figure 5.21.

5.5.2 XRD

2D-WAXS patterns of the melt-spun filaments are shown in Figure 5.24, with more detailed equatorial scans being given in Figure 5.25(a) and (b). The 2D pattern of pure iPP1 filament melt-spun at 360 m/min is characterised by an amorphous halo, which becomes sharper with increasing CNF concentration for similar drive-roll velocities. This appears more clearly in the WAXS intensity profiles (Figure 5.25(a)), where the crystallographic indices are indicated in brackets. The increase of crystallographic peak sharpness with increasing CNF concentration suggested an increase of crystallinity of iPP1 in the filaments with increasing CNF content. The crystallographic indices corresponded to the α-phase structure of iPP1, and a small amount of the β-phase that appeared at 4 wt% CNF. The appearance of the β-phase with increasing nanofillers content was noted previously in section 4.3.1 in the case of iPP1/MMT filaments. The graphitic (002) reflection of CNF, indicated by the arrows in the 2D patterns and in the average intensity profiles at $2\theta \sim 28.5°$ appeared as semi-arcs in Figure 5.25, suggesting some alignment of the CNF with the filament axis. There appeared to be relatively little alignment of the iPP1 matrix in the filaments melt-spun with V_L = 360 m/min consistent with TEM observations (cf Figure 5.14), although the increase in meridional intensity,

(Figure 5.25), indicated some orientation of the crystalline regions.

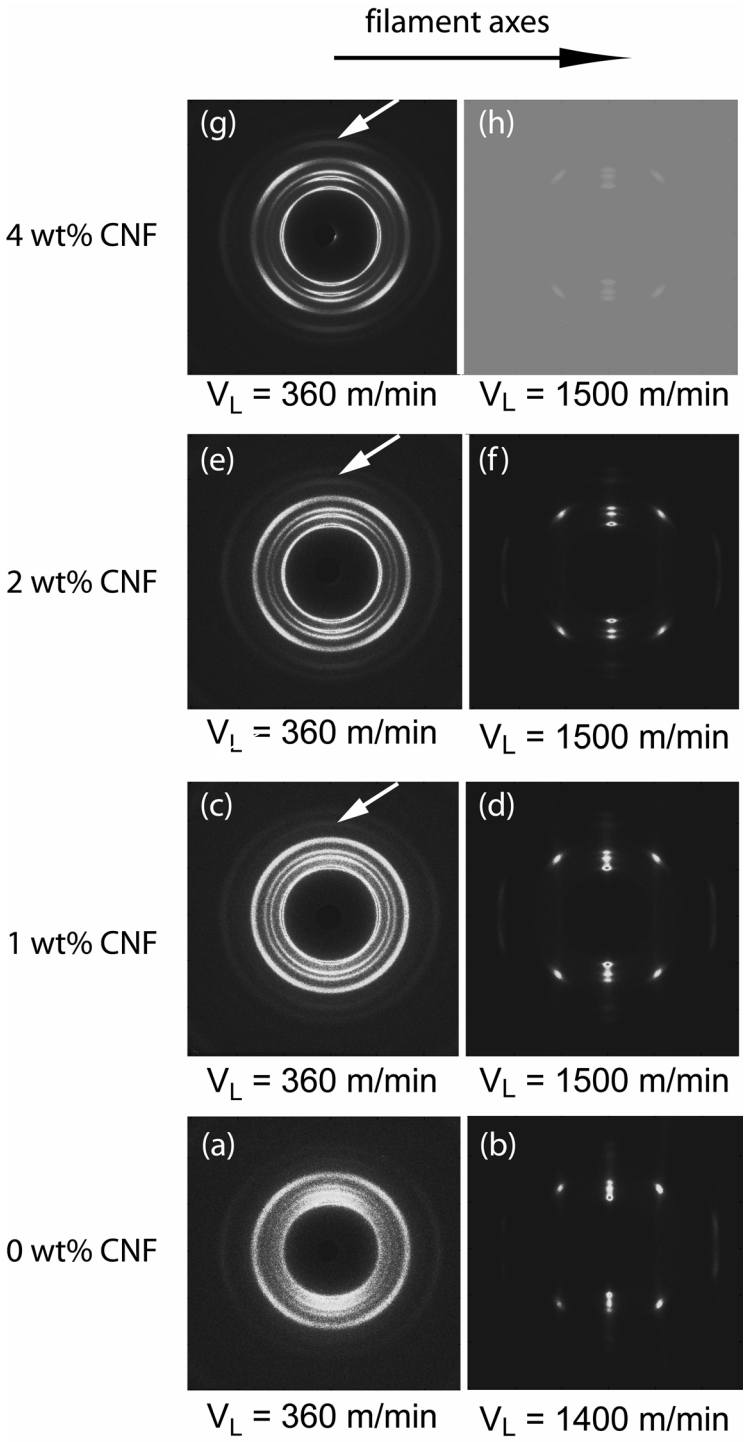

Figure 5.24. 2D-WAXS photographs of iPP1/CNF filaments, DR =1, with different CNF content and drawn at different drive-roll velocities. The filament axis was equatorial.

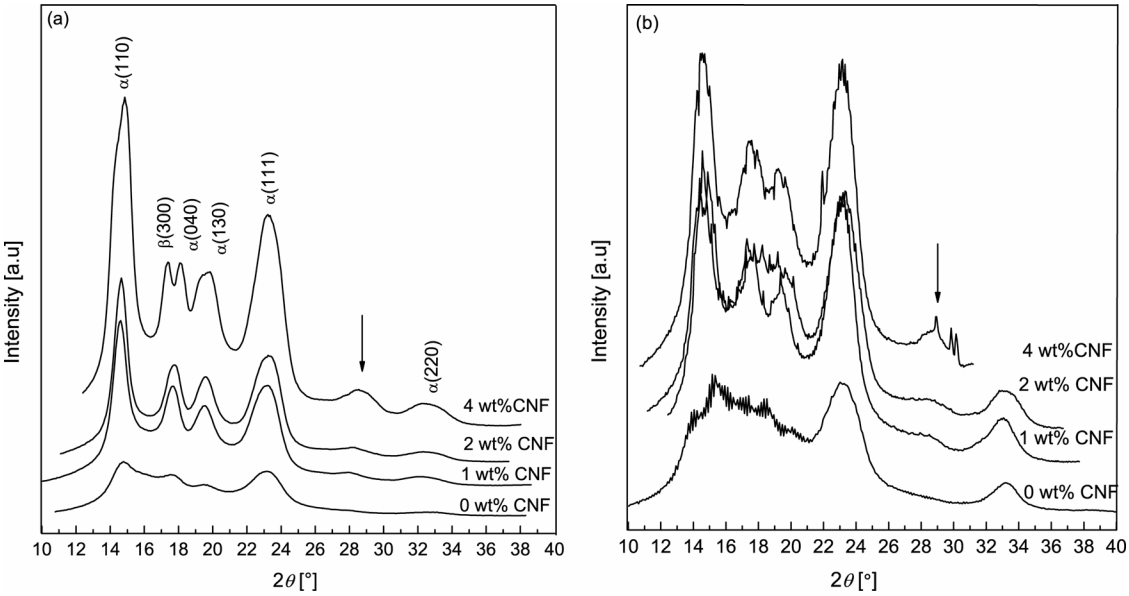

Figure 5.25. Average WAXS intensity profiles of iPP1/CNF filaments with various CNF concentration drawn at (a) V_L = 360 m/min and (b) V_L = 1400 m/min for pure iPP1 filament and V_L = 1500 m/min for iPP1/CNF filaments. The crystallographic indices are indicated in brackets.

Table 5.2. iPP1/CNF filament Herman-Stein orientation factors as a function of drive-roll velocity and CNF concentration.

	0 wt% CNF 360 m/min	1 wt% CNF 360 m/min	2 wt% CNF 360 m/min	4 wt% CNF 360 m/min
f_{a^*}	- 0.10	- 0.010	- 0.02	0.01
f_b	- 0.09	- 0.063	- 0.11	- 0.14
f_c	0.19	0.073	0.13	0.13
	0 wt% CNF 1400 m/min	1 wt% CNF 1500 m/min	2 wt% CNF 1500 m/min	4 wt% CNF 1500 m/min
f_{a^*}	- 0.3	- 0.27	- 0.27	- 0.3
f_b	- 0.3	- 0.25	- 0.26	- 0.27
f_c	0.6	0.52	0.53	0.57

Figure 5.24(b) (d), (f) and (h) show 2D-WAXS patterns of pure iPP1 filaments melt-spun with V_L = 1400 m/min and iPP1/CNF filaments melt-spun with V_L = 1500 m/min respectively. The reduction of the azimuthal spreads of the reflection peaks indicated significant iPP1 alignment in the filament axis. The corresponding crystalline peaks (Figure 5.25(b)) showed high level of noise owing to signal intensity reduction, but they were consistent with the α-phase. On the other hand the alignment of the (002) reflections from the CNF did not appear to be improved compared to Figure 5.25(a). These results

were consistent with Hermann's orientation factors given in Table 5.2, suggesting in both cases an increase of iPP1 lamellar orientation perpendicular to the filament axis with increasing drive-roll velocity for a given CNF concentration and a marginal variation of the orientation factors with increasing CNF concentration.

Figure 5.26 shows the 2D-SAXS patterns of the filaments melt-spun with different drive-roll velocities. The pure iPP1 filament showed a typical diamond shaped SAXS pattern with a second order scattering halo. The azimuthal spread of the second order halo was reduced from pure iPP1 filaments melt-spun at 360 m/min to pure iPP1 filaments melt-spun with V_L = 1500 m/min, indicating the presence of a lamellar structure of iPP1 with the lamellar normals preferentially aligned with the filament axis. For a given V_L, the intensity of the diamond shape tended to increase with increasing CNF concentration. The latter was attributed to the oriented hollow cores of the CNF which superposed onto reflections of iPP1 at the present length scales[13]. In addition, the extent and the intensity of the second order halo also increased with increasing CNF concentration. Ran *et al.*[13] attribute this effect to a certain amount of long-range order of the lamellar structures in the iPP1/CNF filaments due to the nucleating effect of CNF. This will be verified in what follows.

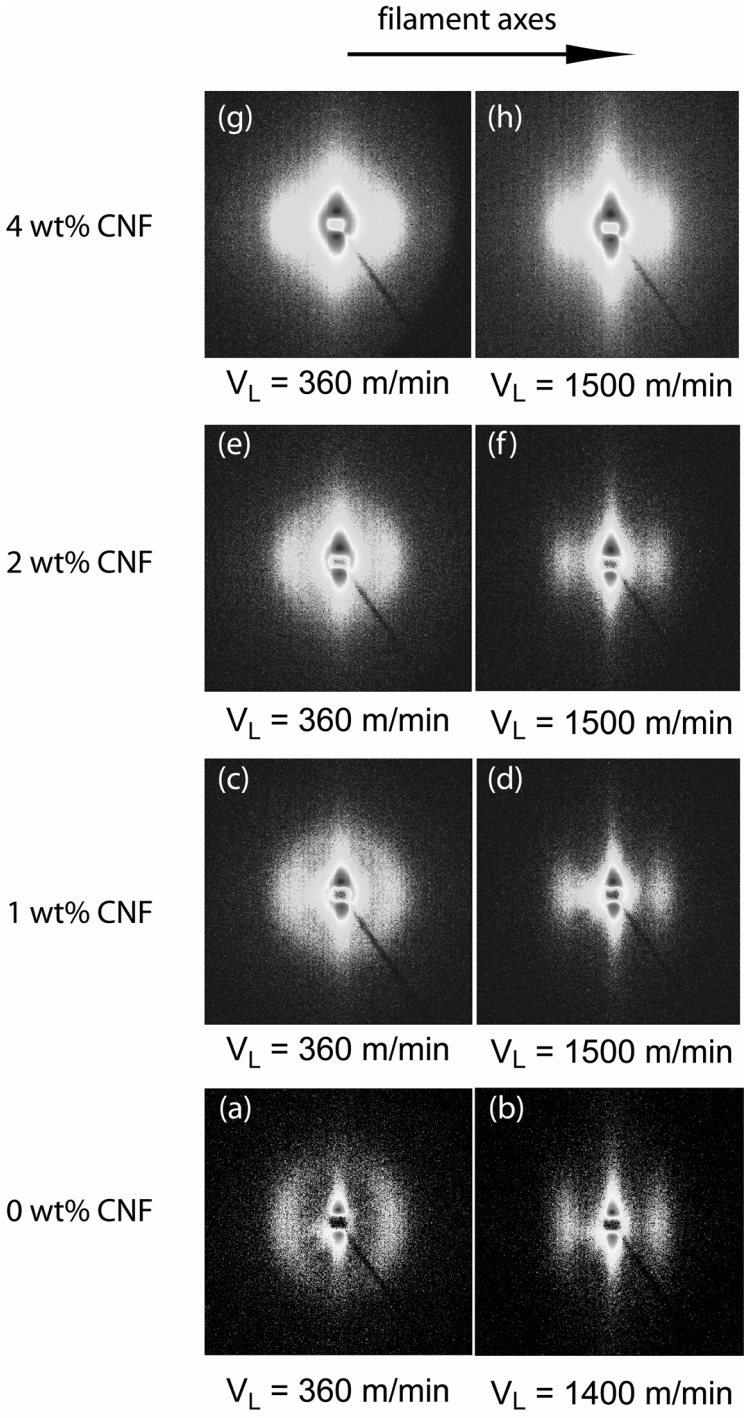

Figure 5.26. 2D-SAXS photographs of iPP1/CNF filaments, DR = 1, with different CNF content and drawn at different drive-roll velocities. The filaments axis is equatorial.

5.5.3 Non-isothermal DSC

The effects of CNF on the DSC thermograms are shown in Figure 5.27 for iPP1/CNF produced by the combined solvent and melt-mixing procedure. The crystallization peak (T_c), the apparent melting temperatures of the crystallized specimens (T_m), the crystallization and the melting enthalpies (H_c and H_m respectively) are given as a function of CNF concentration for iPP1/CNF granulates in Table 5.3. The CNF have a strong effect on the crystallization kinetics of iPP1. It may be inferred from the T_c values, that the addition of CNF to iPP1 increases the nucleation rate during crystallization, with T_c being strongly shifted towards higher temperatures with increasing CNF loadings. These results therefore apparently confirm the enhanced nucleation rates reported elsewhere[14, 15]. H_c and hence X_c were also observed to increase with increasing CNF loadings as shown in Table 5.4.

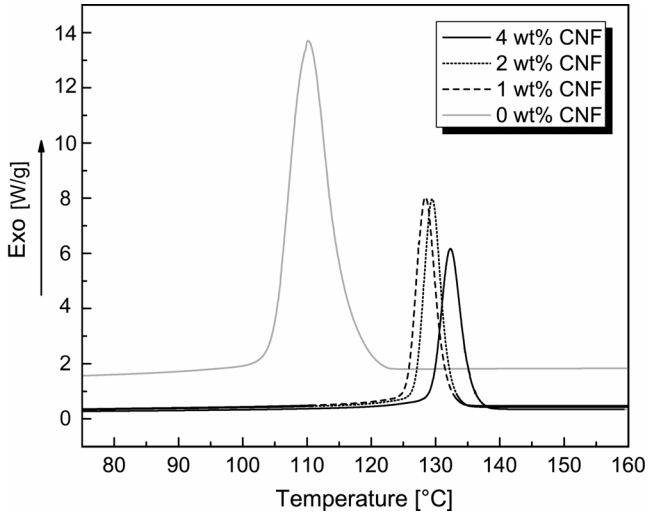

Figure 5.27. Non-isothermal DSC crystallization curves of as-compounded iPP1 and iPP1/CNF nanocomposites produced by the combined solvent and melt-mixing procedure.

Table 5.3. Crystallization temperature (T_c), crystallization enthalpy (H_c), melting temperature (T_m) and melting enthalpy (H_m) of iPP1 and iPP1/CNF composites produced by the combined solvent and melt-mixing procedure.

Materials	T_c [°C]	H_c [J/g]	T_m [°C]	H_m [J/g]
Neat iPP1	110.1	88.9	166.6	83.9
iPP1/1 wt% CNF	128.4	102.4	163.4	95.6
iPP1/2 wt% CNF	129.5	105.5	162.4	94.4
iPP1/4 wt% CNF	132.3	112.6	164.5	88.4

Table 5.4. Degree of crystallinity of as-compounded iPP1/CNF composites produced by the combined solvent and melt-mixing procedure.

Materials	X_c [%]
Neat iPP1	57.3
iPP1/1 wt% CNF	65.9
iPP1/2 wt% CNF	65.7
iPP1/4 wt% CNF	62.8

Results for iPP1/1 wt% CNF yarns cold drawn at different roll-up speeds are given in Table 5.5. T_c slightly shifted towards higher temperatures with increasing V_L. No significant changes were observed in T_m or X_c. T_c of the iPP1/1 wt% CNF yarn drawn at 360 m/min was similar to that of the as-compounded iPP1/1 wt% CNF granulates (Table 5.5), but H_c was much higher in the case of iPP1/1 wt% yarn. Thus the melt-spinning and subsequent cold drawing at relatively low speeds had no influence on the crystallization kinetics but did affect the degree of crystallization, which increased with increasing draw ratio (i.e. drive-roll velocity) (Table 5.4). This behavior is typical of the strain-induced crystallization owing to the melt-spinning process as observed elsewhere for melt-spun iPP1/CNF fibers[13] and iPP1/MMT (section 4.3.1).

Table 5.5. Crystallization temperature (T_c), crystallization enthalpy (H_c), melting temperature (T_m) and melting enthalpy (H_m) of iPP1/1 wt% CNF fibers cold drawn at different drive-roll velocities.

Materials	T_c [°C]	H_c [J/g]	T_m [°C]	H_m [J/g]
DR = 1; V_L = 360 m/min	128.7	111.7	162.7	84.1
DR = 1; V_L = 720 m/min	129.3	109.6	163.5	90.9
DR = 1; V_L = 1500 m/min	129.6	106.1	162.4	87.4

Table 5.6. Degree of crystallinity X_c of iPP1/1 wt% CNF fibers cold drawn at different drive-roll velocities.

Materials	X_c [%]
DR = 1; V_L = 360 m/min	58.0
DR = 1; V_L = 720 m/min	62.3
DR = 1; V_L = 1500 m/min	60.2

5.5.4 Tensile tests

Some typical stress-strain curves of iPP1/CNF filaments are shown in Figure 5.28(a) for filaments melt-spun with V_L = 360 m/min and in Figure 5.28(b) for pure iPP1 filaments

melt-spun with V_L = 1400 m/min and iPP1/CNF melt-spun with V_L = 1500 m/min. The filaments underwent yielding at between 4 and 6 % strain. They could subsequently be strained beyond the limit of the tensile test machine (above 200 % deformation).

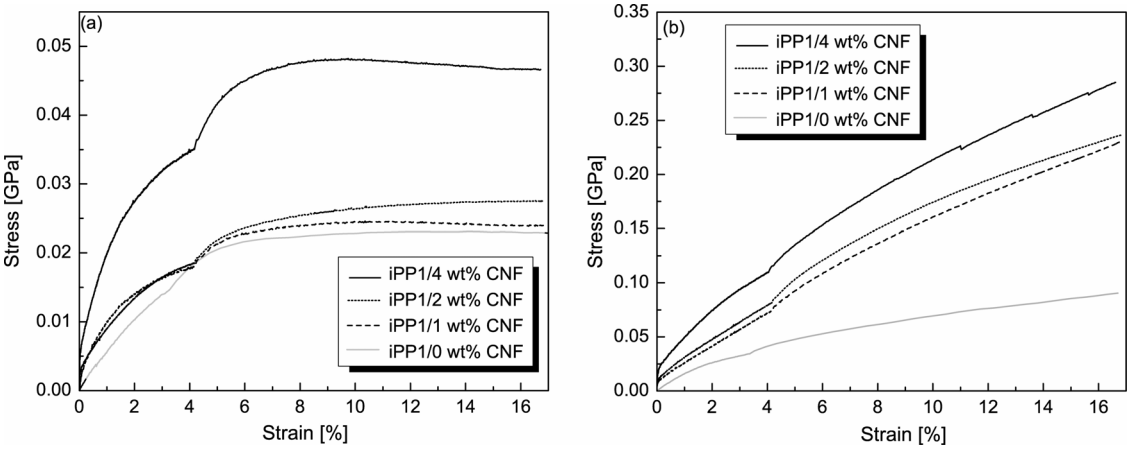

Figure 5.28. typical stress-strain curves of (a) of iPP1/CNF filaments melt-spun with V_L = 360 m/min and (b) of pure iPP1 filaments melt-spun with V_L = 1400 m/min and iPP1/CNF melt-spun with V_L = 1500 m/min.

The normalized Young's modulus of iPP1/CNF injection molding specimens and of iPP1/CNF fibers cold drawn at different drive-roll velocities are given in Figure 5.29 as a function of CNF concentration.

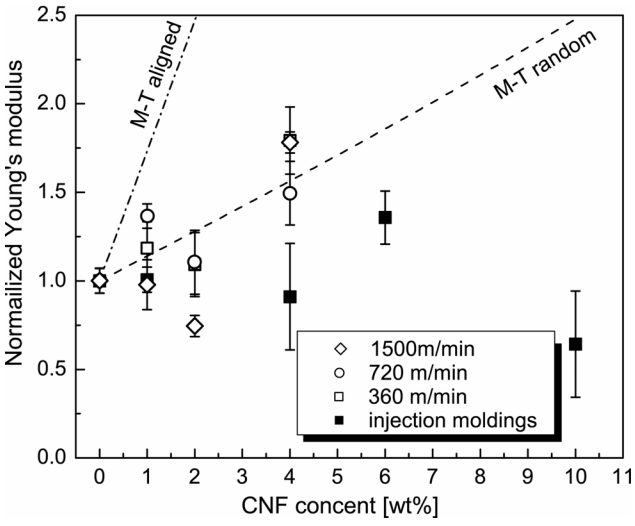

Figure 5.29. Normalized Young's modulus E/E_0 of iPP1/CNF melt-spun fibers (E_0 = 1.1 GPa for V_L = 360 m/min) and injection moldings (E_0 = 1.4 GPa) for different drive-roll velocities and as a function of CNF concentration. The curves correspond to Mori-Tanaka model predictions for: randomly oriented and aligned fibers with an aspect ratio of 300.

The experimental values of stiffness showed considerable scatter, thought to be due to the presence of agglomerates in the iPP1/CNF composites. It appeared that melt-spun filaments had higher normalized Young's moduli than the injection moldings, thought to be due to a certain orientation of the CNF in the filaments, and the overall trend was for increased Young's moduli with increasing CNF concentrations. However, the expected increase in Young's modulus with increasing drive-roll velocity was not clearly confirmed by the experimental data.

Mori-Tanaka predictions (presented in 4.3.2) are shown in Figure 5.29. The properties of the CNF used in this study are not easily measured. For the calculation, the diameter and the length of the CNF were taken to be 0.2 μm and 60 μm respectively, resulting in particles with an aspect ratio of 300. The bulk density of the CNF was estimated to be 2 g/cm^3 and the Poisson's ratio, *v*, to be 0.38, as specified for CNF products from Applied Sciences, Inc.[16]. The modulus of CNF is reported to be in the range 100 - 600 GPa[17, 18], and previous studies have shown that a modulus of 250 GPa fits experimental data reasonably well [1]. Mori-Tanaka theoretical predictions were well above experimental values for both iPP1/CNF injection moldings and filaments. For injection moldings, the low stiffness values may be attributed to the use of theoretical physical properties in the calculation that do not take into account the broad spectrum of possible values. Moreover, it was assumed that the CNF are rigid rods with a single aspect ratio, whereas it was observed in TEM micrographs that the CNF were generally bent in the nanocomposites. Low values of stiffness may also be due to the existence of agglomerates, as observed in the TEM micrographs, that act as macro particles and centers of friction[19], and interfacial interactions between the CNF and the iPP1 matrix may be poor, since no particular surface treatments were applied on the CNF. Finally, the relatively low orientation of the CNF in the filaments, even for low CNF concentrations and high drive-roll velocities is expected to play an important role. However, other studies on iPP/CNF or iPP/CNT composites have suggested it to be possible to achieve increases in Young's modulus by about 50 % at low loading levels with randomly oriented nanocarbons[18, 20]. Such improvements were not achieved here.

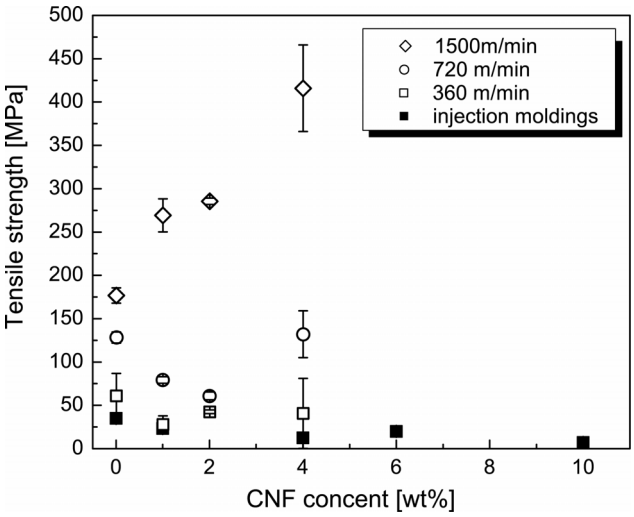

Figure 5.30. Tensile strength of iPP1/CNF melt-spun fibers and injection molding specimens at different processing conditions and as a function of CNF concentration. The drive-roll velocities used for the cold drawing of the fibers are indicated in the legend.

The tensile strengths of iPP1/CNF injection moldings and of iPP1/CNF fibers cold drawn at different drive-roll velocities are shown in Figure 5.30 as a function of CNF concentration. For the injection moldings, the tensile strength was almost constant over the entire CNF concentration range. iPP1/CNF filaments had generally higher tensile strengths than the injection moldings. For a given CNF concentration, the tensile strength of the filaments increased monotonically with increasing drive-roll velocity. For a given drive-roll velocity up to 720 m/min, the iPP1/CNF filaments showed little dependence on CNF content. However, for iPP1/CNF filaments cold drawn at 1500 m/min, the tensile strength increased continuously with increasing CNF concentration. Thus, the effect of CNF on iPP1/CNF increased strongly with increasing draw ratio and the maximum tensile strength improvement was achieved for the maximum CNF concentration (4 wt%) and the maximum drive-roll velocity (1500 m/min). Similar results are obtained by Moore *et al.*[21]. In their study, they distinguished between un-drawn and drawn filaments and observed a nearly 45 % increase in the tensile strength at about 1 wt% of CNF in the drawn filaments, and a monotonic increase in tensile strength with increasing CNF concentration for un-drawn filaments.

5.6 CONCLUSION

In this chapter, melt spinning trials of iPP1/nanocarbons have been presented. Two types of nanocarbons were investigated; vapour grown carbon nanofibers (CNF) and carbon nanotubes (CNT). From trials it appeared that a simple melt-mixing procedure using a standard twin-screw extruder did not provide sufficiently high shear forces to separate CNF bundles in the as-received materials. A combined solvent and melt-mixing

procedure gave better results for the dispersion of nanocarbons in the iPP1 matrix, especially for CNT. However, the latter method is not cost effective because large quantities of solvent are required to obtain homogeneous dispersions of nanocarbons. In addition, handling and health risk issues are raised. Nevertheless, the combined solvent and melt-mixing procedure was selected as a method to produce iPP1/CNF masterbatches, even limited in CNF concentration, in order to prepare the large quantities of iPP1/CNF precursors needed to melt-spin iPP1/CNF filaments. As predicted by rheological measurements, melt-spinning of iPP1/CNF composites was straightforward and conditions similar to those used for pure iPP1 filaments could be used. The morphological characterization of the filaments revealed that cold drawing was essential for any preferential orientation of the CNF to be obtained. Partial orientation of CNF sections was observed by TEM. The semi-arc shape of CNF reflection patterns in WAXS confirmed this. The Young's modulus and tensile strength of the as-compounded iPP1/CNF composites showed improvements compared with those of pure iPP1 particularly for drawn specimens at low CNF concentration. This was argued to be due to orientation of the CNF along the filament axis and to the increase of crystallinity with increasing draw ratio, since the CNF also acted as nucleation sites for iPP1.

5.7 REFERENCES

1 R. J. Kuriger, M. K. Alam, D. P. Anderson and R. L. Jacobsen, **Processing and characterization of aligned vapor grown carbon fiber reinforced polypropylene**, *Composites Part A-Applied Science And Manufacturing*, 2002; **33** (1): 53-62

2 C. Mikâo, **Synthesis, Characterization and Macroscopic Manipulation of Carbon Nanotubes**, Thesis, Lausanne, (2005)

3 J. Muller, F. Huaux, N. Moreau, P. Misson, J. F. Heilier, M. Delos, M. Arras, A. Fonseca, J. B. Nagy and D. Lison, **Respiratory toxicity of multi-wall carbon nanotubes**, *Toxicology and Applied Pharmacology*, 2005; **207** (3): 221-231

4 P. J. F. Harris, **Carbon nanotube composites**, *International Materials Reviews*, 2004; **49** (1): 31-43

5 R. Haggenmueller, H. H. Gommans, A. G. Rinzler, J. E. Fischer and K. I. Winey, **Aligned single-wall carbon nanotubes in composites by melt processing methods**, *Chemical Physics Letters*, 2000; **330** (3-4): 219-225

6 K. Lozano, J. Bonilla-Rios and E. V. Barrera, **A study on nanofiber-reinforced thermoplastic composites (II): Investigation of the mixing rheology and conduction properties**, *Journal of Applied Polymer Science*, 2001; **80** (8): 1162-1172

7 S. B. Kharchenko, J. F. Douglas, J. Obrzut, E. A. Grulke and K. B. Migler, **Flow-induced properties of nanotube-filled polymer materials**, *Nature Materials*, 2004; **3** (8): 564-568

8 K. Lozano and E. V. Barrera, **Nanofiber-reinforced thermoplastic composites. I. Thermoanalytical and mechanical analyses**, *Journal of Applied Polymer Science*, 2001; **79** (1): 125-133

9 I. Balberg, D. Azulay, D. Toker and O. Millo, **Percolation and tunneling in composite materials**, *International Journal Of Modern Physics B*, 2004; **18** (15): 2091-2121

10 P. Pötschke, T. D. Fornes and D. R. Paul, **Rheological behavior of multiwalled carbon nanotube/polycarbonate composites**, *Polymer*, 2002; **43** (11): 3247-3255

11 P. Pötschke, A. R. Bhattacharyya and A. Janke, **Melt mixing of polycarbonate with multiwalled carbon nanotubes: microscopic studies on the state of dispersion**, *European Polymer Journal*, 2004; **40** (1): 137-148

12 H. G. Chae, T. V. Sreekumar, T. Uchida and S. Kumar, **A comparison of reinforcement efficiency of various types of carbon nanotubes in poly acrylonitrile fiber**, *Polymer*, 2005; **46** (24): 10925-10935

13 S. F. Ran, C. Burger, I. Sics, K. Yoon, D. F. Fang, K. S. Kim, C. Avila-Orta, J. Keum, B. Chu, B. S. Hsiao, D. Cookson, D. Shultz, M. Lee, J. Viccaro and Y. Ohta, **In situ synchrotron SAXS/WAXD studies during melt spinning of modified carbon nanofiber and isotactic polypropylene nanocomposite**, *Colloid and Polymer Science*, 2004; **282** (8): 802-809

14 L. Valentini, J. Biagiotti, J. M. Kenny and S. Santucci, **Morphological characterization of single-walled carbon nanotubes-PP composites**, *Composites Science and Technology*, 2003; **63** (8): 1149-1153

15 J. K. W. Sandler, S. Pegel, M. Cadek, F. Gojny, M. van Es, J. Lohmar, W. J. Blau, K. Schulte, A. H. Windle and M. S. P. Shaffer, **A comparative study of melt spun polyamide-12 fibres reinforced with carbon nanotubes and nanofibres**, *Polymer*, 2004; **45** (6): 2001-2015

16 R. J. Kuriger and M. K. Alam, **Thermal conductivity of thermoplastic composites with submicrometer carbon fibers**, *Experimental Heat Transfer*, 2002; **15** (1): 19-30

17 J. Sandler, A. H. Windle, P. Werner, V. Altstadt, M. V. Es and M. S. P. Shaffer, **Carbon-nanofibre-reinforced poly(ether ether ketone) fibres**, *Journal Of Materials Science*, 2003; **38** (10): 2135-2141

18 S. Kumar, H. Doshi, M. Srinivasarao, J. O. Park and D. A. Schiraldi, **Fibers from polypropylene/nano carbon fiber composites**, *Polymer*, 2002; **43** (5): 1701-1703

19 E. Hammel, X. Tang, M. Trampert, T. Schmitt, K. Mauthner, A. Eder and P. Pötschke, **Carbon nanofibers for composite applications**, *Carbon*, 2004; **42** (5-6): 1153-1158

20 J. C. Kearns and R. L. Shambaugh, **Polypropylene fibers reinforced with carbon nanotubes**,

Journal of Applied Polymer Science, 2002; **86** (8): 2079-2084

21 E. M. Moore, D. L. Ortiz, V. T. Marla, R. L. Shambaugh and B. P. Grady, **Enhancing the strength of polypropylene fibers with carbon nanotubes**, *Journal of Applied Polymer Science*, 2004; **93** (6): 2926-2933

CHAPTER 6

iPP/MMT FILMS:EXTRUSION-CALENDERING AND CHARACTERIZATION

6.1 INTRODUCTION

iPP2/MMT films were produced for use as precursors for hybrid GMT composites to be described in chapter 7. In industry, GMTs are manufactured by a continuous process that integrates the production of the polymer films and the impregnation of the glass mats simultaneously. In the present case, iPP2/MMT films were produced separately. The objective of these experimental trials was to identify potential limitations to the production of iPP2/MMT films at a larger scale. In addition, the opportunity was taken to characterize the morphology and mechanical properties of iPP2/MMT films in order to extend the discussion initiated in the previous chapter concerning processing-morphology-property relationships in iPP/MMT nanocomposites.

In what follows, the extrusion-calendering process of iPP2/MMT films is first discussed. A description of he morphology of the films is based on results from techniques such as XRD, TEM and optical microscopy is then given. Finally, results from tensile testing and notched tensile testing are discussed.

6.2 iPP/MMT FILM EXTRUSION-CALENDERING

The experimental conditions for the extrusion-calendering process were given in section 3.1.3. The calendering of iPP2/MMT films was relatively straightforward. Potentially undesirable surface structures resulting from the high extension rates present in the nip of the calendar cylinders[1], and in particular sharkskin (Figure 6.1), were eliminated by optimizing the ratio between the speed of extrusion and the speed of the calendering process. Thus, the extrusion speed was set to 40 rpm and the calenders were run at about 1 rpm. The homogeneity of the films was highly dependent on the dispersion achieved prior to calendering. Under conditions of identical temperature (200 °C) and extrusion speed (40 rpm), when the calender was directly fed with iPP2 and MMT granulates

mixed manually, the resulting iPP2/MMT films systematically showed dark patches (Figure 6.2(a)), owing to poor compounding between iPP2 and MMT granulates. Figure 6.3(a) shows a representative TEM image of a MMT agglomerate in the iPP2 matrix, and Figure 6.3(b) shows the inhomogenity of the nanocomposite produced by direct compounding. Initial attempts to improve the homogeneity of the nanocomposites were unsuccessful. First, the final temperature of the twin screw extruder was increased up to 220 °C in order to increase the mobility of iPP2 chains and to promote the interacalation process. Second, the speed of the twin screw extruder was reduced to about 20 rpm in order to increase the shear forces on the melt during the compounding process. None of these process modifications led to the disappearance of MMT clusters in the films even at low MMT content. However, it was observed that the homogeneity of iPP2/MMT films was improved for higher MMT concentrations. A masterbatch of iPP2/5.9 wt% MMT was therefore initially prepared and lower MMT concentration grade were obtained by dilution with pure iPP2. Two pre-compounding steps were generally sufficient to achieve satisfactory levels of homogeneity in the final nanocomposite films (Figure 6.2(b)).

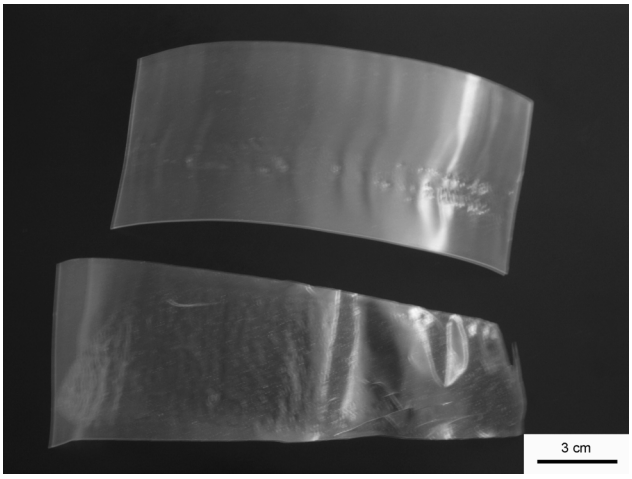

Figure 6.1. Sharskin on iPP2/3.4 wt% MMT films

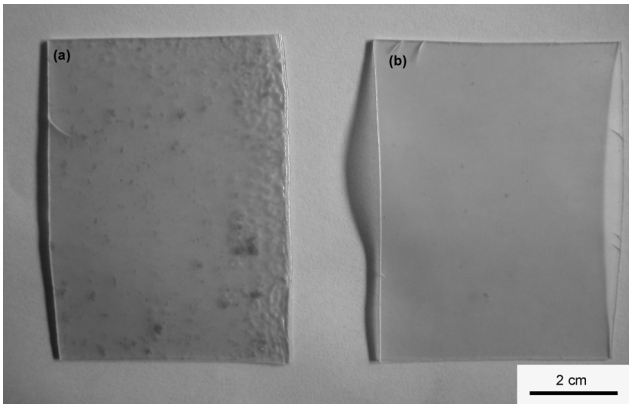

Figure 6.2. (a) Inhomogeneous and (b) homogeneous iPP2/3.4 wt% MMT films.

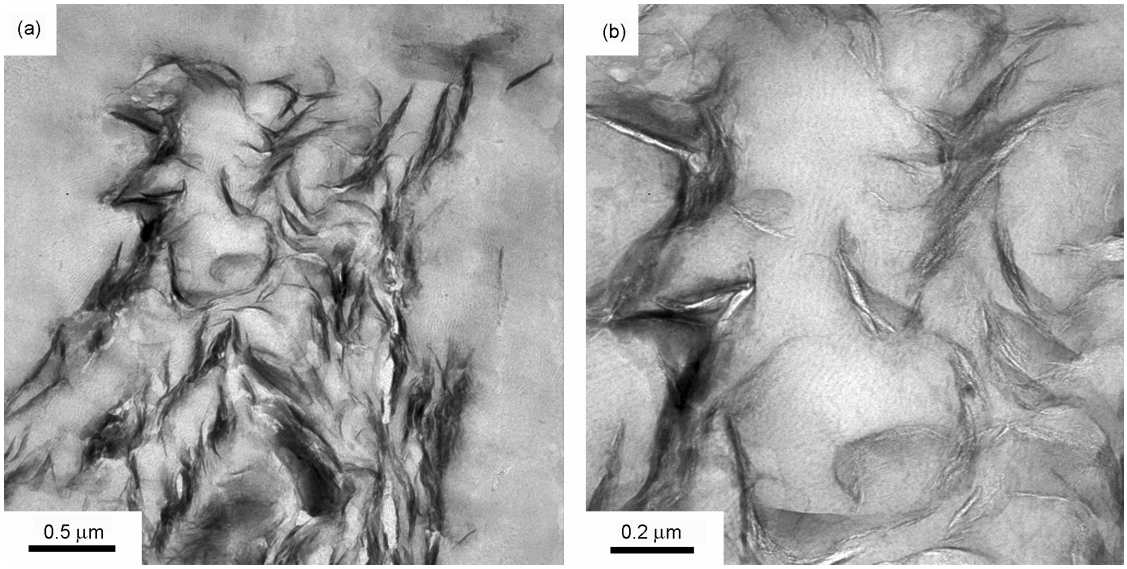

Figure 6.3. TEM micrographs of (a) a MMT agglomerate and (b) poorly dispersed MMT platelets within the iPP2 matrix.

Figure 6.4 shows pure iPP2 and iPP2/MMT films containing 3.4 and 5.9 wt% MMT. Visual inspection of the films indicated that their surface was smooth, and they were transparent with a color ranging from white for pure iPP2 to light brown with increasing MMT content. The final film thickness was about 0.7 mm at all MMT concentrations, for a nip fixed at 0.5 mm, owing to die swell of the viscoelastic iPP2/MMT melts after being constrained in the extrusion die[2].

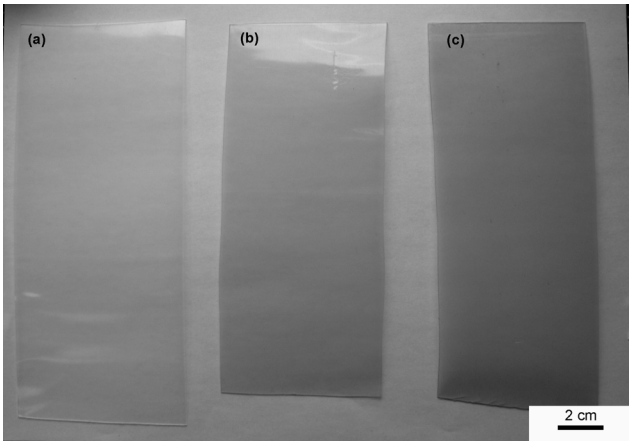

Figure 6.4. Image of iPP2/MMT films with different MMT concentration. (a) 0 wt% MMT, (b) 3.4 wt% MMT and (c) 5.9 wt% MMT.

Identical process parameters for extrusion-calendering could be used for the iPP2/MMT nanocomposite melts and the pure iPP2 melt (temperature, extrusion velocity). From the perspective of scale-up to an industrial line, additional costs may arise from the need for iPP/MMT granulates with the appropriate MMT concentration for direct integration in the global production process, or the set up of a melt compounding line capable of providing well-dispersed, homogeneous iPP/MMT nanocomposite melts.

6.3 iPP2/MMT FILM MORPHOLOGY

6.3.1 OPTICAL MICROSCOPY

In thermoplastic processes such as injection-molding or extrusion, the solidification of a semi-crystalline polymer occurs via flow induced crystallization, and the resulting structure is related to the temperature, the applied shear rate and the total strain[3].

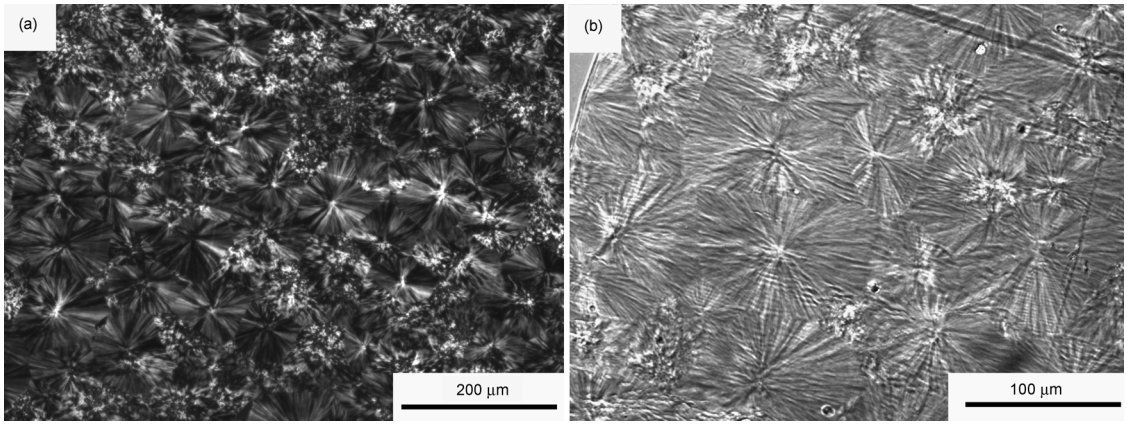

Figure 6.5. Polarized light micrographs of cross-sections from extrusion-calendered iPP2 films at (a) 20X and (b) 50X magnification.

Figure 6.5 shows polarized light micrographs at different magnifications of thin cross-sections taken from the center of extrusion-calendered iPP2 films. A uniform, well-developed polygonal spherulitic morphology was observed. In the case of extruded iPP, changes from a spherulitic to an elliptic morphology are reported to occur at about 50 % reduction in cross sectional area[4]. In the present extrusion-calendered films, the biaxial deformation led to a reduction of 51 % in the thickness of the sample from the extruder die to the exit of the calender, which is closed to this 50 % threshold. Therefore the biaxial extension of the film was not necessarily expected to influence spherulite shape. The spherulites were identified as α-type owing to their low brightness[5]. They were about 90 μm in diameter.

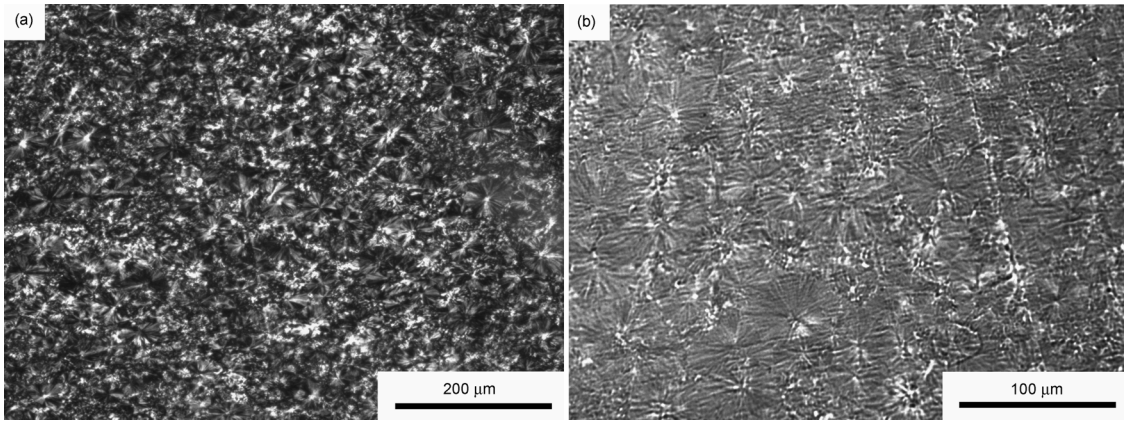

Figure 6.6. Polarized light micrographs from cross-sections of extrusion-calendered iPP2/1 wt% MMT films at (a) 20X and (b) 50X magnification.

It is apparent from Figure 6.6 that the size of the spherulites in iPP2/1 wt% MMT nanocomposite was smaller than that in pure iPP2 (about 46 μm in diameter). This

suggested that MMT particles were detrimental to spherulitic growth in iPP2. This was confirmed for 3.4 wt% MMT (Figure 6.7) and 5.9 wt% MMT (Figure 6.7) where the spherulite size was about 20 μm in diameter. The reduction of spherulite size in iPP on addition of MMT was observed previously by Perrin-Sarazin *et al.*[6], and elsewhere for other systems such as iPP/$CaCO_3$[7] or iPP/Al_2O_3[8].

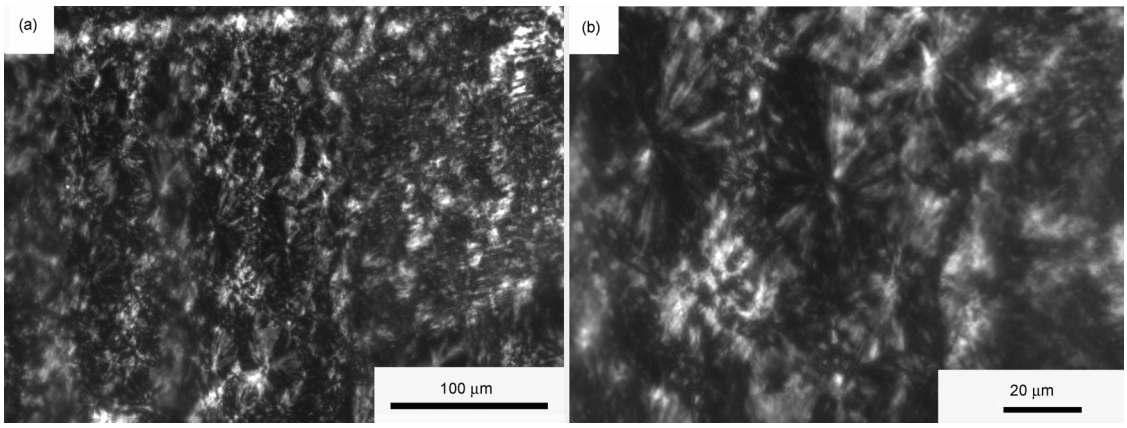

Figure 6.7. Polarized light micrographs of cross-sections from extrusion-calendered iPP2/3.4 wt% MMT films at (a) 20X and (b) 50X magnification.

It was found in section 4.3.1 that the degree of crystallinity of iPP1/MMT compression moldings and filaments did not change significantly on the addition of MMT. Crystallinity is generally controlled by two competitive factors, i.e. nucleation and growth of the spherulites[9]. Since physical hindrance of MMT to the motion of polymer molecular chains, also discussed in section 4.3.1, is known to retard the growth of crystallites, it was assumed for iPP2/MMT films that the addition of MMT was beneficial for the nucleation process, leading to smaller spherulites. Thus these two competing factors may result in unchanged crystallinity on addition of MMT compared with pure iPP2.

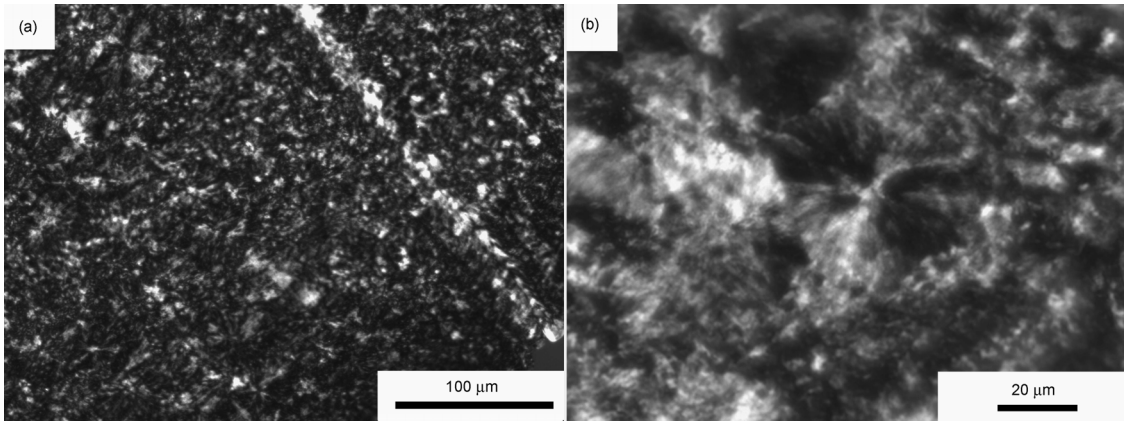

Figure 6.8. Polarized light micrographs of cross-sections from extrusion-calendered iPP2/5.9 wt% MMT films at (a) 20X and (b) 50X magnification.

Small amounts of the trigonal iPP2 β-phase were also observed in all films regardless of the MMT concentration (Figure 6.9). Unlike the α-phase, which is characterized by the presence of cross-hatched crystallites radial lamellae, the β-phase presents purely radial lamellae, resulting in much brighter images under polarized light. These observations were consistent with the presence of the β-phase reflection peaks in the WAXS patterns of iPP1/MMT filaments (section 4.3.1, Figure 4.20, especially at high MMT concentration). Machado *et al.*[10] have pointed out that the β-phase can be formed either by adding nucleating agents or by mechanical deformation of extruded or injection molded products. As the β-phase was observed in both pure iPP2 and iPP2/MMT films, the effect of the mechanical deformation induced by the processing of the films was assumed to be mainly responsible for its presence in this particular case.

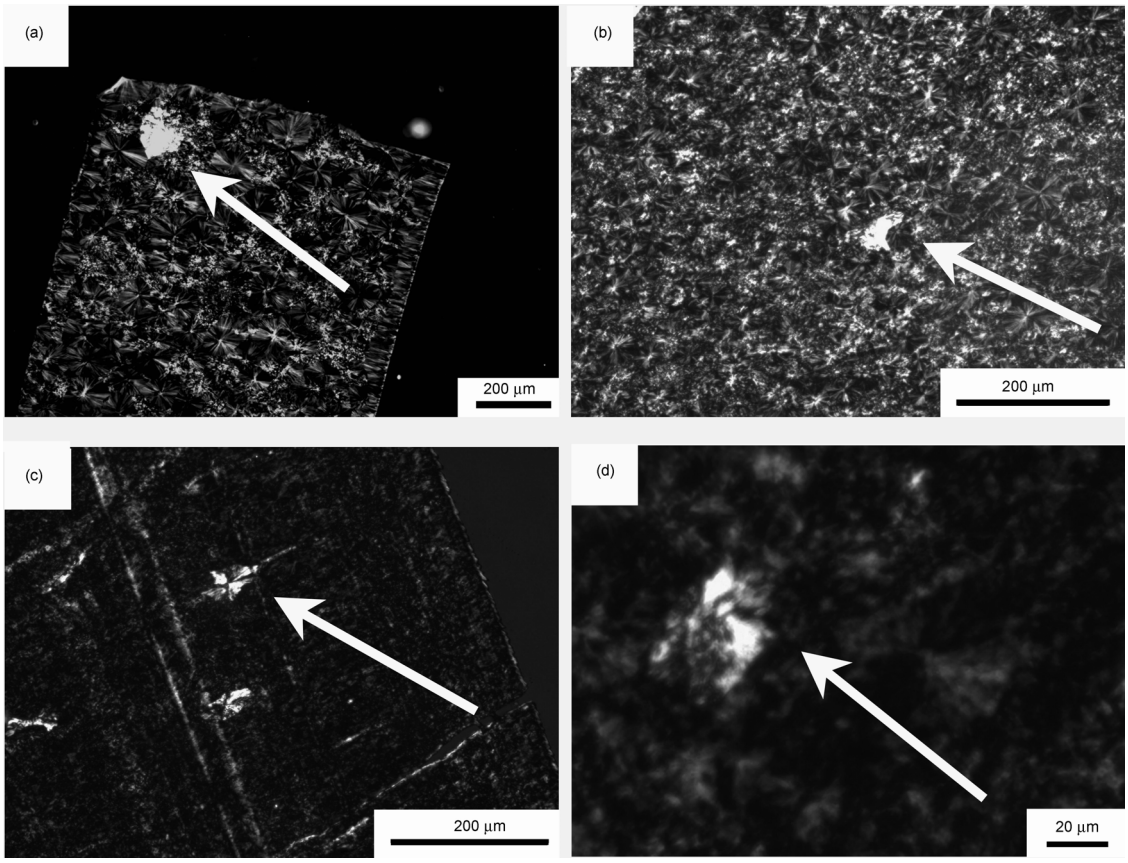

Figure 6.9. Polarized light micrographs of cross-sections from extrusion-calendered (a) iPP2, (b) iPP2/1 wt% MMT, (c) iPP/3.4 wt% MMT and (d) iPP2/5.9 wt% MMT films at different magnifications. The bright areas indicated corresponds to the iPP2 trigonal β-phase.

6.3.2 XRD

The WAXS patterns for different MMT concentrations (Figure 6.10) were similar, indicating a MMT layer spacing of about 3.17 nm regardless of the composition.

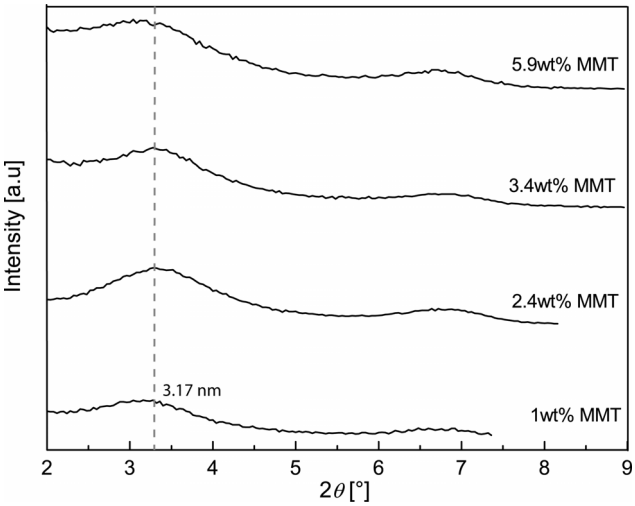

Figure 6.10. XRD patterns obtained from iPP2/MMT at different MMT concentrations. The similar position of the peaks in each case suggested the degree of intercalation to be the same in all the films regardless of MMT concentration.

6.3.3 TEM

Thin sections of iPP2/3.4 wt% films taken parallel and perpendicular to the extrusion direction were investigated by TEM in order to assess the deformation developed in the nip of the calendar, and any preferential MMT platelet orientation.

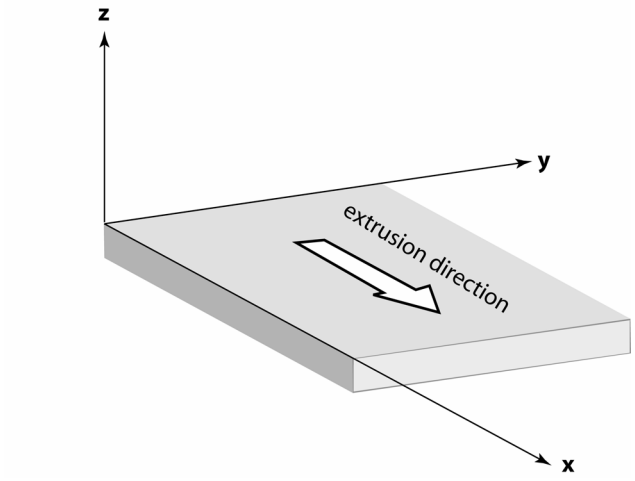

Figure 6.11. Frame of reference for the TEM micrographs taken from the iPP2/MMT films.

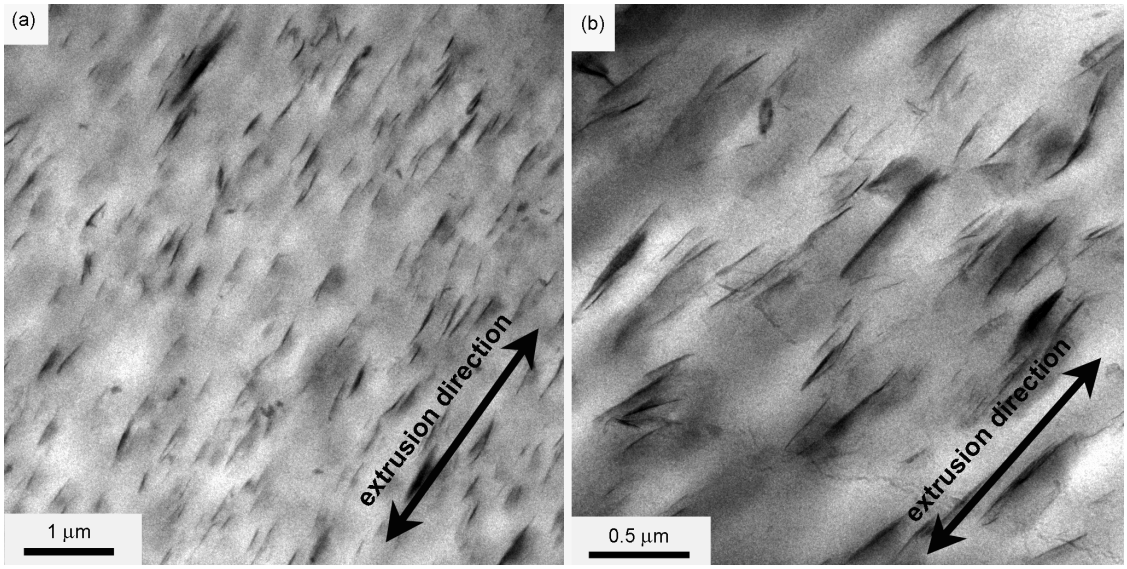

Figure 6.12. TEM micrographs of thin sections of iPP2/3.4 wt% MMT taken in the (xy) plane at different magnifications.

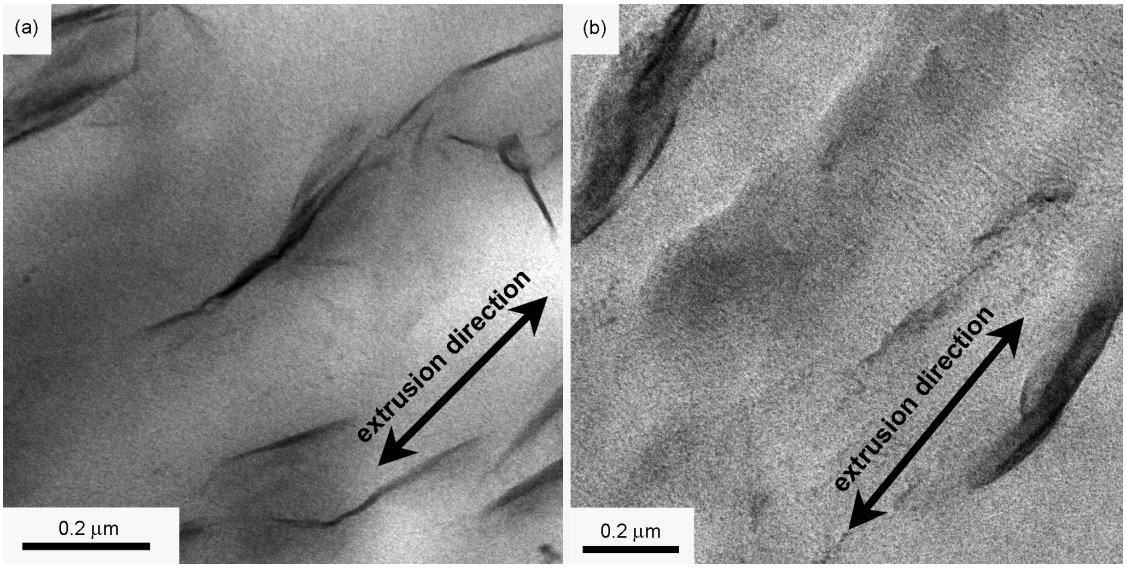

Figure 6.13. TEM micrographs of thin sections of iPP2/3.4 wt% MMT taken in the (xy) plane at different magnifications.

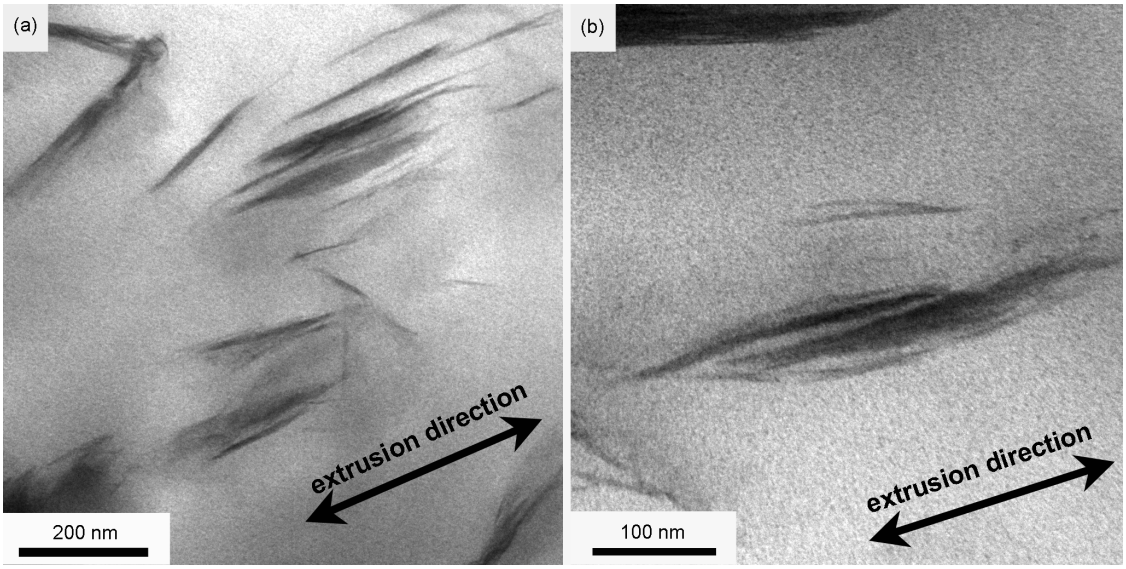

Figure 6.14.TEM micrographs of thin sections of iPP2/3.4 wt% MMT film, taken in the (*xy*) plane at different magnifications

Figure 6.12 shows typical morphologies of the MMT platelets taken in the (*xy*) plane (as seen Figure 6.11). A homogenous distribution of MMT in the iPP2 matrix was observed together with a global orientation of MMT platelets along the extrusion direction. As shown in Figure 6.13(a), MMT stacks were buckled. Single MMT layers (Figure 6.13(a)) as well as larger stacks (Figure 6.14) were also present, characteristic of a mixed intercalated-exfoliated morphology. The particle aspect ratio, α was estimated to be about 30 – 50, which is similar to that estimated from injection molding specimens (section 3.3.2). Shear forces applied on the melt during the extrusion-calendering process were much lower (total draw ratio, λ of 1.5 to 2) than those observed during melt-spinning (λ = 100 to 500), for which α increased to about 150 (section (4.2.2)). However, the shear forces encountered during the extrusion-calendering process were sufficient to induce a preferential orientation of the platelets along the extrusion direction and some orientation of iPP2 lamellae perpendicular to the extrusion direction as shown in Figure 6.13(b) and also observed in the case of iPP1 filaments (section 4.3.1).

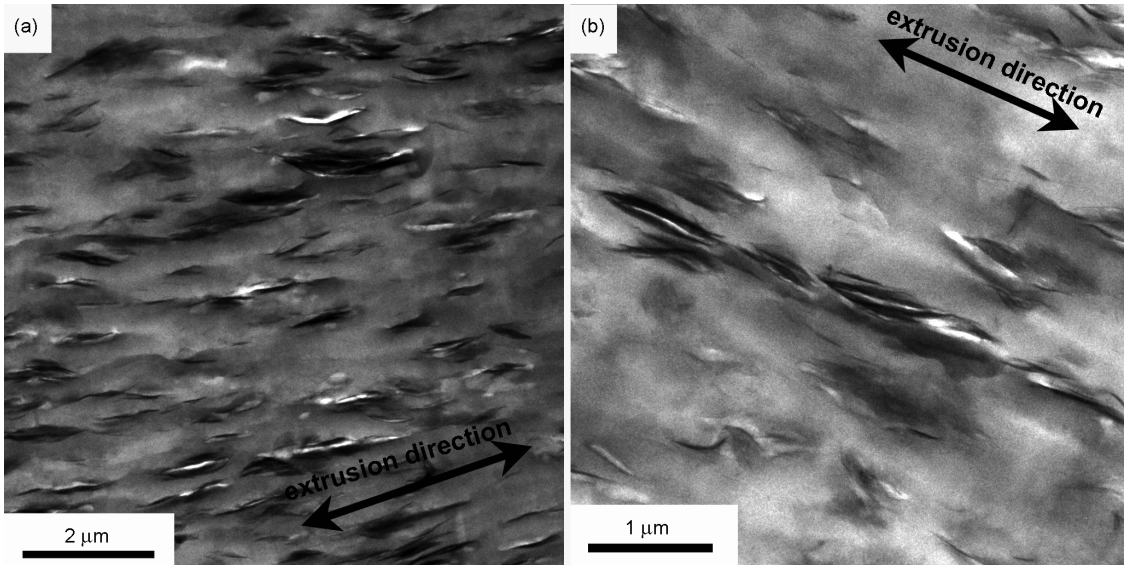

Figure 6.15. TEM micrographs of thin sections of iPP2/3.4 wt% MMT film in the (*xz*) plane at different magnifications.

Figure 6.15 shows typical morphologies of MMT platelets in the (*xz*) plane. As observed in the (*xy*) plane, transverse sections of MMT platelets globally oriented along the extrusion direction were visible. Koo *et al.*[10] and Bafna *et al.*[11] have studied the orientation of MMT tactoids in polymer layered silicate films produced by a melt-extensional rheometer and cast extrusion respectively, using 2D-WAXS and 2D-SAXS. They reported that silicate surfaces were aligned parallel to the film surface, suggesting a preferential orientation direction of MMT cross sections in all film sections. However in the present case, a random orientation of the MMT transverse sections in the (*yz*) plane was observed (Figure 6.16), possibly because of relatively low shear forces involved in the present case.

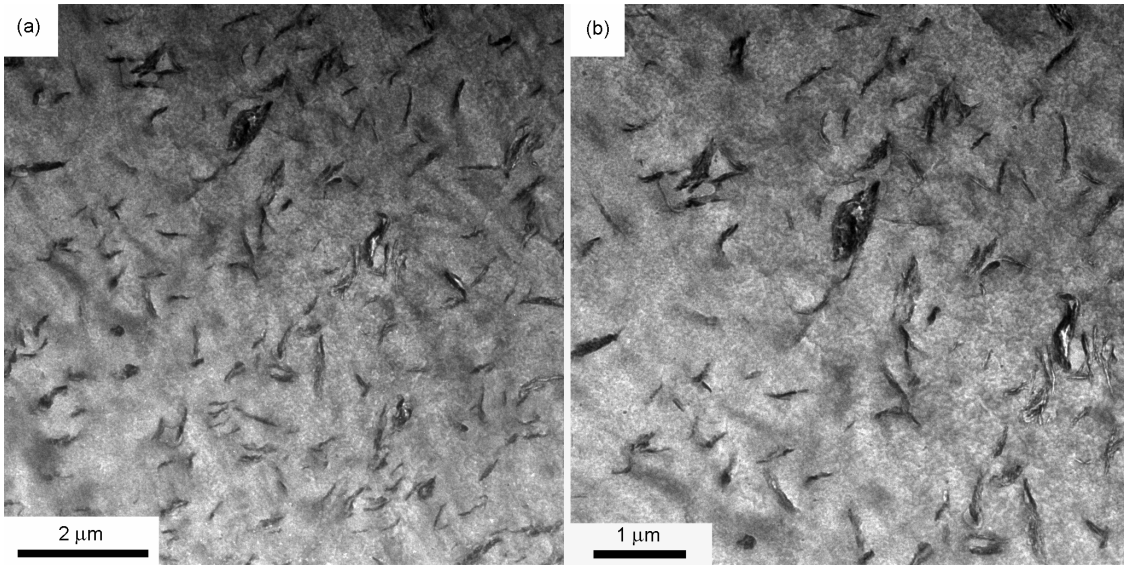

Figure 6.16. TEM micrographs of thin sections of iPP2/3.4 wt% MMT taken in the (*yz*) plane at different magnifications.

6.4 TENSILE ANALYSIS

6.4.1 Tensile tests

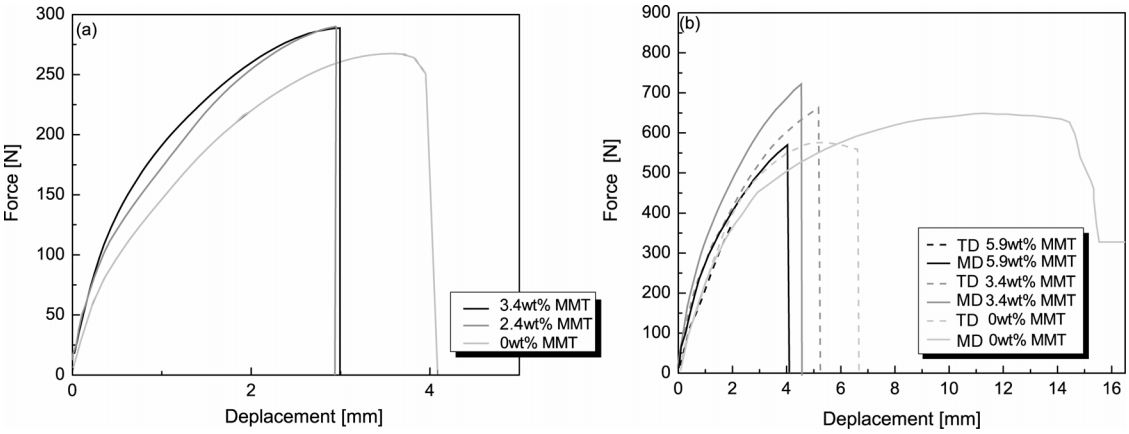

Figure 6.17. Representative force displacement curves of (a) injection molding iPP2/MMT specimens at different MMT concentration and (b) extrusion-calendered iPP2/MMT MD and TD films having different MMT concentration.

Figure 6.17(a), presents the force-displacement curves of injection molded specimens. The iPP2 injection moldings showed ductile behavior with a characteristic yield point.

The ductility and the elongation at break decreased with increasing MMT concentration. For comparison, force-displacement curves of extruded films loaded in the melt flow direction (MD) and in the transverse direction (TD) are given in Figure 6.17(b), the MD specimens showing significantly lower deformation at break iPP2/MMT injection molding specimens showed more fragile behavior but a higher force at break.

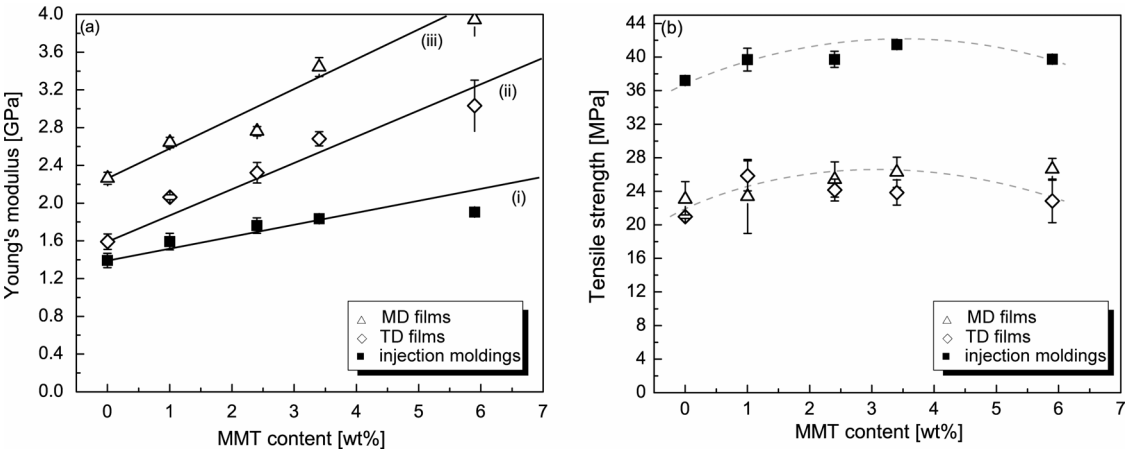

Figure 6.18. (a) Young's modulus as a function of MMT content for injection moldings and extruded films (b) Tensile strength as a function of MMT concentration for injection moldings and extruded films. The curves in (a) correspond to Halpin-Tsai predictions for: (i) an isotropic composite with α =50; (ii) and (iii) a uniaxially oriented composite with α =50.

Figure 6.18(a) compares the Young's moduli as a function of MMT content for injection moldings and MD and TD extruded films. The Young's modulus was systematically higher for MD films than for TD films regardless of the MMT concentration. In the case of iPP2, the increase of modulus on extrusion-calendering compared with that in the injection moldings and the difference between them MD and TD moduli indicated that the extrusion-calendering process induced some molecular orientation of the iPP2 chains, these tending to orient in the extrusion direction. As the extrusion-calendering provided a biaxial deformation of the polymer melt, iPP2 was also somewhat extended in the transverse direction. Therefore, the TD specimens had higher Young's moduli than injection moldings (characterized by a nearly random orientation of polymer chains). For each specimen type, the Young's modulus increased monotonically with MMT concentration and the results could be fitted with the Halpin-Tsai model, described in section 4.3.2, for composites with a filler aspect ratio, $\alpha = 50$, randomly oriented in the case of injection moldings and uniaxially oriented in the case of extrusion-calendered films. The matrix modulus in each case was taken to be that of the corresponding pure iPP2 specimen. The trends of the tensile tests were consistent with TEM images, which showed MMT platelets oriented in the melt direction with an aspect ratio of about 50 (section 5.3.3).

Unlike the Young's moduli, the tensile strengths of films, shown in Figure 6.18(b) were similar, regardless of the direction of testing. However, they were systematically lower

than the tensile strengths of the injection moldings, accounted for again by an orientation of both the polymer chains and MMT platelets during the extrusion-calendering process. Consistent results are found in the literature. Fayolle *et al.*[11] report a tensile yield stress of about 27 MPa in the case of 100 μm thick iPP films prepared by extrusion, and Chen *et al.*[12] report a tensile strength of about 33 MPa for injection molded dumbbell shaped iPP specimens.

6.4.2 Tensile tests on Double Edge Notched (DENT) specimens

a. Introduction

Fracture mechanics is often used to characterize mechanical properties of polymer films. However, to date, few studies have been made of iPP2/MMT films[13], and none that take into account the effect of process induced orientation. In this section, fracture mechanism parameters have been evaluated as a function of MMT content and the film extrusion direction. The objective was to identify any anisotropy in the material properties, and to relate the film properties to the nanocomposite morphology and the MMT particle orientation. The specimens were double edge notched tensile (DENT) specimens prepared according to the ESIS protocol[14]. The films were about 0.7 mm in thickness and were tested at a speed of 20 mm/min as recommended in the protocol. Details of the test conditions and specimen geometry are given in section 3.2.4.

b. Results

- *Force-displacement curves*

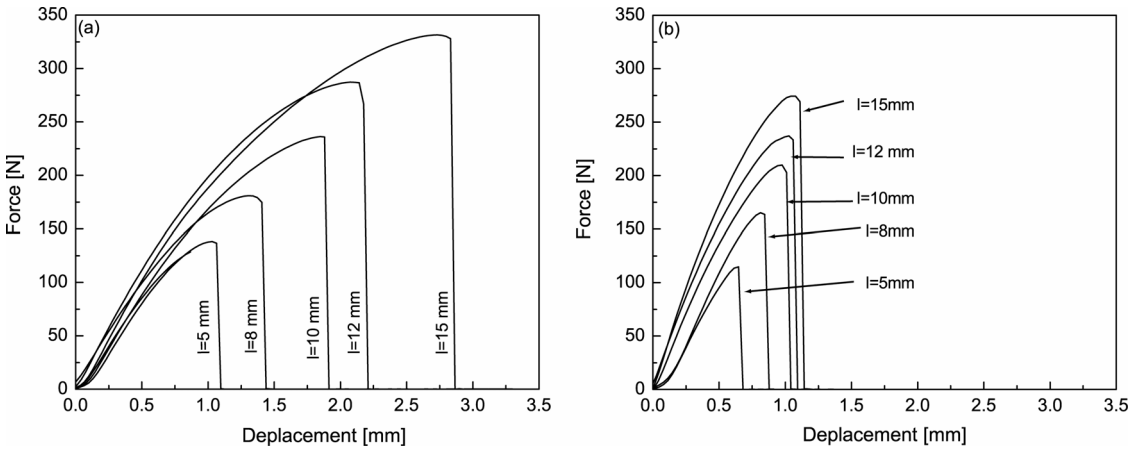

Figure 6.19. Typical force-displacement curves for MD DENT specimens for different *l* in (a) pure iPP2 films, and (b) iPP2/3.4wt% MMT films.

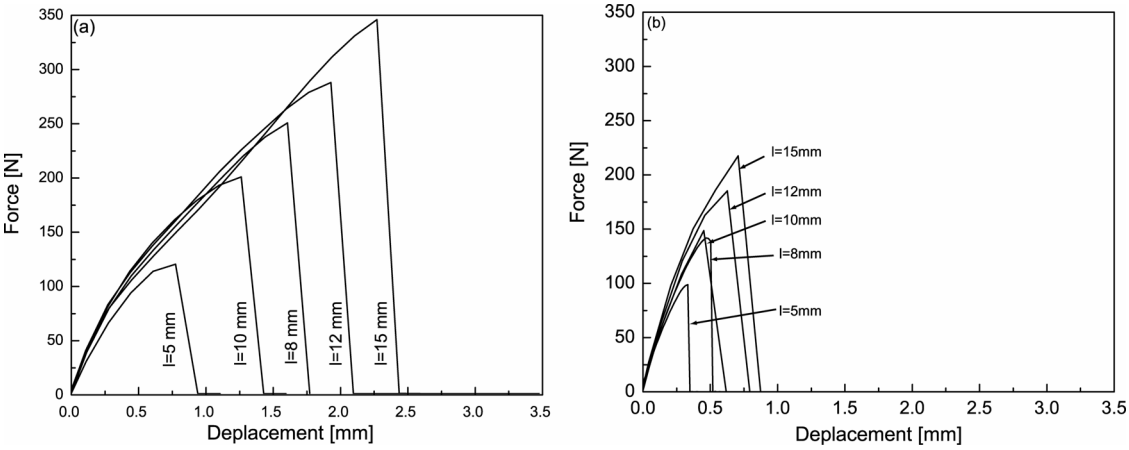

Figure 6.20. Typical force-displacement curves for TD DENT specimens for different *l* in (a) pure iPP2 films, and (b) iPP2/3.4 wt% MMT films.

The load-displacement curves of DENT specimens of iPP2 and iPP2/3.4 wt% MMT MD and TD films with different *l* are shown in Figure 6.19 and Figure 6.20. For a given material, the curves were geometrically similar, and the maximum load and the displacement to failure increased regularly with increasing *l*, indicating fracture to occur under identical stress conditions. For each series of materials, similar trends were observed. The load increased continuously with the displacement up to a sharp drop in load that coincided with fracture of the specimen. This was true at all MMT concentrations for the MD and TD films. These force-displacement curves were typical of semi-brittle materials for which the force displacement curves deviate from linearity after a certain displacement and which show unstable crack propagation. In general, it was found that the maximum load and the displacement to failure decreased with increasing MMT content for a given *l*.

- *Fracture surface analysis*

Analysis of fracture surfaces of MD and TD specimens was performed by SEM. The pictures were taken at the notch tip, at the center of the fracture surface and also in the center at higher magnification.

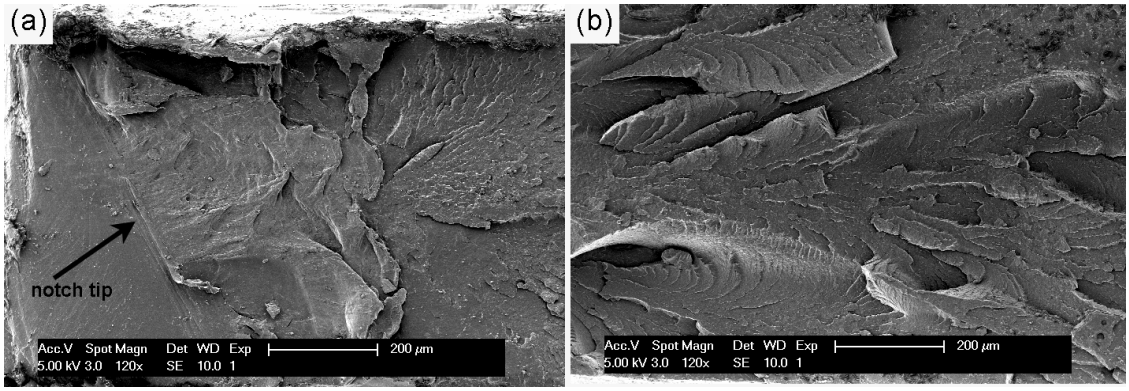

Figure 6.21. SEM pictures of fracture surface of iPP2 MD specimens taken at (a) the notch tip and (b) in the center of the fracture surface.

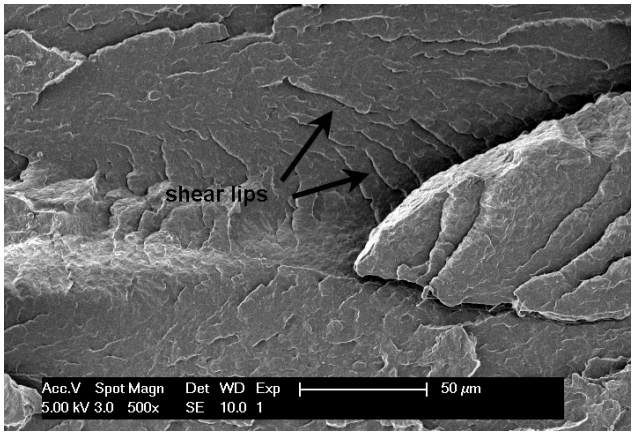

Figure 6.22. SEM picture of fracture surface of iPP2 MD specimens taken in the center of the fracture surface.

A typical fracture surface for unfilled iPP2 is shown in Figure 6.21 for MD specimens and in Figure 6.27 for TD specimens. Shear lips of plastic deformation characteristic of ductile instability were present in the MD specimens. Ductile instability consists at initial ductile crack propagation under loading, followed by unstable crack propagation when the stress reaches a critical value[15]. Unfilled TD specimens exhibited a smooth surface characteristic of brittle failure and unstable crack propagation (Figure 6.27). The fracture surface showed tufts corresponding to crazing (Figure 6.28). The formation of crazes perpendicular to the stress direction facilitates the propagation of the crack and replaces yielding as the dominant microdeformation mechanisms.

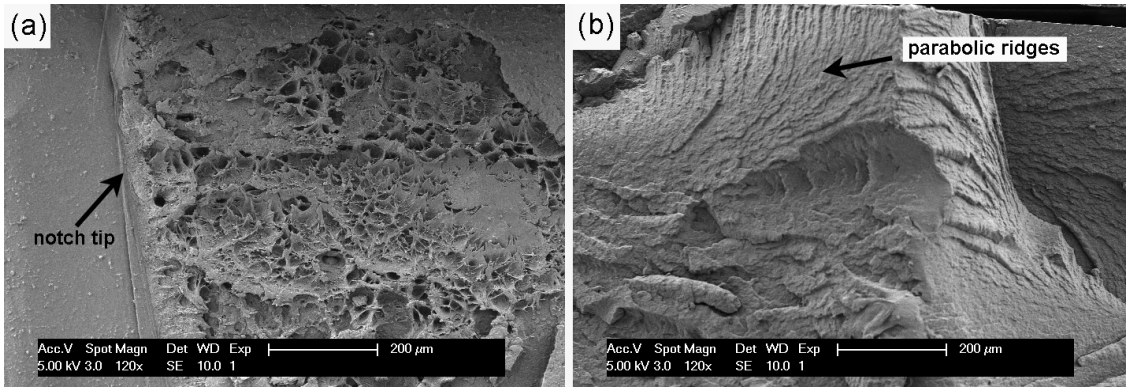

Figure 6.23 SEM pictures of fracture surface of iPP2/1wt% MMT MD specimens taken at (a) the notch tip, and (b) in the center of the fracture surface.

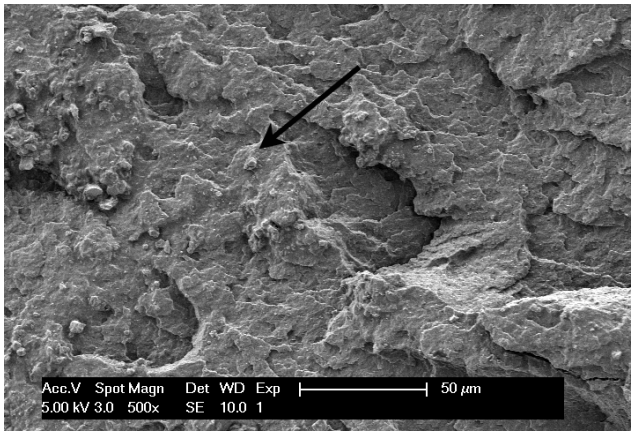

Figure 6.24. SEM picture of fracture surface of iPP2/1wt% MMT MD specimens taken in the center of the fracture surface at high magnification. The black arrow indicates an MMT aggregate.

Certain specific features of iPP2/MMT MD and TD specimens differed significantly from those of unfilled iPP2. For MD specimens at 1 wt% MMT (Figure 6.23(a)), there was evidence of extensive void nucleation at the notch tip together with significant plastic deformation of the matrix in the center of the fracture surface (Figure 6.23(b)). The parabolic ridges observed in Figure 6.23(b) reflect resistance to crack propagation. A rough surface as well as the presence of MMT aggregates at the fracture surface (Figure 6.24) indicated that the MMT layers forced the crack propagation to follow a tortuous path. At high MMT concentrations, Figure 6.25, the fracture surface of MD specimens were less textured across the entire fracture surface compared with iPP2/1 wt% MMT MD specimens. At higher magnification, (Figure 6.24), smaller voids than those observed for iPP2/1 wt% MMT MD specimens were visible as well as some MMT aggregates. The roughness extended to the micron and even sub-micron scale, indicating the fracture mechanism to occur at a very small scale and it appeared therefore that additional mechanisms of energy dissipation were associated with the MMT particles in the form of

localized plastic deformation. The presence of voids at the fracture surface of iPP/MMT nanocomposites has been observed elsewhere[13]. Thus, MMT particles may act as stress concentrators within the plastic zone, which reduces the yield stress compared with unfilled specimens.

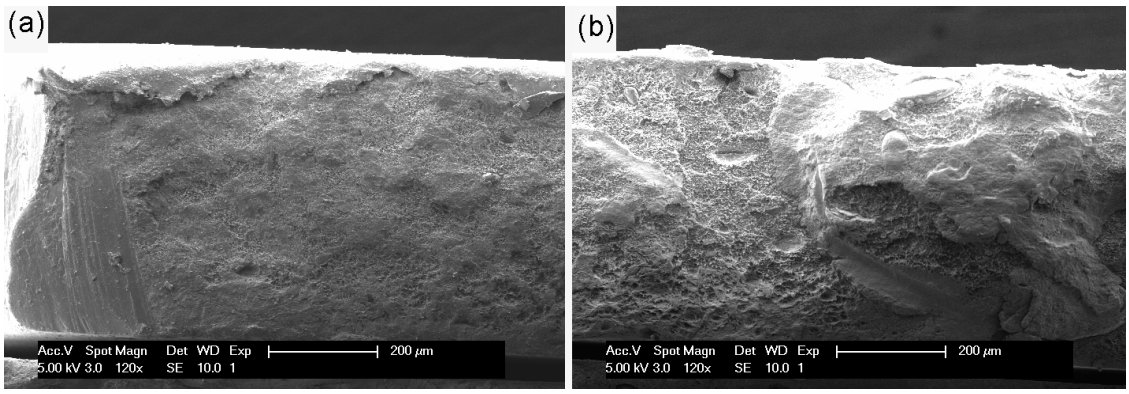

Figure 6.25 SEM pictures of fracture surface of iPP2/5.9 wt% MMT MD specimens taken at (a) the notch tip, and (b) in the center of the fracture surface.

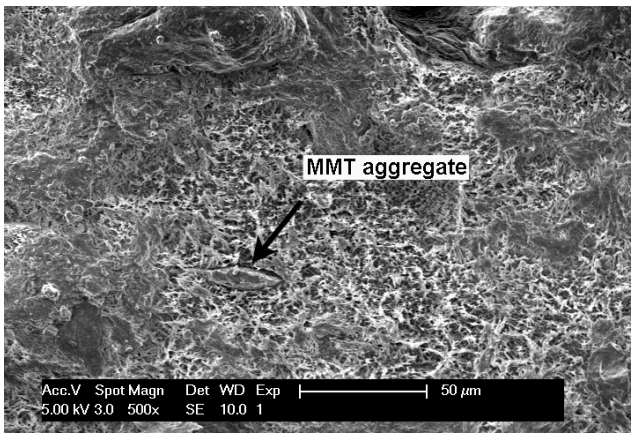

Figure 6.26. SEM picture of fracture surface of iPP2/5.9wt% MMT MD specimens taken in the center of the fracture surface at high magnification.

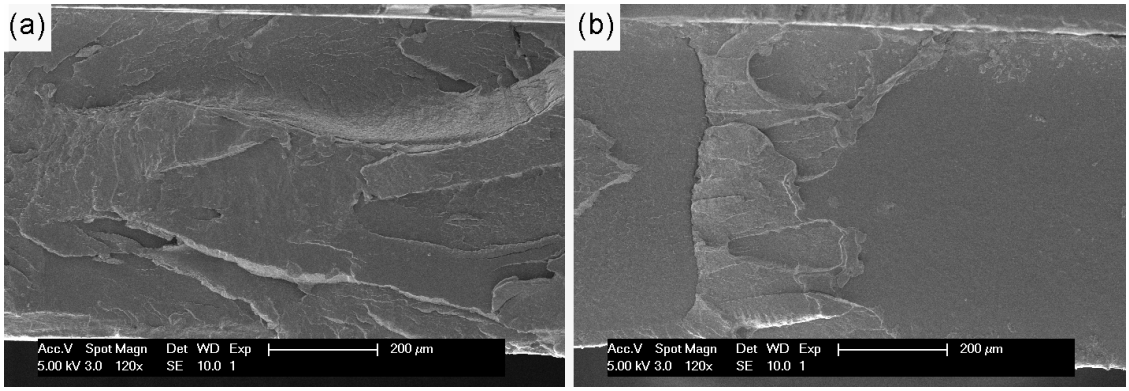

Figure 6.27. SEM pictures of fracture surface of iPP2 TD specimens taken at (a) the beginning, (b) in the center of the fracture surface.

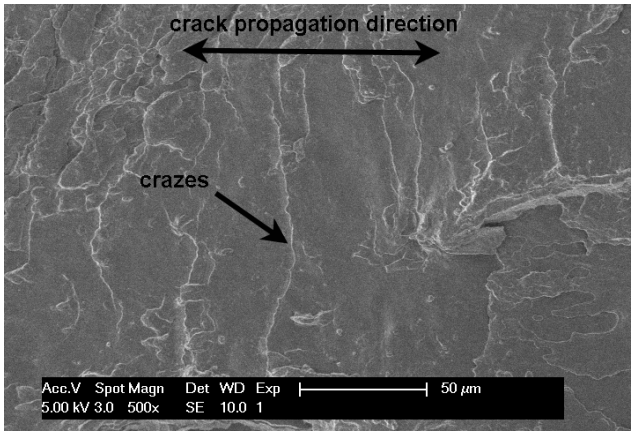

Figure 6.28. SEM picture of fracture surface of iPP2 TD specimens taken in the center of the fracture surface at high magnification.

For iPP2/MMT TD specimens, some voids were visible on the fracture surface at low (Figure 6.29(a)) and high (Figure 6.32(b)) MMT concentrations. However, the fracture surfaces were relatively smooth (Figure 6.30 and Figure 6.31) compared with those of the MD specimens, reflecting the more brittle behavior.

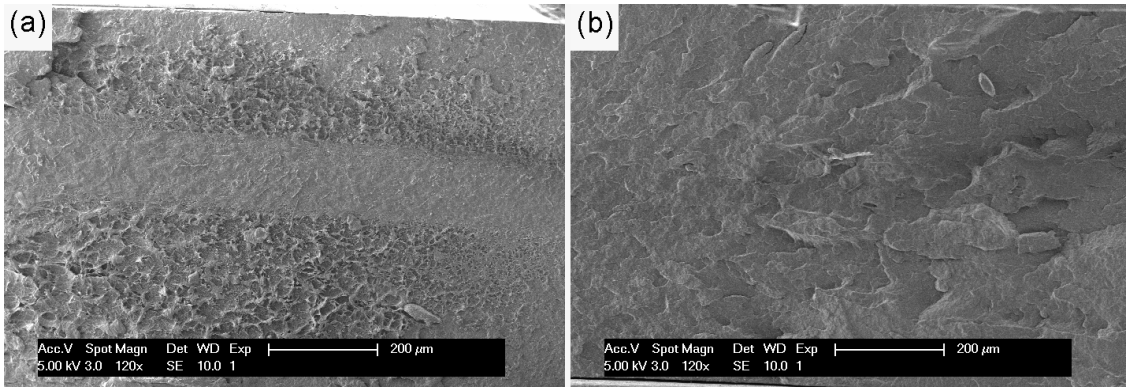

Figure 6.29. SEM pictures of fracture surface of iPP2/1wt% MMT TD specimens taken at (a) the notch tip, and (b) in the center of the fracture surface.

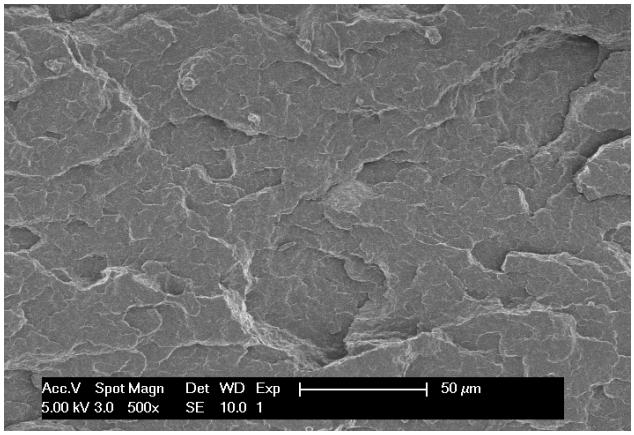

Figure 6.30. SEM picture of fracture surface of iPP2/1wt% MMT TD specimens taken in the center of the fracture surface at high magnification.

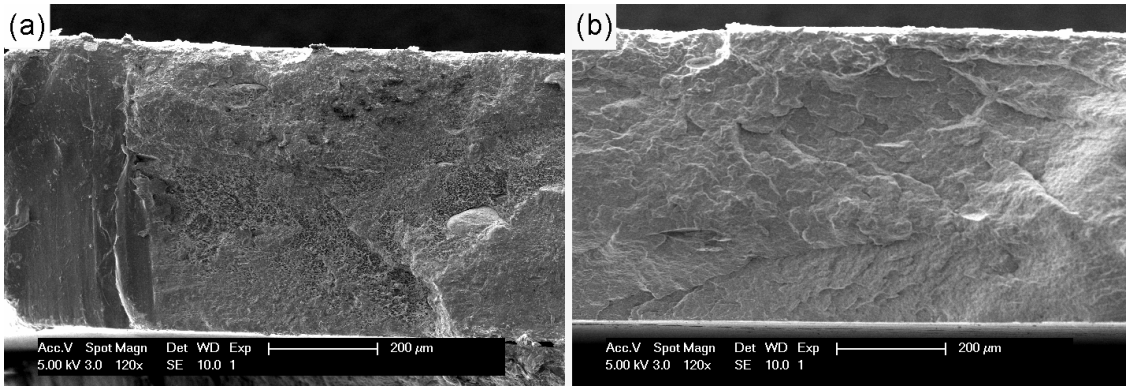

Figure 6.31 SEM pictures of fracture surface of iPP2/5.9 wt% MMT TD specimens taken at (a) the notch tip, and (b) in the center of the fracture surface.

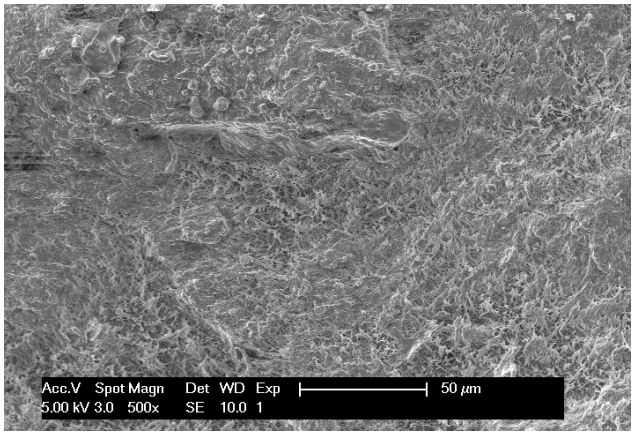

Figure 6.32. SEM picture of fracture surface of iPP2/5.9wt% MMT TDD specimens taken in the center of the fracture surface at high magnification.

- *Yield stress criterion*

It was not possible to detect visually whether crack propagation occurred prior to ligament yielding. Nevertheless, to investigate how the stress state may evolve, the maximum net section stress, σ_{max}, determined from the force-displacement curves, has been plotted against l in Figure 6.33 and compared with the tensile strength, σ'_{max}, of un-notched specimens, Figure 6.18(b). For the MD and TD films, σ_{max} decreased with MMT concentration. For a given MMT concentration, σ_{max} values were of the same order in both testing directions and did not depend on l, except at high MMT concentrations for which σ_{max} values for MD specimens were well below those of TD specimens. According to Hill's plasticity theory, if σ_y is the uniaxial yield stress of un-notched specimens, then under pure plane stress conditions, σ_{max} = 1.15 σ_y for a DENT specimen. When the ligament is in the mixed mode regime, (i.e. both plane stress and plane strain), σ_{max} becomes dependent on ligament length and its value increases with decreasing ligament length. Finally, the plane stress mode corresponds to σ_{max} 1.15 σ_y[11] (i.e. σ_{max} does not exceed the stress at the onset of yielding). As seen in Figure 6.17(b), yielding type behavior was only shown by pure iPP2 MD and TD films, the others having more fragile behavior. Therefore the term "yield stress" was not appropriate to all of the of un-notched specimens. However, to assess the fracture mode of the DENT specimens, σ_{max} was compared with 1.15 σ'_{max} for MD and TD specimens. In the present case, for MD specimens (Figure 6.33(a)), σ_{max} of iPP2 and iPP2/1 wt% MMT was well above 1.15 σ'_{max}, whereas it was below 1.15 σ'_{max} for iPP2/MMT films with higher MMT contents. For TD specimens (Figure 6.33(b)), the overall trend was similar but σ_{max} was generally closer to1.15 σ'_{max}. A pseudo plane stress criterion was therefore verified for MD and TD films with a MMT concentration above 1 wt%, but below this concentration the criterion was not met. However, as pointed out by Arkhireyeva *et al.*[16], Hill's criterion is not satisfied for a wide range of polymers, and in particular those that show strain-softening. Ferrer-Balas *et al.*[17] suggest using the tensile yield stresses of injection molding

specimens rather than those of un-notched specimens. For injection molding specimens a yielding type behavior is more often observed (Figure 6.17(a)) and the tensile strengths in the present case were systematically higher than those observed for the un-notched films, as shown in Figure 6.18(b). Therefore a tensile yield stress σ_y could also be defined for iPP2 and iPP2/1wt% MMT. Under these conditions, 1.15 σ_y = 42.8 MPa for iPP2 and 1.15 σ_y = 45.6 MPa for iPP2/1 wt% MMT, so that the plane stress criterion would also be satisfied for these two materials.

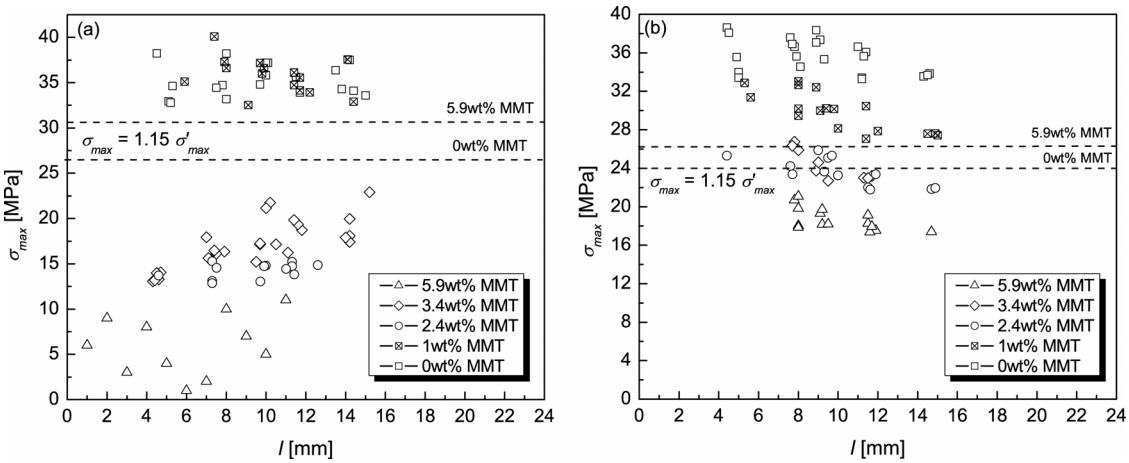

Figure 6.33. Maximum stress, σ_{max}, as a function of ligament length, *l*, at different MMT concentrations for (a) MD specimens and (b) TD specimens. Dashed lines are 1.15 σ'_{max} values at different MMT concentrations, where σ'_{max} are the maximum stress values of un-notched MD and TD specimens.

c. Essential Work of Fracture analysis (EWF)

The assumption of a plane stress state during crack propagation would justify analysis of the results of the tensile tests on DENT specimens in terms of the Essential Work of Fracture (EWF) approach, which will briefly be described in what follows.

- *Background to the EWF approach*

Fracture of a linearly elastic material under plane strain state and at nominal stresses well below the uniaxial tensile yield stress is generally characterized by Linear Elastic Fracture Mechanics (LEFM) [18]. Under these conditions, the extent of plastic flow at the tip of the crack is restricted with respect to the minimum specimen dimensions[16, 19]. In the case of an elastic plastic material, LEFM is no longer valid, but fracture mechanisms can be investigated by considering the energy dissipation at the crack tip. This energy is described by a J-integral defined by Rice[20]. The critical value of the J-integral at the onset of stable crack extension is denoted J_{IC}. In practice, the J-integral is determined from force-displacement curves and is a function of the crack propagation length[21]. Moreover the analysis is again restricted to plane strain crack propagation and restricted plastic deformation at the crack tip.

The EWF approach has been developed specifically to characterize ductile materials in the form of films, for example, in which the geometrical requirements of LEFM and/or elastic plastic fracture mechanics cannot be met. It is based on the idea that the non-linear deformation at the crack tip in (DENT) specimen may be divided into an inner fracture process zone (IFPZ) and an outer plastic deformation zone (OPDZ) as shown in Figure 6.34.

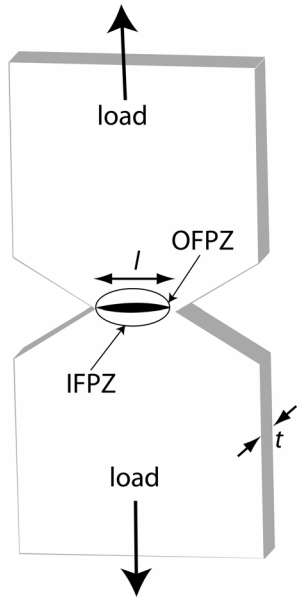

Figure 6.34. Schematic description of a fracture process zones in a DENT specimen. The inner fracture process zone (IFPZ) and the outer plastic deformation zone (OPDZ) are indicated.

The total work of fracture, W_f is then partitioned into two terms: the essential work of fracture, W_e, the work dissipated in the IFPZ to form the fracture surface, and the non-essential work of fracture, W_p, dissipated in the OPDZ, where various types of deformation such as shear yielding and microvoiding may occur[22, 23]. Thus

$$W_f = W_e + W_p \qquad \textbf{Equation 6.1}$$

The principle of the experimental method is to measure the fracture energy of a serie of DENT specimens with different ligament lengths, l. W_e, is associated with surface creation and is therefore proportional to the fracture area and hence l. W_p on the other hand is dependent on the volume of the OPDZ. In plastics, this volume is proportional to the l^2. Thus W_f is given by the expression[14, 24]:

$$W_f = w_e lt + w_p \beta l^2 t \qquad \textbf{Equation 6.2}$$

where t is the specimen thickness, β is a shape factor associated with the form of the OPDZ. w_e and w_p are the specific essential work of fracture and the specific non-essential work of fracture respectively. Dividing by lt one obtains

$$w_f\ (=W_f / lt) = w_e + \beta w_p l \qquad \textbf{Equation 6.3}$$

where w_f is the specific work of fracture.

The total area under the load-displacement curve in a given test defines w_f. The dependence of w_f on l is illustrated in Figure 6.35. Two distinct regimes of behavior may be identified. At large l, plane stress conditions normally dominate, whereas at small l, plane strain conditions may occur, resulting in a decrease of the total work of fracture. w_f is estimated from the intercept at l = 0 of a linear fit $w_f(l)$ (cf. Equation 6.3). The slope of $w_f(l)$ gives βw_p. Two conditions must be satisfied for EWF approach to be valid:

(i) the minimum ligament length must correspond to plane stress conditions.
(ii) complete yielding of the ligament should occur before crack growth to ensure a constant stress state at the crack tip.

For criterion (i) to be valid, all force-displacement curves must have the same shape, the curves (l_r) = f(l) and F_{max} = f(l) must be linear, ((l_r) where is the displacement at crack propagation and F_{max} the maximum force on the force-displacement curves) and σ_{max} = 1.15σ_y must be verified. Criterion (ii) is satisfied when the following ligament size restrictions, recommended for a valid plane-stress determination of w_e, are respected:

$$3t - 5t \le l \le \min(2R_p, W/3) \qquad \textbf{Equation 6.4}$$

with;

$$2R_P = \frac{1}{\pi}\frac{Ew_e}{\sigma_y^{\ 2}} \qquad \textbf{Equation 6.5}$$

where, W is the width of the sample, R_p is the radius of the plastic zone at the crack tip, E is the Young's modulus of the material, and σ_y is the tensile yield stress.

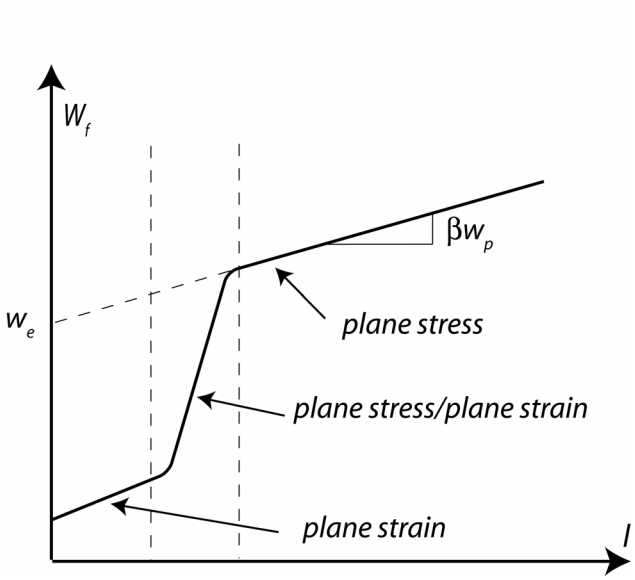

Figure 6.35. Evolution of W_f over large range of l, showing the transition from plane stress to plane strain with decreasing l[25].

- *Specific work of fracture*

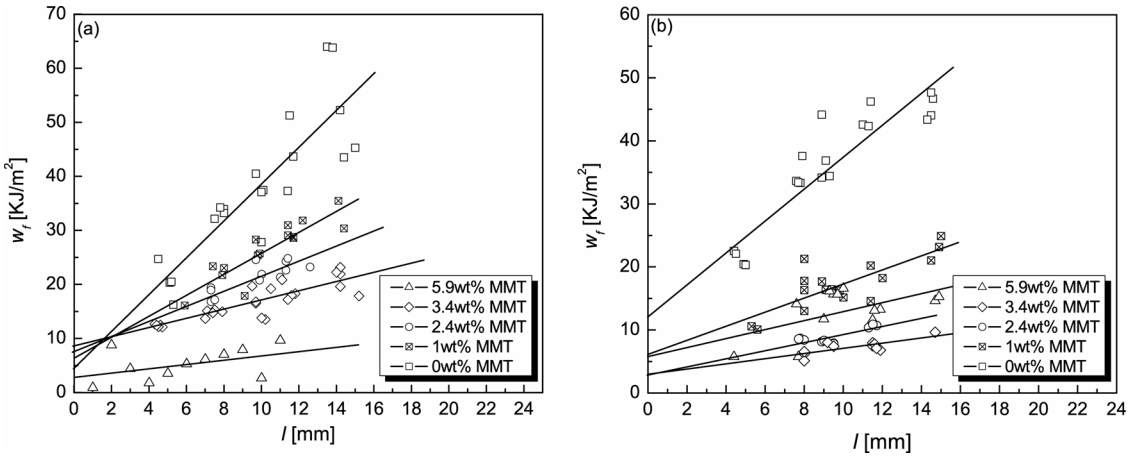

Figure 6.36. Specific work of fracture, w_f , as a function of ligament length at different MMT concentrations for iPP2/MMT (a) MD specimens and (b) TD specimens. The curves are linear regression lines for each data set.

Plots of the specific work of fracture, w_f, against l for the different compositions and orientations are shown in Figure 6.36(a) and (b), together with the regression lines from which the specific essential work of fracture, w_e, and the specific non-essential work of fracture, βw_p were determined. The values of the regression coefficient R were also recorded. A mean value of 0.87 was calculated for MD specimens and 0.82 for TD specimens.

- *Essential work of fracture parameters*

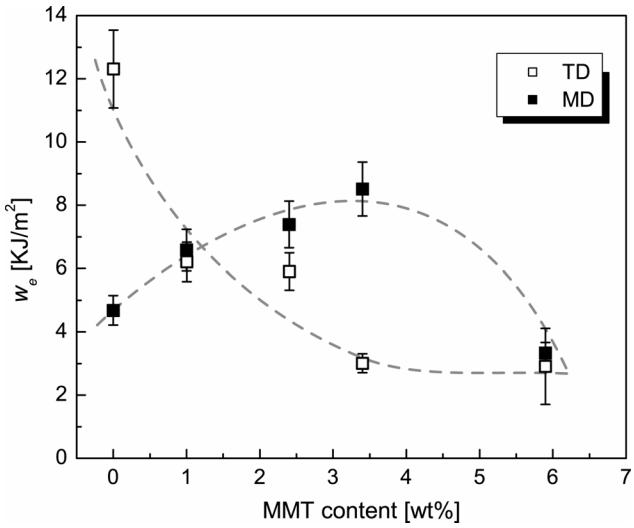

Figure 6.37. Specific essential work of fracture, w_e, as a function of ligament length l at different MMT concentrations for iPP2/MMT MD specimens and TD specimens.

The linear regression of the specific work of fracture for pure iPP2 specimens gave w_e = 4.7 KJ/m^2 for MD specimens and w_e = 12.3 KJ/m^2 for TD specimens. This indicated significant anisotropy in mechanical properties. A dependence on orientation has been reported by Maspoch[26] and Mohanraj[27] on PET films, Gámez-Pérez[15] on EPBC sheets, and by Pegoretti[28] for thermoformed sheets. The results obtained for w_e in the case of pure iPP2 films suggested these films to be anisotropic and that the resistance to crack propagation was higher for TD specimens. It follows from this observation that the iPP2 lamellae were preferentially oriented perpendicularly to the extrusion direction as observed by Prentice[1] for iPP extrusion calendered films. Figure 6.37 also shows that for MD specimens, w_e increased continuously up to about 3.5 wt% MMT, whereas for TD specimens, w_e decreased continuously. Thus above about 1 wt% MMT, w_e for the MD specimens was greater than for the TD specimens. It therefore appeared that MMT was beneficial for the fracture resistance in MD specimens especially at low MMT contents, but not for TD specimens.

- *Fracture resistance of iPP2/MMT films*

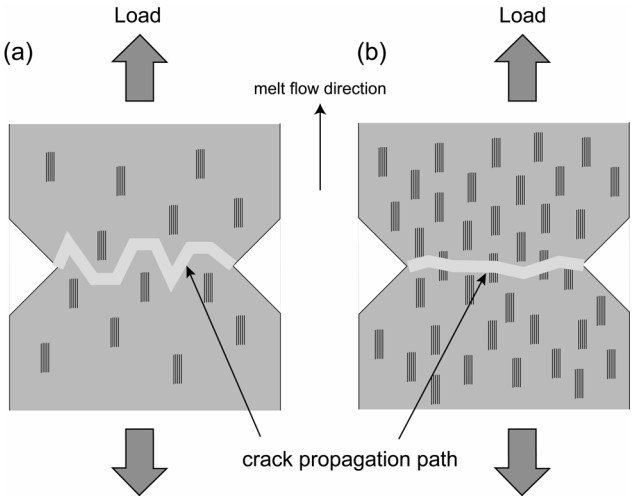

Figure 6.38. Illustration of crack propagation process in iPP2/MMT MD films having (a) low and (b) high MMT content.

In conventional polymer composites, the increase in stiffness imparted by fillers is generally associated with a decrease in toughness. In the case of clay-based nanocomposites, studies based on the J-integral analysis have shown that the toughness also decreases systematically with increasing clay loading[29, 30]. However, Giannelis *et al.*[31] and Zerda *et al.*[32] have shown that an improvement in stiffness as well as in toughness was possible in polymers at low clay loadings (below 5 wt%). They attributed this behavior to orientation and alignment of the nanoparticles which can blunt cracks or retard their growth[31]. In the present case, the fracture resistance was found to decrease on MMT addition for MD and TD specimens except in the case of MD specimen at low MMT loadings. Possible crack propagation mechanisms are illustrated in Figure 6.38 and Figure 6.39. For MD specimens at low MMT loadings, MMT particles may be source of microvoid nucleation observed in Figure 6.23(a). These microvoids released the plastic constraint in the matrix, triggering large scale deformation and resulting in tortuous paths of crack propagation[33] as observed in fracture micrographs Figure 6.24. For MD specimens at high MMT loadings, MMT platelets may form aggregates that are less effective to deflect crack propagation (Figure 6.38(b)) and the constraininig effect of MMT platelets prevented the matrix to yield or deform. In addition, smaller microvoids are observed in fractured surface (Figure 6.26). The high density of MMT nucleation sites may lead to higher void nucleation, reduced void growth and rapid void coalescence which reduced fracture resistance[13].

The decrease in fracture resistance has been attributed to the formation of microcracks associated with the clay[13, 30]. Wang *et al.*[34] suggested that microcracks are initiated between MMT layers, they develop within the particles and then extend into the matrix as the strain increases. They penetrate through the matrix ligaments and merge as

deformation proceeds (Figure 6.39). Finally, the microcracks coalesce and catastrophic fracture occurs resulting in brittle fracture surface observed in Figure 6.30 and Figure 6.31(b). Although TEM has not yet been applied in the present case, the occurrence of this type of deformation mechanism, i.e. cavitation and delamination cannot be excluded. However, it would only be expected to dominate in the case of silicate platelets oriented perpendicularly to the load direction i.e. to the TD specimens. Since the fracture resistance decreases with the addition of MMT in these latter, crack initiation and propagation via breakdown of the MMT particles was detrimental to fracture resistance.

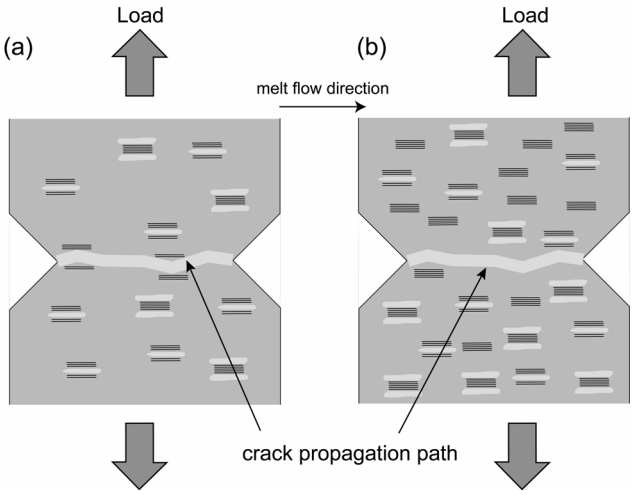

Figure 6.39. Illustration of crack propagation process in iPP2/MMT TD films having (a) low and (b) high MMT content.

- *Validity of the EWF approach*

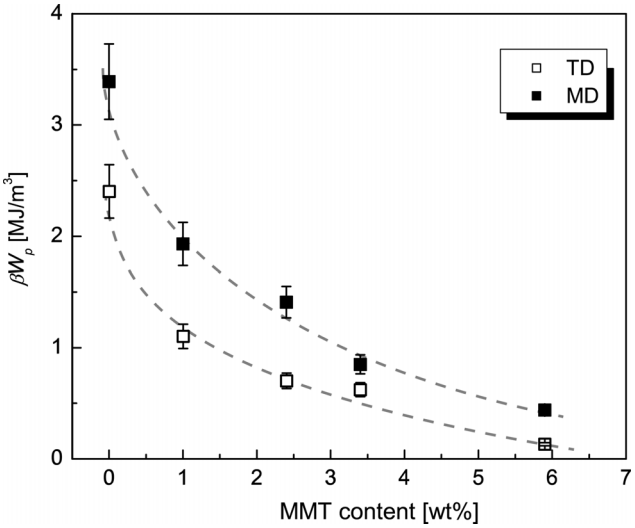

Figure 6.40. Non-essential work of fracture, βw_p, as a function of ligament length l at different MMT concentrations for iPP2/MMT MD specimens and TD specimens.

In Figure 6.40, a monotonic decrease in βw_p was observed for both the MD and the TD specimens. Low βw_p reflects a low dissipation of energy in the outer region (OPDZ) of the crack zone, which raises questions as to the validity of the EWF approach in the present case. It is therefore important to reexamine other criteria for the validity of EWF. This is done explicitly for the MD specimens. The analysis is similar for the TD specimens.

- force displacement curves

The force-displacement curves of pure iPP2 MD specimens were given in Figure 6.19(a). The similarity of the curves indicated that fracture mechanisms were similar at all ligament lengths.

- σ_{max} = f(l)

It was shown previously in this section that the criterion σ_{max} 1.15σ_y was not satisfied for iPP2 and iPP2/1wt% MMT unless σ_y was taken from force-displacement curves of injection moldings as opposed to un-notched films.

- F_{max} = f(l)

Figure 6.41 confirms the linearity of F_{max} versus l for different MMT concentrations, again indicating similarity in fracture mechanisms.

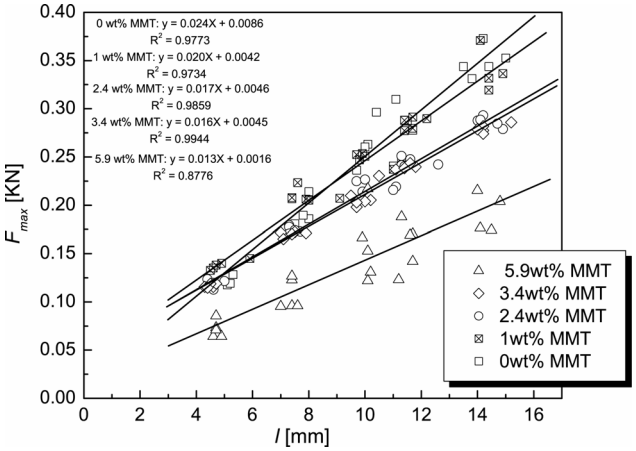

Figure 6.41. Maximum force, F_{max}, as a function of ligament length, l, for iPP2/MMT MD specimens.

- $(l_r) = f(l)$

Again, as shown in Figure 6.42, the linearity of (l_r) versus l indicated similarity in fracture mechanisms.

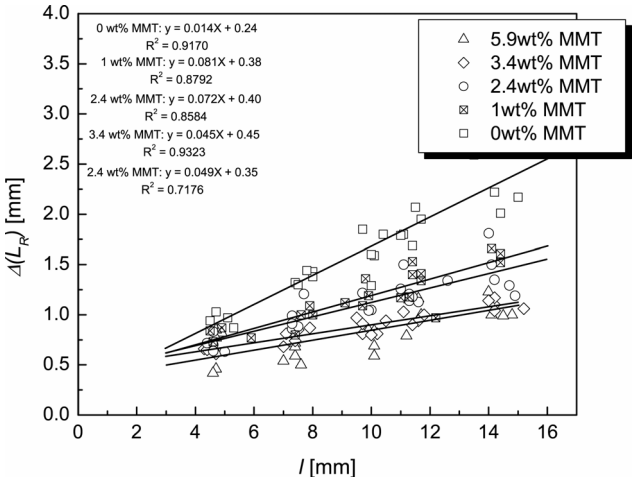

Figure 6.42. Ligament length at crack propagation, (l_r), as a function of ligament length, l, for iPP2/MMT MD specimens.

Necking and tearing were not clearly visible in the DENT specimens. However, this may be explained by the speed of the test (20 mm/min) which was chosen according to ESIS protocol[14]. In most studies on iPP, test speeds were much lower (between 1 and 5 mm/min)[35-37] and it has been demonstrated that w_e and βw_p values decrease with test speed owing to a decrease of polymer chain mobility[38].

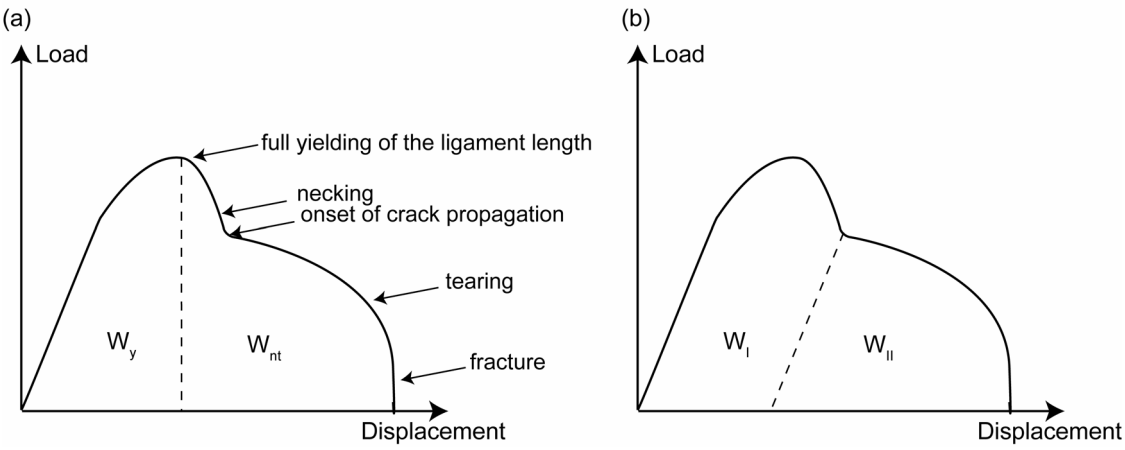

Figure 6.43. Typical load-displacement curves from DENT specimen from a ductile polymer. (a) Energy partitioning suggested by Ferrer-Balas *et al.*[39] (b) Energy partitioning suggested by Hashemi *et al.*[19] In (a) the different crack propagation mechanisms are indicated.

Values of w_e reported elsewhere were indeed much higher than observed in the present work. For example, an iPP film with a thickness of 100 μm produced by extrusion and tested at 5 mm/min had w_e = 60 KJ m^{-2} [11], and for extrusion–calendered films of about 1 mm in thickness, w_e = 29.5 KJ m^{-2} in the extrusion direction[15]. The origin of the low values obtained in the present work should be considered in the light of the iPP2 film grade used in the present which may have a low melt fow rate, a wide molecular polydispersity and short molecular chains resulting in a relatively brittle behavior as observed in the shape of the force-displacement curves. In the studies referred to above, the force-displacement curves showed a continuous slow decrease of the load beyond the maximum with increasing displacement, indicating yielding of the material and a slow stable crack propagation, prior to a sudden drop corresponding to final fracture. In some cases, a small drop was also observed just after the load maximum, which corresponded to necking of the specimen. A schematic description of typical force-displacement curves of this type is given Figure 6.43(a), together with the associated mechanisms. On this basis, it is possible to partition the energy of fracture into two contributions: (i) the energy corresponding to crack initiation, which involves initiation of yielding, localized necking and crack-tip blunting and (ii) the energy corresponding to crack propagation, which also involves necking. Two partitioning methods have been proposed by Ferrer-Balas[39] (Figure 6.43(a)) and Hashemi[19] (Figure 6.43(b)). The first distinguishes the work of yielding (W_y) and the work of necking and tearing (W_{nt}). In the second, on the other hand, the energy partition is made parallel to the elastic loading line, since only the stored elastic energy is assumed to be released during the fracture process. In both cases, specific essential and specific non-essential energies may be determined from:

$$w_y = w_{e,y} + \beta w_{p,y} \qquad \textbf{Equation 6.6}$$

$$w_{nt} = w_{e,nt} + \beta w_{p,nt} \qquad \textbf{Equation 6.7}$$

for case (i), and:

$$w_I = w_{e,I} + \beta w_{p,I}$$ **Equation 6.8**

$$w_{II} = w_{e,II} + \beta w_{p,II}$$ **Equation 6.9**

for case (ii).

The results of the partition are given Figure 6.44. It appears that the energy of propagation dominated for both MD and TD specimens, regardless of the MMT concentration. Thus, much of the energy dissipation in the IFPZ takes place during stage II (propagation). Ligament yielding before crack propagation is therefore doubtful in the case of iPP2/MMT films and the EWF approach may not be appropriate to the fracture mechanisms. However, it still gives some insight to crack initiation, and, as suggested by Ferrer-Balas *et al.*[39]and others[40, 41], since w_e may be an intrinsic material property, it should be compared to J_{IC}. Indeed, J-integral analysis gives J_{IC} = 4.14 KJ/m^2 for a pure iPP matrix[12, 29], which is in accordance with the values of w_e = 4.7 KJ/m^2 for pure iPP2 found here.

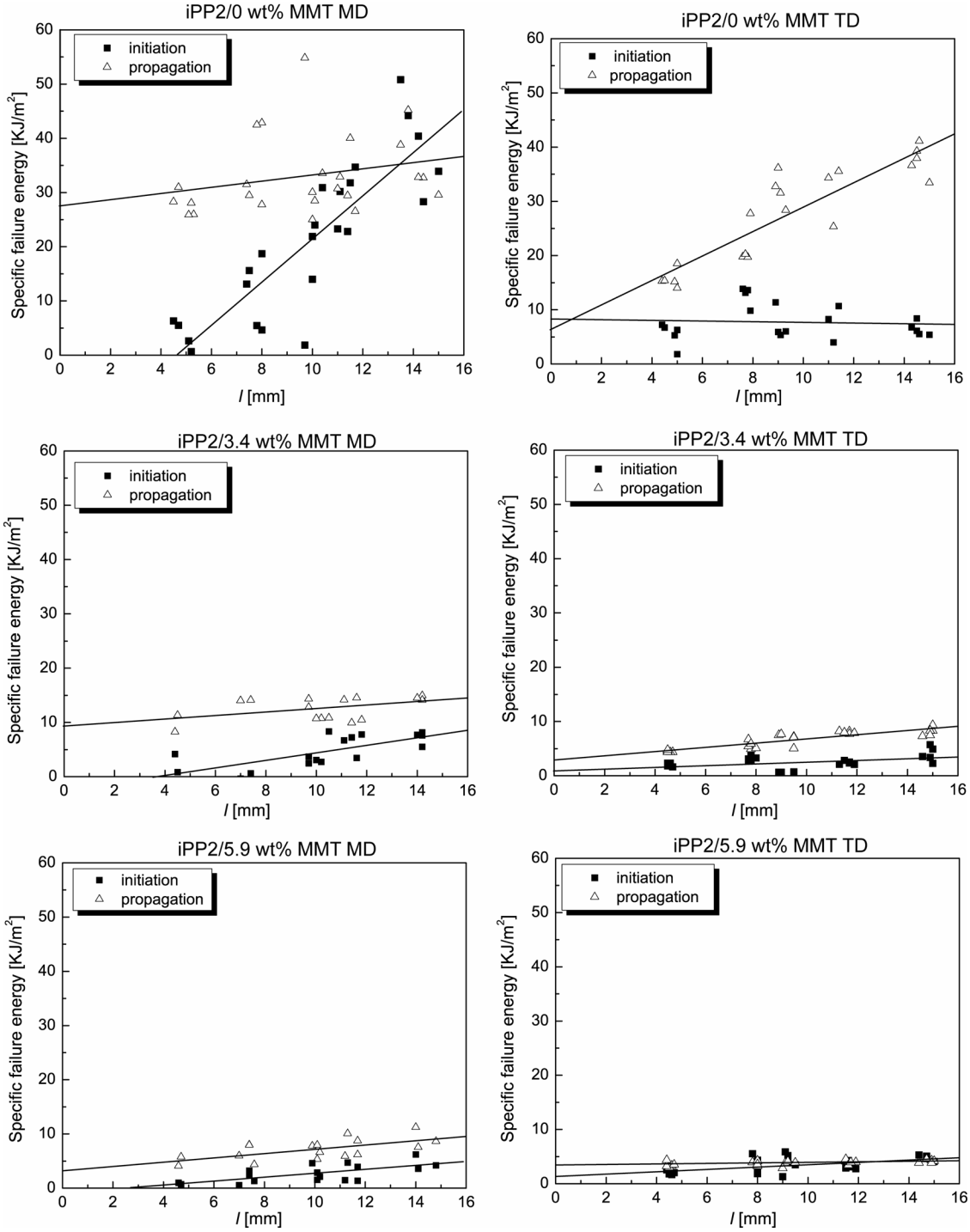

Figure 6.44. Initiation and propagation contributions to the total fracture energy as a function of MMT concentration for MD and TD specimens.

6.5 CONCLUSION

In this chapter, the feasibility of producing iPP2/MMT films containing up to 5.9 wt% MMT by a extrusion-calendering process has been demonstrated. As discussed in the previous chapter, the presence of MMT tends to reduce process instabilities and no modification of the process parameters was required on MMT addition. The degree of MMT agglomeration was reduced by melt compounding prior to extrusion-calendering process. According to XRD diffraction patterns, extrusion did not increase the degree of intercalation of the iPP2/MMT. A qualitative analysis of the film morphology by TEM suggested partial orientation of the MMT particles in the extrusion direction. However, the aspect ratio of MMT platelets was similar to that observed in the extrusion compounded granulates, suggesting the additional shear forces developed in the nip of the calender to be much lower than those involved in melt-spinning. Tensile tests on DENT specimens indicated the MMT to have a significant influence on the fracture resistance of the iPP2 matrix depending on its orientation and alignment. Thus, an increase in crack initiation resistance at low MMT contents was seen in films tested in the extrusion direction and a decrease in crack resistance in films tested in the transverse direction. This anisotropy is explained by the preferential orientation of the silicate platelets in the flow direction, creating tortuous paths of crack propagation for MD specimens and crack initiation sites for TD specimens.

6.6 REFERENCES

1 P. Prentice, **Surface irreglarities of calendered polypropylene**, *polymer*, 1981; **22** 250-254

2 S. M. Sofou, E., **Calendering of pseudoplastic and viscoplastic sheets of finite thickness**, *Journal of Plastic Film and Sheeting*, 2004; **20** 185-221

3 R. Nowacki, B. Monasse, E. Piorkowska, A. Galeski and J. M. Haudin, **Spherulite nucleation in isotactic polypropylene based nanocomposites with montmorillonite under shear**, *Polymer*, 2004; **45** (14): 4877-4892

4 T. Ariyama, **Spherulite Deformation at Low Strains in Uniaxially Extended Polypropylene**, *Journal of Materials Science*, 1992; **27** (18): 4940-4944

5 D. R. Norton and A. Keller, **The Spherulitic and Lamellar Morphology of Melt-Crystallized Isotactic Polypropylene**, *Polymer*, 1985; **26** (5): 704-716

6 F. Perrin-Sarazin, M. T. Ton-That, M. N. Bureau and J. Denault, **Micro- and nano-structure in polypropylene/clay nanocomposites**, *Polymer*, 2005; **46** (25): 11624-11634

7 C. M. Chan, J. S. Wu, J. X. Li and Y. K. Cheung, **Polypropylene/calcium carbonate nanocomposites**, *Polymer*, 2002; **43** (10): 2981-2992

8 H. X. Zhao and R. K. Y. Li, **Crystallization, mechanical, and fracture behaviors of spherical alumina-filled polypropylene nanocomposites**, *Journal Of Polymer Science Part B-Polymer Physics*, 2005; **43** (24): 3652-3664

9 S. C. Tjong, S. P. Bao and G. D. Hang, **Polypropylene/montmorillonite nanocomposites toughened with SEBS-g-MA: Structure-property relationship**, *Journal Of Polymer Science Part B-Polymer Physics*, 2005; **43** (21): 3112-3126

10 G. Machado, E. L. G. Denardin, E. J. Kinast, M. C. Goncalves, M. A. de Luca, S. R. Teixeira and D. Samios, **Crystalline properties and morphological changes in plastically deformed isotatic polypropylene evaluated by X-ray diffraction and transmission electron microscopy**, *European Polymer Journal*, 2005; **41** (1): 129-138

11 B. Fayolle, A. Tcharkhtchi and J. Verdu, **Temperature and molecular weight dependence of fracture behaviour of polypropylene films**, *Polymer Testing*, 2004; **23** (8): 939-947

12 L. Chen, S. C. Wong and S. Pisharath, **Fracture properties of nanoclay-filled polypropylene**, *Journal Of Applied Polymer Science*, 2003; **88** (14): 3298-3305

13 M. N. Bureau, F. Perrin-Sarazin and M. T. Ton-That, **Polyolefin nanocomposites: Essential work of fracture analysis**, *Polymer Engineering And Science*, 2004; **44** (6): 1142-1151

14 D. R. Moore, **Fracture mechanics testing methods for polymers, adhesives and composites**, Elsevie, Amsterdam, (2001)

15 J. Gamez-Perez, P. Munoz, J. I. Velasco, A. B. Martinez and M. L. Maspoch, **Determination of essential work of fracture in EPBC sheets obtained by different transformation processes**, *Journal Of Materials Science*, 2005; **40** (8): 1967-1974

16 A. Arkhireyeva, S. Hashemi and M. O'Brien, **Factors affecting work of fracture of uPVC film**, *Journal Of Materials Science*, 1999; **34** (24): 5961-5974

17 D. Ferrer-Balas, M. L. Maspoch, A. B. Martinez, E. Ching, R. K. Y. Li and Y. W. Mai, **Fracture behaviour of polypropylene films at different temperatures: assessment of the EWF parameters**, *Polymer*, 2001; **42** (6): 2665-2674

18 J. G. Williams, **Introduction to Linear Elastic Fracture Mechanics** in *Fracture mechanics testing methods for polymers, adhesives and composites*, pp 3, Elsevie, Amsterdam (2001)

19 S. Hashemi, **Temperature dependence of work of Fracture parameters in polybutylene terephthalate (PBT)**, *Polymer Engineering And Science*, 2000; **40** (6): 1435-1446

20 J. R. Rice, **A Path Independent Integral And Approximate Analysis Of Strain Concentration By Notches And Cracks**, *Journal Of Applied Mechanics*, 1968; **35** (2): 379-&

21 J. G. Williams, **Introduction to Elastic Plastic Fracture Mechanics** in *Fracture mechanics testing methods for polymers, adhesives and composites*, pp 119, Elsevie, Amsterdam (2001)

22 W. X. Yang, B.-H.; Shi, W.; Zuo, M.; Li, Z.M.; Yang, M.-B., **Essential work of fracture of glass bead filled low density polyethylene**, *journal of Materials Science*, 2005; (letters):

23 A. Arkhireyeva and S. Hashemi, **Fracture behaviour of polyethylene naphthalate (PEN)**,

Polymer, 2002; **43** (2): 289-300

24 J. Karger-Kocsis and D. Ferrer-Balas, **On the plane-strain essential work of fracture of polymer sheets**, *Polymer Bulletin*, 2001; **46** (6): 507-512

25 J. S. Wu and Y. W. Mai, **The essential fracture work concept for toughness measurement of ductile polymers**, *Polymer Engineering And Science*, 1996; **36** (18): 2275-2288

26 M. L. Maspoch, V. Henault, D. Ferrer-Balas, J. I. Velasco and O. O. Santana, **Essential work of fracture on PET films: influence of the thickness and the orientation**, *Polymer Testing*, 2000; **19** (5): 559-568

27 J. Mohanraj, N. Chapleau, A. Ajji, R. A. Duckett and I. M. Ward, **Roll-drawing and die-drawing of toughened poly(ethylene terephthalate). Part 2. Fracture behaviour**, *Polymer*, 2005; **46** (6): 1967-1981

28 A. Pegoretti, A. Marchi and T. Ricco, **Determination of the fracture toughness of thermoformed polypropylene cups by the essential work method**, *Polymer Engineering And Science*, 1997; **37** (6): 1045-1052

29 Y. M. Li, G. X. Wei and H. J. Sue, **Morphology and toughening mechanisms in clay-modified styrene-butadiene-styrene rubber-toughened polypropylene**, *Journal Of Materials Science*, 2002; **37** (12): 2447-2459

30 S. V. Nair, L. A. Goettler and B. A. Lysek, **Toughness of nanoscale and multiscale polyamide-6,6 composites**, *Polymer Engineering And Science*, 2002; **42** (9): 1872-1882

31 D. Shah, P. Maiti, D. D. Jiang, C. A. Batt and E. P. Giannelis, **Effect of nanoparticle mobility on toughness of polymer nanocomposites**, *Advanced Materials*, 2005; **17** (5): 525-+

32 A. S. Zerda and A. J. Lesser, **Intercalated clay nanocomposites: Morphology, mechanics, and fracture behavior**, *Journal Of Polymer Science Part B-Polymer Physics*, 2001; **39** (11): 1137-1146

33 Q. Yuan and R. D. K. Misra, **Impact fracture behavior of clay-reinforced polypropylene nanocomposites**, *Polymer*, 2006; **47** (12): 4421-4433

34 K. Wang, L. Chen, J. S. Wu, M. L. Toh, C. B. He and A. F. Yee, **Epoxy nanocomposites with highly exfoliated clay: Mechanical properties and fracture mechanisms**, *Macromolecules*, 2005; **38** (3): 788-800

35 W. K. Y. Poon, E. C. Y. Ching, C. Y. Cheng and R. K. Y. Li, **Measurement of plane stress essential work of fracture (EWF) for polymer films: effects of gripping and notching methodology**, *Polymer Testing*, 2001; **20** (4): 395-401

36 X. L. Wang, R. K. Y. Li, Y. X. Cao and Y. Z. Meng, **Essential work of fracture analysis of poly(propylene carbonate) with varying molecular weight**, *Polymer Testing*, 2005; **24** (6): 699-703

37 G. Gong, B. H. Xie, W. Yang, Z. M. Li, W. Q. Zhang and M. B. Yang, **Essential work of fracture (EWF) analysis for polypropylene grafted with maleic anhydride modified polypropylene/calcium carbonate composites**, *Polymer Testing*, 2005; **24** (4): 410-417

38 C. Grein, **Relation entre la structure et les propriétés mécaniques de polypropylènes modifiés choc**, Thesis, EPFL, Lausanne, (2001)

39 D. Ferrer-Balas, M. L. Maspoch, A. B. Martinez and O. O. Santana, **On the essential work of fracture method: Energy partitioning of the fracture process in iPP films**, *Polymer Bulletin*, 1999; **42** (1): 101-108

40 A. S. Saleemi and J. A. Nairn, **The Plane-Strain Essential Work Of Fracture As A Measure Of The Fracture-Toughness Of Ductile Polymers**, *Polymer Engineering And Science*, 1990; **30** (4): 211-218

41 H. Li, Y. Chen, C. Ruan, W. Gao and Y. Xie, **preparation of organic-inorganic multifunctional nanocomposite composite via sol-gel routes**, *Journal of nanoparticle research*, 2001; **3** 157-160

CHAPTER 7

GLASS FIBER REINFORCED THERMOPLASTIC BASED ON iPP/MMT AND iPP/CNF NANOCOMPOSITES

7.1 INTRODUCTION

Polymer nanocomposites have considerable potential for improved properties without substantial cost or weight penalties, e.g. in the transport industry (for body panels and under-the-hood parts for example)[1, 2]. Although there has been extensive work on polymer/layered silicate nanocomposites, only a few preliminary studies have been dedicated to the processing of hybrid fiber reinforced composites in which the nanocomposite plays the role of the matrix, as sketched in Figure 7.1. Given that cost/performance efficiency is the main driving force for the use of thermoplastic composites in high volume industrial applications[3], if thermoplastic nanocomposites are to be successfully implemented, it is crucial to develop processing techniques that are both adapted to macroscopic structures and capable of exploiting nanoscale properties efficiently in the final composites[4]. Thus, specific processing and manufacturing methods for incorporating nanofillers into macroscopic functional and structural composites must be developed and optimized.

The objectives of the work described in this chapter are (i) to use the iPP/MMT and iPP/CNF precursors described in chapters 4, 5 and 6, namely iPP1/MMT and iPP1/CNF filaments and iPP2/MMT films, to integrate nanofillers into composite parts, via conventional glass fiber reinforced iPP manufacturing techniques, and (ii) to characterize mechanical properties of the resulting hybrid composite, in order to verify whether or not any improvements observed in injection molded iPP/MMT nanocomposites are efficiently transmitted to the matrix dominated mechanical properties in the final hybrid composite.

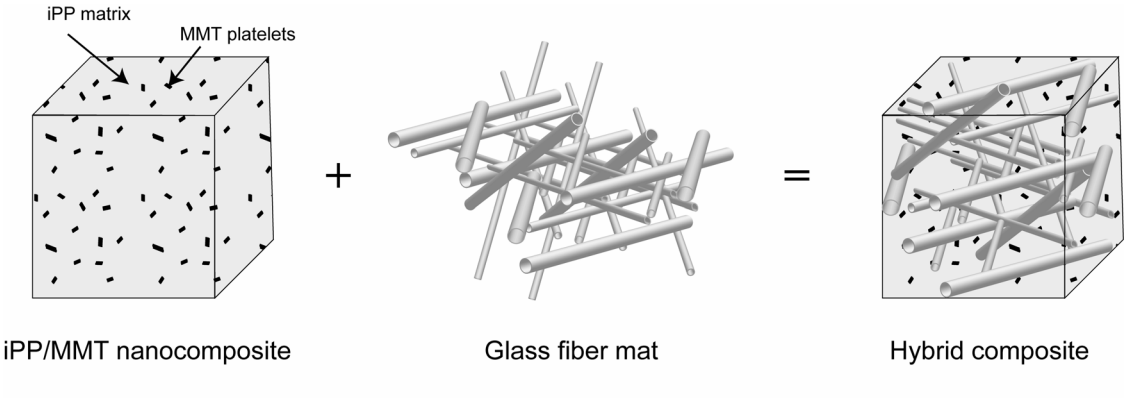

Figure 7.1. Hybrid composite based on a iPP/MMT nanocomposite matrix and a random glass fiber mat.

The composites considered here are (i) long glass fiber (LGF) composites, and (ii) glass mat reinforced thermoplastics (GMT). After a short introduction to impregnation mechanisms, this chapter will first describe a feasibility study of hybrid long glass fiber reinforced iPP1. The processing of hybrid glass mat reinforced iPP2 is then considered in the light of experimental trials and an impregnation simulation developed previously by Michaud *et al.*[5]. The last part of the chapter is devoted to the mechanical characterization of hybrid glass mat reinforced iPP2 composites using flexural and impact tests. The mechanical tests were also performed at different temperatures in order to assess the thermal stability. The results were compared with results from composites with un-reinforced matrices to determine the extent to which modification of the iPP2 is reflected by the behavior of the hybrid composites.

7.2 CONSOLIDATION MECHANISMS

Consolidation is one of the processes by which raw materials, i.e. the polymer matrix and the reinforcing fibers, are transformed into a solid composite structure[6]. Figure 7.2 illustrates a typical processing cycle for a fiber reinforced thermoplastic. Prior to the consolidation process, the materials are generally heated to the processing temperature (above the softening point of the resin), then, during consolidation, an external pressure is applied to ensure intimate mixing between the reinforcing fibers and the molten matrix. Finally, solidification is achieved by cooling the resulting composite.

The consolidation process may be divided into three steps: (i) compaction, (ii) impregnation, and (iii) fusion[6]. Compaction involves mechanical compression of the reinforcing fibers and/or the matrix by external pressure. During impregnation, voids associated with the fibers are filled by the molten matrix (an ideal impregnation step should produce a composite free of voids). Finally, fusion refers to the merging of distinct regions of the matrix to form a homogeneous material. It is assumed in this study that impregnation is the principal mechanism of consolidation. Philips *et al.*[7] have provided evidence in support of this assumption. They have shown that in the particular

case of consolidation of carbon fibers/polyetherimide prepregs, compaction and fusion represent only 1% of the total consolidation time. Similar conclusions have been reached based on experimental observations of the consolidation of commingled yarns[8]. Thus, the focus here will be on impregnation mechanisms. Moreover, impregnation is directly related to the mechanical properties of the final composite parts and is consequently an important aspect of the consolidation process.

Impregnation of glass fibers mats or tows with iPP occurs at two levels, namely macro- and micro- impregnation[9]. Macro-impregnation refers to infiltration of the inter-bundle cavities, and wetting of the outer regions of the bundles, and micro-impregnation refers to the wetting of the individual fibers within the bundles. At the beginning of the impregnation process, the fibers are only partially impregnated as the polymer melt front passes the fiber bundles. The pressure available to drive micro-impregnation is the sum of the local pressure in the pre-form and the capillary pressure.

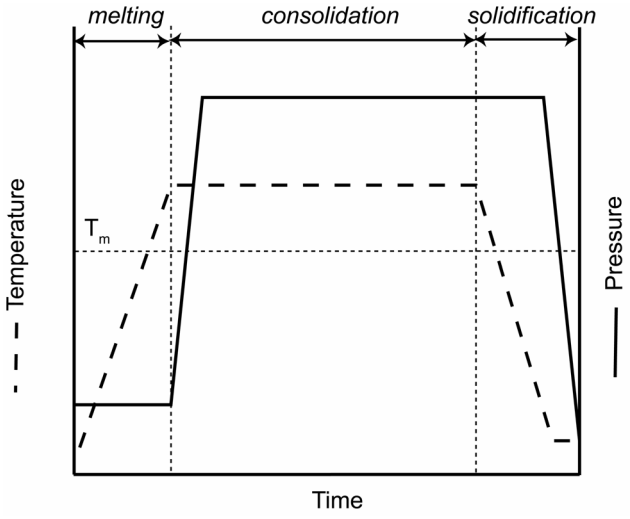

Figure 7.2. Schematic representation of a typical processing cycle for thermoplastic composites

As discussed in chapter 2, use of thermoplastic polymers as matrix materials for fiber-reinforced composites offers the potential for reducing manufacturing costs and improving performance. Nevertheless, a factor limiting the wider use of thermoplastics in composites has been their relatively high melt viscosity (typically 200 - 5000 Pa.s) compared with that of conventional thermoset resins (typically 1-10 Pa.s). The influence of the viscosity on the impregnation rate may be assessed using Darcy's law for laminar flow of Newtonian fluids through homogeneous porous media. Darcy's law for one dimensional saturated Newtonian flow in a non compressible preform may be expressed as[10]:

$$v = \frac{dL}{dt} = \frac{-K_p}{\eta e}\frac{\partial P}{\partial x} \qquad \textbf{Equation 7.1}$$

where v is the velocity of the fluid, e is the porosity of the porous medium, L is the penetration distance in the x direction, t is the time, K_p is the permeability of the porous medium, η is the viscosity of the fluid, and P, the pressure. In the case of non-Newtonian fluids, the above expression may need to be modified depending on the fluid characteristics. By integrating Equation 7.1 twice, and assuming that the permeability remains constant during infiltration of the fluid and neglecting capillary pressure, one obtains the time necessary to fully impregnate the porous medium:

$$t = e\frac{\eta L^2}{2K_P(P_a - P_o)} \qquad \textbf{Equation 7.2}$$

where P_a is the applied pressure and P_o is the atmospheric pressure. As can be seen from Equation 7.2, cycle times depend linearly on η, and they can be optimized by minimizing L. Thus η and L are key parameters for the impregnation process. As observed in chapter 3 section 3.3.3, the presence of MMT can dramatically increase the viscosity of the iPP matrix, especially in the low shear rate regime. Therefore, it is of primary interest to investigate the extent to which the impregnation process will be affected by the addition of MMT platelets.

7.3 LONG GLASS FIBER REINFORCED iPP/MMT AND iPP/CNF HYBRID COMPOSITES: FEASIBILITY STUDY

LGF were selected for this study because they generally require intimate mixing between the reinforcing fibers and the matrix material prior to compression molding, in order to achieve reduced cycle times. The objective of the feasibility study described here was to assess the suitability of iPP1/MMT fibers for classical composite manufacturing processes.

7.3.1 Impregnation experiments

To investigate processing of LGF with integrated MMT and CNF, two types of long glass fiber pre-forms were considered; unidirectional glass fiber/iPP1 yarns (UD) and co-woven glass fiber/iPP1 yarns. Hybrid composites were prepared from the pre-forms by compression molding. In the first case, iPP1/MMT fibers containing either 0 or 3.4 wt% MMT were co-wound around 3 superposed layers of glass fiber yarn. The winding apparatus was developed in-house to ensure an almost perfect alignment of the glass fibers. The final pre-form structure is shown in Figure 7.3, and the final composite had an overall glass fiber content of 40 - 60 vol%. Compression molding involved a holding time of 10 min at 220 °C for all specimens, and the pressure, initially chosen to be 0.6 MPa, was increased up to 1.8 MPa to achieve satisfactory degrees of consolidation. The porosity of the different specimens was estimated from image analysis of optical micrographs of polished sections taken perpendicular to the fiber direction.

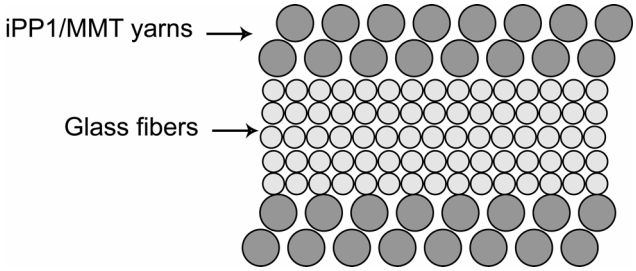

Figure 7.3. Schematic description of co-wound specimen sandwich architecture as produced from laboratory-made equipment.

To obtain a more controlled distribution of the glass fibers in the precursor and to improve the intimacy of mixing between the reinforcing fibers and the matrix, co-weaving of the iPP1/MMT or iPP1/CNF yarns with glass fibers was considered. iPP1/3.4 wt% MMT fibers and iPP/4 wt% CNF fibers melt-spun with DR = 1 and V_L = 360 m/min were combined with the glass fiber yarns using a table-top loom, to produce simple woven textile containing 40 - 50 vol% glass fibers. The wrap consisted of the iPP1/MMT yarn, and the weft was made up of mixed iPP1/MMT fibers and glass fiber yarns, as shown in Figure 7.4(a) (the high degree of commingling achieved in commercially available commingled pre-forms (Twintex from Vetrotex, for example) were not reached). The co-weaving procedure was identical for iPP/CNF yarns. A typical iPP1/MMT-based co-woven specimen is shown in Figure 7.4(b). The co-woven pre-forms were again compression molded for 10 min, at 220 °C, with a pressure of 1.2 MPa.

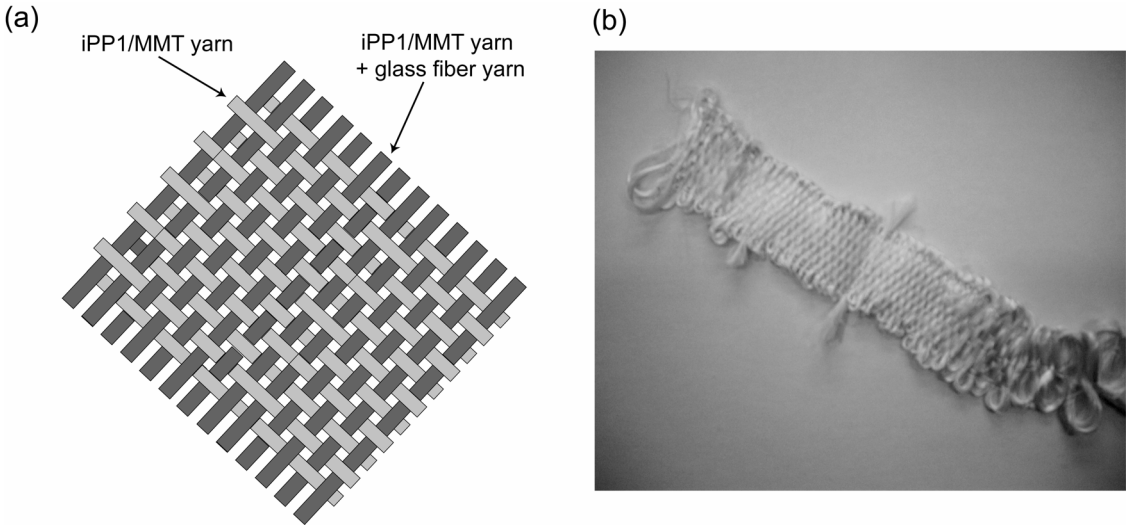

Figure 7.4. (a)Schematic description of hand-made co-woven resulting in a simple canvas textile, and (b) picture of a typical co-woven specimen.

7.3.2 Results

For the co-wound specimens, a pressure of 0.6 MPa provided good consolidation with the pure iPP1 matrix. The porosity was about 5 vol% for specimens with about 40 vol% glass fiber and about 7 vol % for specimens with about 60 vol% glass fibers, as shown in Figure 7.6(a). Similar time-temperature-pressure conditions resulted in poor level of consolidation for iPP1/MMT specimens, however, characterized by large intra-tow voids. A typical example is shown in Figure 7.5. Thus, it was generally necessary to increase the molding pressures in order to improve the consolidation of the specimens containing MMT. Figure 7.6(b) shows that consolidation could be achieved by molding the specimens containing MMT at a pressure of 1.8 MPa. The glass fiber content was about 40 vol % in the specimen shown and the porosity reached 14 vol% to 20 vol%, which was still high compared with the pure iPP1 matrix.

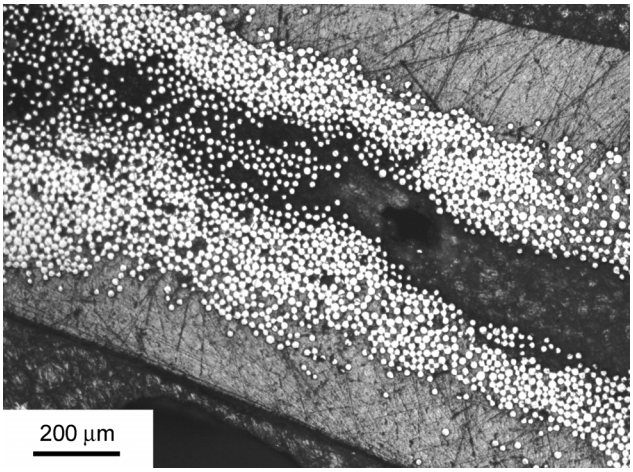

Figure 7.5. Optical micrograph of a poor consolidated co-wound specimen with 40 vol% of glass fibers and made out of iPP1/3.4 MMT fibers, compression molded at 0.6 MPa.

The relatively long processing times necessary here to ensure high degrees of impregnation implied flow rates of as little as 10^{-3} s^{-1}. Comparison with Figure 5.2 therefore suggests that the effective viscosity in the presence of 3.4 wt% MMT may be increased by nearly two orders of magnitude during the latter stages of the process, and hence that high levels of impregnation may be difficult to achieve.

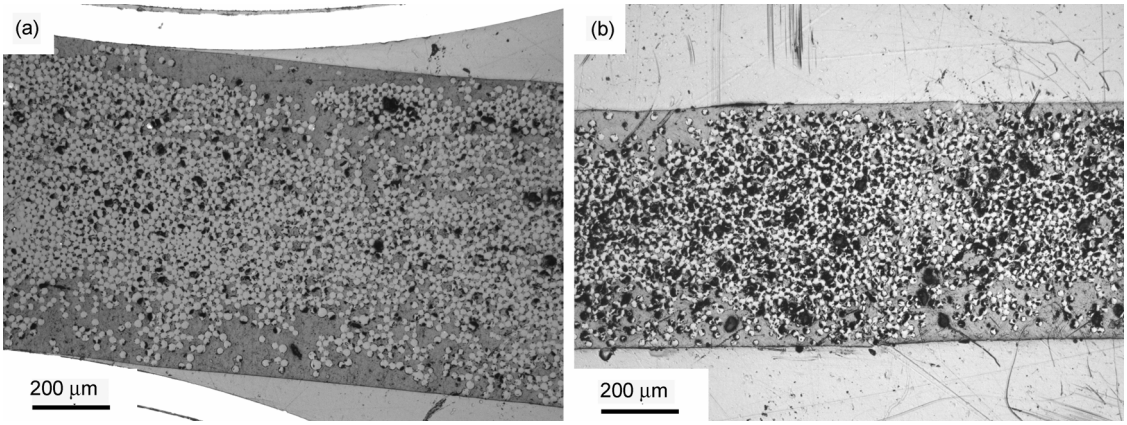

Figure 7.6. (a) Optical micrograph of a co-wound 60 vol% glass fiber hybrid iPP1 composite. (b) Optical micrograph of a co-wound 40 vol% glass fiber hybrid iPP1/3.4 wt% MMT composite.

Under similar processing conditions, co-woven specimens showed lower levels of porosity (about 2 vol%) (Figure 7.7(b)) than their hybrid co-wound counterparts. Here again, the residual porosity was mainly located within the tows, as shown in Figure 7.7(a). The systemic presence of intra-tow voids suggested that for this type of geometry, micro-impregnation dominated the global consolidation process. It follows that capillary pressure may be of primary importance if the local pressure is low and if the specific area within the bundle is high[11].

The capillary pressure, P_c, may be estimated theoretically using the Young-Laplace equation:

$$P_C = \frac{4\gamma_{LV}\cos\theta}{D_e} \qquad \textbf{Equation 7.3}$$

where γ_{LV} is the surface tension of the wetting liquid, θ the contact angle between the solid and the liquid, and D_e the equivalent hydraulic channel diameter. For liquid flow perpendicular to the fiber direction, D_e may be approximated by[12]:

$$D_e = 2D_f\frac{1-V_f}{V_f} \qquad \textbf{Equation 7.4}$$

where D_f is the fiber diameter. The capillary pressure may then be written as:

$$P_c = \frac{2\gamma_{LV}\cos\theta}{D_f}\frac{V_f}{1-V_f} \qquad \textbf{Equation 7.5}$$

For the glass fiber-reinforced iPP1 system, the capillary pressure may be estimated using γ_{LV} = 0.030 J/m^2. A typical wetting angle was determined for iPP2 and iPP2/MMT nanocomposites according to the axisymmetrical undoloid drop method described in section 3.2.5. With this method, θ = 18 ° (± 2), for pure iPP2 and θ = 21 ° (± 3) for iPP2/5.9 wt% MMT and these values are assumed here to be close to those for iPP1 and iPP1/MMT nanocomposites. It was found that the addition of MMT was neither

detrimental nor substantially beneficial for the contribution of wetting to impregnation. From optical microscopy, the mean diameter of the glass fibers D_f was found to be 17 μm. Taking representative values of V_f = 0.4 - 0.6, the capillary pressure was calculated to be P_c = 2238 - 5035 Pa for iPP2 and P_c = 2197 - 4943 Pa for iPP2/5.9 wt% MMT. This is considerably lower (about 200 times) than the applied pressures of 0.6 MPa to 1.8 MPa. Thus, the role played by capillarity in the consolidation rate may be ignored in the present case, and it may be assumed that the polymer melt is forced through the fiber bundle by the external applied pressure and air bubbles may be trapped in the tow[13]. The difference in impregnation behavior of the two types of glass fiber reinforced composite under consideration may therefore be attributed to the glass fiber pre-form geometry. In the co-woven yarns, the pore structure is dual-scale and the spacing between the individual fibers in the tow (~ 5 μm) is at least one or two orders of magnitude less than the spacing between the fiber tows (~ 100 μm). Thus the permeability inside the fiber tow is much lower than in between the fiber tows. Therefore, the iPP1/MMT nanocomposite melt initially flows between the fiber tows rather than through them, as shown in Figure 7.8(a). It follows that the impregnation times were lower in the case of co-woven specimens than for the UD specimens.

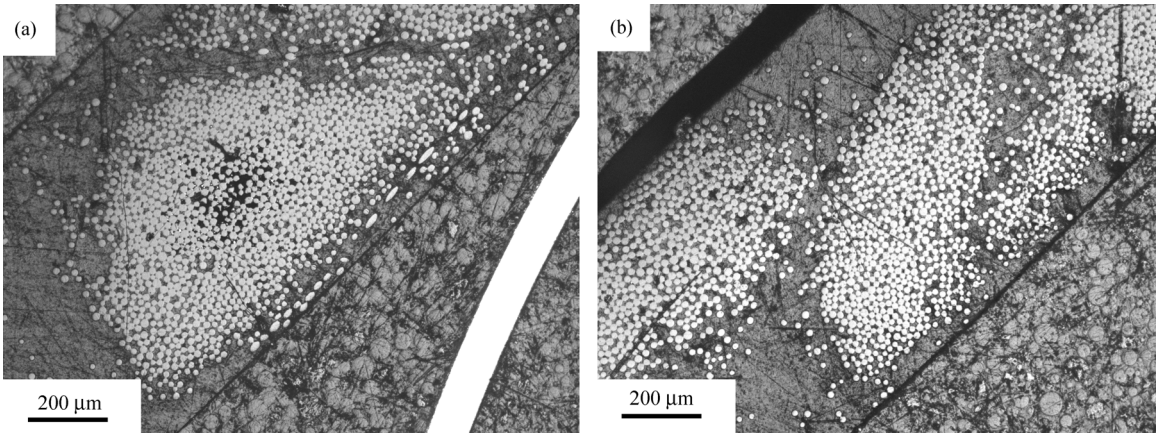

Figure 7.7. (a) Optical micrograph of co-woven specimen, 3.4 wt% MMT and 40 vol% glass fibers, showing some residual porosity within a glass fiber tow. (b) Optical micrograph of a co-woven specimen, 3.4 wt% MMT and 40 vol% glass fibers showing well infiltrated glass fiber tow.

According to the above analysis, the impregnation of the tows depends directly on the applied pressure *P*. However, a portion of the pressure applied during consolidation compresses the fiber bundles. For the elastic compression of a dry mat, this depends on the fiber volume fraction, according to [11]:

$$P = C E_f (v_f^m - v_{f0}^m) \qquad \textbf{Equation 7.6}$$

where *C* is a constant, E_f the stiffness of the glass fibers, V_{f0} the fiber volume fraction in the relaxed state and *m* a power law index. The power law index depends on the mat structure and it was found to increase with increasing order in the fiber arrangement[14]. The lowest value of *m* corresponds to a three dimensional structure (*m* = 3), and the

highest, to aligned glass fibers (m = 15.5). Hence, for two glass fiber pre-forms (1) and (2), with (1) less oriented than (2), $m_2 > m_1$ and from Equation 7.8, $P_2 > P_1$ for fixed values of the remaining parameters, i.e. the load on the more oriented glass fiber pre-form is greater than that on the less oriented pre-form. Because the permeability of the pre-form decreases with pressure, for fixed MMT concentrations and glass fiber contents, the commingled glass fibers are expected to be more permeable than the UD glass fiber pre-forms, consistent with a the higher void contents observed in these latter. It would be necessary to investigate the compressability of the dry glass fibers in order to verify this.

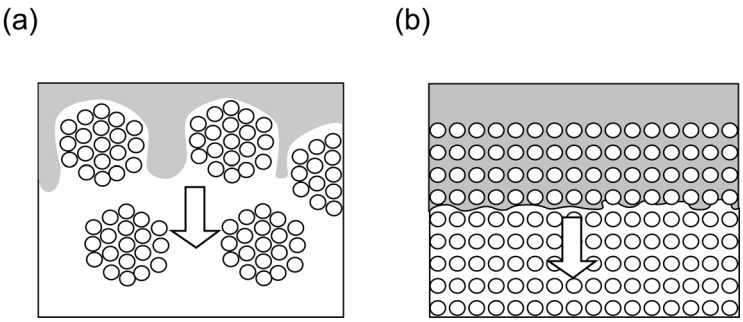

Figure 7.8. Schematic description of different polymer flow paths in fiber beds with different morphologies: (a) a non-uniform porous media and (b) a uniform porous media.

7.3.3 Co-woven PEEK fibers/iPP/MMT composites

Since local shear rates in the polymer matrix are higher than the global shear rates, the pressure driven flow into the micro-scale gaps within the glass fiber tows may generate sufficiently high local shear rates to intercalate the MMT platelets further[15]. On the other hand, particle filtering may also occur during impregnation, and hence prevent uniform particle distribution on completion of consolidation, as has been noted, for example, for well-dispersed slurries that contain submicrometer-sized particles during impregnation of a three-dimensional woven pre-form[16].

Co-woven specimens with PEEK filament tows substituted for the glass fibers were produced under the processing conditions described above. Use of PEEK facilitated sample preparation for the TEM by microtomy and hence allowed direct investigation of the extent to which filtration of the MMT particles occurred during impregnation of the tows. In spite of the relatively coarse MMT particles present in the specimen, MMT was clearly present within the interstices of the PEEK tows, as seen in the transverse section shown in Figure 7.10. These MMT particles were randomly dispersed in the iPP1 matrix as in the iPP1/3.4 wt% MMT nanocomposite precursor. For comparison, representative TEM micrographs of longitudinal sections and transverse sections of the corresponding iPP1/3.4 wt% MMT filaments melt-spun with DR = 1 and V_L = 360 m/min are shown in Figure 7.11 and. Figure 7.12 respectively. As expected, the orientation of MMT platelets observed in the longitudinal section of the filament (Figure 7.11) was lost on compression

molding. In addition, the aspect ratios of the cross-sections of MMT platelets observed in the co-woven composites were similar to that observed in the transverse sections of the corresponding iPP1/3.4 wt% MMT filaments and no additional intercalation of the MMT platelets was observed. Figure 7.13 also shows that the MMT platelets tended to align with the PEEK fiber surface up to a distance of about 0.5 μm.

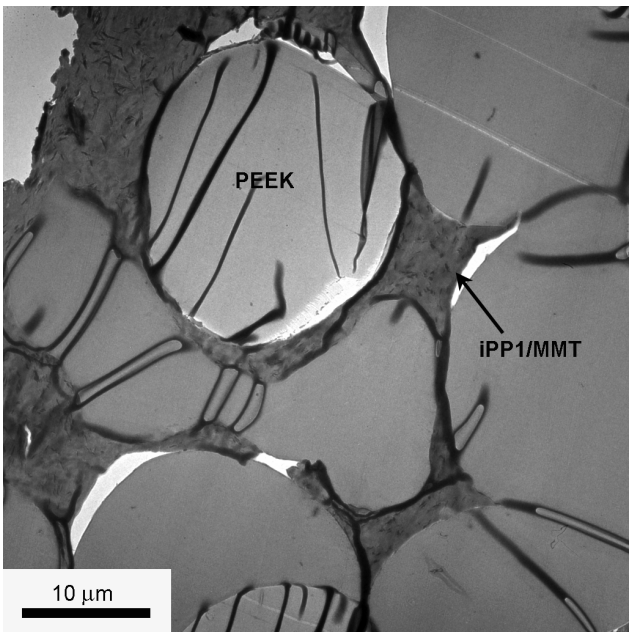

Figure 7.9. TEM micrograph from a co-woven hybrid iPP1/ 3.4 wt% MMT/PEEK nanocomposite yarn compression molded at 220 °C and 1.2 MPa for 10 minutes.

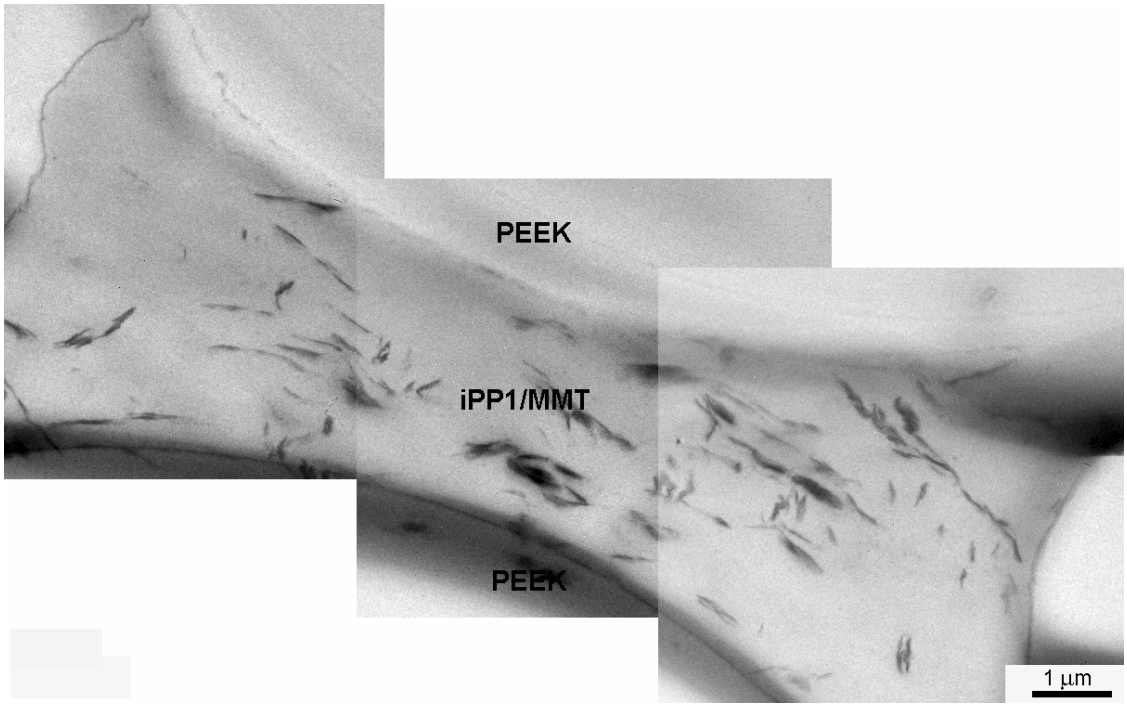

Figure 7.10. TEM micrograph from within a PEEK tow in a co-woven hybrid iPP1/ 3.4 wt% MMT/PEEK nanocomposite yarn compression molded at 220 °C and 1.2 MPa for 10 minutes.

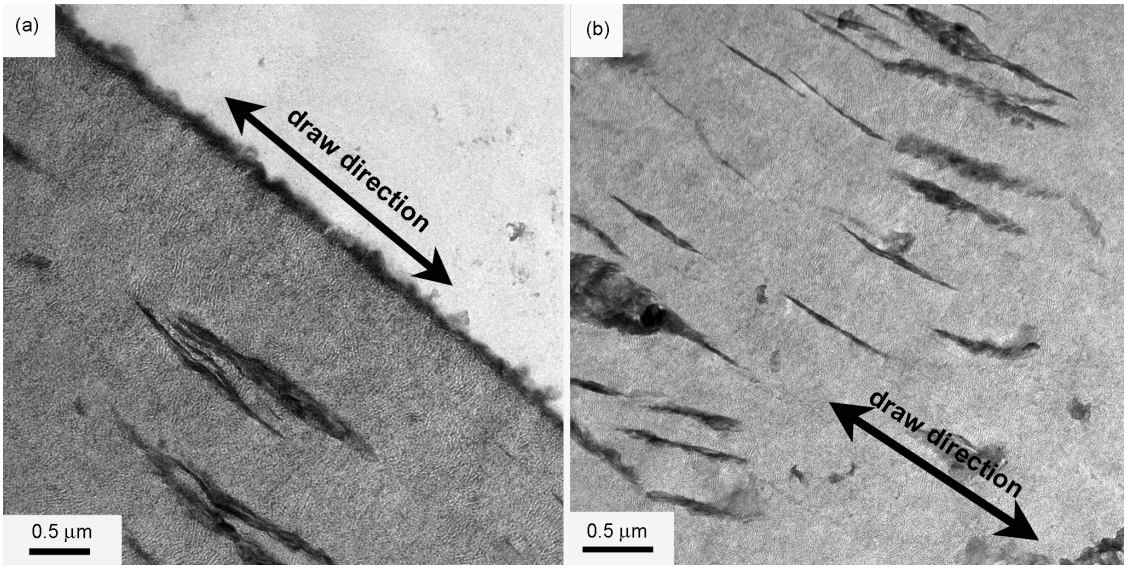

Figure 7.11. (a) and (b): TEM micrographs of longitudinal sections of iPP1/3.4 wt% MMT filaments melt-spun with DR = 1 and V_L = 360 m/min. The arrows indicate the direction of drawing.

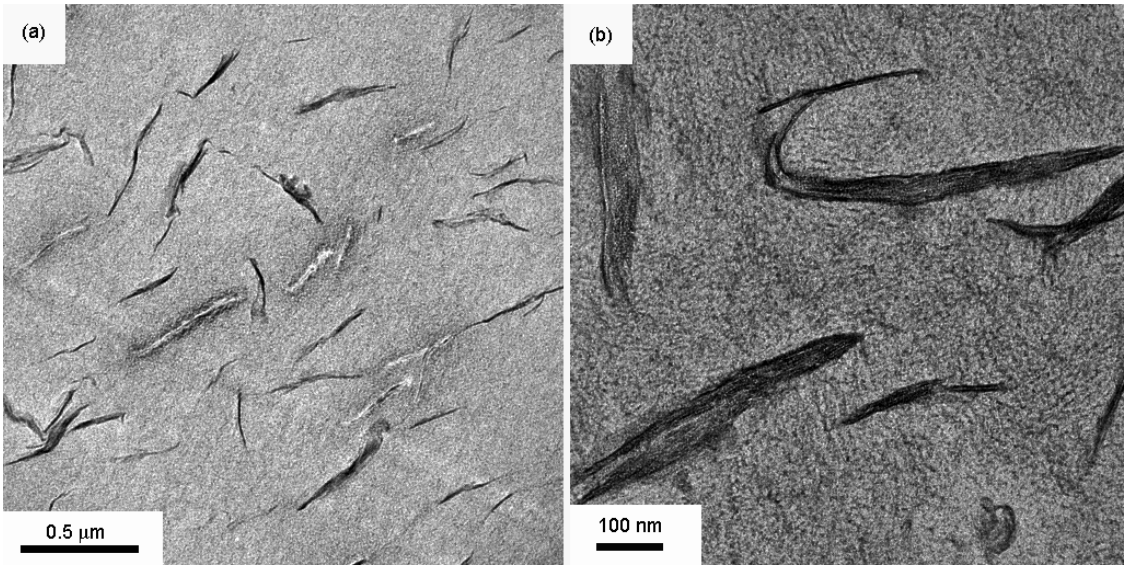

Figure 7.12. (a) and (b): TEM micrographs of transverse sections of iPP1/3.4 wt% MMT filaments melt-spun with DR = 1 and V_L = 360 m/min.

Increasing the flow rate helps to obtain higher levels of tow impregnation, but does not increase the shear rate experienced by the suspension, and only large aggregates can be broken down. Clearly, much higher shear stresses would be required to provide additional intercalation of the MMT platelets with respect to that associated with common compression molding conditions. Hence, hybrid composites with homogeneously dispersed MMT particles can only be achieved if homogeneous iPP1/MMT precursors are used, as also observed by Fan *et al.*[17] when impregnating glass fiber tows with suspensions of CNT.

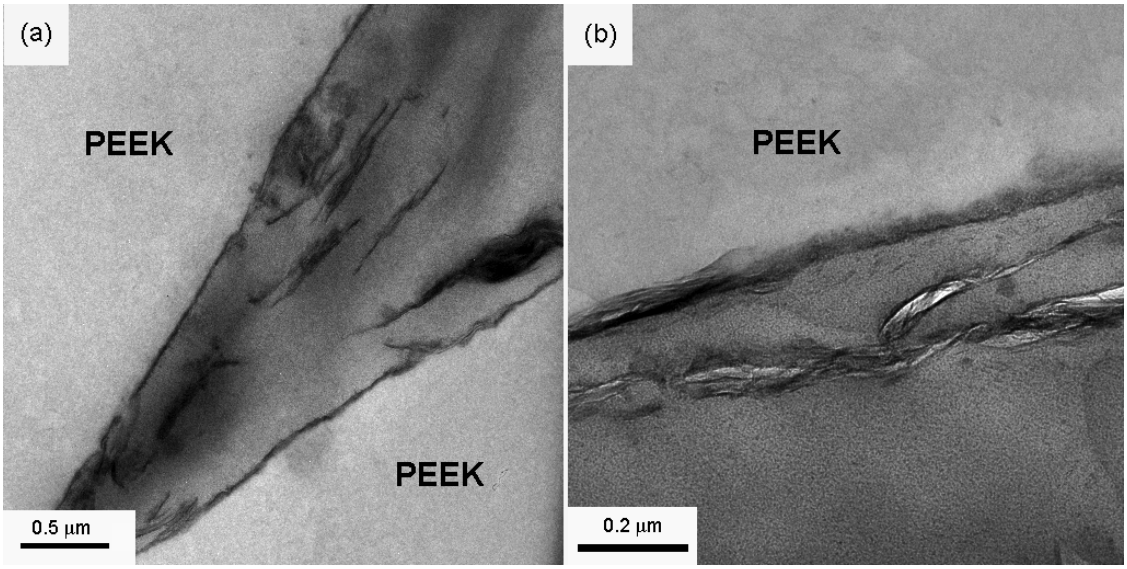

Figure 7.13. TEM micrographs from within a PEEK tow in a co-woven hybrid iPP1/ 3.4 wt% MMT/PEEK nanocomposite yarn compression molded at 220 °C and 1.2 MPa for 10 minutes.

7.3.4 Co-woven PEEK fibers/iPP/CNF composites

Co-woven specimens with PEEK filament tows substituted for the glass fibers were produced under the processing conditions described in section 7.3.1 with iPP1/4wt% CNF fibers melt-spun with DR = 1 and V_L = 360 m/min. iPP1/CNF nanocomposite was clearly present in the interstices between PEEK fibers as observed in the transverse sections shown in Figure 7.14. Only a few sections of randomly oriented CNF fibers were visible, compared with transverse sections of the iPP1/4 wt% CNF melt-spun fiber precursor (Figure 5.23), suggesting some filtration of CNF fibers by the PEEK tows during the impregnation. In addition, the distribution of CNF in the interstices was relatively inhomogeneous, high density and low density regions being seen in Figure 7.14, together with large holes of about 0.5 μm in diameter (Figure 7.14(a)) resulting from the loss of aggregates during the preparation of the film. Both longitudinal and transverse sections of CNF were present, indicating the absence of any preferential orientation in the nanocomposites. However, as observed Figure 7.15, the CNF were preferentially situated at the edge of the PEEK filaments. As observed by Fan *et al.*[17] for the impregnation of vinyl ester resin/MWNTs in nonuniform glass fiber preforms, appropriate shear rates during impregnation may break down some CNF aggregates into smaller ones. However, when the aggregates are too large they are filtered by the reinforcing fiber tow, so that homogeneity of the nanocomposite precursor is crucial for achieving homogenous fiber reinforced nanofilled composites

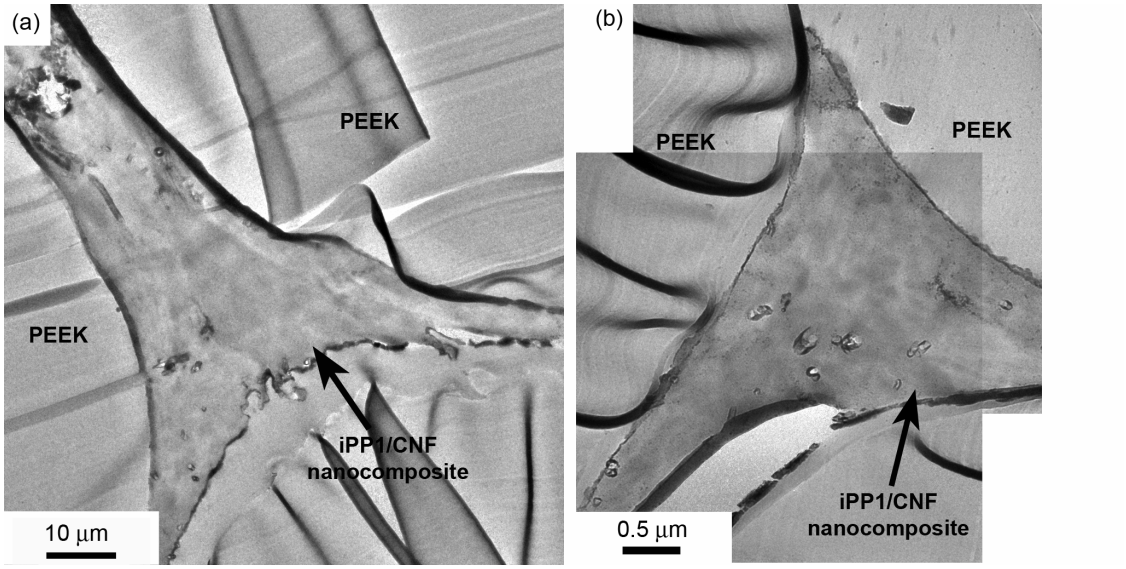

Figure 7.14. (a) and (b)TEM micrographs from within PEEK tows in a co-woven hybrid iPP1/4 wt% CNF nanocomposite yarn compression molded at 220 °C and 1.2 MPa for 10 min.

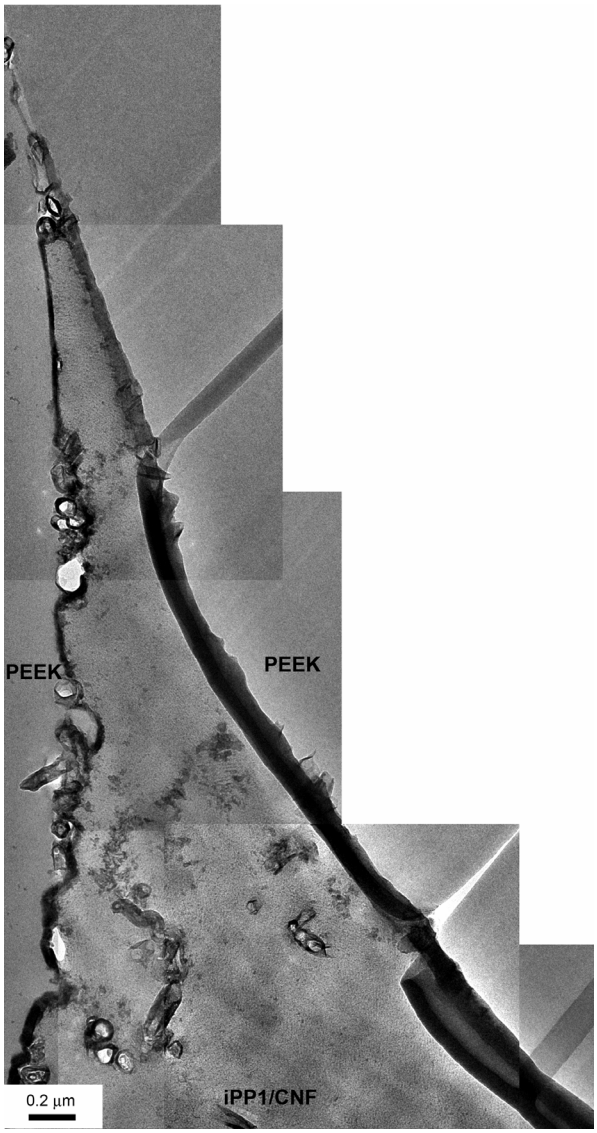

Figure 7.15. TEM micrograph from within PEEK tows in a co-woven hybrid iPP1/4 wt% CNF nanocomposite yarn compression molded at 220 °C and 1.2 MPa for 10 min.

7.4 GLASS MAT REINFORCED iPP/MMT HYBRID COMPOSITES

This section is devoted to the impregnation of GMT preforms during the lamination process, since the state of consolidation of the final part is affected by the initial degree of impregnation. The objective is to discuss quantitatively the influence of MMT on impregnation of a dry glass fiber mat preform. From the observations described in section 7.2, filtering effects are assumed to be negligible and the nanocomposite is considered as

a continuum. Therefore impregnation mechanisms may be described using classical polymer melt theories. The second part of this section presents the results on flexural and impact tests of fully consolidated hybrid GMTs, carried out in order to assess the influence of MMT on the mechanical properties of the composite part.

7.4.1 Impregnation of a compressible pre-form: state of the art and governing equations

The flow of fluids through porous media is crucial to many processes associated for example with the textile, food, pharmaceutical and polymer composite industries. There has therefore been considerable interest in establishing suitable flow laws for optimizing these processes. For economical reasons it is desirable during the processing of GMTs preforms to reduce the time of the lamination process, and hence the time of impregnation. Therefore, various models have been developed to predict the consolidation time and void content for a given set of temperature and pressure parameters[18]. Most of the experimental, theoretical and numerical studies are based on Newtonian fluids flowing through isotropic or anisotropic porous media, described by the linear one dimensional form of Darcy's law[19] (Equation 7.1). Thus, Newtonian flow through porous media such as fiber beds is well understood. Efforts are currently being devoted to the determination of macroscopic flow laws for non-Newtonian fluids through porous microstructure[20]. However, the task is not straightforward, owing to the existence of coupling effects between the microstructure and the rheological response of the fluid[21], and only the ideal case of power law fluids flowing through geometrical simple porous media, such as square or triangular arrays of aligned fibers, has so far provided tractable flow laws[22, 23]. Realistic modeling of the impregnation of an industrial glass fiber mat by a non-Newtonian fluid would therefore require tools that have yet to be established and experimentally verified[24].

Glass fiber mats are highly compressible materials and the application of pressure during impregnation may significantly alter permeability and hence the impregnation kinetics. Moreover, during the molding process, fiber orientation and fiber-matrix separation may occur during flow, leading to a non-homogeneous product. Therefore it is important to clarify these in relation to the molding conditions by measuring the glass fiber content distribution[25]. It is important to recognize that full consolidation is not a simple flow problem. Impregnation involves not only the flow of the fluid within and around the reinforcing tows, but also the reduction of voids and the dissolution of entrapped gases into the molten matrix under continued application of pressure[26-28]. As a first approach, in order to limit the complexity of the problem, we consider an impregnation model based on soil mechanics, developed by Sommer *et al.*[29] for the infiltration of initially dry deformable porous media and extended by Michaud *et al.*[5] to the case of fiber mat reinforced thermoplastic polymer composite impregnation. The model considers macroscopic impregnation of compressible mats by a Newtonian fluid, in order to simulate the kinetics of impregnation and the evolution of the fiber volume fraction profile as the resin front progresses within the mat. The flow direction is assumed to be perpendicular to the reinforcing fiber axis, with simultaneous consolidation in all tows.

a. Description of the model

Figure 7.16 shows schematically the isothermal infiltration in one direction of an initially dry glass mat by a molten polymer under constant applied pressure *P*, exerted by a piston, and the simultaneous occurrence of impregnation and relaxation. During this process, the fiber volume fraction V_f varies along the infiltration direction. At $t < 0$, the mat and the molten polymer are placed in the mold. At $t = 0$, the mold is closed, a pressure *P* is applied to the assembly and the mat is compressed by the polymer melt. As the polymer melt infiltrates the mat at $t < t_{inf}$, this latter partly relaxes, while the un-impregnated part of the mat remains compressed. At $t = t_{inf}$, the polymer has fully infiltrated the mat and has reached the lower part of the mold. At $t > t_{inf}$, the mat may continue to relax and tend to an equilibrium state. Depending of the amount of polymer and the final thickness, at the end of the process, $t = t_{total}$, either the mat has reached the upper part of the mold, without being fully relaxed, or it has enough room to fully relax in the polymer melt.

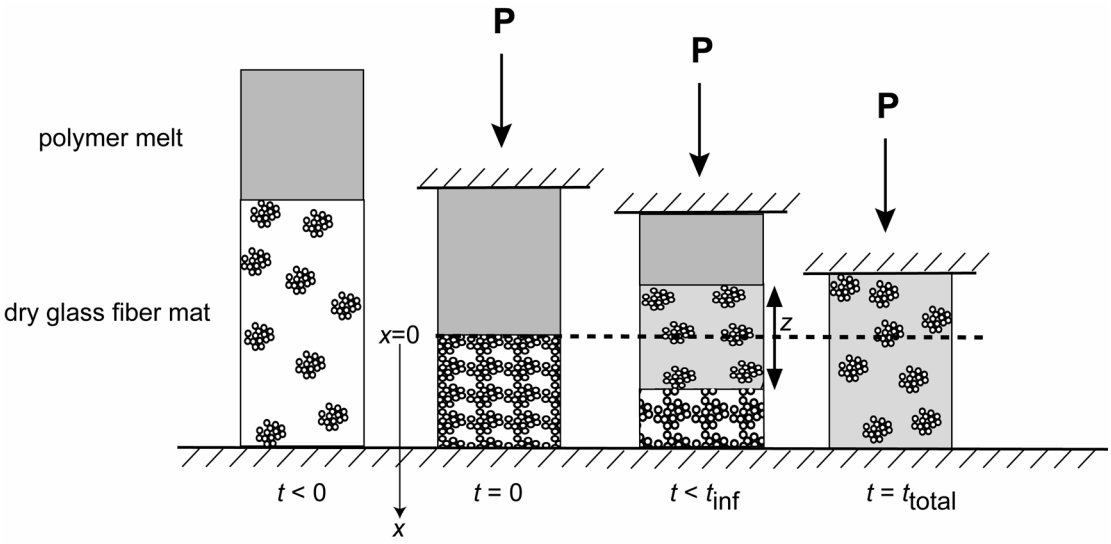

Figure 7.16. Schematic description of the pre-form impregnation process.

The infiltration is assumed to take place in a closed mold, so that one end and the sides of the pre-form are constrained by the mold walls. Lateral friction between the mold walls and the side of the pre-form are ignored. Based on the conclusions of section 7.3.2, capillary forces are also ignored and the presence of an air path in the mold is assumed. The porous medium is considered as a continuum and is assumed to be isotropic in the plane perpendicular to the infiltration direction (*x*-axis). The governing equations are described in Michaud *et al.*[5] together with the associated assumptions and the numerical solution of the finite element code. These equations are expressed in one dimension for a representative volume element, and involve the solution of the coupled mass, momentum and energy balance equations briefly described below.

The impregnation of a fiber mat by a Newtonian polymer melt in the double belt press

can be described by the unidirectional form of Darcy's law. In the particular case of a compressible mat, the relaxation is taken into account and Equation 7.1 is written:

$$v_l - v_s = -\frac{K_p}{\eta(1-V_f)}\frac{\partial P}{\partial x} \qquad \textbf{Equation 7.7}$$

where v_l is the local velocity of the liquid within the pores and v_s the local velocity of the mat. In a quasi-static approach and neglecting gravity and inertial effects, the mechanical equilibrium between the fiber mat and the polymer melt is:

$$\frac{\partial P}{\partial x} = \frac{\partial \sigma}{\partial x} \qquad \textbf{Equation 7.8}$$

where σ is the effective stress acting on the mat along x, taken to be positive in compression. For a representative volume element, V, the mass conservation equation for the fiber mat is given by:

$$\frac{\partial V_f}{\partial t} + \frac{\partial (V_f v_s)}{\partial x} = 0 \qquad \textbf{Equation 7.9}$$

and for the polymer melt:

$$-\frac{\partial V_f}{\partial t} + \frac{\partial}{\partial x}((1-V_f)v_l) = 0 \qquad \textbf{Equation 7.10}$$

Combining the mass conservation equations, Equation 7.9 and Equation 7.10, one obtains a non linear equation relating the fiber volume fraction V_f to the time t and the position x[30]:

$$\frac{\partial V_f}{\partial t} - \frac{\partial}{\partial x}\left(V_f \frac{K_p}{\eta}\frac{d\sigma}{dV_f}\frac{\partial V_f}{\partial x}\right) = 0 \qquad \textbf{Equation 7.11}$$

Equation 7.11 is solved numerically by introducing a kinetic parameter, ψ, and making use of the Boltzman transformation[5, 29]:

$$\chi = \frac{x - x_e}{\psi\sqrt{t}} \text{ and } Z = \psi\sqrt{t} \qquad \textbf{Equation 7.12}$$

where χ is the relative position within the impregnated mat, x_e is the position of the limit between the pure polymer and the infiltrated mat and Z is the impregnated thickness (Figure 7.17). The solution requires knowledge of K_p of the preform as a function of V_f, σ, as a function of V_f during both compression and relaxation and η of the polymer.

b. Boundary conditions

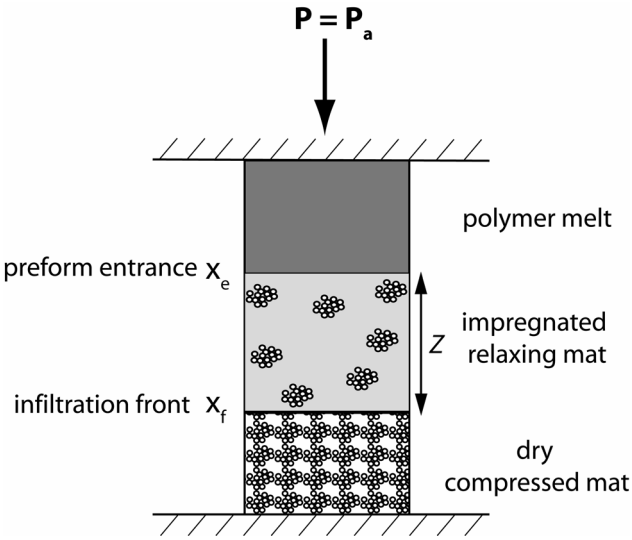

Figure 7.17. Schematic representation of the compressed pre-form and its boundary conditions.

- At the upper part of the mold, the applied pressure $P = P_a$
- At the preform entrance, $x = x_e(t)$, $P = P_a$ and V_f equals its fully relaxed value
- At the infiltration front, $x = x_f(t)$ and V_f equals its maximum value in the compressed state corresponding to the applied pressure
- At the bottom of the mold, the preform is considered to be fixed so that the velocities of both the glass mat and the polymer melt are equal to zero, $v_s = 0$ and $v_l = 0$.

c. Permeability of the glass fiber mat

Given to the similarity of the glass mats used in each case, the permeability function $K_p(V_f)$ was taken from Michaud *et al.*[5]:

$$K_p = 1.0722 \cdot 10^{-9} (1 - V_f)^{10.743} \qquad \textbf{Equation 7.13}$$

d. Compressive behavior of the glass fiber mat

The compressive behavior of the dry fiber mats was investigated by compressing and relaxing two layers of dry fiber mats between two parallel plates in a hydraulic press (Interlaken). The experiments were conducted in an open mold and also in a closed mold. A constant compression rate was applied up to 0.2 MPa, and the relaxation was measured by separating the plates at the same rate. A typical curve obtained in this way is shown in Figure 7.18. The ascending arrow corresponds to the compressive stage, the descending arrow corresponds to relaxation. The observed hysteresis is due to the rearrangement of the fibers.

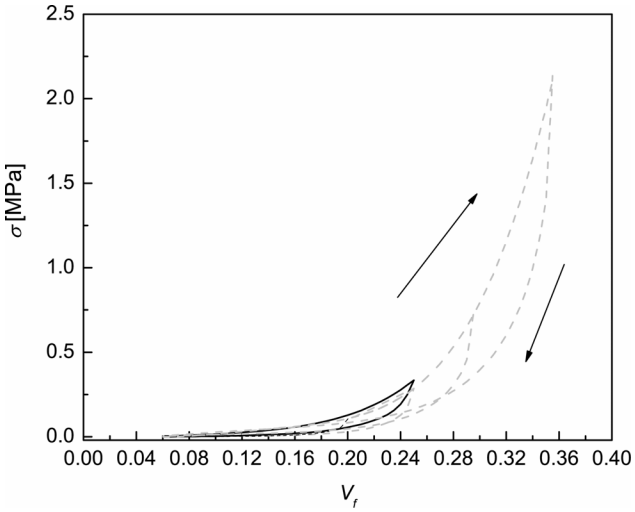

Figure 7.18. Experimental stress-strain curve of three layers of glass mat compressed up to 0.4 MPa (plain curve) and stress-strain curves at 4 different levels of compression given by Michaud *et al.*[31] (dashed curves).

As shown in Figure 7.18, the experimental curve (plain curve) was in good agreement with those measured by Michaud *et al.*[31] (dashed curves). Therefore a similar curve fit was used for the compression stage:

$$\sigma = a_0 + a_1 V_f + a_2 V_f^2 + a_3 V_f^3 + a_4 V_f^4 \qquad \textbf{Equation 7.14}$$

and for the relaxation stage:

$$\sigma = \sigma_c \left(m_0 + m_1 a + m_2 a^2 + m_3 a^3 + m_4 a^4\right) \text{ with } a = \left(\frac{V_f^c - V_f}{V_f^c - V_f^r}\right)^{1/3} \qquad \textbf{Equation 7.15}$$

where σ_c is the maximum stress before unloading, V_f^c is the fiber volume fraction at σ_c, and V_f^r is the fiber volume fraction at $\sigma = 0$, and the coefficients are given in Table 7.1.

Table 7.1. Coefficients of dry glass fiber mat stress-strain curve fitting.

a_0	$1.1958.10^5$	m_0	1.102025
a_1	$-4.8888.10^6$	m_1	-1.0222325
a_2	$6.7048.10^7$	m_2	-4.197025
a_3	$-3.5488.10^8$	m_3	7.300125
a_4	$7.0216.10^8$	m_4	-3.18695

7.4.2 Impregnation of a glass fiber mat: experimental analysis

a. Experimental procedure

To study the impregnation process of a needled glass fiber mat by an iPP2/MMT nanocomposite matrix, use was made of the model system shown in Figure 7.19. It consisted of three layers of iPP2 or iPP2/MMT cut from the extrusion-calendered films, prepared as described in section 6.3, placed on top of three layers of 4 mm 2D needled glass fiber mat. The fiber length was about 50 mm and each bundle contained about 100 fibers. The surface density was 600 g/m^2. Three superposed mats were used to provide a large enough impregnation distance for clear measurement of the macroscopic impregnation.

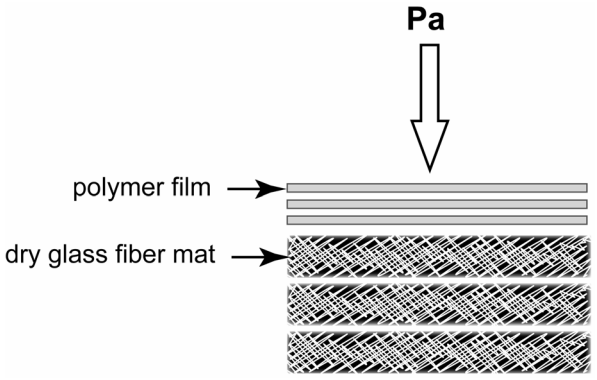

Figure 7.19. Structure of the specimen geometry for consolidation experiments.

Impregnation experiments were carried out using an Interlaken hydraulic press. The polymer-glass mat assembly was placed in a 80 × 50 mm^2 closed mold, pre-heated to 200 °C. The closed mold offers the advantage of providing boundary conditions resembling those in the central part of the double belt press. The assembly was heated for 10 min prior to compression in order to ensure a uniform temperature in the polymer and the mats. 0.2 MPa was then applied for a limited time, after which the assembly was rapidly cooled (10 °K/min) under pressure. Three characteristic impregnation times were defined: “0 s” which corresponds to the time necessary to close the mold, and “30 s” and “10 min”, which correspond to 30 s and 10 min of impregnation before cooling of the preform. Films containing 0 wt%, 1 wt%, 2.4 wt%, 3.4 wt% and 5.9 wt% of MMT were investigated.

The solidified impregnated glass mat (Figure 7.20) plates were cut into 15 mm long samples (Figure 7.21), embedded under vacuum in an Epofix resin (Struers), polished, and the fiber distribution characterized by optical microscopy combined with image analysis. It was assumed that the fiber area fraction was equivalent to the fiber volume fraction[32]. To eliminate contrast and resolution problems encountered when adjusting threshold values for fiber analysis, series of individual images were taken, rather than

scans of the whole sample. The glass fibers were then colored by hand so that the same threshold values could be used for all specimens. The individual images were taken as shown in Figure 7.22. The specimen was divided horizontally and vertically into rectangles of equal size. The images were taken from the centre of each section at a magnification of ×10. For each vertical coordinate *i*, a mean fiber volume fraction $V'_{f,i}$ was calculated from the 10 corresponding images. A relative fiber volume fraction $V_{f,i}$ was then determined for each section with:

$$V_{f,i} = \frac{V'_{f,i}}{\sum_i V'_{f,i}} \qquad \textbf{Equation 7.16}$$

and

$$\sum_i V_{f,i} = 1 \qquad \textbf{Equation 7.17}$$

V_f could then be plotted as a function of *z*. In all cases the experimental dispersion was around 15 %.

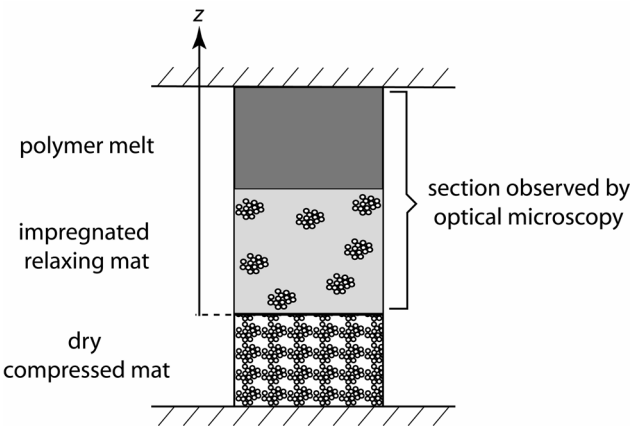

Figure 7.20. Schematic of the impregnated glass mat section observed by optical microscopy.

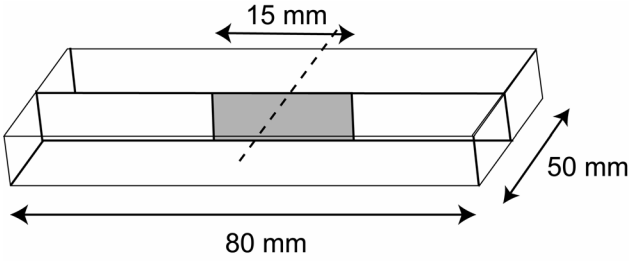

Figure 7.21. Schematic description of a consolidation test specimen. The cross-section analyzed is indicated in light gray.

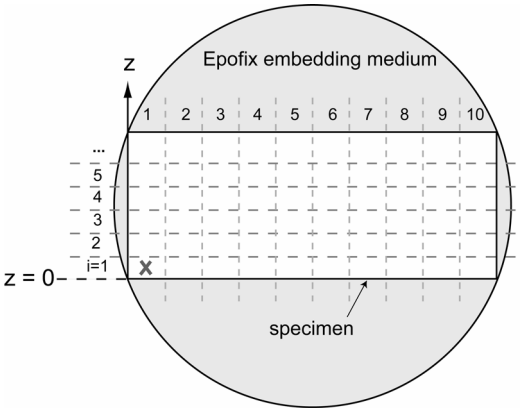

Figure 7.22. Schematic of optical microscopy of samples from consolidation experiments. The direction of the impregnation is indicated as well as the locus of the images.

b. Impregnation results for the iPP2 matrix

It was observed that for all specimens, the inhomogeneity of the fiber mats resulted in a non-uniform impregnation front as shown in Figure 7.23. It was therefore difficult to determine the distance of impregnation unambiguously, even when the flow front was relatively regular, as in the case of specimens with a matrix with a high MMT content. It also appeared from the microscopy images that macro- and micro-impregnation occured simultaneously, since some fiber bundles were impregnated before full consolidation of the sample.

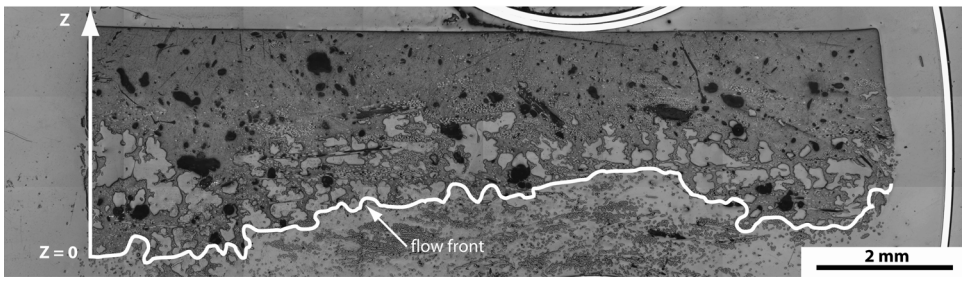

Figure 7.23. Optical micrograph of a glass mat impregnated with iPP2 after 30 s of impregnation, showing the irregular flow front. The black regions correspond to the voids. The embedding medium appears light gray and the iPP2 dark grey.

A typical graph of V_f versus z is shown in Figure 7.24 for the pure iPP2 matrix and different impregnation times. The position $z = 0$ corresponds to the limit between the polymer and the non-impregnated mat, as shown in Figure 7.20. In the case of a pure iPP2 matrix, it was observed that at "0 s" the polymer had penetrated the whole fiber mat and hence reached the bottom of the mold. Thus for longer impregnation times "30 s" and

"10 min", the *z*-axis remained fixed at the bottom of the mold. Since all the specimens had the same origin on the *z*-axis, it was therefore convenient to compare the distribution in V_f directly for specimens produced with different impregnation times.

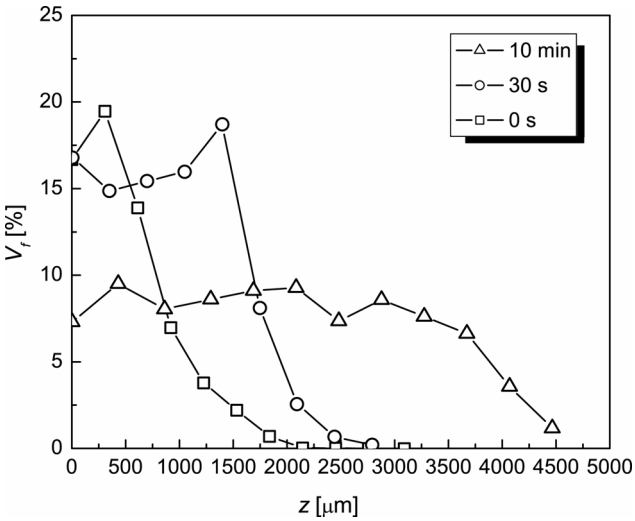

Figure 7.24. Distribution of V_f as a function of the position in the mold *z*, for consolidation experiments with a pure iPP2 matrix at different impregnation times.

Since infiltration was already completed after "0 s" of impregnation, Figure 7.24 reflects only the relaxation of the mat in the polymer matrix. After "0 s" and "30 s" of impregnation, a strong gradient in V_f was observed, indicating that the preform was not fully relaxed. For "0 s" of impregnation, V_f = 20 vol % at the flow front. Between "0 s" and "30 s" of impregnation, the maximum of V_f shifted away from the infiltration front showing that the mat had started to relax. After "10 min" of impregnation, V_f was homogeneous along nearly the entire specimen length.

c. Impregnation results for iPP2/MMT matrices

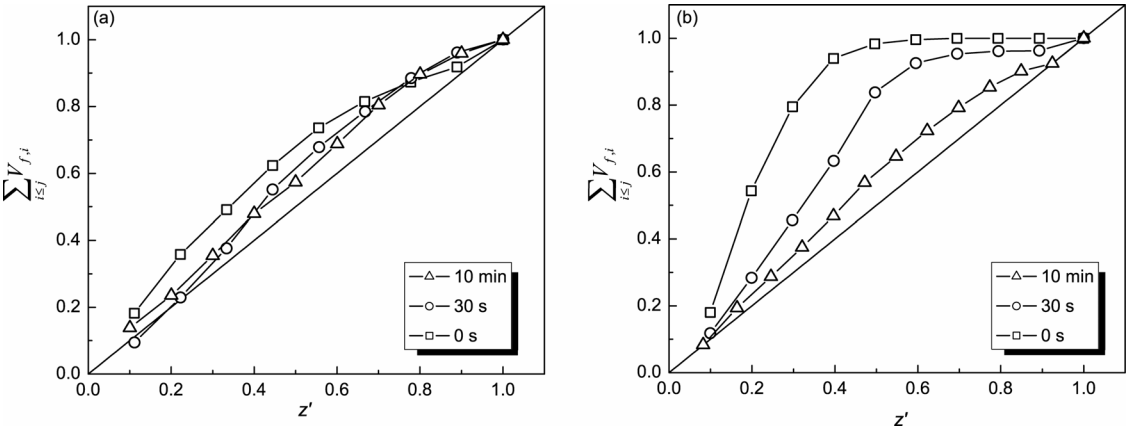

Figure 7.25. Cumulative relative fiber volume fractions from consolidation experiments at different impregnation times with (a) pure iPP2 matrix, and (b) iPP2/5.9wt% MMT matrix.

For the specimens produced with iPP2/MMT nanocomposites, different levels of saturation were observed and the origin of the *z*-axis moved with the flow front, which made direct comparison of V_f versus z for each specimen more difficult. For ease of interpretation of the data, $\sum_{i \le j} V_{f,i}$ (where j is the current position) was plotted as a function of the relative position $z' = \frac{z}{L}$, where L is the impregnated mat thickness. Thus the data in Figure 7.24 transformed to the curves shown in Figure 7.25(a) in this representation. The curve f(*z'*) = *z'* is also shown, which corresponds to a homogeneous distribution of V_f. The closer the experimental curves are to this line, the more homogeneous the distribution of V_f. The strong gradient in V_f seen in Figure 7.24 for short impregnation times appears less clearly in Figure 7.25(a). On the other hand, it was observed that the curves were closer to the homogeneity reference curve (f(*z'*) = *z'*) with increasing time of impregnation, indicating the preform relaxed progressively.

For the specimens impregnated with iPP2/MMT nanocomposites, the gradient in V_f was stronger, as shown in Figure 7.25(b) for iPP2/5.9 wt% MMT. In this case, after "0 s" of impregnation, the curve flattened off beyond *z'* = 0.6, indicating an absence of glass fibers in the upper part of the specimen. With increasing impregnation times, the curves approached f(*z'*) =*z'*, indicating a degree of homogeneity comparable with that obtained with the pure iPP2 matrix after 10 min of impregnation. These trends were also clearly visible in the polished micrographs (Figure 7.26). From Figure 7.26(a) to (c), the glass fiber mat is seen to relax progressively into the iPP2/5.9 wt% MMT matrix. Thus, in Figure 7.26(c), the mat is fully infiltrated but there remains a layer of polymer at the top of the molding with a relatively low glass fiber content. The question therefore arises as to whether full relaxation of the mat is reached after 10 min of impregnation. Comparison of the state of the different matrices after "0 s" of impregnation (Figure 7.27(a)) and after

"10 min" of impregnation (Figure 7.27(b)) provides some insight into this. For very short impregnation times ("0 s"), the extent of relaxation of the glass mat was very different, depending on the matrix viscosity. On the other hand, for long impregnation times ("10 min" in this case, Figure 7.27(b)), the curves were all very similar. It was therefore inferred that these latter curves corresponded to the maximum possible relaxation of the mat for the mold present thickness, even for relatively high MMT loadings.

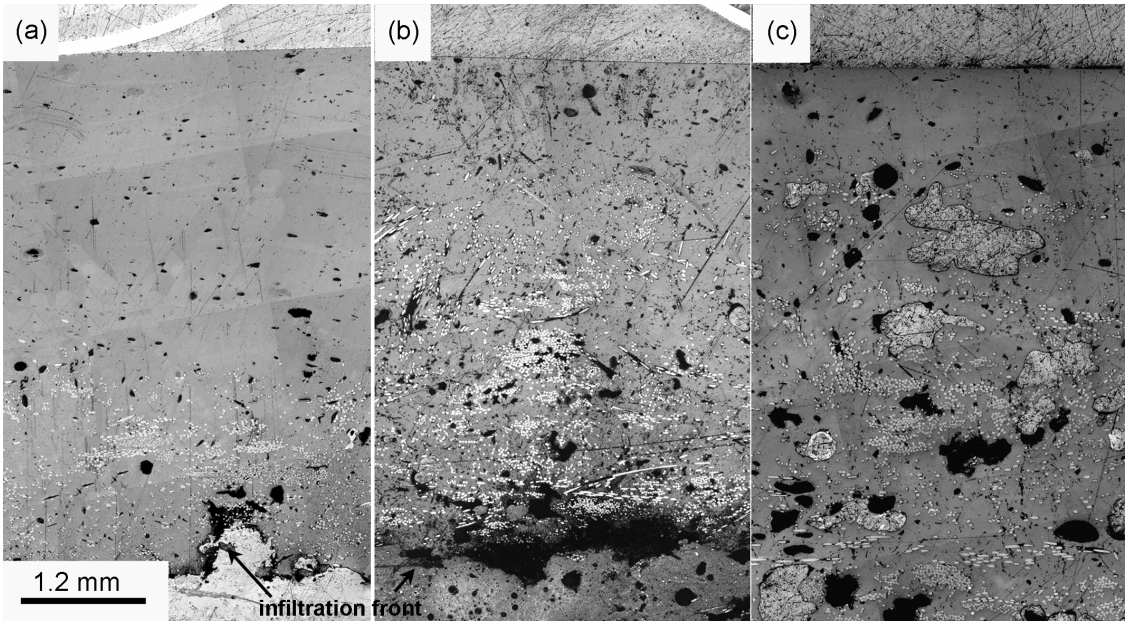

Figure 7.26. Optical micrographs fromconsolidation experiments with a iPP2/5.9 wt% MMT matrix for different impregnation times: (a) 0 s, (b) 30 s, and (c) 10 min, showing impregnation of the fiber mat and relaxation of the mat into the nanocomposite matrix.

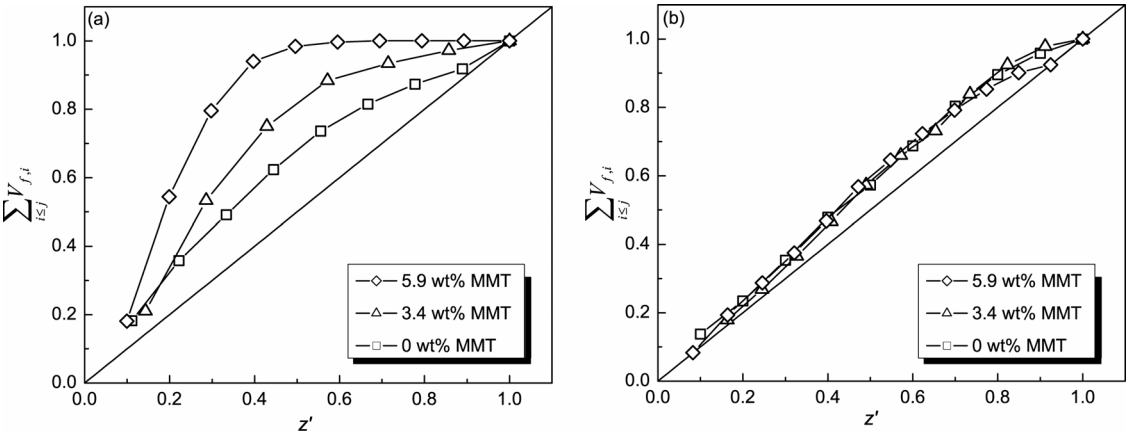

Figure 7.27. Cumulative relative fiber volume fractions from consolidation experiments for different MMT concentrations and impregnation times equal to (a) 0 s and (b) 10 min.

7.4.3 Impregnation of a glass fiber mat: simulation

During processing, the total stress in the material under deformation is the sum of a stress component related to friction between the reinforcing elements and a rate dependent component related to the shearing of the matrix material[11]. The local shear rate in the polymer matrix is dependent on the mold closing speed in the case of compression molding. Experimentally, the range of speeds used here for the impregnation of the glass mat was from 0.020 m/min to 0.10 m/min. From the observation of the impregnated thickness after "30 s" of impregnation, the velocity of the iPP2 flow front was estimated to be 0.15 10^{-3} m/s and that of iPP2/5.9 wt% MMT to be 0.09 10^{-3} m/s, corresponding to a shear rate of about 1 s^{-1} [33]. In the case of the iPP2 matrix, the Newtonian plateau extends well above 1 s^{-1} (Figure 3.26). Thus, the impregnation model developed by Michaud *et al.*[5] is fully applicable, assuming that the infiltration occurs with a small local Reynolds number. On the other hand, this shear rate is at the limit of the range in which the viscosity of iPP2 is strongly influenced by the presence of MMT, and it is therefore important to quantify the effect of the MMT.

The simulation was performed in two steps. First, the infiltration time, i.e., the time for the polymer to reach the lower face of the mold was calculated and then the simulation was used to determine the extent of the relaxation of the glass mat in the polymer matrix. The permeability and the stress-strain behavior of the glass mat were as given by Michaud *et al.*[5], V_f varying between 7 and 23.5 vol% from compression at 0.2 MPa to complete relaxation (Figure 7.18). The theoretical fully impregnated sample thickness at 0.13 vol% was 2.2 mm.

a. Simulation of impregnation with pure iPP2

The theoretical fully relaxed state (V_f = 7 vol%) was not observed experimentally and the mat reached the top of the mold without being fully relaxed. Therefore, the simulation was run until the impregnated specimen thickness reached that of the mold at the end of the experiment. The iPP2 matrix viscosity determined by steady shear rheometry (Figure 3.26) was 64 Pa.s at 1 s^{-1}. The results of the simulation are given in Figure 7.28 for different impregnation times.

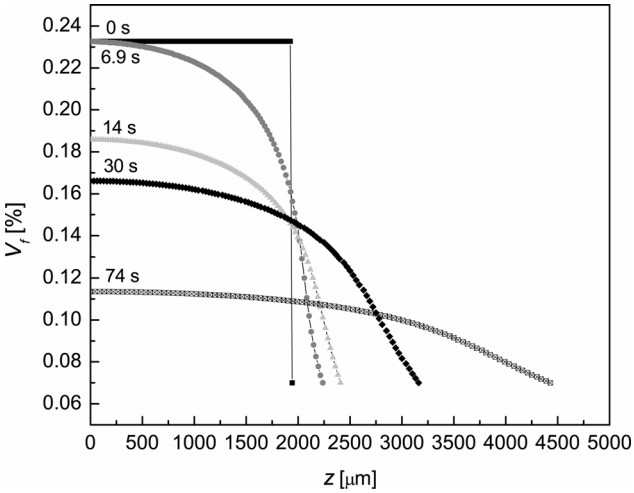

Figure 7.28. Simulation of the glass fiber volume fraction distribution as a function of position in the mold, after infiltration under an applied pressure of 0.2 MPa and various impregnation times.

For a theoretical impregnation time of 0 s, V_f is constant and equal to V_f^c, the glass fiber volume fraction for the glass mat compressed at 0.2 MPa. As impregnation progresses, the glass mat relaxes and the gradient in V_f diminishes. The simulation indicated the time of infiltration to be t_{inf} = 6.9 s. Experimentally (Figure 7.24), the maximum value of V_f after "0 s" of impregnation was 20 vol%, which was lower than the initial value assumed in the simulation. It was found from the simulation that V_f = 0.20 corresponded to an impregnation time of 14 s. This corresponds to the time necessary to close the mold and start the cooling process. For $t >> t_{inf}$, the experimental results correlated well with the theoretical estimates of V_f, particularly close to the impregnation front (for example, after 30 s of impregnation). At large *z*, the experimental values were nevertheless lower than the theoretical predictions, as was also observed previously[31], possibly because of an increase in the experimental scatter with decreasing glass fiber content.

The simulation predicts the glass mat to reach the top part of the mold after 74 s of impregnation and the time necessary to achieve equilibrium of the glass mat to be $t_{equilibrium}$, is 120 s. Experimentally, after 10 min of impregnation, a homogeneous distribution of the glass fibers was observed in the specimen (Figure 7.24), apart from close to the bottom of the mold and the mean V_f was about 8 vol%, which is slightly higher than for the fully relaxed state (7 vol%), owing to friction in the mold, which prevents the mat from fully relaxing. The results were therefore considered to agree well with the theoretical predictions. This model gives reasonable estimation of the time of infiltration, t_{inf}, of the dry fiber glass mat by the polymer melt and the time, $t_{equilibrium}$, required to reach the equilibrium state of the preform. These two parameters are of primary importance for the industrial impregnation process since t_{inf} determines the critical process duration time, and an homogeneous preform is needed to prevent any property gradients in the final composite part[34].

b. Simulation of impregnation with a iPP/MMT matrix

As mentioned previously in section 6.4.1, flow of non-Newtonian fluids through anisotropic porous media cannot be described directly in terms of Darcy's law because of the coupling in the mathematical description between the geometry of the porous media and the viscosity of the fluid. The local shear rate experienced by the iPP2/MMT nanocomposites during infiltration was estimated from the macroscopic velocity of the polymer during the impregnation process to be of the order of 1 s^{-1} whatever the concentration of MMT. This value corresponds to the Newtonian plateau for iPP2/1 wt% MMT, but for higher MMT concentrations, the nanocomposites show neither power-law, nor Carreau-type behavior. In addition, given the anisotropy of the glass mat places, a rigorous description of impregnation under these conditions is beyond the scope of existing models. However, it is of interest to estimate the critical times for the impregnation of the glass mat with the iPP2/MMT nanocomposite matrices and to compare these with the experimental results. For this purpose, Newtonian behavior was assumed and the viscosities taken to be equal to those at a shear rate of 1 s^{-1}. Under these conditions the viscosity of iPP2/3.4 wt% MMT was 294 Pa.s and that of iPP2/5.9 wt% MMT was 692 Pa.s.

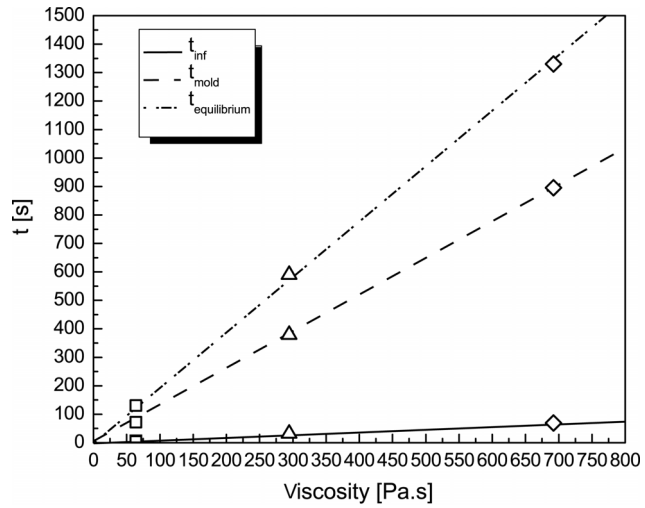

Figure 7.29. Plot of time of infiltration, t_{inf}, time for to reach the end of the mold, t_{mold}, and time to reach the equilibrium state of the mat, $t_{equilibrium}$, as a function of polymer matrix viscosity ((□) 0wt% MMT, (Δ) 3.4wt% MMT, ( ) 5.9 wt% MMT), for impregnation under an applied pressure of 0.2 MPa.

The predicted values of t_{inf}, t_{mold} and $t_{equilibrium}$ are shown in Figure 7.29 for pure iPP2, iPP2/3.4 wt% and iPP2/5.9 wt% MMT for an applied pressure of 0.2 MPa. The model predicted t_{inf} = 30 s for iPP2/3.4 wt% MMT and t_{inf} = 65 s for iPP2/5.9 wt% MMT. These results are in accordance with the experimental observations, infiltration being incomplete after 30 s for iPP2/5.9 wt% MMT. However, contrary to the theoretical model, which predicted that $t_{equilibrium}$ > 10 min, for both iPP2/3.4 wt% MMT and iPP/5.9 wt% MMT, it was observed that after 10 min of impregnation all the specimens had a

similar glass fiber distribution (Figure 7.27(b)), indicating that the equilibrium state had been reached. This discrepancy is assumed to be due to the shear thinning behavior of the nanocomposite matrices, so that the model overestimates the relaxation and equilibrium times. For short impregnation times, i.e. from 0 s to 30 s, the model correlated better with the experimental observations. In this time range, the kinetics of infiltration are significantly dependant on the viscosity of the impregnating matrix and hence decreases markedly with increasing MMT content.

7.4.4 Impregnation in hybrid GMT based on iPP/MMT nanocomposites

In order to investigate whether infiltration and gradients in the glass fibers distribution are likely to be an issue in processing conventional GMT with nanocomposite matrices, the same procedure was adopted to characterize fiber distributions in GMT-like preforms comprising two glass mats sandwiched between three films of the polymer matrix, as shown in Figure 7.30. The GMT-like preforms were compressed at 0.2 MPa, and 200 °C for 30 s. Films containing 0 wt%, 3.4 wt% and 5.9 wt% MMT were again investigated.

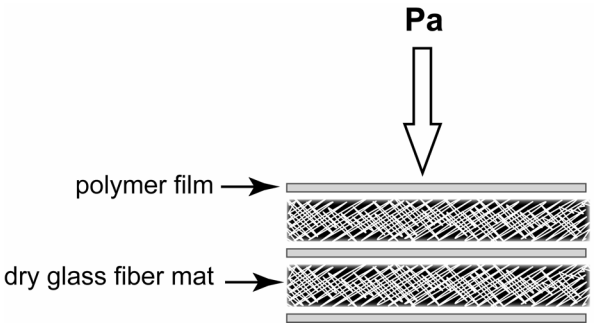

Figure 7.30. Structure of the GMT preform.

For the GMT-like specimens, the distance of impregnation was relatively short, corresponding to one sixth of the impregnation distance considered in the previous section (Figure 7.19), because each mat was sandwiched between layers of polymer matrix. Representative optical micrographs of specimens impregnated with iPP2/0 wt% MMT and iPP2/5.9 wt% MMT matrices are shown in Figure 7.31(a) and (b). After 30 s of impregnation, both specimens were well consolidated and the distribution of the glass fibers was homogeneous. Plots of $\sum_{i \le j} V_{f,i}$ versus z' (Figure 7.31) are consistent with this, all the curves lying close to $f(z') = z'$.

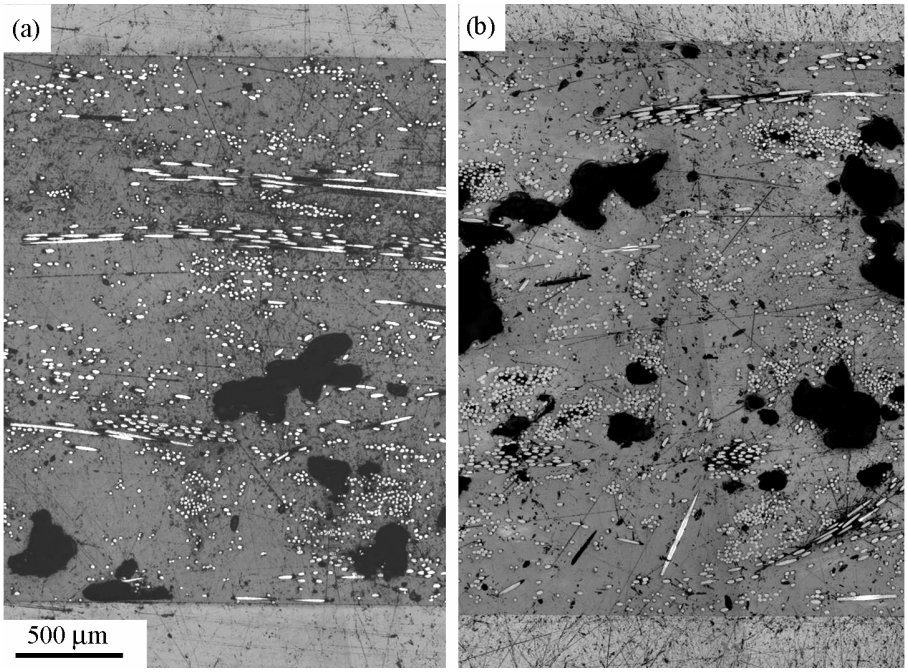

Figure 7.31. Glass fiber distribution in GMT-like specimens after 30 s of impregnation (a) with a pure iPP2 matrix and (b) with a iPP2/5.9 wt% MMT matrix.

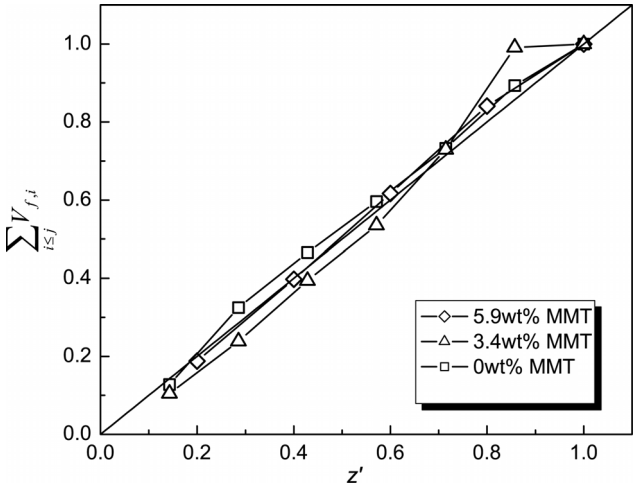

Figure 7.32. Cumulative relative fiber volume fraction from consolidation experiments on GMT-like specimens with different MMT concentrations and impregnation time of 30 s.

The porosity in the GMT-like specimens was determined by image analysis from transverse sections such as those in Figure 7.33(a) and Figure 7.33(b). It appeared that the porosity was mainly located in the matrix in both types of specimens. The results are given in Table 7.2. The porosity diminished slightly when the MMT was added to the matrix polymer. However the results were very sensitive to the location and the size of

the representative sections of the sample and there was considerable scatter in the data (up to 10 %). The size of the pores was similar for all MMT concentrations, except for the hybrid iPP2/5.9 wt% MMT, for which the pores were smaller by about 60 % than in the other specimens.

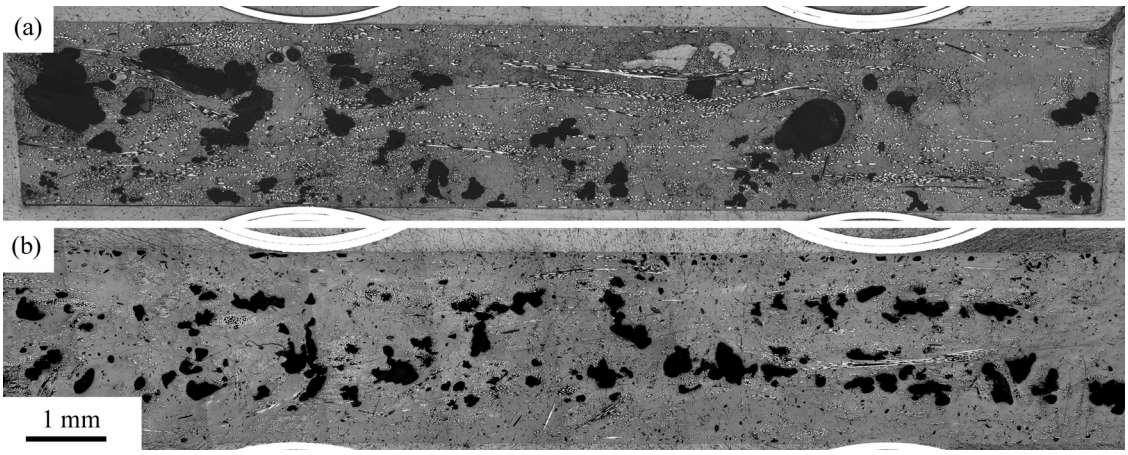

Figure 7.33. Optical micrographs of GMT-like specimens from consolidation experiments showing the porosity after 30 s of impregnation for (a) pure iPP2, and (b) iPP2/5.9 wt% MMT.

Table 7.2. Measured porosity of GMT-like specimens from consolidation experiments after 30 s of impregnation.

MMT content [wt%]	GMT porosity [vol%]
0	17.6
1	14.9
2.4	15.3
3.4	16.0
5.9	11.1

7.5 iPP2/MMT-BASED GMT: MECHANICAL CHARACTERIZATION

7.5.1 Sample processing

The GMT specimens tested in this section were produced by compression molding (Fontijne press) of two glass fiber mats sandwiched between three layers of iPP2/MMT extruded films (Figure 7.30). The stack was placed in a 120 × 50 mm^2 closed mold. The assembly was heated to 200 °C for 10 min at a constant pressure of 2 MPa, maintained at

200 °C for another 10 min, and then rapidly cooled. The resulting specimens had a glass fiber content of approximately 30 wt% and a thickness of about 2 mm. Good impregnation of the fiber beds was achieved and the porosity measured by optical microscopy was below 2 vol% for all specimens. Typical specimens are shown in Figure 7.34, together with a cross-section through a specimen containing 5.9 wt% of MMT embedded in an Epofix resin (Struers), polished and observed by optical microscopy (Figure 7.35). The processing time at temperatures above the melting temperature of the matrix was quite high (more than 10 min) and this may have affected the matrix mechanical properties and hence the mechanical properties of the final composite part[35]. However no sign of degradation in the texture or in the color was observed.

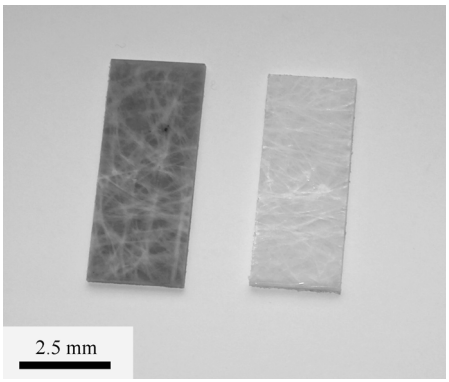

Figure 7.34. Fully consolidated GMT specimens: iPP2/5.9 wt% MMT matrix (left); pure iPP2 matrix(right).

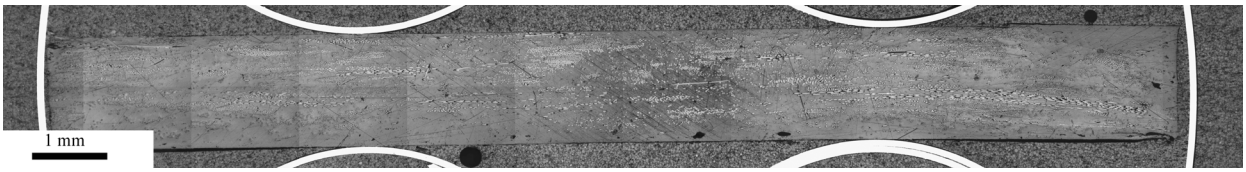

Figure 7.35. Optical micrograph of a iPP2/5.9 MMT matrix GMT showing the low porosity of a fully consolidated GMT specimen.

7.5.2 Tensile and flexural tests

a. Introduction

Bending loads are often encountered in the applications of fiber reinforced composites. Thus, characterizing the flexural behavior is of practical importance. In a fiber reinforced composite, the fibers generally dominate the tensile strength. Therefore, the increased

matrix modulus, due to the presence of silica platelets, is not necessarily expected to lead to a significant increase in the composite flexural modulus. On the other hand, the flexural response of a fiber reinforced composite is dominated by its compressive behavior, because failure usually results from buckling of the reinforcing fibers[36].The compressive strength of a fiber reinforced composite therefore depends strongly on the modulus of the matrix[37], because a higher modulus increases the lateral support of the fibers, and, hence reduces the tendency for fiber buckling. Flexural measurements are consequently a good way to measure the effect of the nanocomposite matrix on the mechanical properties of fiber reinforced composite.

b. Tensile tests on iPP2/MMT injection moldings

Results of tensile tests performed at different temperatures on injection moldings are shown in Figure 7.36(a) and (b). It has already been demonstrated in chapter 4 that the tensile test results from iPP1/MMT injection moldings were consistent with micromechanical models such as the Halpin-Tsai model. In this section, these results are confirmed for the iPP2/MMT formulations. As expected, the Young's modulus and the tensile strength decreased with increasing temperature. Moreover, at a given temperature, a marked increase in the tensile modulus was observed with increasing MMT concentration, as well as an increase in tensile strength at low MMT loadings. To assess the effect of MMT at a given temperature, the relative Young's moduli and tensile strength have been plotted as function of MMT content in Figure 7.37 (a) and (b). At all temperatures the normalized modulus gains were higher for low MMT concentrations (between 1 and 2 wt% MMT), and these gains increased with increasing temperature. Similar trends were observed for the normalized tensile strength. However, the effect of temperature was less marked at high MMT concentrations, and there was a significant drop in the nominal values of the tensile strength. This effect might at least in part be attributed to a poorer dispersion of MMT in the iPP2 matrix at high concentrations.

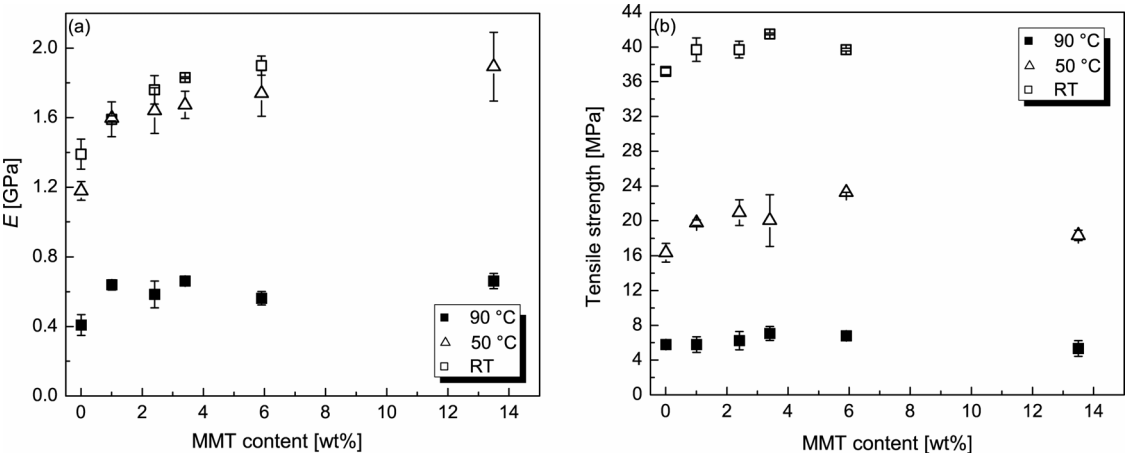

Figure 7.36. (a) Young's modulus and (b) tensile strength of injection molded iPP2/MMT nanocomposites at different temperatures as a function of MMT concentration.

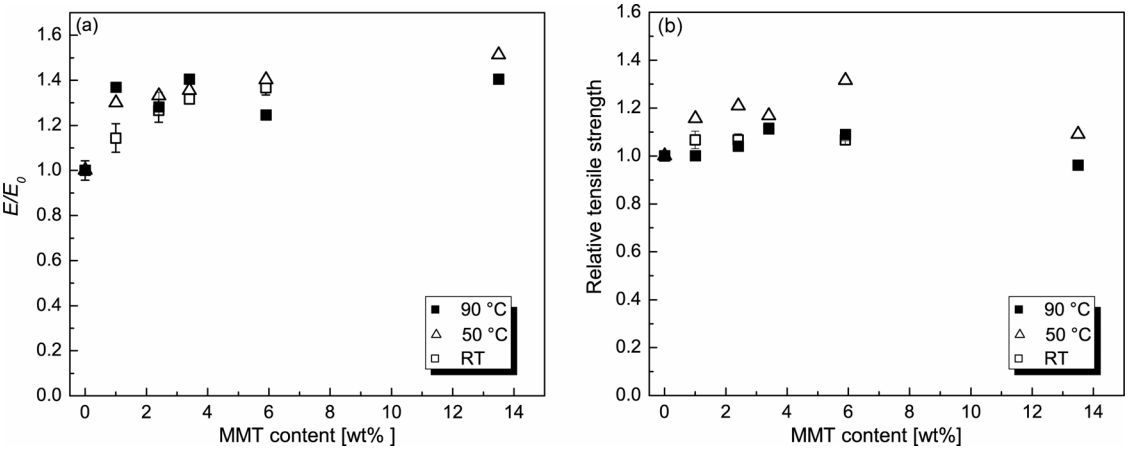

Figure 7.37. Relative (a) Young's modulus and (b) tensile strength of injection molded iPP2/MMT nanocomposites at different temperatures as a function of MMT concentration.

c. Flexural tests on iPP2/MMT-based GMTs

The influence of iPP2/MMT matrices on the flexural properties of hybrid GMT is illustrated Figure 7.38 and Figure 7.39, again at different temperatures. For a given MMT concentration, the flexural modulus and strength decreased with increasing temperature owing to the softening of the matrix. The mechanical response of GMT also showed considerable scatter owing to variations in the local microstructure of the mat[38]. At room temperature, substantial increases in both the flexural modulus and flexural strength were observed with increasing MMT concentration: 45 % for the flexural modulus and about 33 % for the flexural strength at 5.9 wt% MMT compared to the pure iPP2-based GMT specimens. This improvement in the composite mechanical properties with increasing MMT content was still observed at 50 °C but was less marked at 90 °C.

The Young's modulus of a GMT-based composite, E_{GMT}, may be modeled by adapting the rule of mixtures for composites, taking into account the "shear lag" theory developed by Cox-Krenchel[39-41]:

$$E_{GMT} = \eta_0 \eta_L V_f E_f + (1 - V_f) E_m \qquad \textbf{Equation 7.18}$$

where η_0 is a fiber orientation factor, η_L is a fiber length efficiency factor that depends on the aspect ratio of the fibers, and E_f, E_m and V_f are the fiber and matrix stiffness and the fiber volume fraction, respectively. In the case of GMT, η_L =1[33], and the average fiber orientation is random in-plane (η_0 = 0.375) but there is also fiber 3D orientation at the surface (η_0 = 0.2). For glass fibers, E_f = 76 GPa[42], and for iPP2, E_m = 1.4 GPa, as determined from tensile tests on injection moldings (Figure 7.36(a)). Using the modified rule of mixtures (Equation 7.18) for a GMT with V_f = 0.13, it was found for a random in-plane alignment of the fibers that E_{GMT} = 4.9 GPa and for a random 3D alignment, E_{GMT} = 3.2 GPa. The calculated V_f for the hybrid composites was 12.7 and 11.6 vol% respectively for matrix MMT concentrations of 3.4 wt% and 5.9 wt% respectively. In Figure 7.38, these theoretical bounds are shown for room temperature data. It is assumed

that the flexural modulus varies linearly with the tensile modulus[40, 43] and Thomason *et al.*[44] have shown that the flexural modulus may be about 25 % higher than the tensile modulus for 30 vol% short glass fiber reinforced polypropylene composites. The model correlates well with the experimental data for the pure iPP2-based composites, with the lower bound lying 16 % below the experimental GMT flexural modulus. However, the model increasingly underestimated the flexural modulus as the MMT content increased and, at 5.9 wt% MMT, the experimental modulus even exceeded the calculated upper bound. The relatively low flexural modulus of iPP2-based GMT might be attributed to a reduction in porosity with increasing MMT content, resulting in a lower effective V_f and E_M. However, no such reductions were detected experimentally. Alternatively, since the flexural modulus is not influenced by glass fiber-matrix adhesion[45], the mismatch between the experimental data and the predictions of the model may be linked to the nanocomposite matrix properties. Kanny *et al.*[46] have shown that the flexural moduli of iPP/MMT nanocomposites was systematically 20 to 40 % higher than their tensile moduli for up to 3 wt% MMT and that this difference reached 100 % for between 3 and 5 wt% MMT. Therefore the tensile modulus alone may not provide an adequate description of the matrix stiffness. Moreover, in spite of the relatively long impregnation times used for the compression molding, fiber gradients may persist and these may have a significant influence in flexion[34]. In any case, due to the heterogeneity of the glass fiber mat, additional experiments are required at a larger scale with larger specimens to confirm this result. At higher temperatures, the modulus improvement on addition of MMT was apparently reduced, and almost no improvement was observed at 90 °C. This is assumed to be because the properties are increasingly dominated by the glass fibers as the temperature increases.

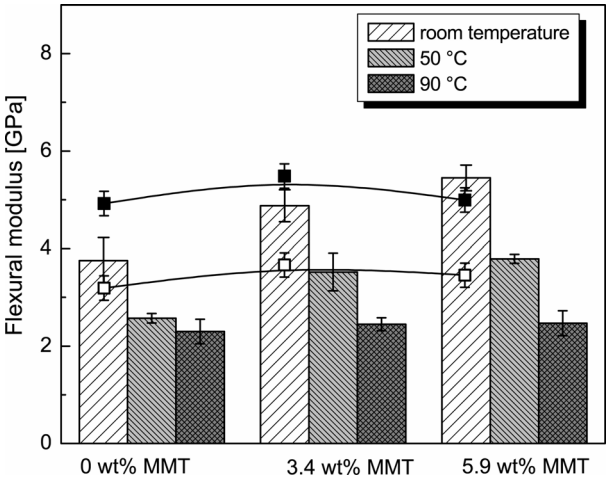

Figure 7.38. Flexural modulus from 3-point bending tests on GMT specimens as a function of MMT concentration at different temperatures. The squares correspond to the values estimated from Equation 7.18 for a pure iPP2 matrix at room temperature for η_0 = 0.375 (upper curve) and η_0 = 0.2 (lower curve).

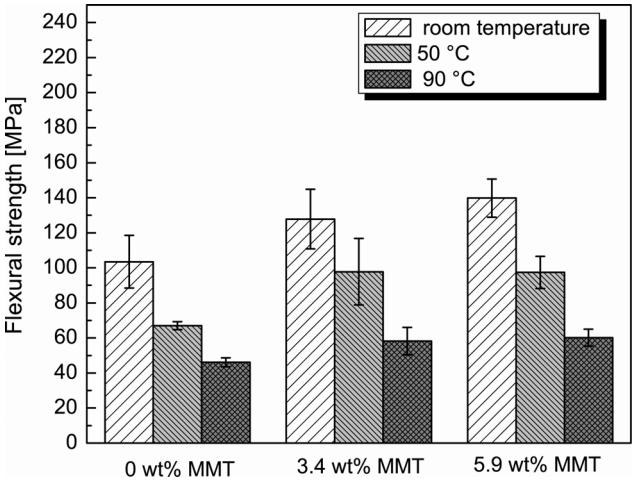

Figure 7.39. Flexural strength from 3-point bending test on GMT specimens as a function of MMT concentration at different temperatures.

Recent studies on hybrid glass fiber reinforced thermoplastics with micro-sized particulate filled iPP matrices have shown similar results. In particular, Hartikainen *et al.*[47] found that in the case of $CaCO_3$ filled iPP, there was an improvement of about 5 % in the tensile modulus on addition of 20 wt% filler to the matrix. The mean particle diameter of the $CaCO_3$ particles was about 0.2 μm in this case. They measured an increase of about 10 – 15 % in the tensile modulus of the corresponding hybrid long glass fiber (LGF) composite with a glass fiber fraction of between 4 vol% and 15 vol%, leading to a higher stiffness than would be expected on the basis of change in the matrix modulus. Crystallinity effects were excluded as an explanation for this behavior, since it was demonstrated by DSC measurements that calcium carbonate did not have a nucleating effect on iPP, as also confirmed here for MMT (section 4.3.1). On the other hand, both the strength and the strain to fail decreased on the addition of calcium carbonate. Zhao *et al.*[48] have obtained similar results with mica fillers, although they also observed a decrease in flexural strength and modulus for concentrations above 10 wt%. They attributed the strength variations to modified fiber-matrix adhesion in the filled matrices. It is well known that the use of a coupling agent (typically maleated polypropylenes and/or sizing agents for glass fibers) can significantly improve the interfacial shear strength between the matrix and the fibers and hence improve the flexural strength of the composite[38, 49]. This has also been demonstrated in the case of hybrid glass fiber reinforced epoxy/MMT composites by Norkhairunnisa *et al.*[50] who have reported an improvement of 66 % and 95 % in flexural modulus and strength respectively on addition of 3 wt% of MMT. X-ray energy dispersive analysis gave evidence for MMT adhesion to the glass fiber resulting in improved glass fiber-matrix interface.

7.5.3 Impact tests

a. Introduction

In the case of random glass fiber reinforced thermoplastics, the main impact energy absorbing mechanisms include matrix cracking, fiber fracture, debonding and fiber pull-out[51]. The use of impact tests in the framework of this study is relevant because GMT parts usually have to withstand transverse loadings and IFWI tests are particularly sensitive to interfacial changes, owing to the presence of shear stresses in the specimen during loading. The objective here is to investigate the effects of matrix modification on the impact test results. Thus, all parameters except the MMT concentration, have been kept constant and the analysis is based on the impact strength and the observation of the damaged samples. Experimental details are given in section 3.2.4.

b. Results

Visual observation of the damaged samples indicated the perforation area of the specimens to be similar for all MMT concentrations and testing temperatures i.e. a circumferential crack with the perforation hole size close to that of the dart. This suggested that the fracture mode was relatively ductile (absence of radial cracking), with efficient stress transfer within the mat. Figure 7.40 and Figure 7.41 show the force versus time and the impact energy versus time curves for the iPP2/MMT-based GMT impacted to perforation at room temperature and at 90 °C. The maximum force and the impact energy decreased with increasing MMT content in the GMT for both temperatures.

The related impact energy and impact strength are shown in Figure 7.42 as a function of temperature and the MMT content. At room temperature, the impact energy decreased markedly with increasing MMT content (Figure 7.42(a)). On the other hand, at 90 °C, the impact energy increased up to about 3.4 wt% MMT but then decreased abruptly for 5.9 wt% MMT. Since the effect of the MMT on the impact energy depended on the temperature, impact testing was inferred to be sensitive to the matrix properties. At room temperature, the increase in brittleness with increasing MMT content indicated the impact energy to be restricted by the limited deformation capacity of the matrix. On the other hand, at 90 °C, where the matrix was relatively soft, a toughening effect due to the MMT was apparent up to 3.4 wt% MMT. As shown in Figure 7.42(b), the impact strength nevertheless decreased markedly with increasing MMT content regardless of the testing temperature. Czigány *et al.*[52] argued that in the case of iPP-based GMT, the impact resistance does not depend on the testing temperature (from -40°C to 90 °C) because the major parameter controlling the fracture behavior is the mat type and its characteristics. This was not borne out by the present results.

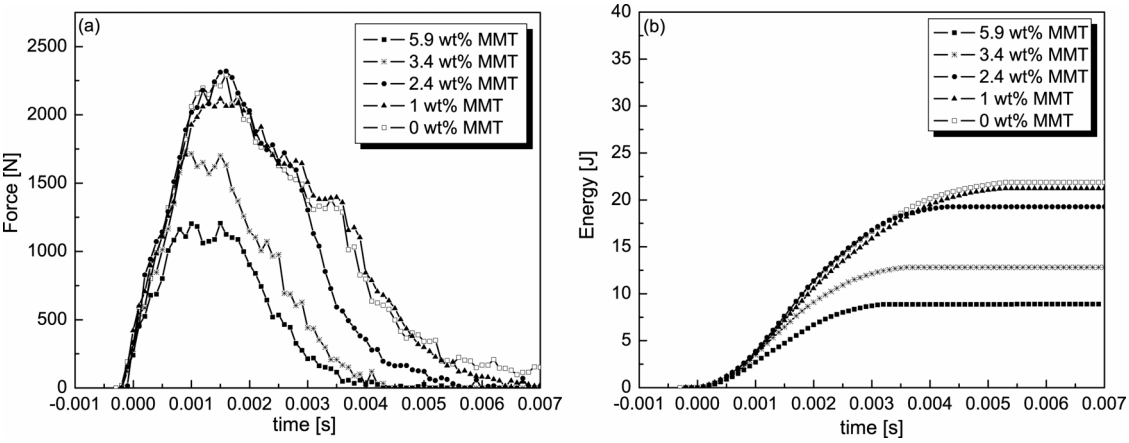

Figure 7.40. Characteristic IFWI force (a) and energy (b) versus time traces for iPP2/MMT formulations impacted at room temperature.

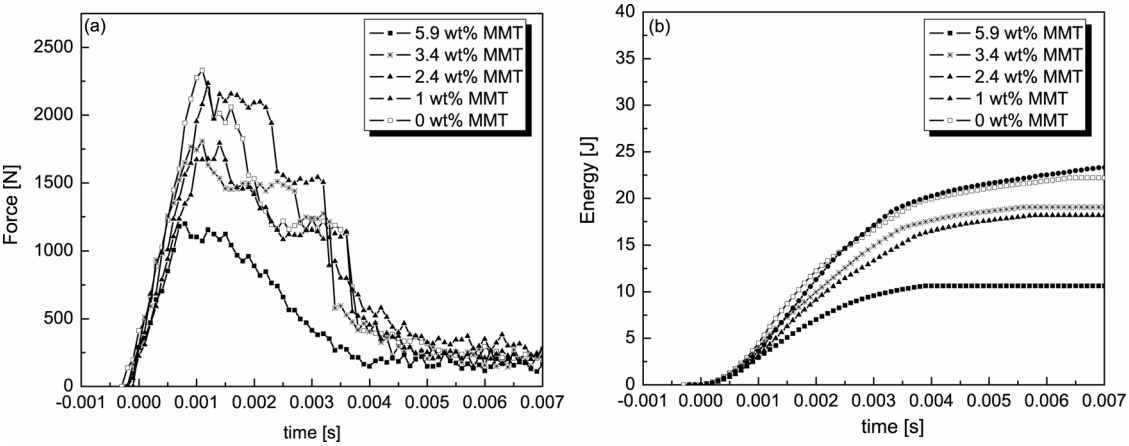

Figure 7.41. Characteristic IFWI force (a) and energy (b) versus time traces for iPP2/MMT formulations impacted at 90 °C.

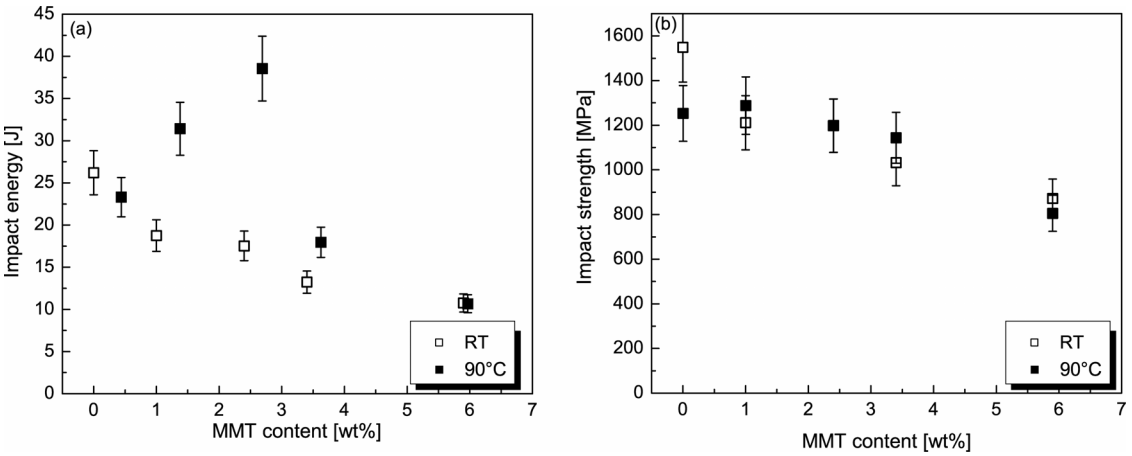

Figure 7.42. (a) Impact energy and (b) impact strength versus MMT content for iPP2/MMT-based GMT impacted at room temperature and 90 °C.

SEM analysis of the fracture surfaces provided additional information on the fracture modes. SEM micrographs were taken from representative perforated surfaces of neat iPP2 and MMT-containing fiber composites. Figure 7.43 shows typical images of the fracture surface of neat iPP2-based GMT (Figure 7.43(a)) and iPP/5.9 wt% MMT-based GMT (Figure 7.43(b)) after impact test at room temperature. For the neat iPP2 based system, the surface of the matrix appeared rather smooth and featureless, indicating brittle fracture and insignificant matrix deformation. However, significant debonding of the glass fibers was also visible, together with very clean glass fiber surfaces. These two observations are characteristic of a poor interfacial adhesion between the glass fibers and the neat iPP2 resin. In the case of the iPP2/5.9 wt% MMT matrix, the fracture surface was rougher. Furthermore, the nanocomposite matrix was present at the surface of glass fibers indicating a good interfacial adhesion between the glass fibers and the nanocomposite matrix[39, 51]. At 90 °C, in the case of the neat iPP2 matrix (Figure 7.44(a)), significant fiber pull-out was observed, but the fracture surface showed evidence for substantial shear yielding, which is consistent with the higher impact energy at 90 °C. For the iPP2/5.9 wt% MMT-based GMT, Figure 7.44(b), no major differences were observed with the specimens tested at room temperature, although the fracture surface was somewhat less rough.

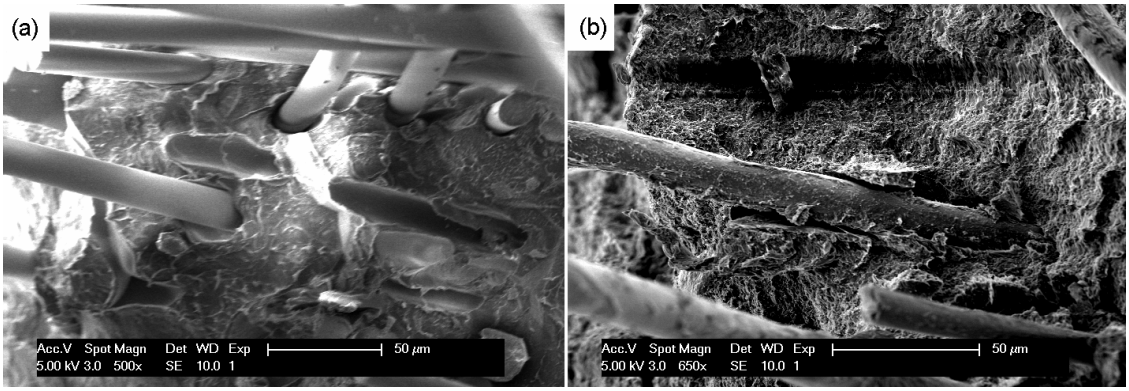

Figure 7.43. SEM micrographs of impact fracture surface of (a) iPP2 – based GMT and (b) iPP2/5.9 wt% MMT, impacted at room temperature.

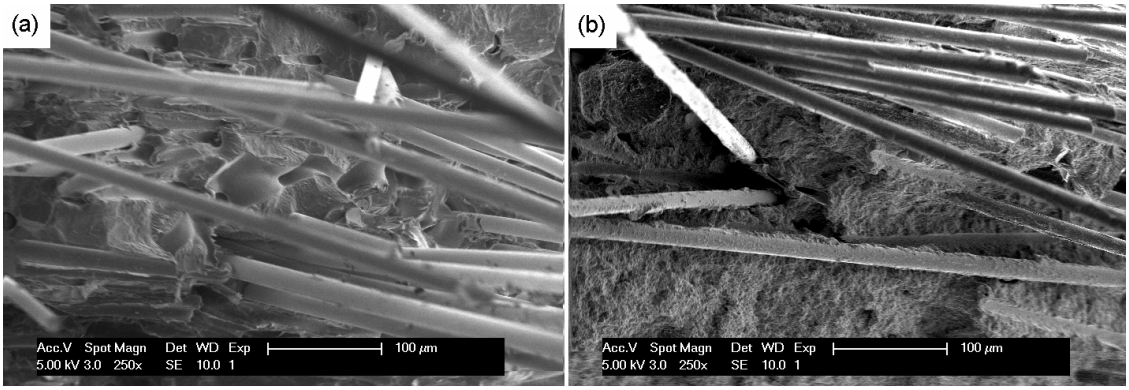

Figure 7.44. SEM micrographs of impact fracture surface of (a) iPP2 – based GMT and (b) iPP2/5.9 wt% MMT, impacted at 90 °C.

7.6 CONCLUSION

It has been shown in this chapter that the effect of the viscosity of the polymer melt on the impregnation is intimately related to the geometry of the dry preform and dependent on the external applied pressure. Thus, for a given applied pressure, the effect of the addition of MMT platelets on the viscosity was negligible when the impregnation distance was reduced. On the other hand, the influence of the viscosity was more marked, for example, in the UD preform geometry, for which the permeability was significantly reduced owing to the applied pressure. It follows that the effect of MMT on impregnation mechanisms is only important for short impregnation times and long impregnation distances. In such cases, significant fiber gradients were observed in the fiber mat in the presence of MMT. Thus it was concluded that morphologies that promote intimate mixing between the reinforcing fibers and the iPP/MMT matrix are desirable to reduce

the impregnation distance, and hence limit the effect of increased viscosity. However, the experimental results were more encouraging than the simulation results in the case of dry glass mats impregnated with iPP2/MMT, and for long impregnation times, saturated and homogeneous glass fiber distributions were obtained at all MMT concentrations. Analysis of GMT-like specimens showed that after 30 s of impregnation, the specimens generally had similar fiber distributions regardless of the MMT content. A small decrease of the porosity in the specimens was observed on the addition of MMT, although no change was observed in the wetting behavior of the nanocomposite melt. The shear deformation associated with the impregnation process in the present case did not lead to any increase in intercalation or the aspect ratio of the silica platelets. Moreover, TEM images revealed no filtration of the nanocomposite platelets by the glass fiber tows as opposed to what observed in the case of iPP1/CNF nanocomposites.

Table 7.3. Mechanical properties of iPP2/MMT injection moldings and iPP2/MMT GMTs

	Injection moldings Tensile						GMT Flexural						GMT Impact					
MMT content [wt%]	Modulus [GPa]			Strength [MPa]			Modulus [GPa]			Strength [MPa]			Energy [J]			Strength [MPa]		
	RT	50	90	RT	50	90	RT	50	90	RT	50	90	RT	50	90	RT	50	90
0	1.39	1.27	0.57	37.2	19.5	10.1	3.75	2.57	2.3	103.5	46.1	-	26.2	-	23.3	1549	-	1252
1	1.59	1.65	0.78	39.7	22.5	10.1	-	-	-	-	-	-	18.7	-	31.4	1211	-	1286
2.4	1.76	1.69	0.73	39.7	23.5	10.5	-	-	-	-	-	-	17.5	-	38.5	1197	-	1197
3.4	1.83	1.72	0.8	41.5	22.7	11.2	4.87	3.52	2.45	127.8	52.7	-	13.2	-	17.9	1032	-	1143
5.9	1.9	1.78	0.71	39.7	25.6	11	5.45	3.79	2.47	139.8	66.7	-	10.8	-	10.6	871	-	804
13.5	1.94	1.92	0.8	34.1	21.2	9.7	-	-	-	-	-	-	-	-	-	-	-	-

The mechanical properties of the iPP2/MMT injection moldings and iPP2/MMT GMTs are summarized in Table 7.3. Tensile tests on injection molding specimens of iPP2/MMT showed that gains in modulus and strength on MMT addition were achieved at low MMT and intermediate temperatures. The influence of the matrix on the mechanical properties of glass fiber reinforced composites is generally difficult to assess since a significant part of the load is taken up by the reinforcing fibers. The addition of MMT to the matrix also led to improvements in the hybrid glass fiber reinforced composites, especially at intermediate temperatures and low MMT loadings, and significant gains in both flexural modulus and strength were observed. For high temperatures, the apparent contribution of the matrix to the mechanical properties of the composite was substantially reduced for all MMT concentrations. In attempts to understand these observations, a classical mechanical model was used to predict the GMT stiffness. It was found that the model calculation underestimated the observed improvements. It was suggested that the reinforcement effect of the MMT was more significant in the flexural response than in the tensile response of the nanocomposites. In addition, SEM images showed an improvement in the interfacial adhesion between the glass fibers and the matrix accounting for the improvement in flexural strength in the hybrid composites.

To summarize, neither the viscosity of the nanocomposite melt nor filtration effects, appear to be critical issues for the consolidation of long glass fiber or glass mat reinforced iPP/MMT composites given suitable processing conditions. Moreover, it appears that

both iPP/MMT yarns and films are suitable precursors for integrating MMT platelets in conventional thermoplastic composites, in particular when intimate mixing between the reinforcing fibers and the matrix precursors is ensured.

7.7 REFERENCES

1 Q. H. Zeng, A. B. Yu, G. Q. Lu and D. R. Paul, **Clay-based polymer nanocomposites: Research and commercial development**, *Journal of Nanoscience and Nanotechnology*, 2005; **5** (10): 1574-1592

2 E. C. Lee, D. F. Mielewski and R. J. Baird, **Exfoliation and dispersion enhancement in polypropylene nanocomposites by in-situ melt phase ultrasoniaction**, *Polymer Engineering and Science*, 2004; **44** (9): 1773-1781

3 P. E. Bourban, N. Bernet, J. E. Zanetto and J. A. E. Månson, **Material phenomena controlling rapid processing of thermoplastic composites**, *Composites Part a-Applied Science and Manufacturing*, 2001; **32** (8): 1045-1057

4 E. T. Thostenson, C. Y. Li and T. W. Chou, **Nanocomposites in context**, *Composites Science And Technology*, 2005; **65** (3-4): 491-516

5 V. Michaud and J. A. E. Månson, **Impregnation of compressible fiber mats with a thermoplastic resin. Part I: Theory**, *Journal Of Composite Materials*, 2001; **35** (13): 1150-1173

6 T. Matsuo, T. Yuba and K. Kawabe, **Impregnation behaviors in composite processing - Theoretical consideration and experiments for thermoplastic composites**, *International Polymer Processing*, 2002; **17** (1): 76-82

7 R. Phillips, D. A. Akyuz and J. A. E. Månson, **Prediction of the consolidation of woven fibre-reinforced thermoplastic composites. Part I. Isothermal case**, *Composites Part A-Applied Science And Manufacturing*, 1998; **29** (4): 395-402

8 L. Ye, K. Friedrich, J. Kastel and Y. W. Mai, **Consolidation Of Unidirectional Cf/Peek Composites From Commingled Yarn Prepreg**, *Composites Science And Technology*, 1995; **54** (4): 349-358

9 C. Mayer, X. Wang and M. Neitzel, **Macro- and micro-impregnation phenomena in continuous manufacturing of fabric reinforced thermoplastic composites**, *Composites Part A-Applied Science And Manufacturing*, 1998; **29** (7): 783-793

10 N. Bernet, **Commingled yarn composites for rapid processing of complex shapes**, Thesis, EPFL, Lausanne, (2000)

11 R. Törnqvist, **Tailored rheological and mechanical properties of fibre mat reinforced thermoplastics**, Thesis, EPFL, Lausanne, (2000)

12 K. J. Ahn, J. C. Seferis and J. C. Berg, **Simultaneous Measurements Of Permeability And Capillary-Pressure Of Thermosetting Matrices In Woven Fabric Reinforcements**, *Polymer Composites*, 1991; **12** (3): 146-152

13 P. Nygard, K. Grundke, E. Mader and C. Bellmann, **Wetting kinetics and adhesion strength between polypropylene melt and glass fibre: influence of chemical reactivity and fibre roughness**, *Journal Of Adhesion Science And Technology*, 2002; **16** (13): 1781-1808

14 S. Toll and J. A. E. Månson, **Elastic Compression of a Fiber Network**, *Journal of Applied Mechanics-Transactions of the Asme*, 1995; **62** (1): 223-226

15 W. H. Ruan, X. B. Huang, X. H. Wang, M. Z. Rong and M. Q. Zhang, **Effect of drawing induced dispersion of nano-silica on performance improvement of poly(propylene)-based nanocomposites**, *Macromolecular Rapid Communications*, 2006; **27** (8): 581-585

16 M. Erdal, S. I. Guceri and S. C. Danforth, **Impregnation molding of particle-filled preceramic polymers: Process modeling**, *Journal Of The American Ceramic Society*, 1999; **82** (8): 2017-2028

17 Z. H. Fan, K. T. Hsiao and S. G. Advani, **Experimental investigation of dispersion during flow of multi-walled carbon nanotube/polymer suspension in fibrous porous media**, *Carbon*, 2004; **42** (4): 871-876

18 M. Wysocki, R. Larsson and S. Toll, **Hydrostatic consolidation of commingled fibre composites**, *Composites Science And Technology*, 2005; **65** (10): 1507-1519

19 S. G. Advani, **Flow and rheology in polymer composites manufacturing**, Elsevier, Amsterdam etc., (1994)

20 R. P. Chhabra, J. Comiti and I. Machac, **Flow of non-Newtonian fluids in fixed and fluidised**

beds, *Chemical Engineering Science*, 2001; **56** (1): 1-27

21 T. S. Lundstrom, H. Sundlof and J. A. Holmberg, **Modeling of power-law fluid flow through fiber beds**, *Journal Of Composite Materials*, 2006; **40** (3): 283-296

22 P. D. M. Spelt, A. Y. Yeow, C. J. Lawrence and T. Selerland, **Creeping flows of Bingham fluids through arrays of aligned cylinders**, *Journal Of Non-Newtonian Fluid Mechanics*, 2005; **129** (2): 66-74

23 J. K. Woods, P. D. M. Spelt, T. Selerland and C. J. Lawrence, **Creeping flows of power-law fluids through periodic arrays of elliptical cylinders**, *Journal Of Non-Newtonian Fluid Mechanics*, 2003; **111** (2-3): 211-228

24 Z. Idris, L. Orgeas, C. Geindreau, J. F. Bloch and J. L. Auriault, **Microstructural effects on the flow law of power-law fluids through fibrous media**, *Modelling And Simulation In Materials Science And Engineering*, 2004; **12** (5): 995-1015

25 H. Yaguchi, H. Hojo, D. G. Lee and E. G. Kim, **Measurement Of Planar Orientation Of Fibers For Reinforced Thermoplastics Using Image-Processing**, *International Polymer Processing*, 1995; **10** (3): 262-269

26 A. C. Long, C. E. Wilks and C. D. Rudd, **Experimental characterisation of the consolidation of a commingled glass/polypropylene composite**, *Composites Science And Technology*, 2001; **61** (11): 1591-1603

27 Y. Leterrier and C. Gsell, **Formation and Elimination of Voids During The Processing of Thermoplastic Matrix Composites**, *Polymer Composites*, 1994; **15** (2): 101-105

28 M. D. Wakeman, T. A. Cain, C. D. Rudd and A. C. Long, **Compression Moulding of Glass and Polypropylene Composites for Optimised Macro- and Micro- Mechanical Properties II. Glass-Mat-Reinforced Thermoplastics**, *Composites Science and Technology*, 1999; **59** 709-726

29 J. L. Sommer and A. Mortensen, **Forced unidirectional infiltration of deformable porous media**, *Journal Of Fluid Mechanics*, 1996; **311** 193-217

30 J. Wolfrath, V. Michaud and J. A. E. Månson, **Deconsolidation in glass mat thermoplastic composites: Analysis of the mechanisms**, *Composites Part a-Applied Science and Manufacturing*, 2005; **36** (12): 1608-1616

31 V. Michaud, R. Tornqvist and J. A. E. Månson, **Impregnation of compressible fiber mats with a thermoplastic resin. Part II: Experiments**, *Journal Of Composite Materials*, 2001; **35** (13): 1174-1200

32 Y. K. Hamidi, L. Aktas and M. C. Altan, **Three-dimensional features of void morphology in resin transfer molded composites**, *Composites Science And Technology*, 2005; **65** (7-8): 1306-1320

33 J. Wolfrath, **Consolidation and deconsolidation in composite processing**, Thesis, EPFL, Lausanne, (2004)

34 J. Wolfrath, V. Michaud and J. A. Månson, **Graded glass mat-reinforced polypropylene**, *Polymer Composites*, 2005; **26** (3): 361-369

35 M. N. Bureau and J. Denault, **Fatigue resistance of continuous glass fiber/polypropylene composites: consolidation dependence**, *Composites Science and technology*, 2004; **64** 1785-1794

36 D. P. N. Vlasveld, H. E. N. Bersee and S. J. Picken, **Nanocomposite matrix for increased fibre composite strength**, *Polymer*, 2005; **46** (23): 10269-10278

37 C. R. Schultheisz and A. M. Waas, **Compressive failure of composites .1. Testing and micromechanical theories**, *Progress In Aerospace Sciences*, 1996; **32** (1): 1-42

38 J. Karger-Kocsis, **Swirl mat- and long discontinuous fiber mat-reinforced polypropylene composites - Status and future trends**, *Polymer Composites*, 2000; **21** (4): 514-522

39 J. L. Thomason and M. A. Vlug, **Influence of fibre length and concentration on the properties of glass fibre-reinforced polypropylene .4. Impact properties**, *Composites Part A-Applied Science And Manufacturing*, 1997; **28** (3): 277-288

40 S. Shibata, Y. Cao and I. Fukumoto, **Press forming of short natural fiber-reinforced biodegradable resin: Effects of fiber volume and length on flexural properties**, *Polymer Testing*, 2005; **24** (8): 1005-1011

41 D. Hull, **An Introduction to composite materials**, Cambridge University Press, Cambridge a.o., (1981)

42 G. Lubin, **Handbook of composites**, Van Nostrand Reinhold, New York a.o., (1982)

43 J. L. Thomason and M. A. Vlug, **Influence of fibre length and concentration on the properties of glass fibre-reinforced polypropylene .1. Tensile and flexural modulus**, *Composites Part A-Applied Science And Manufacturing*, 1996; **27** (6): 477-484

44 J. L. Thomason, **The influence of fibre length and concentration on the properties of glass fibre reinforced polypropylene. 6. The properties of injection moulded long fibre PP at high fibre content**, *Composites Part A-Applied Science And Manufacturing*, 2005; **36** (7): 995-1003

45 H. A. Rijsdijk, M. Contant and A. Peijs, **Continuous-Glass-Fiber-Reinforced Polypropylene Composites .1. Influence of Maleic-Anhydride-Modified Polypropylene on Mechanical-Properties**, *Composites Science and Technology*, 1993; **48** (1-4): 161-172

46 K. Kanny and V. K. Moodley, **Characterization of polypropylene nanocomposite structures**, *Journal of Engineering Materials and Technology-Transactions of the Asme*, 2007; **129** (1): 105-112

47 J. Hartikainen, P. Hine, J. S. Szabo, M. Lindner, T. Harmia, R. A. Duckett and K. Friedrich, **Polypropylene hybrid composites reinforced with long glass fibres and particulate filler**, *Composites Science And Technology*, 2005; **65** (2): 257-267

48 R. Zhao, J. Huang, S. Bin and G. Dai, **Study of the mechanical properties of mica-filled polypropylene-based GMT composite**, *Journal Of Applied Polymer Science*, 2001; **82** (11): 2719-2728

49 J. L. Thomason and G. E. Schoolenberg, **An Investigation of Glass-Fiber Polypropylene Interface Strength and Its Effect on Composite Properties**, *Composites*, 1994; **25** (3): 197-203

50 M. Norkhairunnisa, A. B. Azahar and S. C. W., **Effects of organo-montmorillonite on the mechanical properties of epoxy/glass fiber composites**, *Polymer International*, 2007; **56** 512-517

51 X. D. Zhou, G. Dai and Q. F. Lin, **Improvement in impact property of continuous glass mat reinforced polypropylene composites**, *Journal Of Applied Polymer Science*, 2002; **83** (12): 2680-2688

52 T. Czigany and J. Karger-Kocsis, **Comparison of the instrumented falling weight impact response of polypropylene composites reinforced by continuous and discontinuous fiber mats**, *Journal Of Reinforced Plastics And Composites*, 2001; **20** (12): 996-1012

CHAPTER 8

CONCLUSIONS AND PERSPECTIVES

8.1 GENERAL SUMMARY

The principal objective of this work has been to investigate the feasibility of integrating isotactic polypropylene (iPP)-based nanocomposite matrices into conventional glass fiber reinforced composites using conventional processing routes. The potential of this approach was assessed in terms of the mechanical properties of the resulting hybrid composites. The nanofiller of principal interest was an organically modified montmorillonite clay (MMT), selected for its commercial availability and the reported improvements in e.g. mechanical properties, flame resistance, thermal stability and gas barrier resistance when it is added to a range of thermoplastic polymer matrices. The present work was nevertheless intended to provide a template for the integration of other types of nanocomposite system into conventional composites, and certain methodologies were therefore also extended to iPP/nanocarbon nanocomposites. The study involved three basic processing steps: preparation of iPP-based nanocomposites, manufacture of fiber or film precursors and impregnation/consolidation of co-wound and co-woven long glass fiber composites (LGF) and glass mat reinforced thermoplastics (GMT) based on these precursors. Conventional thermoplastic and thermoplastic-based composite processing techniques were employed throughout, e.g. melt-mixing and compression molding, with the aim of demonstrating the potential for scale-up to industrial processes. However, these processes were also used as a vehicle for obtaining a fundamental understanding of process–morphology–property relationships in iPP-based nanocomposites.

8.2 CONCLUSIONS

8.2.1 iPP-based nanocomposites

Dispersion is a major issue in polymer/nanofiller nanocomposites. In the particular case of iPP, the apolar nature of the polymer and the relatively high viscosity of the melt (about 300 Pa.s at 220 °C) make it difficult to break up nanofiller aggregates during melt-mixing. For iPP/MMT nanocomposites, the two preparation routes investigated, namely

combined solvent and melt-mixing, and direct melt-mixing, provided a homogeneous anisotropic nanocomposite with a mixed intercalated/exfoliated morphology. In the case of the combined solvent and melt-mixing, the interlayer spacing was up to about 57 % larger than that of the organically modified silicates, suggesting it to be possible to achieve a fully exfoliated iPP/MMT nanocomposite with appropriate processing conditions (an increase in compatibilizer content for example). However, this processing route is of limited interest from the industrial point of view, being time consuming and requiring an organic solvent, with the attendant safety and storage issues. Combined solvent and melt-mixing was shown to be more suitable for dispersing carbon nanofibers (CNF), which tended to form agglomerates (about 0.2 μm in diameter). However, the iPP/MMT nanocomposites used for the subsequent processing steps were prepared systematically by direct melt-mixing from a commercial masterbatch consisting of 40 - 50 wt% organically modified MMT, iPP and a iPP compatibilizer. The process conditions were the same as for pure iPP and resulted in a 6 % increase of the interlayer spacing of the MMT with respect to that in the masterbatch.

Injection moldings of the melt-compounded iPP/MMT were shown by TEM to contain randomly oriented MMT particles with an aspect ratio of about 50. The Young's modulus increased monotonically with increasing MMT, with a 40 % increase being observed for iPP/13.5 wt% MMT, for example. A maximum 10 % improvement in tensile strength was observed at about 3 wt% MMT, but the tensile strength decreased on further MMT addition. For a given MMT content, the absolute values of the Young's modulus decreased with increasing temperature, but significant relative modulus gains (up to 50 %) were achieved at low MMT contents (between 2 – 3 wt%), particularly at high temperatures (90 °C).

8.2.2 Fiber and film precursors

Pre-compounding of iPP/MMT nanocomposites was essential for the manufacture of semi-finished products in the form of fibers and films, in order to eliminate processing flow instabilities such as die swell in the case of fibers, and inhomogeneities in the films. The addition of MMT to the iPP matrices therefore involved additional process time and energy consumption compared with that required for the pure iPP matrices. The melt spinnability was assessed in terms of rheological measurements, and a reduced process window was predicted for iPP/MMT owing to a significant increase in melt elasticity, such that the storage elastic modulus *G'* exceeded the loss modulus *G"* and the relaxation times increased by about 140 % on addition of 13.5 wt% MMT. Melt spinning of iPP/MMT nanocomposites was therefore limited to 5 wt% MMT, and the extent of cold drawing was limited even at lower MMT contents, owing to cohesive fracture. This was not of significant concern for composite processing, however, since any orientation or thermal history is expected to be lost on melting of composite preforms. Moreover, excessive drawing may lead to excessive fiber shrinkage, which is detrimental for consolidation processes. Thermo-mechanical analysis (TMA) measurements nevertheless suggested MMT to improve the thermal stability of the fibers, the onset of extensive fiber creep being shifted from 90 °C for pure iPP fibers to about 110 °C for iPP/1.1 wt% MMT fibers. Moreover, shrinkage was also reduced from about 4 % for iPP fibers to less than 1

% for iPP/4wt% MMT fibers, which was considered to represent a potential advantage in further textile based composite processing. The process stability of extrusion-calendering was also improved on MMT addition.

The axial tensile stiffness of the fibers and films increased significantly with respect to that of the injection moldings owing to the preferential orientation of MMT platelets along the melt flow direction, as observed by TEM. During fiber spinning, in which the polymer melt undergoes uniaxial elongational flow, the MMT platelets were not only particularly highly oriented along the fiber axis but also showed increased aspect ratios of the order of 150. The iPP lamellae were also observed to be arranged perpendicularly to MMT platelets in the fibers as a result of iPP chain elongation in the melt flow direction, as confirmed by wide angle X-ray diffraction (WAXS). Thus, the increase in Young's modulus reached 170 % at 2 wt% MMT. This was consistent with the predictions of the Halpin-Tsai and Mori-Tanaka micromechanical models for anisotropic composites with an aspect ratio of 150. The tensile strength of the fibers, on the other hand, was about 50 % lower than for the injection moldings, although a maximum was again observed at about 3 wt% MMT. In the case of the iPP/CNF melt-spun fibers, the processing window extended to higher particle contents, but the stiffness was lower than predicted by micromechanical models on the basis of ideal CNF properties, owing to the presence of aggregates, and only partial orientation of the CNF, which tended to remain coiled or bent. Therefore, for similar filler contents and processing conditions, the stiffness of iPP/CNF fibers was about 50 % lower than that of iPP/MMT fibers.

The forces developed during extrusion-calendering are generally lower than during fiber spinning and only partial orientation of platelets in the flow direction was observed by TEM. However, the tensile moduli were still significantly higher (about 50 %) for specimens tested in the melt direction than for specimens tested in the transverse direction. The stiffness was consistent with micromechanical models for anisotropic composites and the observed MMT particle aspect ratio of about 50. The fracture mechanisms were also directly related to the orientation of MMT platelets in the films. When oriented perpendicularly to the crack propagation direction, the MMT particles provoked deviations in the crack propagation path, and the fracture resistance was therefore increased at low MMT concentrations. In other orientations, however, the fracture resistance was found to decrease, presumably owing to the relative weakness of the particle-matrix interface and/or decohesion of the MMT layers.

8.2.3 Impregnation

Above their melting point, the iPP/MMT nanocomposites were characterized by increasingly solid-like behavior with increasing MMT concentration at low shear rates (a two fold increase in viscosity between 1 and 3.4 wt% MMT) and shear thinning at high shear rates. This behavior was accounted for by the formation of a weak MMT network that broke up at high shear rates. The viscosity is a critical parameter for impregnation kinetics and it was therefore important to assess the effect of the MMT on impregnation times. Experimental trials were carried out on hybrid composites containing 10 to 40 vol% co-wound or co-woven glass fiber/iPP/MMT textile preforms, and glass mat

preforms. The strong dependence of the viscosity on shear rate in the presence of MMT was reflected by the important role of the glass fiber preform geometry in the impregnation kinetics. For the 40 vol% glass fiber co-wound specimens, the porosity in iPP/3.4 wt% MMT composites compression molded at 200 °C and 1.8 MPa was twice that in iPP–based composites compression molded at 200 °C and 0.6 MPa. The flow rates were in this case estimated to be of the order of 10^{-3} s^{-1}, i.e. within the shear rate regime in which the influence of the MMT on viscosity was predominant. However, when intimate mixing between the reinforcing fibers and the matrix was ensured by co-weaving iPP/3.4 wt% MMT fibers and glass fibers, well consolidated composites (porosity of about 2 vol%) were obtained after compression molding at 220 °C and 1.2 MPa. Despite the loss of MMT orientation subsequent to compression molding, the MMT particles maintained the high aspect ratios observed in the precursor fibers. Moreover, no filtering of the MMT was observed, unlike in CNF-based hybrid composites where filtration was unavoidable owing to the presence of large aggregates. For the purposes of modeling the impregnation kinetics of glass fiber mats in GMT preforms, the iPP/MMT matrix was therefore considered to behave as a continuum and to be Newtonian. Experimental observations of glass mat infiltration and relaxation in model preforms indicated that for short impregnation times (0 to 30 s) and relatively high MMT concentrations (5.9 wt%), the level of impregnation and consolidation was significantly less than for pure iPP specimens. The predictions of a linear impregnation model were consistent with the experimental results for the pure iPP matrix. However, it overestimated the times required to impregnate glass mats with iPP/MMT matrices. This mismatch was attributed to the shear thinning behavior of iPP/MMT melts at the deformation rates of the order 1 s^{-1} characteristic of glass mat compression molding. Thus, with geometries representative of industrial GMT preforms, with lower flow distances than in the model preforms, compression molded at 0.2 MPa at 200 °C, the glass mat was fully relaxed after 30 s of compression at all MMT contents and the porosity was in between 11 – 17 vol %. The use of iPP/MMT nanocomposites was therefore concluded to be compatible with industrial processing (residence times typically between 20 and 60 s).

8.2.4 Hybrid composites

Fully consolidated 30 wt% GF-hybrid GMT-like specimens were obtained by compression molding at 2 MPa and 200 °C for 10 min. The porosity of the resulting hybrid composites was about 2 vol %. The impact strength and energy of the hybrid composites, determined by instrumented falling weight impact (IFWI), decreased with increasing MMT at room temperature, reflecting the limited deformation capacity of the matrix, inferred from the data of the precursor films, and a reinforced fiber-matrix interface, as evidenced by fractography of the impacted hybrid GMT. At 90 °C, the impact energy increased with MMT content up to 3 wt% MMT but then decreased at higher MMT contents, resulting from increased matrix ductility at elevated temperature. At any given MMT content, the flexural modulus and strength decreased with increasing temperature. At room temperature, the flexural modulus and strength of iPP/MMT-based GMT increased monotonically with MMT resulting in a 45 % and 33 % improvement, respectively, at 5.9 wt% MMT. Moreover, the extent of the improvement of the flexural modulus on MMT addition was greater than that predicted by a conventional rule of

mixtures including a glass fiber orientation factor and a length factor and using Young's moduli of injection moldings. Although the reasons for this are not clear, it may be in part due to differences in the evolution of the tensile and compression moduli with MMT content. At higher test temperatures, on the other hand, the effect of the MMT was less marked, presumably because the mechanical properties are increasingly dominated by those of the fibers.

8.3 CONCLUDING REMARKS AND PERSPECTIVES

This work has shown that iPP/MMT nanocomposites may be successfully integrated into conventional glass fiber composites using melt-spun fibers and extrusion-calendered films as precursors, with demonstrable improvements in mechanical properties in the case of consolidated GMT-based composites. Even in the presence of the MMT, the kinetics of the impregnation process were sufficiently rapid for this approach to be consistent with industrial processing. When the degree of MMT particle orientation and the particle aspect ratio were increased, as in the melt-spun fibers, the mechanical properties were correspondingly better and the relatively high particle aspect ratios were conserved in the final hybrid composites. This suggests there to be considerable scope for further optimizing the dispersion, intercalation/exfoliation and aspect ratio of the MMT particles in the precursors and semi-finished products, in order to improve further the mechanical properties in the hybrid composites. The next major step in the context of hybrid iPP/MMT GF reinforced composites will be to scale up the present study, in order to measure the level of impregnation of glass fiber mats achieved when using an industrial lamination line and to confirm the mechanical test results. It would also be of interest to investigate the influence of MMT on the flow properties of the melted semi-finished GMT preforms and subsequent composite part processing. In addition to improved mechanical properties, other non-structural functionalities may provide significant added value to hybrid polymer composites and offset price penalties. In the case of hybrid iPP/MMT-based composites, thermal stability, flame resistance and permeability may also be improved, but remain to be characterized. As this general approach may be used for different type of nanofillers, further types of non-structural functionality may also be envisaged. Carbon nanotubes are potentially able to provide combined structural reinforcement and thermal and electrical conductivity for example. Hybrid polymer composite technology is also believed to have significant potential for composites based on engineering polymers, in which performance plays a more important role in development than for commodity polymers such as iPP. To our knowledge, nanocomposites based on technical polymers such as polyphenylene sulfide (PPS) have not yet been considered as composite matrices.

Appendix A – List of symbols

Symbol	*Unit*	*Significance*
Roman letters		
d	m	Particles diameter
d	nm	MMT interlayer spacing
d	m	Single filament diameter
d_0	m	Spinneret channel diameter
D	m	Yarn diameter
D	m	Undoloid drop diameter
D_e	m	Equivalent hydraulic channel diameter
D_f	m	Fiber diameter
DR		Hot draw ratio
E_c	Pa	Composite Young's modulus
E_f	Pa	Reinforcing phase Young's modulus
E_m	Pa	Matrix Young's modulus
E_{peak}	J	Energy at maximum force
E_{tot}	J	Total absorbed energy
F	N	Tensile force
F_L	N	Force in the spinline at a distance L from the spinneret
F_{peak}	N	Maximum force
G'	Pa	Storage modulus
G''	Pa	Loss modulus
H	m	Length of DENT specimens
J_{IC}	KJ m^{-2}	Critical value at the onset of crack propagation
K	Pa	Bulk modulus
K_p	m^2	Permeability
l	m	Filament length in DENT specimens
l_0	m	Spinneret channel length
L	m	Length of the spinline
L_f	m	Filament length
L_f	m	Die length
n		Orientation factor
n		Number of filament in the spineline
n		Power law index
P_c	Pa	Capillary pressure
Q	$m^3\ s^{-1}$	Volume flow rate
R	m	Die radius
r	m	Glass fiber radius
R_f	m	Filament radius
R_0	m	Filament radius at the die exit
t	m	Specimen thickness
T	Tex	Yarn fineness
T_c	°C	Crystallization peak temperature
T_m	°C	Melting temperature
T_0	°C	Extrusion temperature
V_f	mm min^{-1}	Haul-off wheel velocity

V_f	%	Reinforcing phase volume fraction
V_{g1}	m min^{-1}	First godet speed
V_{g2}	m min^{-1}	Second godet speed
V_l	m min^{-1}	Drive-roll velocity
V_0	m min^{-1}	Velocity at the die exit
V_0	m min^{-1}	Extrusion velocity
W	g s^{-1}	Mass flow rate
W	m	Width of DENT specimens
W_f	KJ m^{-2}	Total work of fracture
$W_{fillers}$	%	Fillers weight fraction
W_l	KJ m^{-2}	Essential work of fracture
W_p	KJ m^{-2}	Non-essential work of fracture
X_c	%	Degree of crystallinity

Greek letters

α		MMT platelet aspect ratio
γ_{LV}	J m^{-2}	Surface tension of the wetting liquid
$\dot{\gamma}$	s^{-1}	Shear rate
$\dot{\gamma}_a$	s^{-1}	Apparent shear rate at the wall
$\dot{\gamma}_W$	s^{-1}	True shear rate at the wall
H_c	J g^{-1}	Crystallization enthalpie
$H_f°$	J g^{-1}	Heat of fusion of 100 % crystalline iPP
H_m	J g^{-1}	Melting enthalpie
P	Pa	Pressure drop over the capillary
P_0	Pa	Pressure drop over zero die length
ε_H		Hencky strain
η	Pa s	Shear viscosity
η_0	Pa s	Zero shear rate viscosity
ν		Poisson's ratio
$ø$	%	Particle volume fraction
θ	°	X-ray diffraction angle
θ	°	Contact angle
λ		Global draw ratio
λ	nm	Wavelength of X-ray radiation
μ	Pa.s	Apparent uniaxial viscosity
μ	Pa	Shear modulus
ν_0		Poisson's ratio
ρ_0	g cm^{-3}	Density of the melt
σ	Pa	Melt stress
σ_{max}	Pa	Melt strength
σ_{max}	Pa	Maximum net section stress
σ'_{max}	Pa	Tensile strength
σ_y	Pa	Yield stress
τ_0	Pa	Yield stress
τ_W	Pa	Stress at the channel wall
ω	rad s^{-1}	Angular frequency

Appendix B – List of abbreviations

Abbreviation	*Description*
$CaCO_3$	Calcium carbonate
CNF	Carbon nanofiber
CNT	Carbon nanotube
decalin	Hydrodecanaphtalin
DENT	Double edge notched tensile
DSC	Differential scanning calorimetry
DTMA	Dynamic thermomechanical analysis
EVA	Ethylene vinyl acetate
FTIR	Fourrier transform infrared
GF	Glass fiber
GMT	Glass mat thermoplastic
HDT	Heat deflection temperature
HRR	Heat release rate
IFPZ	Internal fracture process zone
IFWI	Instrumented falling weight impact
iPP	Isotactic polypropylene
LEFM	Linear Elastic Fracture mechanics
LGF	Long glass fiber
LLDPE	Linear low density polyethylene
MD	Melt direction
MMT	Montmorillonite
MWNT	Multi-walled carbon nanotube
OFPZ	Outer fracture process zone
PA	Polyamide
PEEK	Polyetheretherketones
PET	Polyethylene terephtalate
PPMAH	Maleic anhydride modified polypropylene
PPOH	Hydroxyl modified polypropylene
PPS	Polyphenylene sulfide
RuO_4	Ruthenium tetraoxide
SAXS	Small angle X-ray diffraction
SEM	Scanning electron microscopy
sPP	Syndiotactic polypropylene
SWNT	Single-walled carbon nanotube
TD	Transverse direction
TGA	Thermogravimetric analysis
TMA	Thermomechanical analysis
UD	Unidirectionnal
VGCF	Vapor grown carbon nanofiber
WAXS	Wide Angle X-ray diffraction
XRD	X-ray diffraction

Chrystèle Houphouet-Boigny
Passage Mathias Mayor 4
1004 Lausanne - Switzerland
(+41) 78 757 43 93
chrystele.houphouet@a3.epfl.ch

Born August 16th, 1977
Ivory Coast, France

WORK EXPERIENCE

2002 – 2007 **Laboratory of Composite and Polymer Technology**, Swiss Federal Institute of Technology (EPFL), Lausanne, Switzerland
- Ph.D thesis:"Fiber Reinforced Polypropylene Nanocomposites"

2001 (6 months) **Diamed/ADS SA,** Cressier s/Morat, Switzerland
- Graduate thesis: "Immobilization of Streptavidin on Polystyrene"

1999 - 2000 (12 months) **Surface Engineering and Molecular Assemblies Laboratory**, Iowa State University, Ames, United States
- Research assistant

EDUCATION

2002 **International Institute for Management Development (IMD)**, Lausanne, Switzerland
- Building on Talent Program

1997 - 2002 **Swiss Federal Institute of Technology (EPFL)**, Lausanne, Switzerland
- MSc in Material Sciences

1999 - 2000 **Iowa State University**, Ames, United States
- BSc in Material Sciences

CONFERENCES & PUBLICATIONS

- C. Houphouet-Boigny, C.J.G. Plummer, M.D. Wakeman, J-A.E. Månson, *Hybrid Glass-Fiber Reinforced Thermoplastic Nanocomposites*; Sampe Europe. 2005. Paris

- C. Houphouet-Boigny, C.J.G. Plummer, M.D. Wakeman, J-A.E. Månson, *Hybrid Glass-Fiber Reinforced Thermoplastic Nanocomposites*; ICCM 15. 2005. Durban; To appear in Journal of Thermoplastic Composite Materials

- C. Houphouet-Boigny, C.J.G. Plummer, M.D. Wakeman, V. Michaud, J-A.E. Månson, *Glass Fiber Reinforced Polypropylene Nanocomposites*; ICCM 16. 2007. Kyoto

- C. Houphouet-Boigny, C.J.G. Plummer, M.D. Wakeman, J-A.E. Månson, *Towards Textile-Based Fiber Reinforced Thermoplastic Nanocomposites: Melt-spun Polypropylene-Montmorillonite Nanocomposite Fibers*; To appear in Polymer Engineering and Science

- C. Houphouet-Boigny, C.J.G. Plummer, M.D. Wakeman, V. Michaud, J-A.E. Månson, *Glass Fiber Reinforced Polypropylene Nanocomposites*; To be submitted